COMISION NACIONAL DE ENERGIA ATOMICA

TANDAR

NUCLEAR PHYSICS WORKSHOP

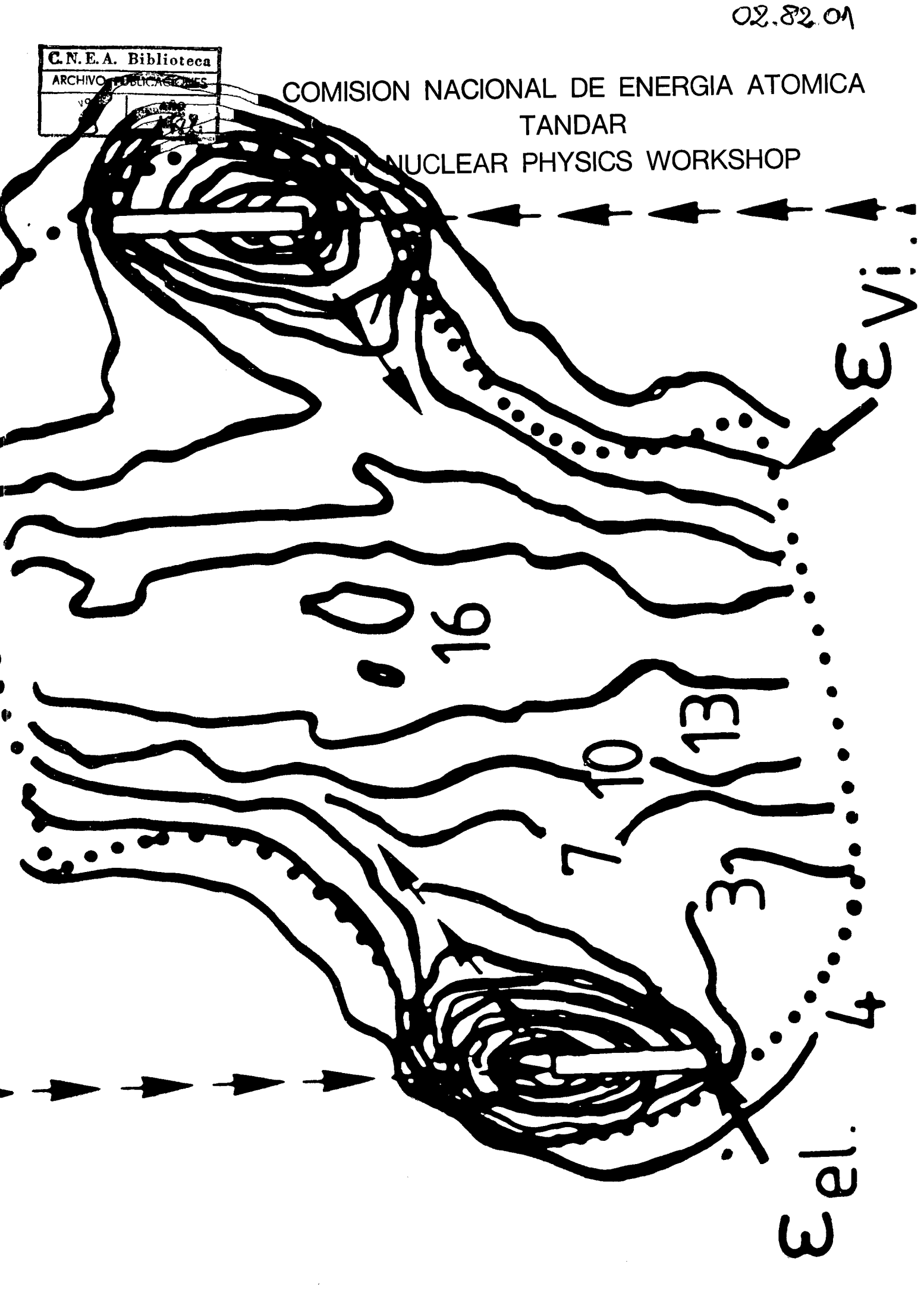

CNEA - NT. 8/82

IV Nuclear Physics Workshop

Buenos Aires 18 - 29 May, 1981

Department of Physics

Comisión Nacional
de Energía Atómica

Dirección de
Investigación y Desarrollo

Gerencia de
Investigaciones

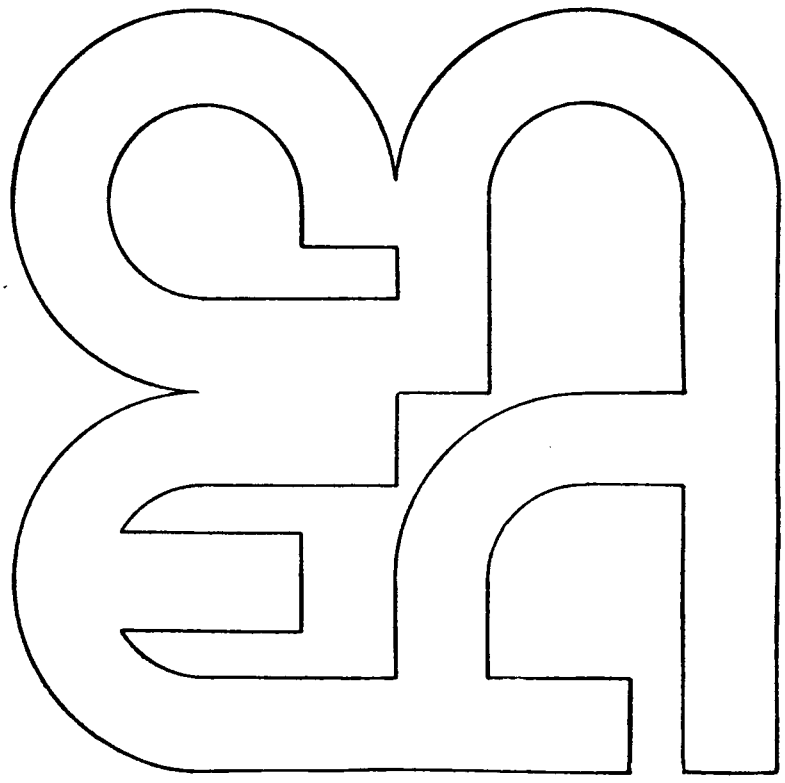

Buenos Aires - Argentina
1981

The IVth Nuclear Physics Workshop was sponsored by the Comisión Nacional de Energía Atómica. A grant from the Consejo Nacional de Investigaciones Científicas y Técnicas (National Research Council) is graeatfully acknowledged.

INTRODUCTION

The IVth Nuclear Physics Workshop represents our contribution of a compromise which after four year has become a tradition of the TANDAR Project.

The construction of the new laboratoires has entered during 1981 a whole new stage. The assembling of the accelerator is a task rich in details, all of them important, all of them requiring special cares. In circumstances like this, the interruption of our usual daily chores represented a rewarding task, by rendering our projects richer and by recharging our hopes.

The subjects that were chosen for this opportunity are closely related to those of the preceeding Workshop. They have helped us to get involved in the details and enjoy the fascination of some fields that are now within the reach of our new machine.

In addition to our friends of other institutions of Argentina and Brazil, we had invited lectures by S.Bjørnholm from the Niels Bohr Institute and M.Macfarlane of the Indiana University. We received from them not only exciting conferences but also help for our present and future work in physics.

The organizing committee wishes to thank to all those which in one way or another helped in the success of the meeting. We also wish to mention specially the invaluable collaboration of María Teresa Carmuega and Marta Gismondi that took care of the typing and edition of these proceedings and to Drs. D.Otero and A.Proto for their carefull proofreading.

Organizing Committee

R.P.J.Perazzo
O.Dragún

INTRODUCCION

Con los anales de esta IVa. Reunión de Trabajo de Física Nuclear contribuimos a dar continuidad a un compromiso que, a lo largo de cuatro años, ha comenzado a ser ya una tradición más del Proyecto TANDAR.

La construcción de los laboratorios ha entrado de lleno, durante 1981 en la etapa de montaje del acelerador que se multiplica en una continua diversidad de detalles, todos importantes, todos de cuidado. Es en estas circunstancias que la interrupción de las tareas cotidianas que impone la Reunión cumple mejor su cometido de recargar las esperanzas y enriquecer los proyectos.

Los temas elegidos para esta oportunidad guardan una estrecha relación con los de la anterior y han servido para adentrarse en los detalles y disfrutar más aún del campo de trabajo que se abre ante nosotros con la nueva máquina.

Además de nuestros amigos de otras instituciones, tanto de Argentina como de Brasil, nos han visitado en esta oportunidad, como conferenciantes invitados los Dres. Sven Bjørnholm del Instituto Niels Bohr de Copenhagen y Malcolm Macfarlane de la Universidad de Indiana. De ellos no sólo recibimos excelentes exposiciones sino el apoyo para nuetro trabajo en física presente y futuro.

El Comité Organizador desea agradecer especialmente a todos aquellos que de una u otra manera contribuyeron al buen éxito de la Reunión. Deseamos mencionar especialmente la invalorable colaboración prestada por María Teresa Carmuega y Marta Gismodi que tuvieron a su cargo el dactilografiado, composición y edicion de notas así como a los Dres. D.Otero y A.Proto por su cuidadosa lectura y corrección de pruebas.

Comité Organizador

R.P.J.Perazzo
O.Dragún

TIME	Monday 18	Tuesday 19	Wednesday 20	Thursday 21	Friday 22	Tuesday 26	Wednesday 27	Thursday 28	Friday 29
9.30 to 10.30 am	FREE	Macfarlane	Seminar(2)	Macfarlane	Seminar(4)	Macfarlane	Seminar(6)	Macfarlane	Macfarlane
	C O F F E E			C O F F E E			C O F F E E		
10.30 to 11.45 am	FREE	Seminar(1)	VISIT	Bjornholm	Bjornholm	Seminar(5)	Bjornholm	Bjornholm	Bjornholm
12.00 to 1.00 pm	L U N C H		TO	L U N C H			L U N C H		
			TANDAR						
2.30 to 3.30 pm	Macfarlane	*	ABS.	*	*	*	*	*	*
4.00 to 4.30 pm	Bjornholm								
4.30 to 5.30 pm	*	*		Seminar(3)	*	*	*	Seminar(7)	*
	C O F F E E			C O F F E E			C O F F E E		

*) Free for informal discussions.

TABLE OF CONTENTS

1. DIRECT REACTION STUDIES WITH LIGHT AND HEAVY IONS AT LOW INTERMEDIATE ENERGIES.

Prof. Malcolm Macfarlane

1.I Effective interactions and a brief history of nuclear shell theory 1
1.II Calculational technique for direct reactions 32
1.III Heavy-ion transfer reactions. Energy-depedence and channel-coupling effects 53

2. THE DYNAMICS OF HEAVY ION FUSION REACTIONS

Prof. Sven Bjørnholm

2.I Introduction 77
2.II One-dimensional fusion models in theory and in practice 79
2.III W.J.Swiatecki's three-dimensional dynamical model of nuclear coalescence and reseparation in theory and practice (reported from an internal report, W.J.Swiatecki, "The dynamics of nuclear coalescence or reseparation" , June 1980, LBL-10911.....104
2.IV From entrance to exit channel: gamma-ray multiplicities and saddle shapes 152
2.V From entrance to exit channel: the pre-scission stage 168
2.VI From entrance to exit channel: angular distributions and total reaction times 171
2.VII Summary and Conclusion 176
REFERENCES 177

3. NUCLEI AT VERY HIGH ANGULAR MOMENTUM

Prof. Sven Bjørnholm

3.I Introduction. Nuclear structure under rotation.....181
3.II Shell model nuclei 186
3.III Deformed nuclei 194
REFERENCES 213

4. INVITED TALKS

4.I On the quantum mechanics of DIC. A tropical rhapsody on northern themes

A.F.R. de Toledo Piza 217

4.II A new tool in nuclear spectroscopy: Pair exchange reactions

D.R.Bes, O.Dragún and E.E.Maqueda 229

4.III Dependence of energy loss of heavy ions on the number of the stopping medium

M.N.Rao 237

4.IV Schrödinger damping of collective motion

S.Hernández 243

4.V Charge-exchange collective states

F.Krmpotić 251

5 PARTICIPANTS 285

DIRECT REACTION STUDIES WITH LIGHT AND HEAVY IONS AT LOW AND INTERMEDIATE ENERGIES

PROF. MALCOLM MACFARLANE

DEPARTMENT OF PHYSICS, INDIANA UNIVERSITY
INDIANA, U.S.A.

CHAPTER I

EFFECTIVE INTERACTIONS AND A BRIEF HISTORY OF NUCLEAR SHELL THEORY

#I.1 Statement of Main Themes

Direct reactions-those that occur in about the time it takes the colliding particles to cross the interaction region-have told us much of what we know about the internal structure of nuclei. They also play a special role in the attempt to understand the low-energy properties of nuclei viewed as many-body systems of interacting nucleons. In this undertaking, the theory of direct reactions is the extension of the many-particles shell model - the most fundamental of nuclear models - to the continuum. These lectures deal with various aspects of the spectroscopic approach to nuclear direct reactions, discussing the underlying many-body theory, various technical aspects of direct-reactions calculation and recent pertinent experiments in light- and heavy-ion physics. There are three main themes.

A) I will discuss the status of attempts to derive the key effective interactions - the optical potentials and channel coupling potentials for light and heavy-ion direct reactions, the shell-model effective interaction -from the force between free nucleons. Calculations of effective interactions always yield two distinct sorts of contributions - a nuclear-matter-like contribution that varies slowly from one nucleus to the next and a part that depends explicitly on the particular collective excitation possessed by the nucleus or nuclei under consideration. The nuclear-matter component is common to all effective interactions

discussed here -it is a G-matrix, a 'soft' tractable two-body effective interaction that replaces and thereby defangs the bare nuclear-nuclear interaction with its strong shortrange repulsion. It will be useful to consider the shell-model and direct-reaction variants of effective interaction in parallel and to consider some historical parallels as well.

B) There have been recent technical developments of great potential significance in multi-channel direct-reaction calculations. These developments in computational technique were inspired by dire necessity in studies of heavy-ion direct reactions but may well have their greatest impact in light-ion physics. In the middle 1960's, radical improvements in our ability to carry out many-particle shell-model calculations played a central part in providing a many-body foundation for nuclear shell theory. It is likely that the comparable technical developments, described in some detail below, in multi-channel reaction calculations will change the future course of direct-reactions physics.

C) A direct reaction has two characteristic empirical features-its asymmetric, usually forward-skewed angular distribution, and its smooth energy-dependence. Past studies of direct reactions have overwhelmingly concentrated on the first of these characteristic properties. This stems in part from the nature of the models used to interpret the data and in part form the history of accelerator-development. The stress on angular distribution studies has had an immense influence on the fields - an influence for both good an ill. The good influence is too well-known to need much discussion here - it is simply the gathering of a vast body of information on single-particle, single-hole and other nuclear excitations their widths, strengths, positions and variation throughout the nuclear periodic table, The ill effects are also pronounced; they stem from the fact that in discussing angular distributions and

relative strengths of groups of direct transitions at a given energy, it is often fatally easy to conceal shortcomings in the reaction model by parameter-adjustments. A shift of attention to the second and more basic characteristic of a direct reaction- its energy-dependence-will reveal much more of the underlying reaction dynamics. I will discuss what has been learned from the few studies so far carried out of light-and heavy-ion reactions over wide energy ranges and argue that future experiments should trace the crosssections of selected transitions -selected for simplicity or intrinsic interest of the nuclear states involved- over wide ranges of energy.

#I.2 Truncation and Effective Interactions

Whatever may be said about the nature of physics, there is no doubt that a vital property of theoretical physicists is the fact that they can give exact solutions to a very small number of problems. Thus much of the practical application of theoretical physicists consists in attempts to force one of a small stock of solutions down the protesting throat of a complex problem. It is therefore not surprising that the same theoretical techniques and constructs should recur over and over again in solid-state, molecular, nuclear and high-energy physics; it is even less surprising that the same approach should be used in different but related context will nuclear physics.

Faced by the intractable infinite Hilbert-space $\mathcal{H}$ of the A-body nuclear system, the nuclear physicist reacts by thrawing most of it away and confining attention to a finite, although possible quite large, subspace d. This finite subspace d is called a "model space"; it is hoped that many properties or processes of interest can be adquately represented (modelled) within d. The price to be paid is that the 'true' nucleon-

nucleon interactions in $\mathcal{H}$ are replaced by effective interactions in d.

Complete Hilbert space of system	Finite model space d
(ΣV_{ij} in $\mathcal{H}$)	(V_{eff} in d)

(I.1)

Thus truncation of the complete Hilbert space yields an effective interaction V_{eff} in d that reflects the influence on affairs within of the excluded part of Hilbert space[2,3].

a) Many-particle shell model

The basic act of truncation here rests on the empirical properties of the nuclear single-particle spectrum, in particular on the fact that nuclear single-particle states occur in bunches (major shells) with sizeable energy-gaps between. To describe low-lying states of a given nucleus, it is then assumed that most of the nucleons form an inert core and that a model space may be used in which a few 'active' nucleons populate a few 'valence orbits'.

$$\text{e.g.} \left\{ \begin{array}{c} \mathcal{H} \\ \text{for } {}^{19}F \end{array} \right\} \longrightarrow \left\{ \begin{array}{c} d \\ ({}^{16}O) + (1d_{5/2}, 2s_{1/2}, 1d_{3/2})^3 \end{array} \right\} \qquad \text{(I.2)}$$

The effective shell-model interaction is then

$$H_{eff} = H_{s.p.} + V_{eff} \qquad \text{(I.3)}$$

where $H_{s.p}$ is the single-particle potential and V_{eff} the residual interaction between nucleons. It is usually assumed that V_{eff} is a two-body inteaction although no many-body theory gives this as an exact result if the number of active nucleons is greater than two!

b) Coupled-channel reactions models

In direct-reactions studies, truncation of the Hilbert space is

based on the fact that some reactions channels are more strongly coupled to the incident or elastic channel than others. The Schrodinger equation is then solved in a finite model space spanned by the elastic channel, the channel whose reaction cross section is under consideration and those other channels strongly coupled to the channels of primary interest.

If only the elastic channel is retained in the model space we obtain the single-channel optical model, describing only elastic scattering. The effective interaction, describing the main effects of coupling to (and absorption into) excluded channels, is the optical potential.

$$V_{eff} \longrightarrow V_{opt} \qquad (I.4)$$

To discuss a non-elastic reaction, for example a (d.p) reaction A (d,p)A+1 in this simple framework we may assume that the model space contains two elastic channels A+d, (A+1)+p, with a weak coupling between them. The coupled equations for this two-channel model space can then be solved in first Born approximation. No coupled equations are actually solved, instead two optical-model calculations are carried out and a transition matrix element evaluated. The elements of the effective interaction are the two diagonal optical potentials and the transition potential including nuclear-transfer This procedure is of course the distorted-wave Born approximation (DWBA) .

The shell-model analog of the extreme single-channel optical model is of course the single-particle shell model, wherein nuclear ground states are described by single Slater determinants. It is well-known that this description of most nuclear ground states is so inadequate that it is hopeless to try to relate the effective interaction that give the nuclear ground-state energy in the single-particle model to the free-nucleon interaction. Only when many-particle shell-model technology had progressed to the point of making two-to-eight-particle calculations routinely possible did significant progress occur in giving a many-body

interpretation of phenomenological shell-model interactions. The question naturally arises whether a similar situation occurs in direct-reaction theory. It is known, of course, that the single-channel optical model has far greater physical content than the single-particle model of nuclear ground states. As discussed later, it seems that the single-channel optical potential for nucleon-nucleus scattering below 60 MeV can be related quantitatively to the free-nucleon interaction. The situation for higher-energy nucleon-nucleus collision and for heavy-ion reactions is less clear. It is possible that no microscopic derivation of optical and coupling potentials that is valid over wide ranges of bombarding energy can be achieved without invoking multi-channel model spaces. The danger is that necessary model spaces become so large that the necessary coupled-channel calculations are either impossible or too cumbersome and time-consuming to be worthwhile. Recent advances in the calculational technique for direct reactions make this danger significantly less threatening than it appeared to be two or three years ago and therein, of course, lies their importance.

#I.3 The Many-Particle Shell Model and its Effective Interaction

Return now to the first of the effective-interaction problems mentioned above - the derivation of many-particle shell-model Hamiltonians from the free-nucleon interaction. This problem has been extensively studied over the past fifteen years; for a description of the wide varie-ty of relevant studies, see the review article of Barrett and Kirson[4]. In the past five years, activity in the field has noticeably diminished. This reflects the fact the type of "shell-model" that emerges from many-body theory is not the same as the phenomenological

shell model; the many-body shell model has an effective interaction with three and more-body components that varies with the number of valence nucleons. The point where development has stopped is that at which the nuclear-matter, two-body part of the effective interaction has been brought under control; faced by the fact that the next step in the many-body derivation leads away from the phenomenological shell-model, theorists have simply abandoned the microscopic approach and treated the remaining corrections phenomenologically.

There are compelling reasons for this apparently-timorous strategy. The shell-model is not only used directly to provide detailed description of nuclear level - properties; more frequently and more significantly it serves as the starting point for such enterprises as Hartree-Fock-Bogoliubov calculations for deformed nuclei[5], the interacting-boson approximation[6], nuclear field theory[7], and boson-expansion studies of many-nucleon system[8], all of which seek to provide a microscopic foundation for nuclear collective models. Such studies, which are in some sense the heart of theoretical nuclear physics, are complicated enough with conventional two-body, number-independent shell-model Hamiltonians; they would be driven out of the realm of possibility by the introduction of many-body terms in the interaction or by giving the interaction matrix-elements some complicated explicit dependence on the number of active nucleons. Thus the place of the shell-model in the larger view of nuclear physics dictates that is should be the shell-model in its simple conventional form that emerges from microscopic derivations and not some more involved variant.

Studies of microscopic shell-model effective interactions have a number of highly-technical aspects[4] extension of closed-shell perturbation expansions to open-shell nuclei, ensuring the Hermiticity of the effective interaction, studies of the convergence of the expansions,

separation of core and valence contributions and so forth. To present the main ideas without becoming enmeshed in technical details, I will adopt a historical approach.

Two important and influential studies - one by Kuo and Brown[9] of microscopic effective interactions for ^{18}O, ^{18}F , the other by Chung and Wildenthal[10] of refinements of the Kuo-Brown interaction for the entire ds-shell will provide the focus of my presentation. They have led to a shell-model description of ds-shell nuclei that is both remarkably successful in reproducing the data and soundly-founded in many-body theory (although not, as we will see, exactly derived there from!). I shall weave a description of the current state of microscopic nuclear shell theory around a discussion of these papers.

The shell model truncation procedure for ds-shell nuclei is sketched in figure I.1. The 1s and 1p orbits are filled to make up the inert ^{16}O core; the remaining active nucleons populate the ($1d_{5/2}$, $2s_{1/2}$, $1d_{3/2}$) orbits in the next major shell while the orbits of all higher shells are empty. The model spaces for positive-parity states in ds-shell nuclei

$$\{ {}^{16}O, {}^{17}O, {}^{17}F, {}^{18}O, {}^{18}F, {}^{19}O, {}^{19}F, \ldots {}^{24}Mg, \ldots {}^{28}Si, \ldots {}^{39}Ca, {}^{40}Ca \}$$

are built by placing ν neutrons and π protons in the (1d,2s) orbits;

$$\left.\begin{aligned} d\left(n, \tfrac{\nu-\pi}{2}\right) &= \left(1d_{5/2}, 2s_{1/2}, 1d_{3/2}\right)^{\nu,\pi} \\ \nu + \pi &= n \end{aligned}\right\} \qquad (I.5)$$

with n = o for ^{16}O, n= 2 for ^{18}O, ^{18}F .... n = 24 for ^{40}Ca.

Shell-model calculations within these and similar model spaces proceed in four shell well-defined steps.

1) An effective interaction within the model spaces

$$H_{eff} = H_{s.p} + V_{eff} \qquad (I.6)$$

is devised (by procedures discussed in I.3, I.4).

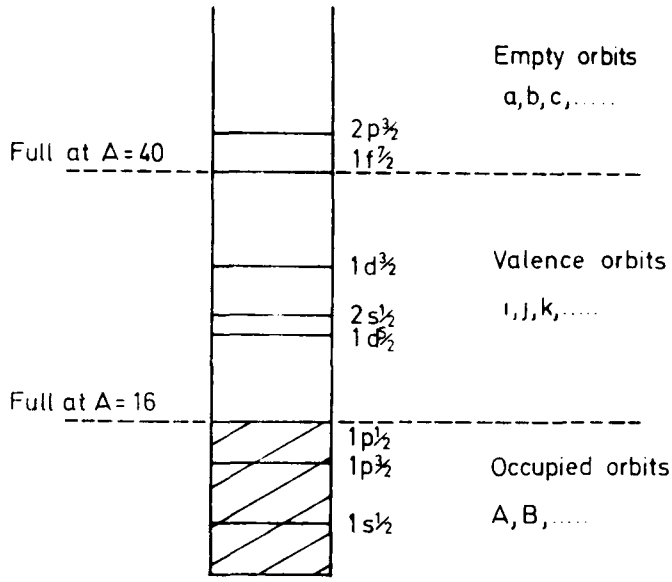

Figure I.1:

Illustration for (1d,2s)-shell nuclei of the major-shell gaps and the associated shell-model truncation-procedure. The notation used is in the text for emply, valence and occupied orbits is also shown.

2) A complete basis of n-particle states of specified total angular momentum J, isospin T is constructed in each model space.

3) The matrices of Heff in these bases are constructed and diagonalized. The eigenvalues are compared with observed level energies.

4) The energy eigenvalues are used, with appropriate effective transition operators, to compute moments and transitions rates.

Techniques for carrying out steps 2) to 4) of many-particle shell-model calculations were greatly improved during the years 1965-70; they are discussed for example by Kurath in ref.[2] and do not concern us here.

In the phenomenological shell-model, two further assumptions, without foundation in many-body theory, are made about the effective interaction. It is assumed:

1) V_{eff} is a two-body operator

2) The single-particle and two-body components $H_{s.p}$, V_{eff}

of the effective interaction are the same for all nuclei considered. These assumptions have the important consequence that the effective interaction within the model spaces is characterized by a finite number of two body matrix elements. For the ds-shell these matrix elements are as follows.

$H_{s.p}$: 3 single-particle matrix elements

$$\langle i|H_{s.p.}|i\rangle \ , \ i = d_{5/2},\ s_{1/2},\ d_{3/2}. \tag{I.7}$$

V_{eff}: 63 two-body matrix elements

$$\langle ijJT|V_{eff}|klJT\rangle A$$

$$(i,j,k,l) = (d_{5/2}\ s_{1/2}\ d_{3/2}) \tag{I.8}$$

and it is assumed that single-particle wave functions are used that diagonalize $H_{s.p.}$. The subscript A in (I.8) indicates that the matrix elements are taken between antisymmetric two-particle states.

There are in principle two sorts of procedure that could be followed to derive the necessary interaction matrix elements.

1) Microscopic procedure. Derive $H_{s.p.}$ and V_{eff} from the interaction between free nucleons. Now it is known[12] that the zero-energy limit of the nucleon-nucleus optical potential is a real potential whose bound-state spectrum (for each value of A) yields an adequate description of single-particle levels near the Fermi surface. The essential task is thus derivation of the two-body residual interaction, with derivation of the single-particle energies a minor part of the calculation of the nucleon-nucleus optical potential.

2) Phenomenological procedure. Determine the 66 interaction parameters by a least-squares fit to observed levels energies.

Kuo and Brown adopted the first or microscopic approach; this is discussed in #I.4. Chung and Wildenthal used a hybrid of the two approaches, producing a phenomenological fine-tuning of the microscopic

Kuo-Brown interaction; this is described in #1.5. In their attempt to describe all ds-shell nuclei, Chung and Wildenthal find that it is impractical to demand that a single effective interaction be used across the entire ds-shell. This is hardly surprising since from such a viewpoint late ds-shell nuclei have more valence nucleons than core nucleons[1]. Thus CW carry out two distinct calculations - a 'particle' calculation in which the interaction is fitted to 200 level energies in nuclei from ^{18}O to ^{24}Mg and a 'hole' calculation in which the interaction is fitted to level energies in nuclei from ^{32}S to ^{39}K. It is then verified that the two interactions yield similar results in the middle of the shell, from A = 25 to A = 31. In the following sections only the 'particle' calculation, for early ds-shell nuclei, will be discussed.

#I.4 Microscopic Shell-Model Effective Interaction

Kuo and Brown[9] calculated a shell-model interaction for positive-parity levels in ^{18}O and ^{18}F, within the model space

$$d = (1d_{5/2},\ 2s_{1/2},\ 1d_{3/2})^2 \quad , \tag{I.9}$$

starting from the free nucleon-nucleon interaction of Hamada and Johnston[14]. Theirs was not the first such attempt to achieve a considerable degree of success, but it was by far the most influential. Before Kuo and Brown, discussion centered on whether or not it is possible to compute shell-model interactions from many-body theory. After Kuo and Brown the possibility was generally accepted and debate shifted to the reliability of the necessary approximations and to the accuracy attainable in the description of observed level-properties.

Kuo and Brown work within the framework of the Brueckner-Bethe theory of nuclear matter, which is based on the fact that nuclear matter

is a rather low-density system. This property is obvious from the fact that the mean-free path of a nucleon in the nucleus is of the order of the nuclear radius; nucleons spend most of the time outside the range of their mutual interactions[15]. Under such circumstances, calculations[16] of such quantities as the binding energy, optical potential or two-body effective interaction use expansions in power of the density. In a low-density system, the probability of finding two, three, four... particles simultaneously within range of their interaction falls off rapidly with the number of particles. Thus the first term in the density expansion treats two-particle correlations exactly, the next, three-particle correlations, and so on. The lowest-order contribution invariably centers on the precise treatment of two-nucleon correlations, embodied in the scattering-matrix for two nucleons in the nuclear medium, or G-matrix.

An effective interaction takes into account the effect of states excluded from the model space. Given that the model space under consideration ((I.9)) is a two-particle space and that two-body correlation effects are expected to dominate, the first excluded states to be considered are obviously two-particle excitations from valence to empty orbits. If all possible two-particle excitations are included, but only in second-order perturbation-theory, the effective two-body interaction G is given by

$$\langle ij|G(\omega)|kl\rangle = \cong \langle ij|V|kl\rangle - \sum_{ab} \langle ij|V|ab\rangle \frac{1}{\varepsilon_a+\varepsilon_b-\omega} \langle ab|V|kl\rangle \qquad (I.10)$$

in the notation for core, valence and empty orbits illustrated in Fig. I.1. The sum in (I.10) runs over all empty two-particle states (single-particle energies $\varepsilon_a+\varepsilon_b$) and ω is the starting-energy parameter, whose value depends on the particular context in which the G-matrix arises. In diagramatic form, eq. (I.10) becomes

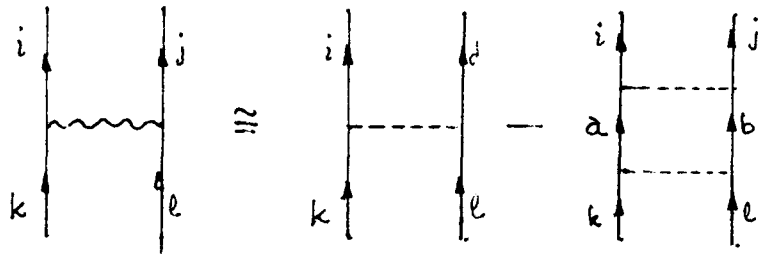

(I.11)

where a curly line indicates an effective G-interaction, a dotted line a bare V-interaction. In simplified operator form, eq. (I.10) or (I.11) can be written

$$G \approx V - V \frac{Q}{e} V \tag{I.12}$$

where

$$Q = \sum_{ab} |ab\rangle\langle ab| \tag{I.13}$$

is the projector on to the space of unoccupied two-particle states and

$$e(\omega) = \varepsilon_a + \varepsilon_b - \omega \tag{I.14}$$

is the energy denominator.

Eq. (I.12) is recognizable as the first iterate, starting with G=V, of an iterative solution of the equation

$$G = V - V \frac{Q}{e} G \tag{I.15}$$

This equation or its equivalent,

$$\langle ij|G(\omega)|kl\rangle = \langle ij|V|kl\rangle - \sum_{ab} \langle ij|V|ab\rangle \frac{1}{\varepsilon_a + \varepsilon_b - \omega} \langle ab|G(\omega)|kl\rangle \tag{I.16}$$

defines the Brueckner reaction (G) matrix.

In a two-particle scattering problem with a Hamiltonian

$$H = H_0 + V \tag{I.17}$$

where H_0 describes the internal states and non-interacting relative mo-

tion of the particles, V the interaction that induces transitions, transitions probabilities (or reaction rates) are given by

$$P_{ij} \propto |T_{ij}|^2 \tag{I.18}$$

where the T- or scattering-matrix for incident energy E satisfies

$$T(E) = V + V\frac{1}{E - H_o + i\epsilon}T(E) \tag{I.19}$$

In (I.10), the factor iε ensures outgoing-wave boundary conditions in all open reaction-channels. But the defining eqution (I.15) for G(ω) can be written

$$G(\omega) = V + V\frac{Q}{\omega - H_o}G(\omega) \tag{I.20}$$

Comparison of (I.19), (I.20) reveals that G is a T-matrix with the intermediate-state sums reduced by the projection operator Q out of the space of occupied states. This additional factor prevents two-particle scattering into states forbidden by the Pauli principle. As expected from the discussion at the beginning of this section, the G-matrix describes the scattering of two nucleons in the nuclear medium.

As a first estimate of the effective interaction for ^{18}O and ^{18}F Kuo and Brown used the G-matrix $\langle ij|G|k\ell\rangle$ calculated from the Hamada-Jhonston interaction with the symmetric choice

$$\omega = \frac{1}{2}(\varepsilon_i + \varepsilon_j + \varepsilon_k + \varepsilon_\ell) \tag{I.21}$$

of starting energy. Their results for ^{18}O are shown in figure I.2 (first and fourth spectrum). Agreement with experiment is not good; as is characteristic when bare G-matrices are used as effective interactions to calculate identical-nucleon spectra, the shell-model spectrum is much more compressed than is observed.

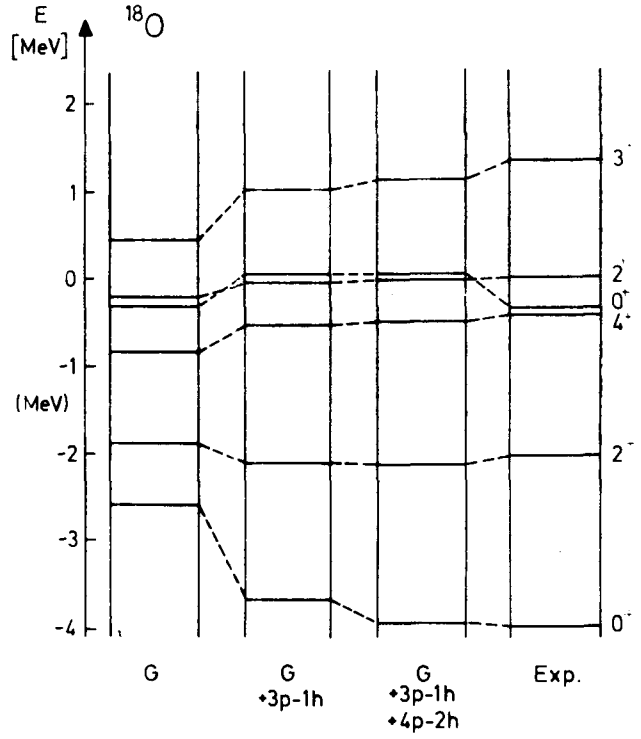

Figure I.2:

Energy-levels of ^{18}O, with energies referred to that of the ^{16}O closed shell. The measured values are compared with those calculated at various stages of the Kuo-Brown effective-interaction calculation (ref.9).

Since the G-matrix itself is not adequate, the obvious next step is to include some of the ffects of other excluded states that seem likely to be important. Now it is known that the marked enhacement of all E2 moments and transition rates in light nuclei is largely due to "breathing-mode" excitation -1s→2s, 1p→2p..- of the nuclear cores. This suggests the inclusion of 1p-1h excitations of the ^{16}O core. The extension of the model space implied by inclusion of 1p-1h core-polarization may be symbolized by

$$(1d,2s)^2 \longrightarrow \{(1s^{-1})(1d,2s)^3 + (1p^{-1})(1d,2s)^2(2p,1f)\} + \{(1s^{-1})(1d,2s)^2(2d,3s) + (1p^{-1})(1d,2s)^2(3p,2f)\} + \ldots \quad \text{(I.22)}$$

confining attention, as above, to states of positive parity. The first term in curly brackets includes excitations across two major shells-$2\hbar\omega$ excitations in oscillator parlance. The next bracket contains $4\hbar\omega$ excitations ... and so on.

Starting with the G-matrix as the basic renormalized effective interaction, the corrected V_{eff} is given by an obvious adaptation of eq. (I.15);

$$V_{eff} = G - G\left(\frac{Q_{3p\text{-}1h}}{e}\right) V_{eff} \qquad (I.23)$$

where Q_{3p-1h} projects on to the space of excluded 3p-1h excitations (indicated in eq.(I.22).

In calculating the effective interaction with correction for core-polarization, Kuo and Brown made two further restrictive assumptions.
i) Core-polarization was taken into account only to lowest order in perturbation theory; this involves replacement of (I.23) by

$$V_{eff} = G - G\left(\frac{Q_{3p\text{-}1h}}{e}\right) G \qquad (I.24)$$

indicated graphically in figure I.3.
ii) Only $2\hbar\omega$ excitations (1s → 2s, 1p → 2p) were retained in Q_{3p-1h}.

As shown in fig. I.2 (second and fourth spectra) the resulting effective interaction yields impressive agreement with experiment. A further embellishment, was the inclusion in lowest-order perturbation theory of $2\hbar\omega$ 4p-2h excitations. This produces changes in V_{eff} that are small but in such a direction as to further improve agreement with the observed spectrum of ^{18}O (fig. (I.2), third and fourth spectra). The spectrum of ^{18}F is also reproduced with satisfactory accuracy, except for a few states, such as the second 1^+ state, that are known to belong predominantly to 4p-2h configurations; under such circunstances the

lowest-order estimate of 4p-2h effects cannot possibly be adequate.

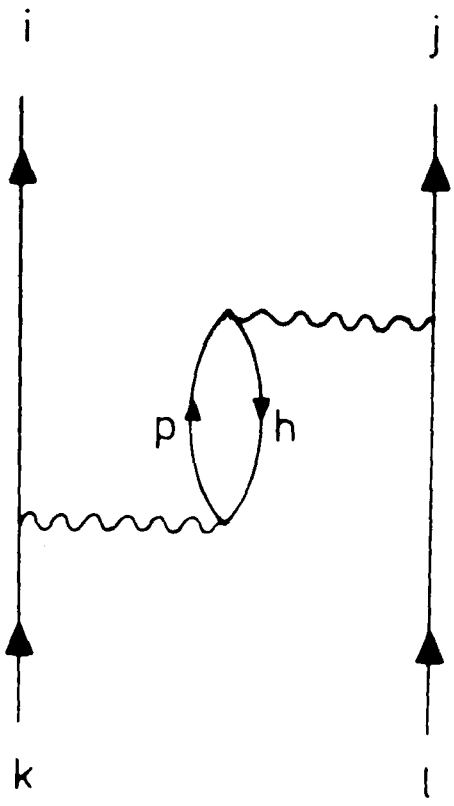

Figure I.3:

A 1p-1h core-polarization diagram

Kuo and Brown went much further by advocating the use of their mass-18 interaction as a two-body interaction in shell-model calculations for ^{19}O, ^{19}F, ^{20}O, ^{20}Ne, with three or four valence nucleons. Although there is no quantitative theoretical justification for this step, it works very well, as shown for ^{18}F in figure I.4 (first and third spectra). At the time of the Kuo and Brown papers (1966-67), shell-model technology could not cope with more then four or five nucleons in the ds-shell. When calculations for ds-shell nuclei out to mass 24 or 25 became possible in the mid 1970's, it emerged that the empirical success of the Kuo-Brown

effective interaction deteriorates steadily as the number of valence particles grows. This deterioration was not known in 1966 and the remarkable success of the Kuo-Brown effective interaction, in the ds-shell and in other mass-regions, produced an irreversible change in attitude towards nuclear shell theory. Shell-model calculations, hitherto a purely-phenomenological exercise, now acquired a solid many-body foundation. Furthermore, the microscopic Kuo-Brown effective interaction was not an impenetrably complicated object with many-body components and including multiparticle correlations. It was, apart from the inessential 4p-2h corrections, a G-matrix, the exact two-body scattering interaction in the nuclear medium, corrected in lowest order for 1p-1h core polarizarion.

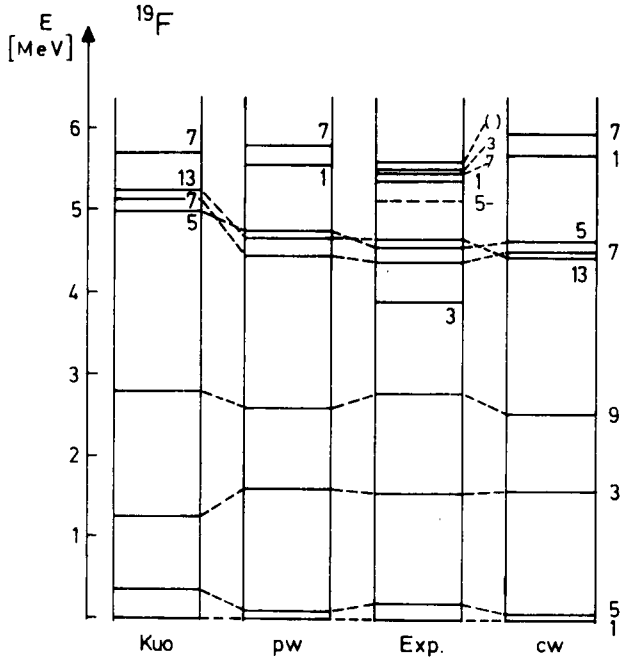

Figure I.4:

Comparison with experiment of various shell-model predictions for the energy levels of ^{19}F. The labels at the bottom of each spectrum are explained in #I.4, #I.6 of the text.

#I.5 Corrections to the Lowest-Order Effective Interaction

In the ten years following the publication of the Kuo-Brown papers their various simplifying assumption were tested, with the following conclusions:

i) 1p-1h core excitation (represented by the projection operator Q_{3p-1h}) cannot be treated adequately in lowest-order perturbation theory. Significant corrections are found[17] up to 4th or 5th order. This desperately-slow convergence has been traced to the long-range tensor part of the free nucleon interaction.

ii) It is quite incorrect to include only $2\hbar\omega$ particle-hole excitations of the ^{16}O core. Significant effects have been found[18] up to $12\hbar\omega$, again because of the long-range tensor interaction.

In short, each of Kuo and Brown's simplifying assumptions is invalid and the necessary corrections worsen agreement with experiment. In the end, corrected results for the G-matrix plus core-polarization corrections yield spectra similar to those obtained with the bare G-matrix. This would seem to take us back to square zero, but, as I will now argue, such a conclusion would be much too pessimistic.

To produce a microscopic effective interaction that gives high-quality agreement with experiment in many-particle shell-model calculations, it appears necessary to include the effects of a variety of excitations spanning many major shells, to do so non-perturbatively and also to study the influence of nuclear-matter multi-particle correlations. Such calculations would be of hideous complexity and would be likely to lead away from the conventional form of the shell model a direction that I believe to be undesirable (see #I.3). The alternative, to be examined in the following section, is to retain the conventional form of the shell model and to make phenomenological adjustements to the lowest-order

microscopic interaction. If the necessary adjustements are small, as the success of the Kuo-Brown effective interaction seems to indicate, the resulting fine-tuned microscopic interaction may still be said to constitute a many-body basis for the shell model.

Another significant point is that the shell-model results are insensitive to the details of the free-nucleon interaction. Replacement of the now-outmoded Hamada-Johnston interaction by the much-improved nucleon-nucleon potential of Reid[19] makes no significant qualitative difference. The same statement could probably be made if the Reid potential were replaced by the latest-generation Bonn[20] and Paris[21] potentials. The low-lying shell-model spectra and transition rates are sensitive only to the most primitive aspects of the free-nucleon interaction; one-pion and ρ - exchange contributions would probably suffice.

#I.6 Phenomenological Fine - Tuning of a Microscopic Effective Interaction

Kuo and Brown succeeded in giving a reasonable account of low-lying levels in the early ds-shell with a simple micorscopic effective interaction consisting[2] of a G-matrix, corrected in lowest-order perturbation theory for particle-hole excitations into neighboring shells. Attempts to correct simplifying approximations and to include other excitations led into a morass. It was concluded that for high-quality fits to data, the microscopic effective interaction should be adjusted phenomenologically.

In the ds-shell, (see #2.3) there are 66 parameters - 3 single - particle energies and 63 two-body matrix elements - to be determined by a least - squares fit to observed level-energies in a suitably-selected set of ds-shell nuclei. The error matrices in such fits reveal that only about 20 linear combinations of the interaction parameters are significan-

tly constrained by the data. Fits start from G_{KB} and, in order that the interaction determined

$$V_{eff} = G_{KB} + \Delta V \qquad (I.25)$$

be as close as possible to the microscopic turning point, parameter-variations should be confined to the well-determined aspects of the interaction.

In 1972, Preedon and Wildenthal[23] made a first attempt to tune the Kuo-Brown interaction, varying only the 16 two-body matrix elements involving only the $d_{5/2}$ and $s_{1/2}$ orbits. These matrix elements were fitted to level energies in nuclei with mass numbers from 18 to 22. The resulting fits were a considerable improvement over those obtained with the Kuo-Brown interaction. Within the mass-range of the fit, agreement with experiment is generally excellent; this is shown in figure I.4 (second and third spectra) for ^{19}F. Beyond the range of the fit, agreement with experiment is still only fair as illustrated for ^{24}Mg in figure I.5 (second and fourth spectra). The modifications in the interaction produced by the fit (matrix elements of ΔV) are on the average less than 15 % of the magnitudes of the corresponding Kuo-Brown matrix elements, but seem to follow no discernible physical pattern.

The main flaw in the Preedom-Wildenthal calculation is that, while the well-determined combinations of interaction parameters for early ds-shell nuclei are indeed dominated by the $d_{5/2}$, $s_{1/2}$ matrix elements, they nevertheless contain significant $d_{3/2}$ contributions. Chung and Wildenthal built into their fitting procedure the requirement that parameter-variations be allowed only along those directions in parameter-space corresponding to a certain pre-assigned minimun information-content. Their procedure for varying only those linear combinations of parameters well-determined by the data is described in Appendix A to

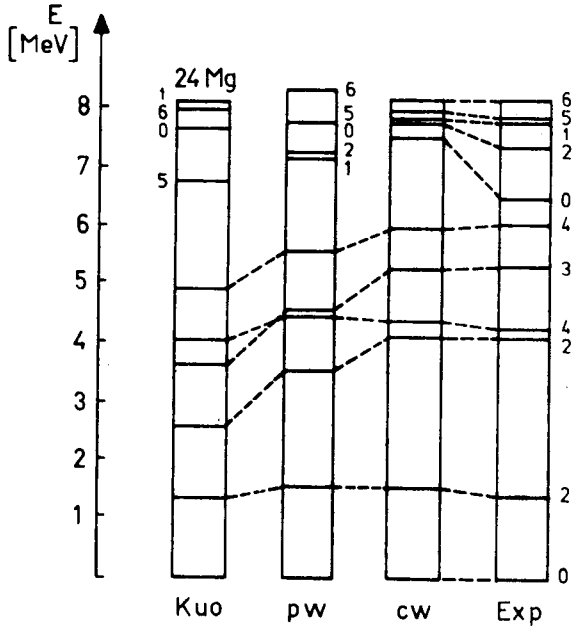

Figure I.5:

Comparison with experiment of various shell-model predictions for the energy levels of ^{24}Mg. The labels at the bottom of each spectrum are as in figure I.4 .

Chung and Wildenthal carried out, then, a constrained least-squares fit to some 200 level energies in ds-shell nuclei with $18 \leq A \leq 24$. The resulting fit is of excellent quality over the entire mass-range of the fit, as shown for ^{19}F in fig. I.4 (third and fourth spectra) and for ^{24}Mg in fig. I.5 (third and fourth spectra). The r.m.s. deviation between calculated and observed level energies is about 220 keV. Since the average level spacing over the range of masses and excitation energies under consideration is about 750 keV, the "figure of merit" for this

shell-model fit is[24]

$$f = \frac{[\text{r.m.s. error}]}{[\text{mean level spacing}]} \cong .3 \qquad \text{(I.26)}$$

That the Chung-Wildenthal fit is of high quality can now be seen by comparing its figure-of-merit to that of the Cohen-Kurath[25] description of 1p-shell nuclei; this study, the accepted standard of excellence in shell model fits, has $f \underset{\sim}{\sim} .25$. In other words, an average error of 1/4 to 1/3 of the mean level-spacing is the best accuracy yet achieved in shell-model descriptions of ranges of nuclei. In addition, the Chung-Wildenthal interaction gives excellent fits up to A=28 and has been used with great success to describe M1 transitions, magnetic moments and the results of electron- and proton-scattering experiments.

Let $\langle | \frac{\Delta V}{G_{KB}} | \rangle$ denote the ratio of the magnitudes of corresponding matrix elements of G, ΔV, averaged over all 63 two-body matrix elements within $(d_{5/2}, s_{1/2}, d_{3/2})^n$. In the Chung-Wildenthal fit

$$\langle | \frac{\Delta V}{G_{KB}} | \rangle \lesssim 10\% \qquad \text{(I.27)}$$

Thus the phenomenological adjustement changes the Kuo-Brown matrix elements by less than 10% per matrix element. In this sense, the Chung-Wildenthal interaction is a phenomenological fine-tuning of the microscopic Kuo-Brown interaction. Furthermore, a physically-significant pattern can now be discerned in the changes ΔV in the Kuo-Brown matrix elements. As shown in Table I.1, the penomenological fine-tuning systematically reduces the magnitude of the attractive shell-shell interactions $\varepsilon(j_1 j_2)$ defined by

$$\varepsilon(j_1 j_2) = \frac{\sum_{JT} (2J+1)(2T+1) \langle J_1 J_2 JT | V_{eff} | J_1 J_2 JT \rangle}{\sum_{JT} (2J+1)(2T+1)} \qquad \text{(I.28)}$$

Table I.1:

j_1 , j_2	$\varepsilon(j_1 j_2)$ Kuo	$\varepsilon(j_1 j_2)$ CW
5/2 3/2	- 133.1	- 74.5
5/2 1/2	- 44.6	- 20.5
3/2 1/2	- 20.8	- 16.0

Shell-shell interaction energies $\varepsilon(j_1 j_2)$, defined by eq.(I.28) in the text, with the Kuo-Brown and Chung-Widenthal interactions. Energies are given in MeV (from ref.10).

Smaller shell-shell matrix elements imply a smaller degree of configuration-mixing. Thus, as shown in Table I.2, the Chung-Wildenthal interaction yields fractional ground-state occupation-numbers for ^{28}Si much closer to those (1,0,0) for a closed $d_{5/2}$ shell than is the case with the Kuo-Brown interaction. Now it is true in a general way that the higher the particle rank of an interaction, the less efficient it is in producing centroid-splittings and shell-shell interactions for a given amount of individual-level splitting. The smaller shell-shell interactions of the Chung-Wildenthal interaction may therefore indicate that is has absorbed the effects of many-body components in the effective interaction, averaged over many nuclei.

Before summarizing the main conclusions of this chapter, two points are worth making about shell-model calculations.

1) Transition and interaction operators enter many-particle shell model studies only through finite sets of numbers, the matrix elements. No explicit assumptions are made about the radial single-particle wave functions nor about the radial dependence, nor the detailed spin-isospin

dependence of the operators. The great successes of the phenomenological shell-model has been achieved by the process of avoiding detailed assumptions about radial structure.

2) During the period covered in the above historical survey (1966-76), great advances in shell-model technology took place. At the beginning of the period, ds-shell calculations for A=21 nuclei (energy matrices of dimension up too 200) were just within the bounds of possibility. Ten years later, calculation for ^{28}Si were routinely possible, involving 3000 x 3000 matrices, while least-squares fits involving about 100 matrices, with dimensions from 50 to 2000, could also be carried out. An account of the advances of technique involved will be found in refs. 25 and 26.

Table I.2:

Orbit	Kuo	CW
$1d_{5/2}$	.57	.76
$2s_{1/2}$	.67	.36
$1d_{3/2}$	.31	.18

Fractional ground-state occupation number (1 for a filled orbit, 0 for an empty one) for the $1d_{5/2}$, $2s_{1/2}$ and $1d_{3/2}$ orbits in the ^{28}Si ground state, calculated with the Kuo and Chung-Wildenthal interactions. (From ref.10).

We conclude that high-precision many-particle shell-model calculations use effective interactions that, although very close to microscope interactions, contain an essential element of phenomenological fine-tuning. In general, from the work of Chung and Wildenthal and other

similar studies, the effective interaction is of two-body nature and has two distinct parts;

$$V_{eff} = V_{mic} + \Delta V \tag{I.29}$$

The first and usually predominant part V_{mic} is a G-matrix, possibly corrected for the lowest-order effects of nearly, low-energy excitations strongly-coupled to the model space. ΔV simulates the influence of all other excitations excluded from the model space. It is treated phenomenologically and involves averaging over a number of nuclei (or number of valence nucleons). There is some evidence[27,28] that as the dimensions of the model spaces used for a given range of nuclei increases,

$$V_{eff} \longrightarrow G \tag{I.30}$$

in the sense that the "nearly excitations" included in V_{mic} come into the model space and $\langle | \frac{\Delta V}{G} | \rangle$ decreases. Given, however, that parts of the free-nucleon interaction (in particular the tensor part) are capable of exerting their influence over many major shells and recalling that the dimension of multishell model spaces increase according to a Malthusian exponential law, it is very unlikely that "exact" shell-model calculations with unadorned microscopic interactions will ever reach the point of producing detailed high-precision fits to nuclear level-properties. I believe that any microscopic effective interaction, for the shell-model or for direct-reactions, is likely to require a touch of empirical finetuning in order to achieve accurate description of high-precision nuclear data.

Appendix to Chapter I. Suppression of Parameter - Variations with low information content in iterative least - squares fits

Least-squares fits of model parameters to experimental data lend themselves naturally to the control of parameter-variations in directions of low information-content. Let there be n model parameters, forming the parameter-vector.

$$\vec{x} : \quad x_i \quad (i = 1,2,\ldots,n) \tag{I.30}$$

In the shell-model fits discussed in #I.3 and #I.6 the quantities x_i are are the matrix elements of the effective interaction, but the discussion here will have a much wider range of validity. The parameters x_i are to be determined by minimization of a χ^2 function - a weighted sum of squared deviations between experimental and model quantities;

$$\chi^2(\vec{x}) = \sum_{\alpha=1}^{N} W_\alpha \left(\textcircled{M}_\alpha^{exp} - \textcircled{M}_\alpha^{th}(\vec{x}) \right)^2, \tag{I.31}$$

with N experimental entries (n<<N). In the shell-model fits $\textcircled{M}_\alpha$ is an observed level-energy $\left(\textcircled{M}_\alpha = E_\alpha\right)$. We define the "residual" F_α by

$$F_\alpha = \sqrt{W_\alpha} \left(\textcircled{M}_\alpha^{exp} - \textcircled{M}_\alpha^{th}(\vec{x}) \right) \tag{I.32}$$

whence

$$\chi^2(\vec{x}) = \sum_\alpha F_\alpha(\vec{x})^2 \tag{I.33}$$

Iterative least-square fits depend on the gradient (firstderivative) vector

$$\vec{g} : \quad g_i = \frac{\partial \chi^2}{\partial x_i} = 2 \sum_\alpha F_\alpha \frac{\partial F_\alpha}{\partial x_i} \tag{I.34}$$

and the second-derivative or inverse error-matrix

$$D_{ij} = \frac{\partial^2 \chi^2}{\partial x_i \partial x_j} = 2 \sum_{\alpha} \frac{\partial F_\alpha}{\partial x_i} \frac{\partial F_\alpha}{\partial x_j} + 2 \sum_{\alpha} F_\alpha \frac{\partial^2 F_\alpha}{\partial x_i \partial x_j} \qquad (I.35)$$

$\chi^2(\vec{x})$ is minimized by a procedure in which the magnitudes of the derivatives g_i are made as small as possible. (The first derivative vanish at an exact extremun). This is achieved by a process of cancellation. The two factors in the expression (I.34) for the gradient are of entirely different character. F_α is proportional to the difference between an experimental and a theoretical or model quantity; its sign as a function of alpha is random. The derivative $\frac{\partial F_\alpha}{\partial x_i}$ on the other hand, is a pureley model quantity, independent of the experimental quantities; if the experimental points are ordered in some systematic fashion, the sign of $\frac{\partial F_\alpha}{\partial x_i}$ tends to have a regular, non random variation with α . Thus $|g_i|$ becomes small by a process wherein random function F_α "beats" against the regularly-varying function $\frac{\partial F_\alpha}{\partial x_i}$. At the same time, the same sort of process is making the similar ⊕ quantitiy $\sum_{\alpha} F_\alpha \, \partial^2 F_\alpha / \partial x_i \partial x_j$ small also. Thus the second term in eq. (I.35) may be dropped, leaving the linearized second-derivative matrix

$$D_{ij} \cong 2 \sum_{\alpha} \frac{\partial F_\alpha}{\partial x_i} \frac{\partial F_\alpha}{\partial x_j} \qquad (I.36)$$

This approximation to the second-derivative matrix is excellent in all fits of model parameters to experimental quantities, is positive definite and involves no significant extra computational labor once the gradient-vector has been calculated[29].

The iterative minimization of χ^2 proceeds as follows. Suppose that an estimate $\vec{x}_k$ of the parameter-vector has been obtained, either by guessing or by a number of previous iterations. An improved estimated

$$\vec{x}_{k+1} = \vec{x}_k + \Delta\vec{x}_k \tag{I.37}$$

is now obtained by choosing the step $\Delta\vec{x}_k$ in parameter-space such that

$$\chi^2(\vec{x}_k + \Delta\vec{x}_k) \cong \chi^2(\vec{x}_k) + \Delta\vec{x}_k^T \cdot \vec{g}_k + \frac{1}{2}\,\Delta\vec{x}_k^T \cdot D_k \cdot \Delta\vec{x}_k \tag{I.38}$$

is a minimun as a function of $\Delta\vec{x}_k$. Here we use an obvious matrix notation with $\Delta\vec{x}$ a column-vector, $\Delta\vec{x}^T$ the corresponding row-vector. The minimun of the quadratic function (I.38) is given by

$$\vec{g}_k + D_k \cdot \Delta\vec{x}_k = 0 \tag{I.39}$$

This may be solved for the desired "step";

$$\Delta\vec{x}_k = - D_k^{-1} \cdot \vec{g}_k \tag{I.40}$$

Elementary precautions are usually taken to ensure that the step (I.40) stays within the region in which the quadratic approximation (I.38) is valid; if $\chi^2(\vec{x}_k + \Delta\vec{x}_k) > \chi^2(\vec{x}_k)$ than the direction of $\Delta\vec{x}_k$ is retained but its length reduced until χ^2 is decreased. The positive-definite character of the linearized second-derivative matrix (I.36) ensures that a step along $\Delta\hat{x}_k$ is at least initially downhill. The step (I.40) is repeated until either $|\vec{g}|$ is smaller than some desired accuracy or $|\Delta\vec{x}_k|$ has been very small for two or three successive steps.

The process of identifying directions of low information-content may now be stated quite simply. Let D_k be diagonalized by a similarity transformation;

$$D = A^T \begin{bmatrix} d_1 & & 0 \\ & d_2 & \\ 0 & & \ddots \\ & & & d_n \end{bmatrix} A \tag{I.41}$$

The inverse of D is then

$$D^{-1} = A^T \begin{bmatrix} d_1^{-1} & & 0 \\ & d_2^{-1} & \\ 0 & & d_n^{-1} \end{bmatrix} A \qquad \text{(I.42)}$$

As is clear from the one-dimensional example in figure I.6, a small d_i (large error d_i^{-1}) corresponds to a poorly-defined minimum in the direction specified by the i^{th} eigenvector of D. A large value of d_i (small error d_i^{-1}) implies a sharply-defined minimum. Let the eigenvalues of D, which are all positive since the linearized second-derivative matrix (I.36) is positive definite, be placed in descending order in (I.41) from top left to bottom right. Suppose that a minimum acceptable level of information has been specified by the parameter ϵ ; no significant information will be said to be available in the direction of eigenvector i if

$$d_i < \epsilon\, d_1 \qquad \text{(I.43)}$$

where of course d_1 is the maximum eigenvalue of D. This criterion will select a block of eigenvalues to the bottom right of (I.41). Steps in the direction of eigenvectors whose information-content is less than the acceptable minimum can be suppressed by replacing d_i^{-1} by 0 in the error matrix (I.42). The 'frozen' error-matrix

$$\tilde{D}_k^{-1} = A_k^T \begin{bmatrix} d_1^{-1(k)} & & 0 & \vdots & \\ & \ddots & & 0 & \\ 0 & & d_\mu^{-1(k)} & \vdots & \\ \cdots & \cdots & \cdots & \cdots & \cdots \\ & 0 & & 0 & \\ & & & \ddots & \\ & & & & 0 \end{bmatrix} A_k \qquad \text{(I.44)}$$

is then to be used in the iterative step (I.40);

$$\Delta\vec{x}_k = -\tilde{D}_k^{-1} \cdot \vec{g}_k \qquad \text{(I.45)}$$

The linear combination of parameters corresponding to low information-content are left unaltered.

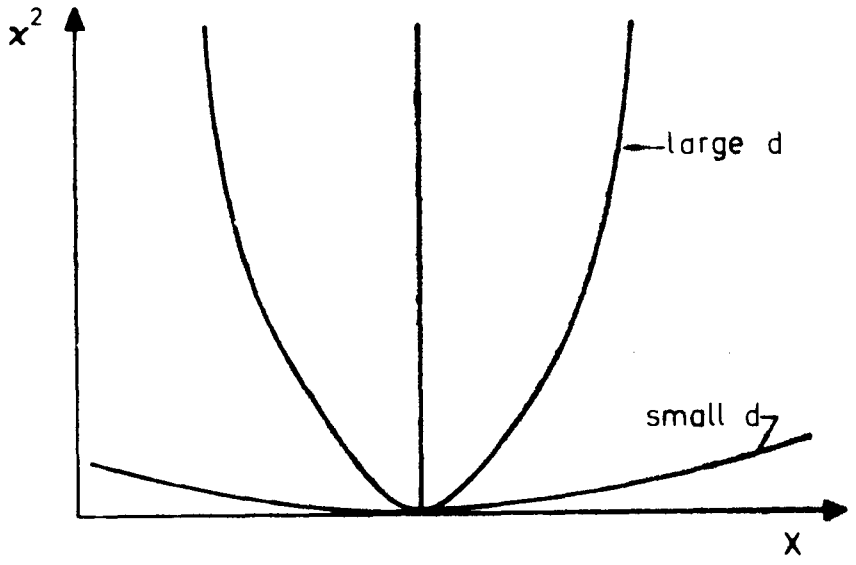

Figure I.6:

Minima of a function $\chi^2(x)$ of one variable, with
d = the second derivative at minimum.

This procedure was the one used by Chung and Wildenthal[10] in the ds-shell calculations discussed above. It is also widely used to control steps in least-squares fits that lead to nonsensical parameter-values; such steps are almost always due to large excursions in directions of low information-content.

CHAPTER II

CALCULATIONAL TECHNIQUES FOR DIRECT REACTIONS

1. INTERPOLATION AND EXTRAPOLATION IN PARTIAL-WAVE EXPANSIONS

#II.1 The importance and nature of the technical innovations

Calculations with effective interactions present a choice between competing simplicities-small model space, bizarre effective interaction or large model space, simple effective interaction. A balance must be sought; techniques must be developed to permit calculations in model spaces just large enough to yield tractable effective interactions. Tractability in this context has two distinct aspects; the effective interaction must be of sufficiently simple form to permit high-precission phenomenological fits to data and it must permit quantitative linking to the free-nucleon interaction.

In shell-model studies, the minimal size of model space for tractable effective interactions seems to require up to 10 valence nucleons or holes in the four or five single-particle orbits nearest to the Fermi surface. Technical advances mentioned in Chapter I have made shell-model calculations of this magnitude routinely possible for light nuclei and for a few heavier nuclei near doubly-closed shells. Direct-reaction spectroscopy is in a more primitive state. Only for low-energy light-ion physics are the phenomenological parameterizations clearly-appropriate and the effective interactions firmly grounded in many-body theory. Because of computational limitations, most quantal direct-reaction calculations in heavy-ion physics and intermediate-energy light-ion physics

involve the single-channel optical model, with transitions to other channels treated in first-order perturbation theory (DWBA). In such severely-restricted model spaces, high precision fits to data are inhibited and many-body derivations of the effective potentials out of the question. It is possible that the main omission from the model space is a relatively small set of strongly-coupled inelastic-scattering and transfer channels; detailed study of the influence of these channels on cross-sections and effective potentials requires the ability to handle model spaces containing up to 50 physical channels[30].

Calculations of this magnitude may soon become routinely (and cheaply) possible because of recent development in the technology of direct-reaction calculations, analogous to those that appeared in shell-model technology during the years 1963 to 1973. We shall discuss these technical development in Chapter II and IV of these lectures. In most of these discussiones we shall work in r-space with the coupled equations expressed either in differencial or in integral form. The technical advances and simplifications are in fact of three distinct varieties.

1) Extensive use of interpolation and extrapolation in angular momentum to reduce the number of partial waves for which the transition amplitudes must be evaluated explicitly. This is possible because the pertinent S-matrix elements are smooth functions of angular momentum and have readily-identifiable asymptotic behavior at large angular momentum. It is seldom necessary to carry out explicit calculations for more than 20 or 30 partial waves, even when hundreds contribute significantly to the cross-sections.

2) The use of iterative or basis-expansion methods to solve the coupled equations. The traditional procedure has been to solve each set of N coupled equations N times with different choices of starting values so as to synthesize solutions with the desired large-r asymptotic form. Iterative methods eliminate this N-fold waste of time.

3) Efficient treatment of Coulomb excitation. Nuclear interactions die out at radial distances of around 15 fm. In light-ion calculations, the end of the nuclear or interior region is the beginning of asymptopia wherein only diagonal Coulomb interactions survive. Interior solutions of the coupled equations are then matched to the appropriate asymptotic forms, involving Coulomb functions and S-matrix elements. In heavy-ion calculations, the interior region and asymptopia are separated by a wide intermediate zone, wherein offdiagonal Coulomb interactions are active; these couplings produce Coulomb excitation and are proportional to low powers of 1/r. In heavy-ion reactions, the intermediate zone may extend over hundreds of fermis. Adapted light-ion programs spend huge amounts of time and money integrating across the intermediate zone. This may be completely avoided by techniques discussed in Chapter IV.

A further point of some importance is that the bound-state contributions to channel-coupling potentials and DWBA matrix elements are usually very smooth functions of one of their two radial variables. As discussed briefly in Chapter III, this permits use of interpretation to achieve sizeable reductions in computational labor. The remainder of this chapter deals with the first of three technical developments listed above extrapolation and interpolation in angular-momentum expansions.

#II.2 Elastic scattering and angular momentum interpolation

Direct-reaction S-matrices and transition amplitudes are smooth functions of angular momentum. This is well known and not unexpected for heavy ions, but is true to a remarkable extent for light ions also.

It is not necessary to compute these S-matrix elements at each angular momentum that contributes significantly to the cross-section. The S-matrices are simple functions of angular momentum, adequately charac-

terized by their values at a few judiciously-selected angular-momentum values. The S-matrix elements at intermediate angular momenta can be determined by the simple interpolation method described below.

The ideas and techniques involved are most simply illustrated in the treatment of the elastic scattering of spinless particles. We shall assume a single-channel optical-model description where the radial functions $R_\ell(r)$ in each partial wave are obtained by numerical solution of a radial wave equation containing the complex optical potential V(r). The S-matrix elements are defined by the asymptotic form of $R_\ell(r)$, beyond the range of nuclear interactions;

$$R_\ell(r) \sim I_\ell(kr) - S_\ell O_\ell(kr) \qquad \text{(II.1)}$$

where k is the wave-number of the relative motion, I_ℓ and O_ℓ are ingoing and outgoing-wave Coulomb functions[31]. The travelling-wave Coulomb functions are related to the regular and irregular Coulomb functions F_ℓ and G_ℓ by

$$I_\ell^*(kr) = O_\ell(kr) = G_\ell(kr) + i F_\ell(kr) \qquad \text{(II.2)}$$

F_ℓ and G_ℓ are real functions.

The nuclear part of the elastic-scattering amplitude has the partial wave representation

$$F_N(\theta) = \frac{1}{2ik} \sum_\ell (2\ell+1)(S_\ell - 1) e^{2i\sigma_\ell} P_\ell(\cos\theta) \qquad \text{(II.3)}$$

where σ_ℓ is a the Coulomb phase-shift, an explicitly-known function of the kinematic parameters of the reaction. The differential cross-section is given by

$$\frac{d\sigma}{d\Omega}(\theta) = \left| F_{Ruth}(\theta) + F_N(\theta) \right|^2 \qquad \text{(II.4)}$$

where F_{Ruth} is the Rutherford-scattering amplitude and Θ is the center-of-mass scattering angle.

The ℓ-dependence of a typical heavy-ion elastic-scattering S-matrix is exhibited in Figures II.1, II.2 . To this end, the S-matrix is expressed in phase-amplitude form

$$S_\ell = |S_\ell| e^{i\,Arg(S_\ell)} \qquad (II.5)$$

For scattering by a real potential $S_\ell \to 1$, Arg $S_\ell \to 2\delta_\ell$, where δ_ℓ is the real phase-shift. The reaction represented in Figs. II.1 to II.6 is the elastic scattering of 103.6 MeV ^{16}O ions from ^{40}Ca; the optical-model parameters, which are of no interest here, were obtained by fitting the elastic data and are given in ref.[32]. It is obvious from the diagrams that $S(\ell)$ varies very smoothly with ℓ and that interpolation between rather widely-spaced values of ℓ is likely to be successful.

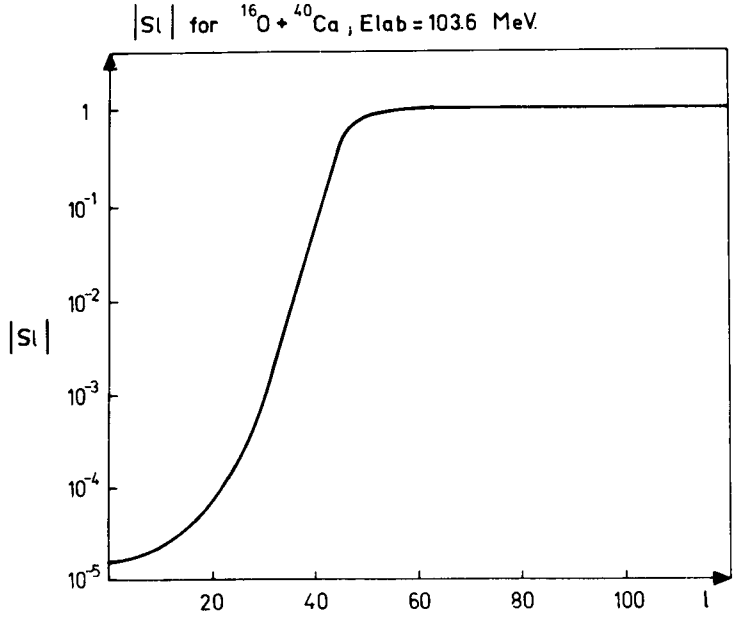

Figure 1:

ℓ-depedence of the magnitude of the S-matrix elements for the elastic scattering of 103.6 MeV. ^{16}O ions from ^{40}Ca.

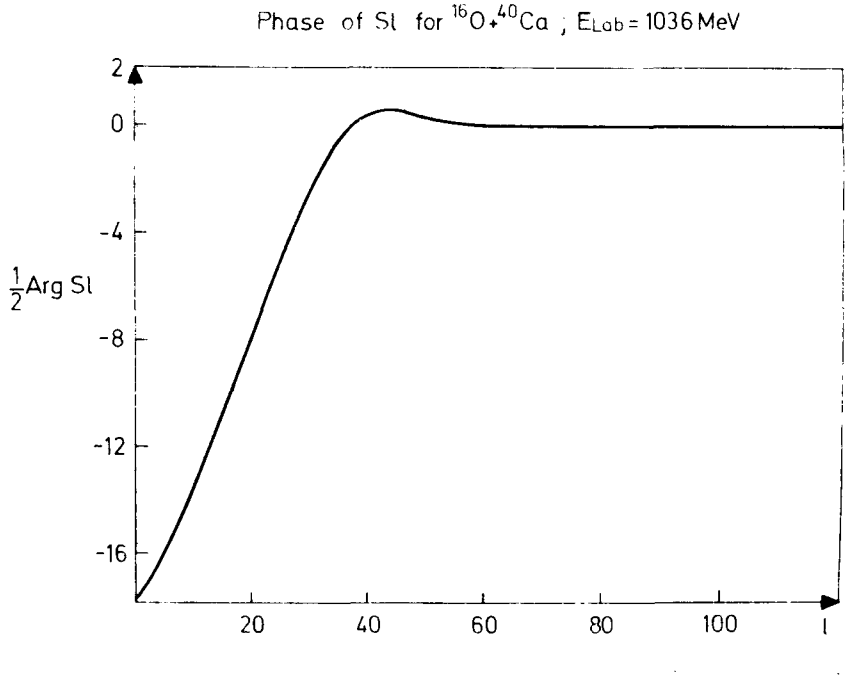

Figure II.2:

ℓ-dependence of the phase of the S-matrix elements whose magnitude is exhibited in Fig. II.1 .

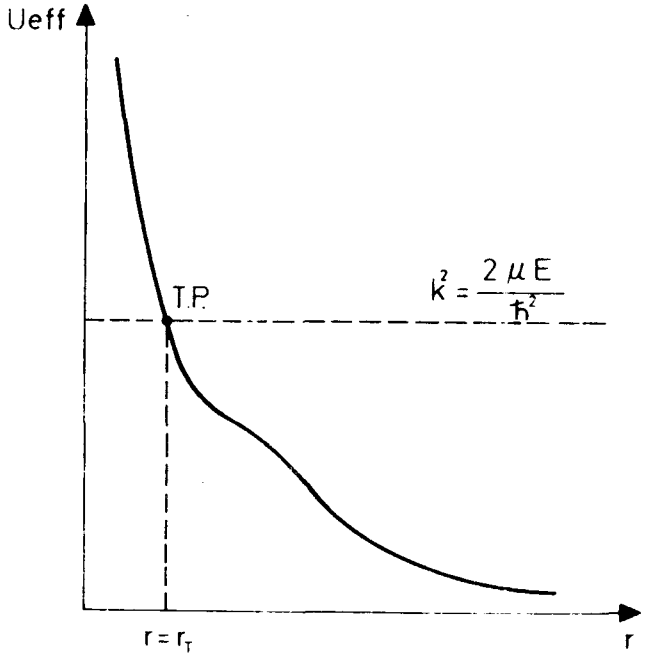

Figure II.3:

The classical turning point for scattering at energy E by the effective potential $U_{eff}(\ell,v)$. See #II.3 of the text.

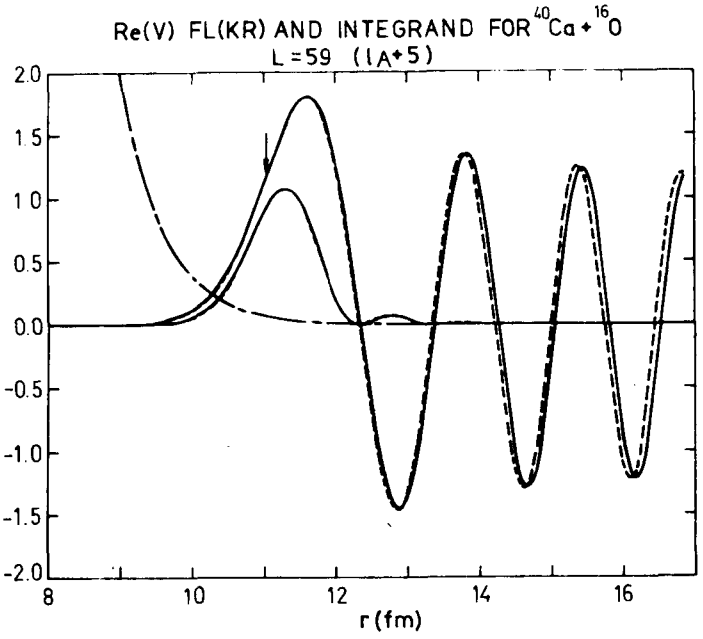

Figure II.4:

Regular Coulomb function, exponential (dashed line) and Born integrand, as discussed in #II.3 of the text, for the partial wave ℓ=59 in the elastic scattering of 103.6 MeV. ^{16}O ions on ^{40}Ca. The heavy-line oscillatory function is $F_{59}(\rho)$. The dotted-line oscillatory function is the approximation $F_{54}(\rho-\Delta\rho)$. The corresponding exact and approximate Bom inegrands are also shown.

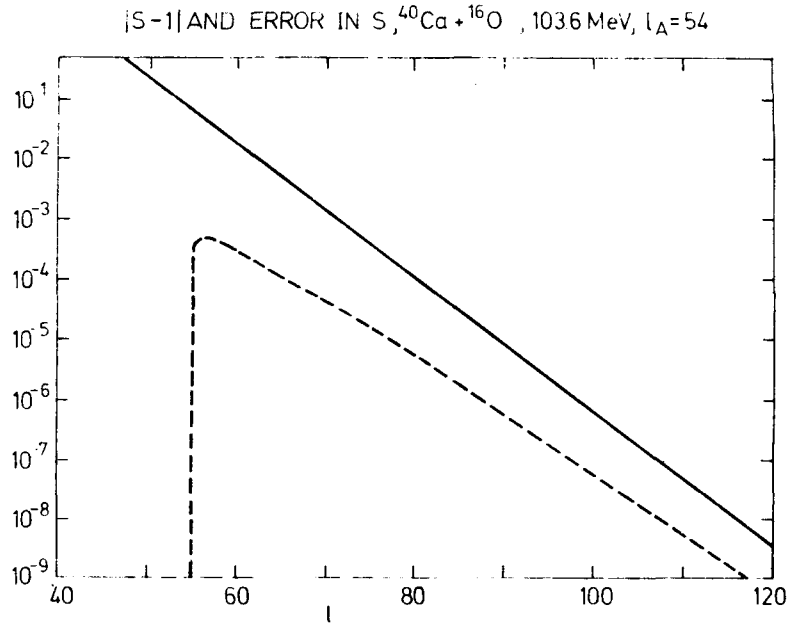

Figure II.5:

Magnitude of the T-matrix elements ( ) and absolute value of the error made in calculating them from the extrapolation formula (II.2b), for the reaction represented in Fig.II.1 .

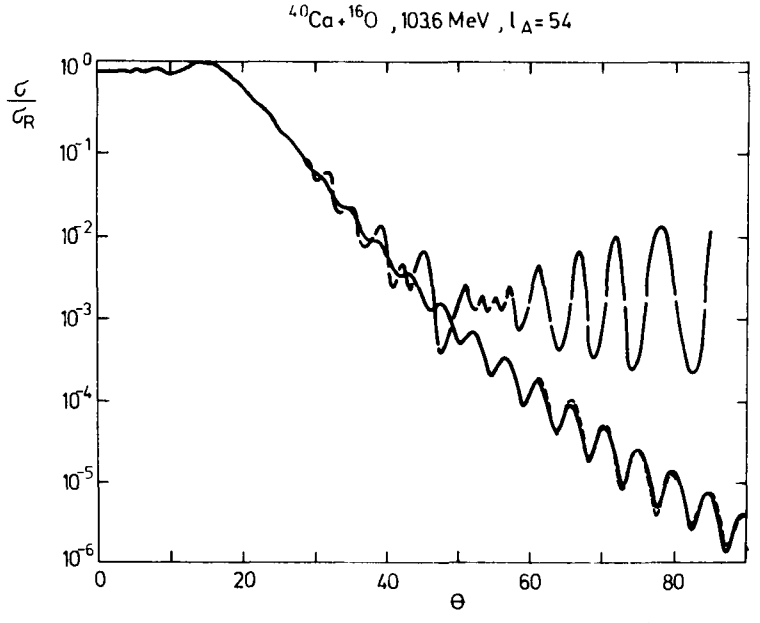

Figure II.6:

Comparison of exact and interpolated-extrapolated cross sections for the reaction represented in Fig.II.1 . The dash-dot line gives the cross-section obtained by cutting off (setting S =1) at ℓ =54.

The choice of interpolation-method is not a critical matter, either for elastic scattering or for other types of direct reaction. The method used in the program Ptolemy[33], on which most of the direct-reactions calculations discussed in these lectures are based, represents the S-matrix as a complex continued fraction of a very simple and convenient sort. Suppose that radial equations have been solved at a set of ℓ-values

$$\left.\begin{array}{llllll} \ell_1 & \ell_2 & \ell_3 & \ldots. & \ell_M \\ \text{yielding S-matrix elements} & & & & \\ S_1 & S_2 & S_3 & & S_M \end{array}\right\} \qquad \text{(II.6)}$$

It is then straightforward to represent the S-matrix by a complex continued-fraction (expressible by standard techniques in equivalent form as a rational function) of the form

$$S_\ell = A_1 + \cfrac{(\ell-\ell_1)}{A_2 + \cfrac{(\ell-\ell_2)}{A_3 + \cfrac{(\ell-\ell_3)}{A_4 + \ldots}}} \qquad \text{(II.7)}$$

The coefficients A_1, A_2, ... A_M are determined so that

$$S(\ell_i) = S_i \qquad (i = 1,2, \ldots M) \qquad \text{(II.8)}$$

or, in other words, so that the function $S(\ell)$ reproduce the computed values of the S-matrix elements at the designated ℓ-values. This can be done quite easily. Suppose that the first k coefficients A_i have been determined such that $S(\ell_i) = S_i (i=1,2...k)$. Substitute ℓ_{k+1} in eq.(II.7); A_{k+1} must then be chosen so that

$$A_1 + \cfrac{(\ell_{k+1}-\ell_1)}{A_2 + \cfrac{(\ell_{k+1}-\ell_2)}{A_3 + \ddots \; A_k + \cfrac{(\ell_{k+1}-\ell_k)}{A_{k+1}}}} = S_{k+1} \qquad \text{(II.9)}$$

All reference to coefficients A_i with $i > k+1$ has now disappeared and eq.(II.9) is an explicit expression for the next coefficient A_{k+1} in terms of known quantities. The computational labor involved in determining the coefficients A_i and hence the interpolating-function $S(\ell)$ of eq.(II.7) is trivial relative to that involved in solving radial Schrodinger equations.

S-matrix elements for values of ℓ between the designated values ℓ_1, ℓ_2,... are obtained from the interpolating continued fraction (II.7). This can be done using standard techniques for the evaluation of continued fractions; when many ℓ-values are involved it is more convenient and more efficient to evaluate and use the rational function equivalent to the continued fraction (II.7). In the specific example considered here ^{16}O and ^{40}Ca at 103.6 MeV - it is clear form Fig.II.6 that the errors introduced by interpolation with a step size $\Delta\ell = 3(\ell_i = \ell_{min}, \ell_{min} + 3, \ell_{min} + 6...)$ are utterly negligible.

Incidentally, the continued-fraction interpolating-function (II.7) can also be used to continue $S(\ell)$ off the real axis into adjacent regions of complex ℓ-space. It provides a stable continuation method, from which zeroes and poles of the S-matrix, in the region of ℓ-space reasonably close to the physical piece of the real axis, are readily located.

The interpolation-method described above has been applied to other classes of direct-reaction-inelastic scattering, DWBA transfer and coupled-channel calculations. It is sufficiently stable and reliable to be used routinely in our direct-reaction program Ptolemy[33]. We view its

is a faster and more accurate way to evaluate T-matrix elements. In eq. (II.21), the nuclear potential is treated as a perturbation of Coulomb scattering and the large-r from (II.17) of the Woods-Saxon potential has been used.

Use of the Born approximation at large ℓ is already a great improvement over conventional procedures. But the character of the integrals in eq. (II.21) and the peculiarities of the regular Coulomb function $F_\ell(\rho)$ permit us to go much further and derive an explicit asymptotic formula for the large-ℓ bahavior of elastic T-matrices.

Consider again the reaction discussed in #II.2 - ^{16}O ions at 103.6 MeV on ^{40}Ca. The S-matrix element $|S_\ell| \simeq .97$ when $\ell = 54$. Let us now attempt to use eq. (II.21) to <u>deduce</u> values of T_ℓ for $\ell > 54$ from the computed value of $|T_{54}|$. We denote by ℓ_A the greatest ℓ-values for which the Schrodinger equation is solved explicitly. The regular Coulomb function $F_\ell(\rho)$ for

$$\ell = \ell_A + \Delta\ell = 59 \qquad \text{(II.22)}$$

is shown in Fig. II.4, with the exponential $e^{-r/a}$ on the same scale (by a suitable but uninteresting renormalization). It is at once clear that the radial integrals in (II.21) receive significant contributions only in the first main oscillation of $F_\ell(\rho)$. In this region, a simple approximate expression

$$F_{\ell_A+\Delta\ell}(\rho) \simeq F_{\ell_A}(\rho - \Delta\rho) \qquad \text{(II.23)}$$

holds, where

$$\Delta\rho = \rho_T(\ell+\Delta\ell) - \rho_T(\ell) = \sqrt{\eta^2 + (\ell+\Delta\ell)(\ell+\Delta\ell+1)} - \sqrt{\eta^2 - \ell(\ell+1)} \qquad \text{(II.24)}$$

use, not as an approximation to "exact" S-matrices, but rather as a numerical technique of the same sort as the use of polymonial representations in the numerical integrations for the radial wave functions. Since the extension of the interpolation-method to other types of reaction is absolutely straight forward, we need say no more about its technical aspects in these lectures.

#II.3 Elastic scattering and large-ℓ extrapolation

At large angular-momenta, direct-reaction S-matrix elements have simple characteristic properties. The magnitudes usually[34] fall off exponentially while the phases are very close to some multiple of π. Simple explicit representations of this asymptotic behavior can usually be obtained from the observation that, at large-enough angular momentum, nuclear interactions are a perturbation of the dominant Coulomb potentials.

Again let us illustrate the ideas and techniques involved in the treatment of the optical-model elastic scattering of spinless particles. We start by introducing a few important quantities and approximations. It will be assumed that the optical potential is of conventional Woods-Saxon form,

$$V(r) = -V\left\{1 + \exp\left(\frac{r-R}{a}\right)\right\}^{-1} - iW\left\{1 + \exp\left(\frac{r-R_I}{a_I}\right)\right\}^{-1} \qquad \text{(II.10)}$$

although all that is needed in the present discussion is that both parts of the potential fall off exponentially at large r. The effective potential in partial wave ℓ is

$$U_{eff}(\ell,r) = \frac{2\mu V_{eff}}{\hbar^2} = U_N(r) + \frac{\ell(\ell+1)}{r^2} + \frac{2\eta k}{r} \qquad \text{(II.11)}$$

where

$$k^2 = \frac{2\mu E}{\hbar^2} \tag{II.12}$$

$$U_N = \frac{2\mu V}{\hbar^2} \tag{II.13}$$

μ is the reduced mass and η is the usual Coulomb parameter. The (outermost) classical turning point (CTP) in partial wave ℓ is defined to be the largest value of r for which $V_{eff}(\ell,r) = E$, or

$$U_{eff}(\ell,r) = k^2 \tag{II.14}$$

its signicance is sketched in Fig. II.3 . For pure point-Coulomb scattering, the Coulomb TP is given explicitly by

$$\rho_T = \eta + \sqrt{\eta^2 + \ell(\ell+1)} \tag{II.15}$$

with

$$\rho = kr \tag{II.16}$$

Radial scattering functions in general and the regular Coulomb functions $F_\ell(\rho)$ in particular fall off exponentially inside the TP, rise just outside it to their greatest value, and thereafter settle into their asymptotic sinusoidal oscillation (see Fig.II.4). In all the reactions considered here, asymptotic expressions in ℓ apply only to partial waves in which the pertinent classical turning points lie far into the region in which the Woods-Saxon functions decay exponentially. The nuclear potential reduces to

$$U_N(r) = -\mathcal{U} e^{-r/a} - i\mathcal{W} e^{-r_I/a_I} \tag{II.17}$$

where

$$U = \frac{2\mu V}{\hbar^2} e^{R/a} \quad , \quad W = \frac{2\mu W}{\hbar^2} e^{R_I/a_I} \tag{II.18}$$

At large ℓ, (see Fig.II.1) the modulus of elastic S-matrix elements approaches unity;

$$|S_\ell| \longrightarrow 1 \tag{II.19}$$

Yet it is often impractical to cut off the partial-wave expansion (II.3) until $|S_\ell^{-1}|$ reaches truly tiny values ($\sim 10^{-5}$ or less). This will happen whenever large-angle data, with values of σ/σ_R down to 10^{-6} or less must be analized. As the scattering angle increases, the number of contributing partial waves increases, contributions from near-grazing partial waves ($|S_\ell| \sim 1/2$) cancelling to ever-higher degree. Accurate values of S-matrix elements very close to unity are needed.

In the present discussion, it is more convenient to use the transition-or T-matrix T_ℓ defined in terms of S_ℓ by

$$T_\ell = \frac{S_\ell - 1}{2i} \tag{II.20}$$

S-matrix elements near unity correspond to very small T-matrix elements. In most optical-model computer programs, very small large-ℓ T-matrix elements are usually derived by the same procedure- numerical solution of the radial Schrodinger equation - as is used for near-grazing partial waves. This is utter foolishness; it amounts to repeated re-evaluation of slightly-perturbed regular Coulomb functions by a singularly inappropriate procedure[35].

Whenever $|T_\ell| \leq 10^{-3}$ (or perhaps $\leq 10^{-2}$), the Born approximation

$$T_\ell \simeq -\frac{1}{k}\left\{ U \int_0^\infty F_\ell(kr)^2 e^{-r/a} dr + i W \int_0^\infty F_\ell(kr)^2 e^{-r/a_I} dr \right\} \tag{II.21}$$

is the shift in TP induced by the change $\Delta\ell$ in ℓ . The accuracy of this approximate relation, for $\Delta\ell=5$, in the special case under consideration, is clear from Fig. II.4. Eq. (II.23), which continues to hold to useful accuracy in the first main oscillation of F_ℓ for steps $\Delta\ell$ up to 100 or more, reflects the fact that $F_\ell(\rho)$ at or near the TP varies very slowly with ℓ; in fact[36]

$$F_\ell(\rho_T(\ell)) \propto \ell^{-1/6} \qquad \text{(II.25)}$$

Replacement of the $\ell^{-1/6}$ dependence by a constant and extension to values of ρ not too far from ρ_T yields eq. (II.23).

Sustitute eq. (II.23) into the radial integrals in (II.21). A change of integration-variable to $r' = \frac{\rho-\Delta\rho}{k}$ yields the remarkable relation:

$$T_{\ell_A+\Delta\ell} \cong \exp\left(-\frac{\Delta\rho}{ka}\right) \mathrm{Re}\, T_{\ell_A} + i \exp\left(-\frac{\Delta\rho}{ka_I}\right) \mathrm{Im}\, T_{\ell_A} \qquad \text{(II.26)}$$

where $\Delta\rho$ is given by (II.24). The relative error in T-matrices computed from eq. (II.26), with $\ell_A = 54$ and values of $\Delta\ell$ up to 70, is shown in Fig. II.5. We see that the error in T_ℓ is always more than an order of magnitude smaller than $|T_\ell|$. The error in the cross-section, committed by replaced T_ℓ for $\ell>54$ by values obtained from the extrapolation formula (II.26), is shown in Fig. II.6. The differential cross-section is not featureless; there are pronounced diffractive oscillations. Yet the errors in the cross-section are almost imperceptible out to $\Theta\simeq120°$, where $\sigma/\sigma_R \simeq 10^{-6}$. To demonstrate the fact that significant contributions to the cross section arise from the region of ℓ-values treated on the basis of eq. (II.26), the effect of cutting off the partial-wave expansion at $\ell=54$ is also shown in Fig.II.6.

The extrapolation formula (II.26) is remarkably robust. It can be used with safety to compute the contributions of all T-matrix elements with

$$|T_\ell| \lesssim 10^{-2} \qquad \text{(II.27)}$$

The errors in the cross-sections are often smaller than those obtained use the exact Born-approximation amplitudes (II.21) and are no cause for concern unless $\sigma/\sigma_R << 10^{-6}$. For such very small cross-sections it may be necessary to increase the largest computed ℓ to that partial wave ℓ_A for which $|T_{\ell_A}| \simeq 10^{-3}$.

#II.4 Interpolation and extrapolation in angular momentum for non-elastic reactions

The methods described in #II.2, #II.3 can be extended to reactions other than elastic scattering. The interpolation procedure described in #II.2 carries over without significant change, but each type of reaction has its own characteristic large-ℓ asymptotic form to which the extrapolation procedure must be adapted. Since it is impossible to go into exhaustive detail, we shall again illustrate the procedures in a specific example- the heavy-ion single-nucleon transfer reaction

$$^{208}Pb\,(^{16}O,{}^{15}N)\,^{209}Bi\,(3/2^-;\,3.12\ MeV)$$
$$E_{Lab} = 312.6\ MeV \qquad \text{(II.28)}$$

The optical-model parameters and the experimental data will again be suppressed; they can be found in Ref.[37].

In the single-proton stripping reaction (II.28), a nucleon is transferred from the 1p 1/2 orbit in ^{16}O to the 3p 3/2 orbit around ^{208}Pb.

The total angular momentum λ transferred is the vector sum of the transferred angular momenta (1/2 and 3/2) at the two "vertices"; in addition the transferred angular momentum must also be a possible vector sum of the two single-nucleon orbital angular momenta. In this case,

$$\lambda = 1, \text{or } 2 \qquad \text{(II.29)}$$

and the total transferred parity is $+1$ $\left((-)^1 \times (-)^1\right)$. As described in more detail in #III.2, the transition amplitudes for a transfer reaction such as (II.28) are proportional to radial integrals $I^{\lambda}_{\ell_i \ell_f}$ in which the transfer operator (a spherical tensor of rank λ) couples or connects ingoing partial waves ℓ_i to outgoing partial waves ℓ_f. In the case considered here this yields four families of radial integrals

$$I^{\lambda}_{\ell_i \ell_f} : \quad \begin{cases} & I^{\lambda=1}_{\ell,\ell} & \\ I^{\lambda=2}_{\ell,\ell-2} & I^{\lambda=2}_{\ell,\ell} & I^{\lambda=2}_{\ell,\ell+2} \end{cases} \qquad \text{(II.30)}$$

The fact that the transferred parity is + 1 implies that only partial waves of the same parity are connected, so that $\ell_f = \ell_i - 2, \ell_i, \ell_i + 2$. Each of the four families in (II.3) are sequences of complex numbers $g(\ell)$ to which the techniques of II.2 are directly applicable.

To obtain appropriate extrapolation formulae, the phase and magnitude of the radial integrals must be treated separately. In order to separate the four distinct families of integrals in (II.30), set

$$I^{\lambda}(\ell, \delta\ell) = I^{\lambda}_{\ell_i, \ell_f}$$

where $$\ell = \ell_i \quad , \quad \delta\ell = \ell_i - \ell_f \qquad \text{(II.31)}$$

The variation with ℓ of the modulus $|I^{\lambda}(\ell, \delta\ell)$ is shown for $\lambda = 1, \delta\ell = 0$ in Fig. II.7. The smooth bell-shaped curve is characteristic of the ℓ-variation of inelastic amplitudes for strongly-absorbed ions. The large-ℓ

tail of the curve is very close to exponential in ℓ ; in order to permit the connecting ℓ , ℓ_A, to be as small as possible, we use a Woods-Saxon extrapolating function;

$$|I^{\lambda}(\ell,\Delta\ell)| = A\left\{1+\exp\left(\frac{\ell-B}{c}\right)\right\}^{-1} \qquad \text{(II.32)}$$

where A,B,C, are functions of λ , $\Delta\ell$. The parameters in (II.32) are determined by least-squares fit to the magnitudes of the three computed integrals up to and including that with $\ell = \ell_A$. The phase of the radial integrals at large ℓ is given with remarkable accuracy by a remnant of the Sopkovitch approximation[31] (which is quite useless for the entire radial integral in the region of grazing ℓ -values);

$$\text{Arg } I^{\lambda}_{\ell_i\ell_f} = \kappa\left\{e^{i(\delta\ell_i+\delta\ell_f)}\right\} \qquad \text{(II.33)}$$

where $2\delta\ell_i$, $2\delta\ell_f$ are the phases of the elastic S-matrix elements in the ingoing and outgoing partial waves, while κ is a normalization constant determined from the computed phase at the connecting angular momentum ℓ_A .

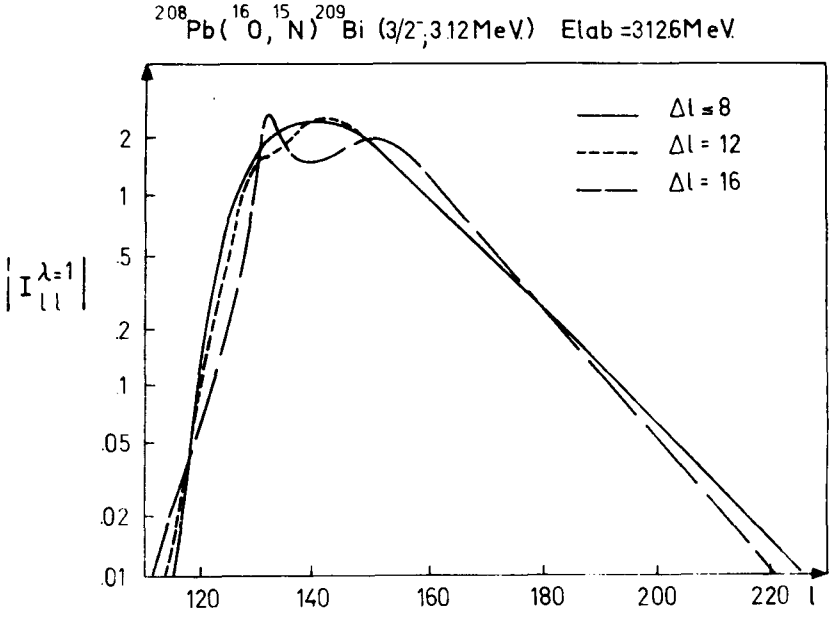

Figure 7:

Comparison of exact and interpolated-extrapolated values of the magnitude of the radial integrals $I^{\lambda=1}_{\ell\ell}$, in the reaction $^{208}Pb(^{16}O,^{15}N)^{209}Bi(3/2^-;$ 3.12 MeV) at 312.6 MeV. "Exact" and approximate curves are indistinguishable for $\Delta\ell \leq 8$.

Detailed application of these procedures to the reaction (II.28) then proceeds as follows. It is found that the smallest and largest values of ℓ that contribute significantly to the differential cross-section (at the .1% level) are

$$\ell_{min} = 110 \quad , \quad \ell_{max} = 230 \tag{II.34}$$

Thus 120 partial waves must be taken into account. The boundary-line between interpolated integrals and use of the large-ℓ extrapolation formulae (II.32), (II.33) is taken to be

$$\ell_A = 182 \tag{II.35}$$

See Fig.II.9 for a symbolic summary of the various ℓ-ranges involved. Radial integrals outside the range $\ell_{min} \leq \ell \leq \ell_{max}$ are dropped; radial integrals in the range $\ell_{min} \leq \ell \leq \ell_A$ are computed at intervals $\Delta\ell$ in ℓ and augmented by interpolation; radial integrals in the range $\ell_A \leq \ell \leq \ell_{max}$ are represented by the extrapolation formulae. The resulting representations of the radial integrals of the family $I^{\lambda=1}_{\ell_i \ell_f}$ are shown in Fig. II.7 The interpolated-extrapolated integrals are graphically indistinguishable from the "exact" integrals for any step-length $\Delta\ell \leq 8$. Significant errors are obtained with $\Delta\ell$ =12, large errors with $\Delta\ell$ =16. The effects on the cross section are shown in Fig. II.8, where of course all four families of integrals have been interpolated and extrapolated in the manner described above for λ =1. Extrapolation and interpolation with a step-size $\Delta\ell$=8 are seen to yield a cross-section accurate to within a fraction of a percent. Although 120 partial waves contribute to the cross-section, only 10 need to be computed explicitly .

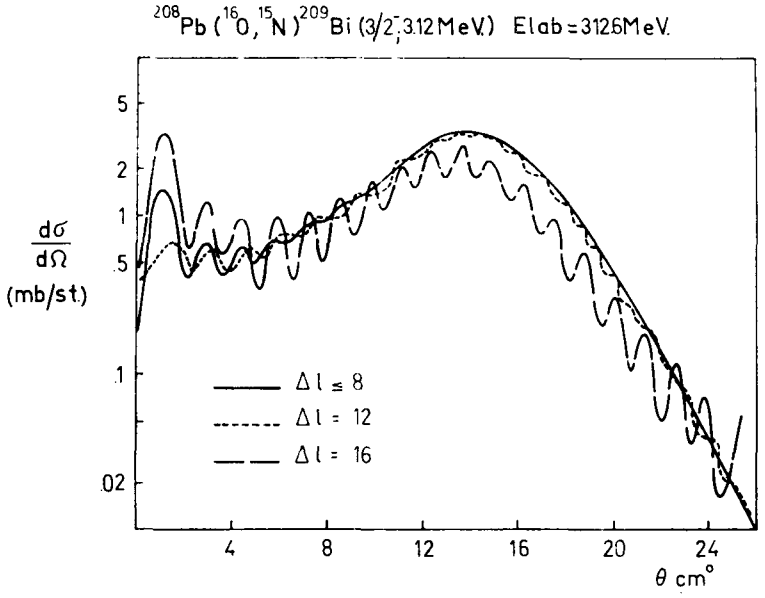

Figure II.8:

Comparison of exact and interpolated-extrapolated differential cross-sections for the reactions represented in Fig.II.7 . "Exact" and approximate curves are indistinguishable for $\Delta\ell \leq 8$.

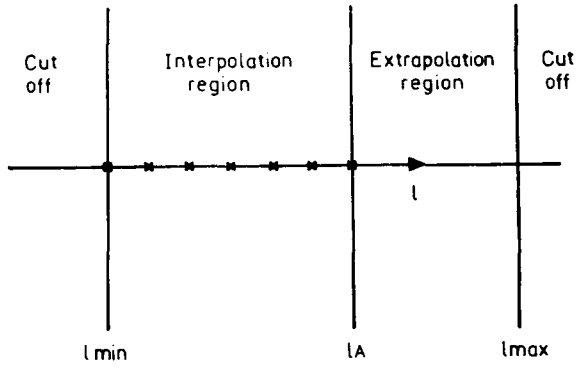

Figure II.9:

Graphical representation of the various ranges of angular momenta that play a role in interpolation and extrapolation in partial-wave expansions. ℓ_{min} and ℓ_{max} are the smallest and largest angular momenta for which the S-matrix elements differ significantly from 0 (or 1). ℓ_A is the connecting angular momentum beyond which extrapolation formulae are to be used.

These techniques apply, in one form or another, to all direct-reaction calculations. The extrapolation-formulae for large angular momenta should always be used and are always applicable. The interpolation methods work best when they are most needed. For nucleon-induced reactions at low energies, or for light heavy-ion systems in which resonant structures are observed, it may be necessary to compute every partial wave up to the large-ℓ asymptotic region; but for such reactions the number of contributing partial waves is rather small. For high-energy or heavy-ion reactions, ℓ-steps from 5 to 50 may be possible. We conclude that it should never be necessary in any direct-reaction calculation to compute explicit S-matrix elements for more than 20 to 30 partial waves. The saving of computational labor is enormous; put in reverse, direct-reaction calculations which do <u>not</u> make extensive use of extrapolation and interpolation in angular momentum are wasting a factor of from 3 to 10 in time and money.

CHAPTER III

HEAVY-ION TRANSFER REACTIONS

ENERGY-DEPENDENCE AND CHANNEL-COUPLING EFFECTS

#III.1 The structure of theories of transfer reactions

The vast majority of transfer reactions, particularly those involving heavy ions, are treated on the basis of the distorted-wave Born approximation (DWBA). In these lectures, the theory of direct reactions is viewed as a model-space theory, wherein coupled-channel Schrodinger equations are constructed and solved within the truncated vector spaces spanned by finite sets of physical channels. If not all the selected physical channels correspond to the same partition of the total number of nucleons, the model space will permit description of "rearrangement processes" or, in less ornate parlance, nucleon-transfer reactions.

In a well-ordered world, DWBA should be derived as the weak-coupling limit of a model-space theory of direct reactions, including transfer. Unfortunately, no well-established theory of this sort exists; controversy still rages over the influence of truncation on the form of the equations and interactions in coupled-channel reaction theories including rearrangement[38]. DWBA is obtained instead from plausibility arguments. Since the effective transition operators are not specifically adapted to precisely-defined model spaces, the DWBA analysis of transfer data is a blend of theory, convention and tradition. In this chapter, the structure of DWBA amplitudes is described, some discussion of computational matters is presented and the shortcomings of the whole procedure are exhibited in an analysis of heavy-ion single-nucleon transfer

over a wide range of bombarding energies.

Consider the stripping reaction

$$A(a,b)B \qquad \text{(III.1)}$$

represented graphically in Fig.III.1 . A cluster of nucleons x is transferred from the bound state a = b+x to the bound state B=A+x. The inverse pick-up reaction is obtained by reading Fig.III.1 backwards. It is clear that if x is viewed as a single body, the reaction (III.1) is a three-body reaction with bodies (A,b,x). Viewing x as a single body amounts to the assumption that the sum of two-body interactions between nucleons of x and nucleons of core A or core b may be replaced by a potential depending only on the co-ordinates r_{Ax} or r_{bx} of the center-of-mass of x relative to A or b. This assumption, known as the cluster assumption is reasonable for single-nucleon transfer but an approximately of doubtful origin and validity for multi-nucleon transfer. The 3-body reaction produced by the cluster assumption will be shown to lead to a 3-dimensional numerical integration for the transition amplitude. Without the cluster assumption, x-nucleon transfer is an (x+2) - body problem with internal structure, leading to a 3x-dimensional numerical integration. The cluster assumption will be made throughout these lectures.

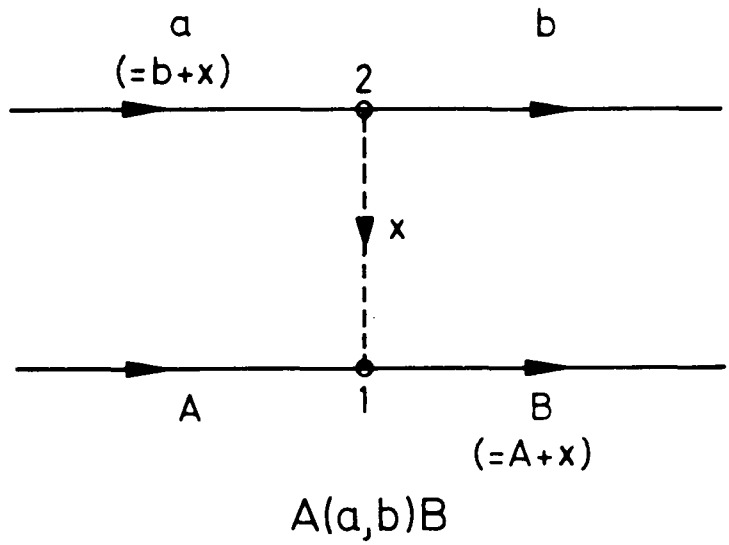

Figure III.1:

Diagramatic representation of a transfer reaction.

A formally-exact expression can be given for the transition (III.1) on the assumption that we know the wave-function $\Psi^+(\vec{k}_i,\vec{r}_i)$ that describes the exact scattering state produced by the colliding nuclei A,a in the incident channel. Let us first give this expression in the form appropriate to the outgoing-channel partition

$$H = H_B(\varphi_B) + H_b(\varphi_b) + T_{rel} + \sum_{i\in B}\sum_{j\in b} V_{ij} + \ldots \qquad \text{(III.2)}$$

of the Hamiltonian of the system. Here $H_B(\varphi_B)$, $H_b(\varphi_b)$ are internal nuclear Hamiltonians, T_{rel} is the relative kinetic energy.

The desired transition amplitude is then[39]

$$T_{if} = \left\langle e^{i\vec{k}_f\cdot\vec{r}_f}\,\phi_B\phi_b \;\middle|\; \sum_{i\in B}\sum_{j\in b} V_{ij} \;\middle|\; \Psi^+(\vec{k}_i,\vec{r}_i)\right\rangle \qquad \text{(III.3)}$$

where $(\vec{k}_i,\vec{r}_i)$, $(\vec{k}_f,\vec{r}_f)$ are wave-number and relative co-ordinates.

The DWBA transition amplitude follows from two formal steps of quite different character.

1) Replacement of Ψ^+ by its entrance-channel component, with the additional assumption that this can be represented by an optical-model wave function $\chi^+(\vec{k}_i,\vec{r}_i)$, eigenfunction of the optical potential $U_{Aa}(\vec{r}_i)$.

$$\Psi^+(\vec{k}_i,\vec{r}_i) \longrightarrow \chi^+(\vec{k}_i,\vec{r}_i) \qquad \text{(III.4)}$$

2) Replacement of the plane-wave state by an ingoing-wave distorted wave-function $\chi^-(\vec{k}_f,\vec{r}_f)$, eigenstate of the optical potential $U_{Bb}(\vec{r}_f)$, using the Gell-Mann-Goldberger transformation[40]. This requires subtraction of the distorting potential for the interaction in (III.4).

$$\exp(i\vec{k}_f\cdot\vec{r}_f) \longrightarrow \chi^-(\vec{k}_f,\vec{r}_f)$$

$$\sum_{i\in B}\sum_{j\in b} V_{ij} \longrightarrow \sum_{i\in B}\sum_{j\in b} V_{ij} - U_{Bb}(r_f) \qquad \text{(III.5)}$$

We obtain for the DWBA transition amplitude

$$T_{if} = J \int d^3\vec{r}_i \, d^3\vec{r}_f \; \chi^{-*}(\vec{k}_f, \vec{r}_f) \langle Bb | V_{eff} | Aa \rangle \chi^{+}(\vec{k}_i, \vec{r}_i) \qquad \text{(III.6)}$$

introducing variables $\vec{r}_i$, $\vec{r}_f$ for the three-body dynamics (Jacobian J) with

$$V_{eff} = \sum_{i \in B}' \sum_{j \in b} V_{ij} - U_{Bb}(r_f) \qquad \text{(III.7)}$$

and $\langle Bb | V_{eff} | Aa \rangle$ integrated over <u>internal</u> co-ordinates φ_A, φ_b , φ_x .
The Jacobian J is in fact given by

$$J = \alpha^3 \qquad \text{(III.8)}$$

where alpha is defined in eq. (III.24).

We further reduce the effective interaction by partitioning the nucleons of B=A+x into constituents of A and constituents of x.

Then

$$\begin{aligned} V_{eff} &= \sum_{i \in b} \sum_{j \in x} V_{ij} + \Delta V \\ \Delta V &= \sum_{i \in b} \sum_{j \in A} V_{ij} - U_{Bb}(r_f) \end{aligned} \qquad \text{(III.9)}$$

According to the cluster assumption, the b-x interaction therm in eq.(III.9) is to be replaced by the one-body potential $V(r_{bx})$. Δ V may be estimated by replacing the sum of two-body interactions between the cores b and A by a core-core optical potential whose parameters are the same as those in the outgoing-channel potential U_{Bb}. These approximation yield the post form of DWBA interaction;

Post

$$\begin{aligned} V_{eff} &= V(r_{bx}) + \Delta V \\ \Delta V &= U_{Ab}(r_{Ab}) - U_{Bb}(r_f) \end{aligned} \qquad \text{(III.10)}$$

A similar "derivation", based on the entrance-channel analog of the par-

tition (III.2), yields the prior form of DWBA interaction;

$$\text{Prior} \qquad \begin{aligned} V_{eff} &= V(r_{Ax}) + \Delta V \\ \Delta V &= U_{Ab}(r_{Ab}) - U_{Aa}(r_i) \end{aligned} \qquad \text{(III.11)}$$

In properly-constructed DWBA computer programs, the post and prior forms of V_{eff} yield cross-section that agree to 2% or less.

In DWBA analyses of data, the distorting potentials and distorted waves are usually chosen to fit elastic scattering in initial and nuclear channels. This is a plausible assumption that has the merit of suppressing parameter-variation, but there is nothing in the above "derivation" that requires it.

#III.2 The spectroscopic part of the DWBA amplitude

Let the cluster x be transferred from and into a single orbit at each reaction vertex. (see Fig. III.1).

$$\begin{aligned} &1. \quad B \longrightarrow A + x : \ \text{orbit } (n_1 \ell_1) \\ &2. \quad a \longrightarrow b + x : \ \text{orbit } (n_1 \ell_1) \end{aligned} \qquad \text{(III.12)}$$

We also assume that the total angular momentum transferred at the two vertices

$$\begin{aligned} \vec{\ell}_1 + \vec{\mathcal{J}}_x &= \vec{J}_1 \\ \vec{\ell}_2 + \vec{\mathcal{J}}_x &= \vec{J}_2 \end{aligned} \qquad \text{(III.13)}$$

can take only a single value (the generalization to multiple angular-momentum transfer will be briefly noted). The total transferred angular

momentum is given by

$$\vec{\lambda} = \vec{J}_1 - \vec{J}_2$$

$$\vec{\lambda} + \vec{J}_2 = \vec{J}_1 \qquad \text{(III.14)}$$

For single-nucleon transfer, the spectroscopic factor for addition of a nucleon in orbit $(n_1\ \ell_1\ J_1)$ to the core nucleus in state J_A is by definition the probability of finding, in the final state J_B, the singleparticle excitation $\left[J_A\right] \times J_1$. Formally,

$$\sqrt{\mathcal{A}(J_A + J_1 \rightarrow J_B)} = \langle J_B \| a^{+J_1}(n_1 \ell_1) \| J_A \rangle \qquad \text{(III.15)}$$

where the reduced matrix element is defined by the Wigner-Eck theorem in the form

$$\langle jm \mid T^k_q \mid j'm' \rangle = C^{j'kj}_{m'qm} \langle j \| T^k \| j' \rangle \qquad \text{(III.16)}$$

A definition similar to (III.15) applies at vertex 2.

We now wish to define a spectroscopic factor for the process

$$J_A + (\ell_1\ \mathcal{A}_x\ J_1) \longrightarrow J_B \qquad \text{(III.17)}$$

when x is a many-particle cluster, in the internal state $(x\,\mathcal{A}_x)$. The difficulty here is that the generalization of (III.15) defines a spectroscopic factor for transfer of x independent shell-model nucleons, assuming that states J_A, J_B are represented by shell-model wave functions. What is needed is rather an amplitude for the transfer of x nucleons in a definite internal state $(x\,\mathcal{A}_x)$, with orbital angular momentum ℓ_1 relative to the mass-center of A. To achieve the necessary separation of center-of-mass and internal motion, proceed as follows[41].

adjustments are clearly unphysical, and only serve to emphasize that we are facing a complete breakdown of the standard model, with its one eyed emphasis on the interaction of two spherical bodies. (The nature of the deviations also precludes an explanation in terms of an ℓ-cutoff whatever its origin, because an ℓ-cutoff with normal capture radii will allow the cross section to rise initially as predicted by the model, followed by a downsloping curve at some point. This is not the way the experimental data behave.) It should also be clear that the deviations are not directly related to the disappearance of a pocket in the two-body potential. This happens when the predicted cross section curve (thin line in figure 10) bends over.

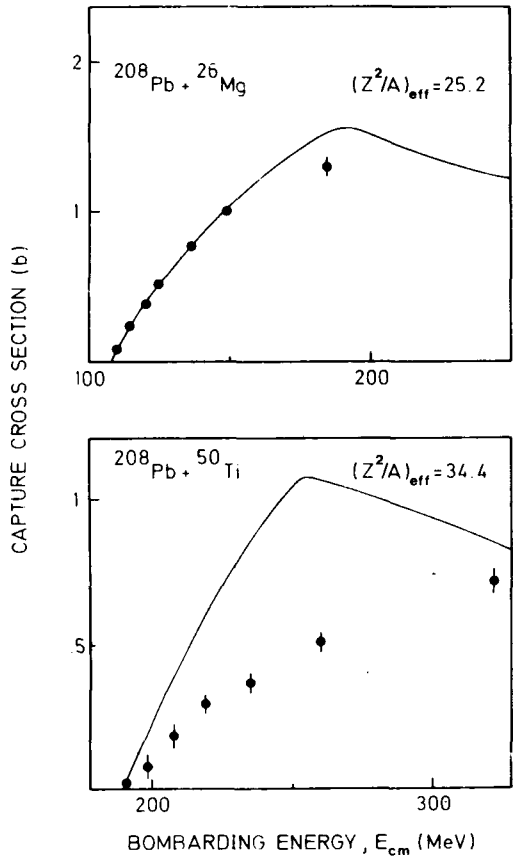

Figure 10:

Comparison of the predictions of the one-dimensional capture (fusion) model (thin line) with experiment (points) for two different cases. The experimental capture cross sections are based on the yields within the symmetric mass peakes on fig.9 .

One way of looking at the deviations between calculated and measured capture cross sections is to interpret them in terms of an extra amount of energy needed to obtain a certain cross section. This is the same as saying that sometimes there has to be a finite radial kinetic energy at

Let $\{\psi^{J_1 J_1}_M\}$ be a complete set of shell-model states for x nucleons in the orbits active in states J_A and J_B, with $a^{\dagger \gamma, J_1}_M$ the operators that create these states from vacuum. Project these x-particle states on to states of the x-nucleon system with definite internal and c.o.m. quantum numbers. Thus define

$$K_{J_1}(\ell_1 \times \mathcal{J}_x ; \jmath_1) = \int d^3R_x \, d\varphi_x \left[\phi^{\ell_1}(R_x) \times \Phi^{x \mathcal{J}_x}(\varphi_x) \right]^{J_1 *}_M \psi^{J_1 J_1}_M \qquad \text{(III.18)}$$

The x-nucleon spectroscopic amplitude at vertex 1 is now given by

$$\sqrt{\mathcal{J}(J_A + (\ell_1 \mathcal{J}_x J_1) \to J_B)} = \sum_{\jmath_1} K_{J_1}(\ell_1 \times \mathcal{J}_x ; \jmath_1) \langle J_B \| a^{\dagger \gamma J_1} \| J_A \rangle \qquad \text{(III.19)}$$

summed over the shell-model labels $\jmath_1$.

Insertion of parentage expansions for the composite states B, a in $\langle Bb | V_{eff} | Aa \rangle$ leads to the expression[33]

$$A(\lambda J_1 J_2 ; n_1 \ell_1 n_2 \ell_2) = \sqrt{2\lambda+1} \sum_{x \mathcal{J}_x} (-)^{\mathcal{J}_x - J_1 + \ell_1 + \ell_2} W(\ell_1 J_1 \ell_2 J_2 ; \mathcal{J}_x \lambda) \times \sqrt{\mathcal{J}(J_A + (n_1 \ell_1 \mathcal{J}_x J_1) \to J_B)} \times \sqrt{\mathcal{J}(J_b + (n_2 \ell_2 \mathcal{J}_x J_2) \to J_a)} \qquad \text{(III.20)}$$

for the spectroscopic contribution to the internal matrix element in (III.6). In eq.(III.20), W is a Recah coefficient and the sum is over internal states of the cluster. In practice[43], contributions from terms with the cluster in its ground state usually predominate.

#III.3 The geometrical part of the DWBA amplitude

Apart from spectroscopic factors, the internal matrix element $\langle Bb | V_{eff} | Aa \rangle$ in eq.(III.6) reduces, after integration over the internal co-ordinates of A,b and x, to

$$\phi_{n_1 \ell_1}(r_{Ax}) \, V_{eff} \, \phi_{n_2 \ell_2}(r_{bx}) \left\{ Y^{\ell_1}(\hat{r}_{Ax}) \times Y^{\ell_2}(\hat{r}_{bx}) \right\}^{\lambda}_{\mu} \qquad \text{(III.21)}$$

where V_{eff} is a function of r_{Ax} or r_{bx}. This quantity is to substituted in the amplitude (III.6) and integrated over r_i , r_f. But $\vec{r}_{Ax}$, $\vec{r}_{bx}$ are given as linear combination of $\vec{r}_i$, $\vec{r}_f$ by[33]

$$\begin{bmatrix} \vec{r}_{Ax} \\ \vec{r}_{bx} \end{bmatrix} = \begin{bmatrix} s_1 & t_1 \\ s_2 & t_2 \end{bmatrix} \begin{bmatrix} \vec{r}_i \\ \vec{r}_f \end{bmatrix} \tag{III.22}$$

where

$$\begin{bmatrix} s_1 & t_1 \\ s_2 & t_2 \end{bmatrix} = \alpha \begin{bmatrix} 1 & -\gamma \\ \delta & -1 \end{bmatrix} \tag{III.23}$$

with $\alpha = aB/(A+a)x$, $\gamma = b/a$, $\delta = A/B$ (III.24)

In order to carry out the integration over $\vec{r}_i$, $\vec{r}_f$, the bound-state form factor must be expressed in terms of the variables of integration. From angular-momentum conservation, the transformation must have the form

$$\phi_{n_1\ell_1}(r_{Ax})\, V_{eff}\, \phi_{n_2\ell_2}(r_{bx}) \left[Y^{\ell_1}(\hat{r}_{Ax}) \times Y^{\ell_2}(\hat{r}_{bx}) \right]^{\lambda}_{\mu} =$$

$$= \sum_{\ell_i \ell_f} \mathcal{H}^{\lambda}_{\ell_i \ell_f}(n_1\ell_1 n_2\ell_2 ; r_i, r_f) \left[Y^{\ell_i}(\hat{r}_i) \times Y^{\ell_f}(\hat{r}_f) \right]^{\lambda}_{\mu} \tag{III.25}$$

The key quantity in deriving the transformation-function $\mathcal{H}^{\lambda}_{\ell_i \ell_f}$ is the scalar product

$$A_{12} = (2\lambda+1)^{-1} \left(\left[Y^{\ell_i}(\hat{r}_i) \times Y^{\ell_f}(\hat{r}_f) \right]^{\lambda *} \cdot \left[Y^{\ell_1}(\hat{r}_{Ax}) \times Y^{\ell_2}(r_{bx}) \right]^{\lambda} \right) \tag{III.26}$$

It is a scalar function of $\vec{r}_i$, $\vec{r}_f$, independent of radial functions, hence a scalar function of $\hat{r}_i$, $\hat{r}_f$; A_{12} is thus a function only of

$$x = \hat{r}_i \cdot \hat{r}_f \tag{III.27}$$

the cosine of the angle between $\vec{r}_i$, $\vec{r}_f$.

There are two distinct ways of evaluating A_{12} (x), leading to two distinct forms of DWBA integrals.

1) To use[42] the solid-harmonic expansion:

$$\mathcal{Y}^{\ell}_{m}(\vec{r}) = \sum_{\lambda=0}^{\ell} \left\{ \frac{4\pi}{2\lambda+1} \binom{2\ell+1}{2\lambda} \right\}^{1/2} s^{\ell-\lambda} t^{\lambda} \left[\mathcal{Y}^{\ell-\lambda}(\vec{r}_1) \times \mathcal{Y}^{\lambda}(\vec{r}_2) \right]^{\ell}_{m} \qquad \text{(III.28)}$$

where

$$\vec{r} = s\vec{r}_1 + t\vec{r}_2$$

and

$$\mathcal{Y}^{\ell}_{m}(\vec{r}) = r^{\ell} Y^{\ell}_{m}(\hat{r}) \qquad \text{(III.29)}$$

2) To proceed as in standard treatments of the three-body problem choosing axes so that $\vec{r}_{Ax}$, $\vec{r}_{bx}$, $\vec{r}_i$, $\vec{r}_f$, lie in the xy-plane with $\vec{r}_i$ along the x-axis.

The resulting expressions for $A_{12}(x)$ are given in Refs.[33,42] and [43]. Once $A_{12}(x)$ has been evaluated, the transformation functions $\mathcal{H}^{\lambda}_{\ell_i\ell_f}(n_1\ell_1 n_2\ell_2, r_i r_f)$ in (III.25) follow from

$$\mathcal{H}^{\lambda}_{\ell_i\ell_f}(n_1\ell_1 n_2\ell_2, r_i r_f) = \int_{-1}^{1} dx\, A_{12}(x) \left[\phi_{n_1\ell_1}(r_{Ax}(x))\, V_{eff}(x)\, \phi_{n_2\ell_2}(r_{bx}(x)) \right] \qquad \text{(III.30)}$$

When (III.25) is substituted in the DWBA amplitude (III.6) and partial-wave expansions for the distorted waves introduced, the integrals over $\hat{r}_i$, $\hat{r}_f$ can be carried out explicitly. The geometrical parts of the DWBA amplitude are then given, in terms of the radial integrals

$$I^{\lambda}_{\ell_i\ell_f}(n_1\ell_1 n_2\ell_2) = \int r_i\, dr_i\, r_f\, dr_f\, \chi^{*}_{\ell_i}(r_i)\, \mathcal{H}^{\lambda}_{\ell_i\ell_f}(r_i r_f)\, \chi_{\ell_f}(r_f) \qquad \text{(III.31)}$$

where $\chi_{\ell}(r)$ are the radial distorted wave-functions, by

$$\beta^{\lambda(J_1J_2)}_{\mu}(n_1\ell_1 n_2\ell_2; \theta) = \sqrt{4\pi}\, i^{\lambda+\ell_1-\ell_2} \sum_{\ell_i\ell_f} C^{\ell_f\lambda\ell_i}_{\mu-\mu\,0}\, I^{\lambda}_{\ell_i\ell_f}(n_1\ell_1 n_2\ell_2)\, Y^{\ell_f}_{-\mu}(\theta) \qquad \text{(III.32)}$$

The conventional way to evaluate the scalar product $A_{12}(x)$ (eq. (III.26)) and hence to evaluate the radial integrals uses the solid-harmonic expansion (III.29). This requires that the radial functions in (III.21) be multiplied and divided by factors

$$r_{Ax}^{\ell_1} \, r_{bx}^{\ell_2} \sim R^{\ell_1+\ell_2} \qquad \text{(III.10)}$$

with R a typical nuclear radius, to make the harmonics solid. This introduces systematic cancellations in the expressions obtained for the radial integrals. For heavy-ion reactions, radial integrals are given as sums of terms, each of which is larger than the final result by a factor of about $10^{\ell_1+\ell_2}$. There is a basic rule[44] in many-body physics and numerical analysis; "Thou shalt not split small things into large pieces". Violation of this rule can be avoided by use of the Balian-Brozin procedure[33].

#III.4 DWBA cross-sections and procedures

Spectroscopic and geometrical parts of the DWBA amplitude combine to yield the differential cross section;

$$\frac{d\sigma}{d\Omega}(\theta) = \frac{1}{E_i E_f} \frac{k_f}{k_i} \left(\frac{2J_B+1}{2J_A+1}\right) \sum_{\lambda\mu}' \left| G_\mu^{\lambda(J_1J_2)}(\theta) \right|^2 \qquad \text{(III.34)}$$

where the multiple transition amplitude is given by

$$G_\mu^{\lambda(J_1J_2)}(\theta) = \sum_{n_1\ell_1 n_2\ell_2} A(\lambda J_1 J_2 ; n_1\ell_1 n_2\ell_2) \, \beta_\mu^{\lambda(J_1J_2)}(n_1\ell_1 n_2\ell_2 ; \theta) \qquad \text{(III.35)}$$

The spectrocopic amplitude A is given by eq. (III.20), the geometric am-

plitude beta by (III.32). If several different values of the total angular momentum transfer (J_1, J_2) at each vertex are allowed, make the replacement

$$\sum_{\lambda\mu} \longrightarrow \sum_{J_1 J_2} \sum'_{\lambda\mu} \tag{III.36}$$

in (III.34).

There are three main stages in a standard DWBA analysis of transfer reactions.

1) Fit elastic scattering in initial and final channels to determine the distorted waves.

2) Determine radial wave functions $\phi_{\ell_1}(r_{Ax})$, $\phi_{\ell_2}(r_{bx})$ at the vertices by the "separation-energy method". In this method, which is more of a recipe than a method, a Woods-Saxon potential is used to generate the bound-state wave functions at the vertices. (see Fig. III.1) The radius and difuseness parameters are given values appropriate to the low energy A+x, b+x systems and the depths are adjusted to yield the observed separation energies.

3) Spectroscopic factors are either computed from suitable model wave functions or determined empirically from analysis of other transfer reactions between the same nuclear states.

We have already noted that the first step, the use of distorted waves fitted to elastic data, is without solid foundation in any detailed theory of the transfer process. Steps 2 and 3, factorization of overlap-functions into products of radial wave functions and spectrocopic factor and use of the separation energy procedure for radial wavefunctions, also rest on shaky foundations. From the Schrödinger equations for the nuclear states A,a,B,b, Schrödinger-like equations can be derivered[45] for the overlap functions for the break-up processes

$$\begin{aligned} B &\longrightarrow A + x \\ a &\longrightarrow b + x \end{aligned} \tag{III.37}$$

The separation-energy method provides a simulation of rather than a controlled approximation to these overlap functions. It is reasonably accurate in transitions that carry a sizeable fraction of the sum-rule strength of the giant transfer resonances to which they belong; serious errors are likely in dealing with weaker transitions, for displaced in energy from the centroids of their excitations.

#III.5 Energy dependence of single nucleon transfer

There is ample evidence from single-energy analysis that, in multi-nucleon transfer reactions induced by both light[46] and heavy[47] ions, multistep processes often complete on equal terms with single step DWBA process. Both coupling to inelastic excitations of the collision partners and sequential transfer play an important part. Here we discuss evidence of another sort - from an analysis of a few transitions of simple spectroscopic chatacter over a wide range of bombarding energies that the single-channel DWBA description of heavy-ion induced single-nucleon transfer is also in serious trouble.

The reactions in question here are elastic scattering and single-nucleon transfer induced by the bombardment of ^{208}Pb with ^{16}O ions at 19 energies over the range

$$E_{lab} \quad \text{from } 69.1 \text{ MeV} \quad \text{to } 312.6 \text{ MeV}$$

$$E/E_B \quad \text{from } .9 \quad \text{to } 3.9 \qquad \text{(III.38)}$$

In (III.38), E is the center-of-mass energy in the incident channel, E_B(75 MeV) is the height of the Coulomb barrier. The energy-range covered extends from well below the Coulomb barrier to an energy per incident nucleon approaching the Fermi energy of nucleons in the nucleus.

The reaction studied are as follows:

Elastic scattering

At 12 energies from 80 to 102 MeV	(Brookhaven[48])
At 104, 138.5, 216.6 and 312.6 MeV	(Berkeley[37 49])
At 129.5 and 192 MeV	(Oak Ridge[50])

$^{208}Pb(^{16}O,^{15}N)^{209}Bi$

At 69.1 MeV	(Minnesota[51])
At 104, 138.5, 216.6 and 312.6 MeV	(Berkeley[37 49])

$^{208}Pb(^{16}O,^{15}O)^{209}Pb$

At 138.5, 312.6 MeV	(Berkeley[37 49])

$^{208}Pb(^{16}O,^{17}O)^{207}Pb$

At 104, 138.5 and 216.6 MeV	(Berkeley[49])

The elastic and transfer data is analyzed following to the standard DWBA procedure outlined in #III.4, in Refs.[37] and [49]. No other direct reaction has ever been analyzed (apart from elastic scattering and elementary-particle reactions!) over such a wide range of energies.

It is not my purpose here to discuss the details of this multi-energy analysis, nor to point out the variety of spectrocopic information derived. I will focus on the energy-dependence of the transfer reactions. To that end, consider the reactions $^{208}Pb(^{16}O,^{15}N)^{209}Bi$. The low-lying spectrum of ^{209}Bi, with that of ^{208}Pb for comparison, is shown in Fig. III.2. Apart form the well-established septuplet of levels near 2.6 MeV that arise from coupling the 1h9/2 single-proton state to the 3- first excited state of ^{208}Pb, all the observed states of ^{209}Bi up to about 3.5 MeV are of pronounced single-particle character. The spectroscopic factors obtained in the multi-energy analysis under discussion,

arbitrarily normalized at 216.6 MeV and those from a (^{3}He,d) reaction[52] and a model calculation[53] are exhibited in Table III.1. While the overall normalization is uncertain, it is clear that all the levels in question are good single-proton states ($\mathcal{S} \gtrsim .5$), with the purity decreasing as the excitation energy increases.

Table III.1:

Various estimates of the spectroscopic factors for single-proton states in ^{209}Bi. The spectroscopic factors in the last two columns were normalized to the value .74 (From Table VIII, ref.[49]).

State	(^{16}O,^{15}N)	(^{3}He,d) 20 MeV	Theory
$1h_{9/2}$	.95	1.1	.83
$2f_{7/2}$	.74	.74	.74
$1i_{13/2}$	.61	.53	.61
$2f_{5/2}$	.61	.83	.58
$3p_{3/2}$	.55	.63	.64
$3p_{1/2}$	.52	.46	.47

A wide variety of optical-model parameterizations were obtained of the entrance-channel elastic data over the entire energy-range. These included individual fits at each energy, energy-dependent fits with the optical parameters assumed to be constant, linear, and quadratic in E_{LAB} and in $1/E_{LAB}$, all with Woods-Saxon forms for the potentials. Many satisfactory descriptions of the elastic data were obtained and the optical potentials used to generate distorted waves for the transfer calculations. In the absence of exit-channel elastic data, the same

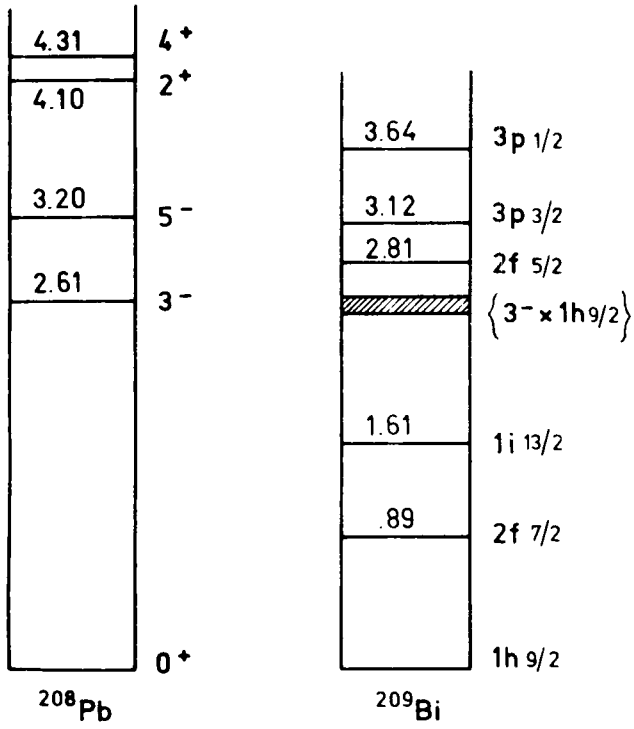

Figure III.2:

Spectra of ^{208}Pb and ^{209}Bi .

energy - and mass - independent parameters used in the entrance channel were used to produce exit-channel optical potentials. Since the pertinent single-particle (and single-hole) states have been extensively studied in other reactions, it was possible to use bound-state radial functions consistent with a wide variety of other experimental data.

The main conclusions from this analysis may be summarized as follows

1) The conventional DWBA analysis account very well for angular distributions and relative cross-sections at each energy. These aspects of the transfer cross-sections are very insensitive to the optical-model parameters.

2) Absolute cross-sections at each energy are also insensitive to changes in the optical-model parameters. The energy-dependence of the cross-sections over the full energy-range is also very insensitive to the optical-model parameters.

Observed and calculated differential cross-sections for the transition $^{208}Pb(^{16}O,^{15}N)^{209}Bi(1h9/2;g.s.)$ are compared in Fig.III.3 . The calculated cross-sections shown here use our best individual-energy optical-model parameterization of the elastic data (Fit Q in refs.[37 49] The shapes of the angular distributions are well reproduced at all energies; however, the DWBA absolute cross-section is too low at the lower energies, roughly correct at 216.6 MeV and too high by a factor 1.5 to 2 at 312.6 MeV.

This discrepancy in the energy-dependence of the cross-sections is seen more vividly in the angle-integrated cross-sections for the $1h_{9/2}$, $2f_{7/2}$ and $1i_{3/2}$ transitions, shown in Fig. III.4. The observed cross-sections increase through the Coulomb barrier, level off by about 150 MeV, then start to drop with increasing energy. The DWBA cross-section, in contrast, follow experiment through the Coulomb barrier, then either stay constant or continue to increase. It is clear that if the cross-

section of each direct transition to a specific final state either stays constant or increases with energy, the total 'peripheral' contribution to the reaction cross-section must increase rapidly with energy as new channels open. The experimental situation seems to be that the cross-section of each individual transition decreases rapidly enough with energy to maintain a roughly-constant peripheral contribution to the total reaction cross section. In other words, the standard single-channel DWBA analysis fails to reproduce the energy-dependence of the transfer cross sections.

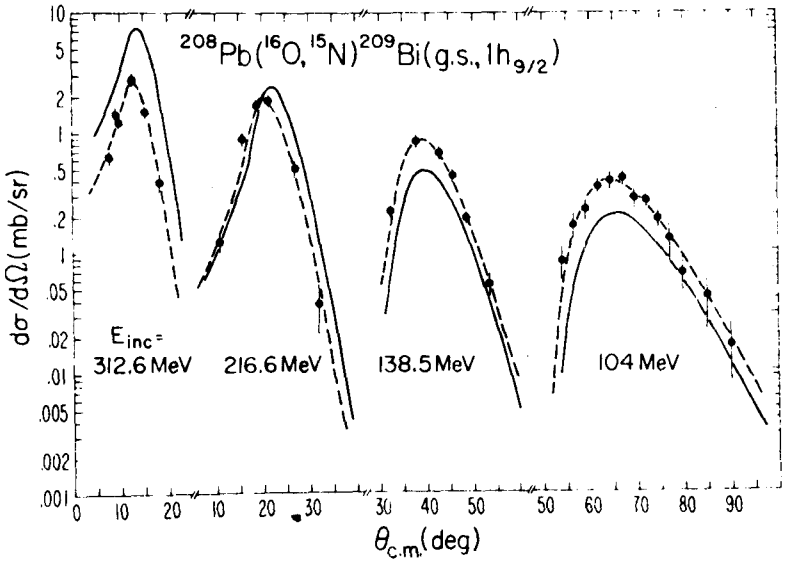

Figure III.3:

Comparison of measured and calculated differential cross-sections for the transition $^{208}Pb(^{16}O,^{15}N)^{209}Bi$ ($h_{9/2}$;g.s.) at various bombarding energies (from ref.[37])

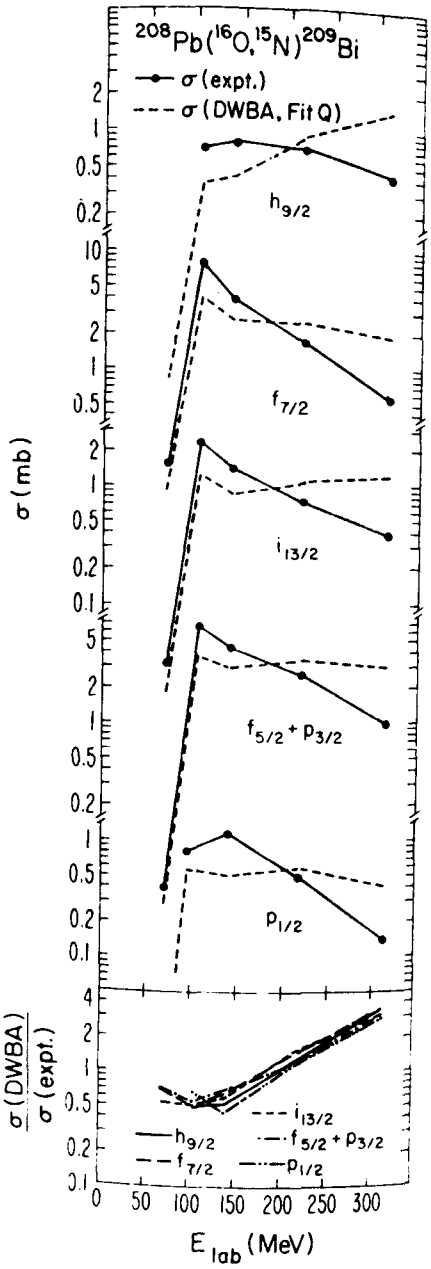

Figure III.4:

Comparison of theory (dotted line) and experiment (continuous line) for the angle-integrated cross-sections of various single-particle transitions in the reaction $^{208}Pb(^{16}O,^{15}N)^{209}Bi$ at various bombarding energies (from ref.[37]).

The only transfer-reaction study over a comparable energy-range that we could find[52] involves the ground-state transition $^{58}Ni(^{3}He,d)^{59}Cu$ from 15 to 205 MeV. The ratio of DWBA to measured total cross-sections is plotted in Fig. III.5. The heavy line indicates the curve through the points drawn by the authors; their conclusion was that the ratio of DWBA to experimental cross-section is roughly energy-independent. However, their 205 MeV point is questionable since no elastic-scattering data exists near that energy to constrain the choice of optical-model parameters. If that point is eliminated, the best-fit straight-line through the remainig points (dotted line in Fig. III.5) shows a marked upward trend with energy, consistent with our findings from the transfer reactions induced by ^{16}O on ^{208}Pb.

A simultaneous remeasurement of the ground-state ($^{3}He,d$) transition, and the elastic scattering of ^{3}He on ^{58}Ni at energies near 200 MeV, is obviously desirable.

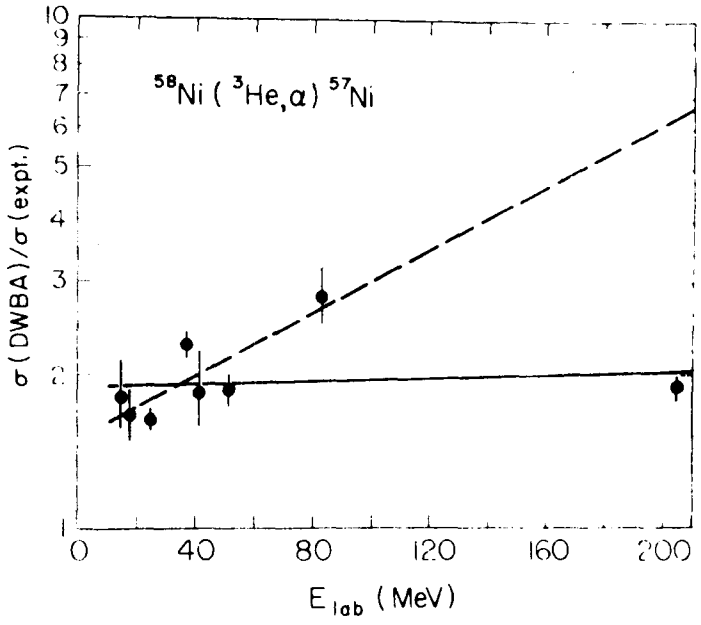

Figure III.5:

Comparison of DWBA and experimental values for the angle-integrated cross-section of the reaction $^{58}Ni(^{3}He,d)^{57}Ni$ ($3/2^-$; g.s.) at various bombarding energies (from ref.[52]).

#III.6 Energy dependence and transfer theories

Experimental studies of elastic scattering and selected transfer reactions, induced by light and heavy ions, should be carried out over wide ranges of bombarding energies. Such studies are likely to demand much more of reaction models than single-energy experiments have done. The key energy-parameters in this connection is E/E_B, the ratio of the center-of-mass energy to the barrier height. The $^{16}O+^{208}Pb$ experiment discussed in #III.5 ranged over values of E/E_B form .9 to 4. The same range could be covered for $^{16}O+^{40}Ca$ with variable ^{16}O-beam energies up to 180 MeV and with lower-energy beams for lighter ions.

If further study confirms our, necessarily tentative, conclusion that single-channel DWBA has the wrong energy-dependence, a serious flaw in current reaction-models has been uncovered. Various suggestions have been made concerning the origin of the discrepancy in the $^{16}O+^{208}Pb$ reactions. One[53] is that surface-transparent optical potentials should be used; this helps matters at energies around 100 MeV but is unlikely to suppress the continued rise in DWBA transfer cross-sections between 200 and 300 MeV. Another[54] proposes a modified analysis in which the exit-channel distorted waves no longer need reproduced the elastic data; here too the largest effects are at the lowest energies. The discrepancy, if confirmed in other studies, is more likely to be a general indication of the inadequacy of current models of transfer reactions. What is needed is a consistent model-space theory including transfer channels. It is likely that within such a framework, the numerical techniques discussed here for evaluating DWBA kernels and solving coupled equations will continue to be useful.

The reader that has reached this stage will have perhaps noted that Chapter IV is missing.

The Organizing Committee has failed to obtained it and humbly asks for excuses. It later turned out that there was a reason.

Buenos Aires happens to house a renowned opera theatre. This missing chapter should have been written during a night in which Traviata was performed.

Let this missing chapter stand as a modest tribute to the art of music and "bel canto".

THE DYNAMICS OF HEAVY ION FUSION REACTIONS

S. BJORNHOLM

NIELS BOHR INSTITUTE, UNIVERSITY OF COPENHAGEN,
DK-2100 DENMARK

I. INTRODUCTION

In reactions between heavy ions, the total reaction cross section is generally composed of two well separated components. One represents a more or less damped scattering process, whereas the other involves a thorough amalgamation of the two colliding systems, usually referred to as fusion. For light systems fusion is the dominant part, but with increasing charge and size of the reaction partners the deep inelastic scattering becomes increasingly important. See for example ref.[1] and references therein.

Studies of the strongly damped scattering process as well as of the fission process have given insights into the dynamics of large scale motion of nuclear matter. By contrast, fusion studies have mainly provided information on the static interaction between two rigid spheres[1,2,3,4]. The only dynamical element required to understand fusion so far has been the rather uncritical assumption that there is sufficient friction at contact to trap the system whenever it enters into a pocket in the static one-dimensional, two-center potential acting between the reaction partners.

This situation makes it relatively simple to predict and interpret fusion cross sections[5]. At the same time no information is obtained from such measurements about the complex dynamical process of amalgamating two spheres in contact into one whole system. Apparently, fusion is decided at the moment of contact, leaving us in the dark about the further dynamical evolution, until either a compound residue or (for heavier compound systems) a pair of fission products emerge at some unspecified later time, see figure 1.

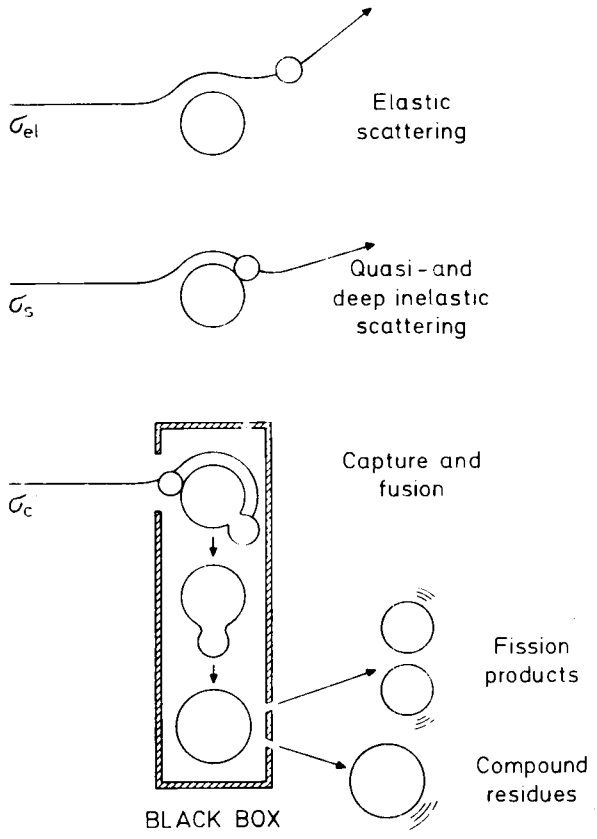

Figure 1: Heavy ion reactions tend to proced through two distinct channels. Either the nuclei scatter from each other and we observe two products of approximately the same mass as the initial nuclei with angular distributions peaked near the grazing angle. We have learned a great deal about nuclear dynamics from the loss of energy, orbital angular momentum and isospin asymmetry in such reactions. The two nuclei may alternatively fuse together and result in the formation of compound residues or in the appearance of two fission products of approximately equal mass. This process clearly involves a more far reaching dynamical rearrangement of the reaction system; yet what can be observed has so far been describeble in terms of the static two center potential at contact. The dynamical aspects were hidden in a black box until recently.

In these lectures we shall review new evidence that remedy this unsatisfactory situation to a considerable extent:

1) firstly, in collisions between the heavier nuclei it proves essential to consider dynamical deformations induced upon contact in order to understand the measured excitation functions for the mass equilibration reactions associated with fusion;

2) second, the gamma ray multiplicities indicate that the two incident heavy nuclei merge very intimately together before they reseparate into two nearly equal halves; and,

3) thirdly, angular distributions show that the entire process of amalgamation and reseparation can occur in less than 10^{-20} sec.

II. ONE-DIMENSIONAL FUSION MODELS IN THEORY AND IN PRACTICE

A. Theoretical fusion models describe the capture process.

In this section the cross sections and the excitation functions for fusion of ^{208}Pb projectiles with targets of Mg, Al, Ca, Ti, Cr, Fe and Ni will be compared with model calculations of the type that accounts well for a large body of fusion data with lighter reaction systems, refs.[2,3,5]. Such models do not really describe the fusion reaction in its full complexity. They simply define reaction conditions where two interacting spherical nuclei will experience a net attraction as they come close to each other. It is then assumed that this net attraction will eventually lead to the formation of a compound nucleus. The success[5] of capture models in describing fusion reaction cross sections lends support to this assumption. The models are also successful in

describing capture followed by fission (plus compound residues) for medium light systems[5]. Its character as a model of the capture process as opposed to fusion in its full complexity is here clearly illustrated. The model can actually describe fission cross sections also in those cases where the ℓ-values contributing to fission are larger than the ℓ-value, $\ell_{(B_f=0)}$, corresponding to a vanishing fission barrier[6,7,8]. For such ℓ-values there cannot be fusion into a true compound nucleus, but capture followed by mass equilibration is apparently possible, and the cross section for this process is well described by the model in many cases. In general, therefore, the excitation functions for symmetric fragmentation of asymmetric entrance channel systems are in good agreement with standard capture models. For sufficiently heavy systems, however, or for large angular momenta, the models break down. This is a new result that has come out of a series of recent measurements[9,10], made with the ^{208}Pb-beam of the UNILAC accelerator at GSI, Darmstadt. I will describe these measurements in this section and use them in section III as a basis for exploring the validity of a more general reaction model developed by Swiatecki[11].

B. The proximity model for the capture of two spheres.

In our analysis of the cross sections for fusion and symmetric fragmentation we shall first compare the experimental results with calculations of the capture cross section obtained with the proximity model[2,3,5]. In this model the nuclear interaction is

$$V_N(r) = 4\pi\gamma\bar{C}\, b\, \Phi_{prox}((r-C_1-C_2)/b) \qquad (1)$$

where

$$R_i = 1.28\, A_i^{1/3} - 0.76 + 0.8\, A_i^{-1/3} \tag{2}$$

$$C_i = R_i - b^2/R_i \tag{3}$$

$$\bar{C} = \frac{C_1 \cdot C_2}{C_1 + C_2} \tag{4}$$

$$\gamma = 0.9517\ (1-1.7826(1-2\cdot \frac{Z_1+Z_2}{A_1+A_2})^2) \tag{5}$$

and $\hat{\Phi}_{prox}(\xi)$ is a universal function given in refs.[2,3].

Proximity friction due to particle transfer is included in the dynamical calculations of trajectories, and capture followed by fusion is assumed to occur when the trajectories are trapped in a pocket in the effective one-dimensional interaction potential $V_{eff}(\ell,r)$ consisting of the point-charge Coulomb, the nuclear, and the centrifugal potentials. For a given system and center of mass energy E_{cm}, all trajectories up to a certain impact parameter ρ_c or angular momentum ℓ_c are found to contribute to the capture cross section σ_c, i.e. the model is effectively a sharp cut-off model with

$$\sigma_c = \pi\, \rho_c^2 = \pi\, \frac{h^2 \ell^2}{2\, \mu E_{cm}} \tag{6}$$

In the high energy region the maximum angular momentum for capture is found approximately to be a constant ℓ_m and as noticed in ref.[5] $\ell_m \simeq 7/5\ .\ell_p$ where ℓ_p is the maximum angular momentum for which there

is a pocket in the entrance channel potential. In fact, it can be shown that the condition of rolling for touching spheres together with proximity friction leads exactly to this relation.

It is therefore possible to formulate a schematic model for capture that reproduces the capture cross sections obtained with the complete proximity model with sufficient accuracy. The main features of this simple model are that there is a maximum angular momentum for capture $\ell_m = 7/5.\ell_p$ and that all trajectories that can surmount the barrier in the effective interaction are captured, see figure 2a).

In the simplifying approximation that the information takes place at constant interaction reactions R_{int}, independent of ℓ , we can express angular momentum conservation in two ways, figure 2.

$$\ell = \rho(2\mu E)^{1/2} = R_{int} \quad 2\mu(E-V_{int}(\ell=0))^{1/2} \tag{7}$$

giving

$$\sigma = \pi\rho^2 = \pi R_{int}^2 (1 - \frac{V_{int}(\ell=0)}{E}); \quad \ell \leq \ell_m \tag{8}$$

which is valid for low bombarding energies. When trajectories with $\ell=\ell_m$ begin to reach the interaction distance R_{int} at higher energies the cut-off at $\ell = \ell_m$ = const. leads to: $\ell_m = \rho(2\mu E)^{1/2}$ or

$$\sigma = \pi\rho^2 = \pi \cdot \frac{\ell_m^2}{2\mu E} \quad ; \quad \ell \geq \ell_m \tag{9}$$

Thus the cross section plotted against 1/E will at first rise linearly and the extrapolated line will intersect the (1/E=0)-axis at the geometrical cross section value, πR_{int}^2 , eq.(8). From a certain point on the curve will turn down passing through the origin, eq.(9), see also fig.2. We shall here be concerned mostly with the raising part

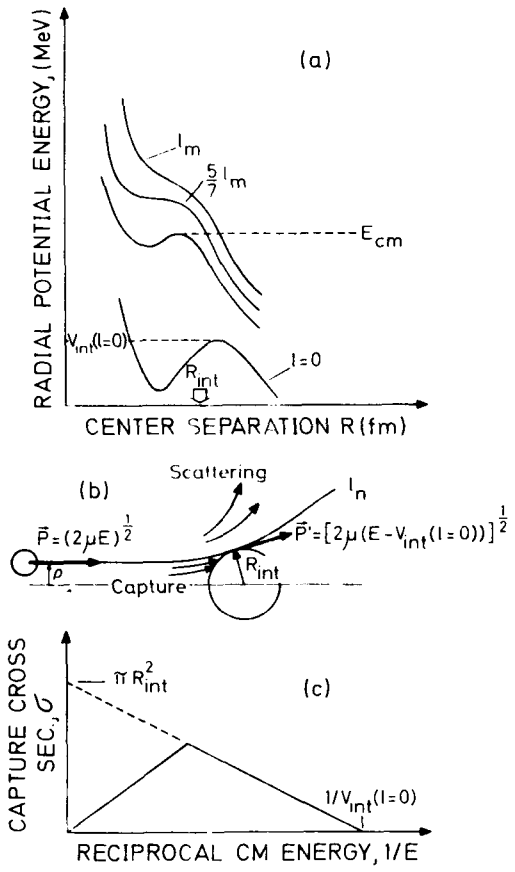

Figure 2:

Schematics of the one-dimensional fusion models.
(a) Radial potential energy as a function of the two-center separation distance for various values of angular momentum. E_{cm} is the bombarding energy in the center of mass system.
(b) The critical trajectory with ℓ_c, separating scattering ($\ell > \ell_c$) from capture reactions ($\ell \leq \ell_c$).
(c) The excitation function for capture (and fusion) expected on the basis of one-dimensional fusion models.

of the excitation function, and note that its slope is directly related to the size of the two interacting nuclei.

In doing a more precise calculation, we shall first define an angular momentum dependent interaction radius $R_{int}(\ell)$. For $\ell \leq \ell_p$ (i.e. when there is a pocket in the effective interaction) we shall use for this quantity the center of mass distance at the barrier R_{int} of the effective interaction. For $\ell > \ell_p$ we shall use, as a reasonable estimate, the center of mass distance at the highest existing barrier, viz. $R_{int}(\ell_p)$.

We can now define a quantity that we shall call the interaction barrier

$$V_{int}(\ell) = V_{eff}(\ell, R_{int}(\ell)) \tag{10}$$

which, for $\ell < \ell_p$, is just the barrier of the effective interaction in the entrance channel. For a given center of mass energy E_{cm} we can now determine an angular momentum ℓ_E as the solution to the equation

$$V_{int}(\ell_E) = E_{cm} \tag{11}$$

and thus determine the capture cross section in eq.(6) with

$$\ell_c = \begin{cases} \ell_E & \text{for } \ell_E < \ell_m \\ \ell_m & \ell_E > \ell_m \end{cases} \tag{12}$$

The results obtained using this schematic model are shown in figure 3 with ℓ_m determined by three different conditions; i) sliding ($\ell_m = \ell_p$); ii) rolling ($\ell_m = 7/5.\ell_p$); and iii) sticking, where ℓ_m is the maximum angular momentum for which there exists a pocket in the effective potential for co-rotating spheres. Also shown is the capture cross section calculated within the proximitly model including friction. It is seen to agree rather well with the results of the schematic model for rolling.

Moreover, the dashed curve in figure 3 is the estimated total reaction cross section defined by

$$\sigma_R = \pi R_{CB}^2 (1 - V_C/E_{cm}) \tag{13}$$

where

$$R_{CB} = (1.7445 - 0.04338 \ln (Z_1 . Z_2))(A_1^{1/3} + A_2^{1/3}) \qquad (14)$$

and

$$V_C = Z_1 Z_2 C^2 / R_{CB} \qquad (15)$$

is the estimated Coulomb barrier.

Finally, figure 3 shows the maximum capture cross section compatible with true fusion-fission. Larger cross sections will involve ℓ-values in excess $\ell_{(B_f=0)}$ where the fission barrier vanishes[8].

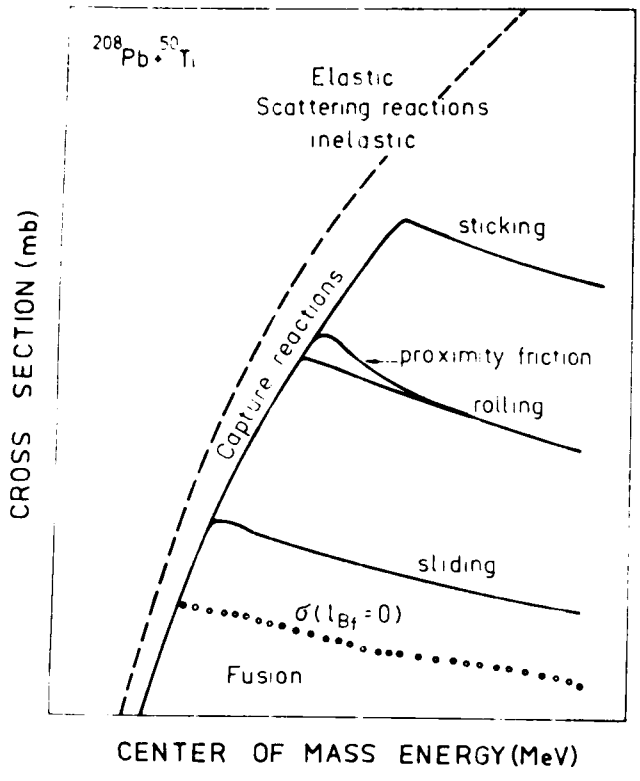

FIGURE 3:

Calculated cross section curves as a function of center of mass energy. The reaction $^{208}Pb + ^{50}Ti$ is chosen as an example. The dashed line is the total reaction cross section, below are three schematic versions of the capture (and fusion) cross sections expected on the basis of a one-dimensional static interaction potential. They differ in the amount of angular momentum dissipation assumed to take place before capture occurs. The fourth curve, marked proximity, is the result of a full calculation with a static potential and dynamics in the form of proximity friction, ref.[2,3,5]. The dotted line below is the upper limit for genuine fission.

C. Bass parameter and effective fissility.

In order to be able to classify various target-projectile combinations, we shall make use of the parameter suggested by Bass[12] and defined as the ratio of Coulomb and nuclear forces between two spherical nuclei at maximum nuclear attraction:

$$X_{Bass} = \frac{F_{Coulomb}}{(F_{Nuclear})_{max}} \qquad (16)$$

A value of $X_{Bass} \geq 1$ means that there is no pocket in the effective potential for any ℓ-value, hence the capture cross section is expected to vanish completely. For decreasing values of X_{Bass}, a potential pocket will appear for an increasing number of ℓ-values and the maximum capture cross section is expected tc increase. Thus the Bass-parameter (eq.16) should give a first orientation into the type of excitation function one should expect accorcing to the model.

In the sharp surface, liquid drop model[9] the maximum nuclear attraction is $4\pi\gamma R_1 . R_2/(R_1+R_2)$ and it occurs at contact (i.e. $r = R_1+R_2$). The corresponding Bass parameter is a kind of generalized "effective fissility" for asymmetric systems

$$X_{Bass}^{LD} = \frac{e^2}{16\pi\gamma r_0^3} (Z^2/A)_{eff} \qquad (17)$$

where

$$(Z^2/A)_{eff} = \frac{4 \cdot Z_1 Z_2}{A_1^{1/3} A_2^{1/3} (A_1^{1/3} + A_2^{1/3})} \qquad (18)$$

For symmetric systems, $Z_1 = Z_2 = Z/2$ and $A_1 = A_2 = A/2$, this expression for X_{Bass} reduces to 5/6 times the usual fissility parameter for the compound system.

In the proximity description[2,3] the maximum nuclear attraction deviates somewhat from the liquid drop expression, mainly due to the fact that the central radii in eq.(1) are smaller than the liquid drop nuclear radii, whereas gamma is considered a constant. For the reactions considered in these lectures one finds that the Bass-parameter, within the proximity description, is given to a good approximation by

$$X_{Bass}^{Prox} = \left[(Z^2/A)_{eff} + 7.8\right] /53 \qquad (19)$$

Thus there are no pockets in the effective proximity potential for $(Z^2/A_{eff} \geq 45.2$, not even for $\ell = 0$.

D. Measurements of capture cross sections in heavy systems.

Fusion begins with the capture of two incident nuclei to form a quasistable complex of the two nuclei in contact. This is what distinguishes it from scattering, which is a faster process. To measure fusion cross sections or more correctly, capture cross sections it is sufficient that the total reaction probability, or the cross section σ_R , can be divided into two terms, $\sigma_R = \sigma_s + \sigma_c$, where σ_s represents scattering and σ_c is the capture cross section. Experimentally, such a distinction is possible when the mass asymmetry in the entrance channel is large. In that case, the binary reaction products generally fall into two more or less distinct groups: i) a group of target-projectile-like scattering products, representing σ_s, and ii) a group of capture products with nearly half the mass of the total system, representing σ_c, (in the mass region under consideration here, the yield of compound residues is negligible), see also figure 4.

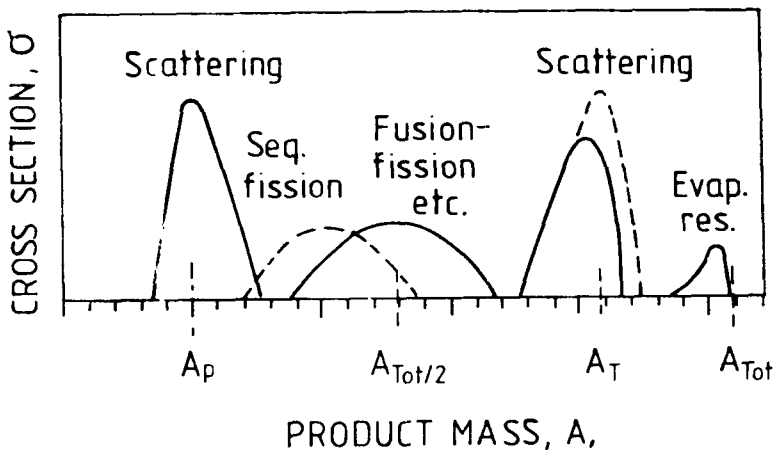

Figure 4:

Illustration of a typical mass distribution of reaction products after a heavy ion reaction. The evaporation residues and the yield of products with approximately one half the total mass represent the capture (fusion) cross section. Scattering products appear primarily as peaks near the target and projectile masses, but there can also be a contribution of products with approximately one half of the target mass A_T, stemming from sequential fission of the heavy scattering products. It is possible to distinguish the two types of fission on the basis of kinematical coincidence measurements[15].

As mentioned in subsection A, the observed yields[6,7] of symmetric products are sometimes so large that they have to involve angular momenta in excess of the value, where the fission barrier one calculates for the fused system vanishes[8]. In such cases there can be no true compound nucleus formation with subsequent statistical decay into the fission channel. When it happens, there is a tendency for the mass distribution to become wider than normally observed in fission[7]. To avoid ambiguity we will refer to the observed process as symmetric fragmentation or capture, reserving the narrower term fission to genuine compound nucleus formation, followed by decay into two fragments.

I shall discuss a series of measurements with very heavy systems of

I shal discuss a series of measurements with very heavy systems of high initial mass asymmetry, namely the symmetric fragmentation (capture) of systems involving ^{208}Pb beams and targets of ^{26}Mg-^{64}Ni at energies 1.0-1.8 times the interaction barrier energy, see table 1. To the extent that they really fuse, these systems will lead to very highly fissile nuclei. One way of expressing this is that the angular momentum required[8] to reduce the fission barrier to zero is relatively low ($\ell_{(B_f=0)}$, table 1). In the entrance channel, the Coulomb repulsion is comparable although not quite equal to the maximum nuclear attraction as expressed[11,12] through the ratio $(Z^2/A)_{eff}$ in table 1, see also eq.(18). Thus the Coulomb force is likely to play a crucial role, whereas in lighter systems the centrifugal force is more important. In contrast to what is observed with lighter systems[5], one finds that the presence of a pocket in the potential between the two initial spheres is unsufficient to guarantee capture, and the observed deviations have the character of a critical phenomenon. It is as if systems with $(Z^2/A)_{eff}$-values in excess of a critical threshold value require an extra inward radial velocity (extra push[11]) in order to be caught and develop towards fusion.

TABLE 1

Properties of systems produced in reactions with ^{208}Pb

ENTRANCE CHANNEL			COMPOSITE SYSTEM				
Target	V_c (MeV)	$(Z^2/A)_{eff}$	(Z_λ, A_λ)	<TKE> (MeV)	Fissility parameter Z^2/A	$B_f(\ell=0)$ (MeV)	$\ell_{B_f=0}$ (MeV)
^{26}Mg	110.3	25.2	(94,234)	174.8	37.8	3.9	71
^{27}Al	119.3	27.9	(95,235)	177.9	38.4	3.3	69
^{48}Ca	173.6	31.9	(102,256)	196.6	40.6	1.2	58
^{50}Ti	190.5	34.4	(104,258)	203.0	41.9	0.71	52
^{52}Cr	207.3	36.9	(106,260)	209.6	43.2	0.38	45
^{58}Fe	222.0	38.0	(108,266)	215.3	43.8	0.22	40
^{64}Ni	236.5	39.0	(110,272)	221.0	44.5	0.12	36

For all combinations of the ^{208}Pb projectile and the targets used in the experiment, the table contains the Coulomb barrier V_C (eqs. (14) and (15)) and the parameter $(Z^2/A)_{eff}$, both associated with the entrance channel. The quantity $(Z^2/A)_{eff}$ is defined in eq.(18), and the force ratio of Coulomb repulsion to nuclear attraction at contact, X_{Bass}, can be estimated from eq.(19). It varies from 0.62 to 0.89 across the table. For the combined systems, with charge and mass numbers (Z_T, A_T), the mean total kinetic energy expected for symmetric fission <TKE> (see ref.16) is given together with the liquid drop parameters; viz. the fissility parameter (Z^2/A), the fission barrier $B_f(\ell=0)$ for zero angular momnetum and the critical angular momentum $\ell_{B_f=0}$ for which the fission barrier goes to zero. The liquid drop quantities are calculated according to ref.8) using the numerical constants proposed therein. The fissility parameter X can be obtained from the (Z^2/A)-value by dividing by 46.

The equipment used for the experiments is shown in figure 5. The center of mass motion, imposed by shooting a heavy projectile on a light target, concentrates the symmetric fragmentation products within a cone centered around the beam axis. The key element is therefore a large ring counter placed downstream and recording kinematic two-body coincidences. The ring counter has very good efficiency for detection of symmetric and near-symmetric mass products within a broad range of Q-values and center of mass scattering angles, see figure 6. The two asymmetric scattering products are more difficult to catch in coincidence. Only for specially favourable scattering angles is this possible, and the reaction dynamics does not always favour just those angles.

The binary processes recorded by the counter can be fully determined by the measurement of three quantities, namely the two scattering angles and the time difference between the arrival of the products in either half of the counter. Adding to this the assumption of conservation of total (projectile plus target) mass, allows one to deduce: i) the center of mass scattering angle Θ_{cm} ; ii) the masses of the two products, A_1 and A_2 ; and iii) the total kinetic energy TKE in the center of mass system, for each event. Integrating the events belonging to the symmetric mass peak over all angles and energies then gives the cross section for the capture reaction. It involves a small extrapolation to angles outside the counter acceptance. For each energy and target-projectile combination one also obtains angular distributions, mass distributions and TKE-distributions.

The equipment includes three NaI-counters to measure gamma ray multiplicities.

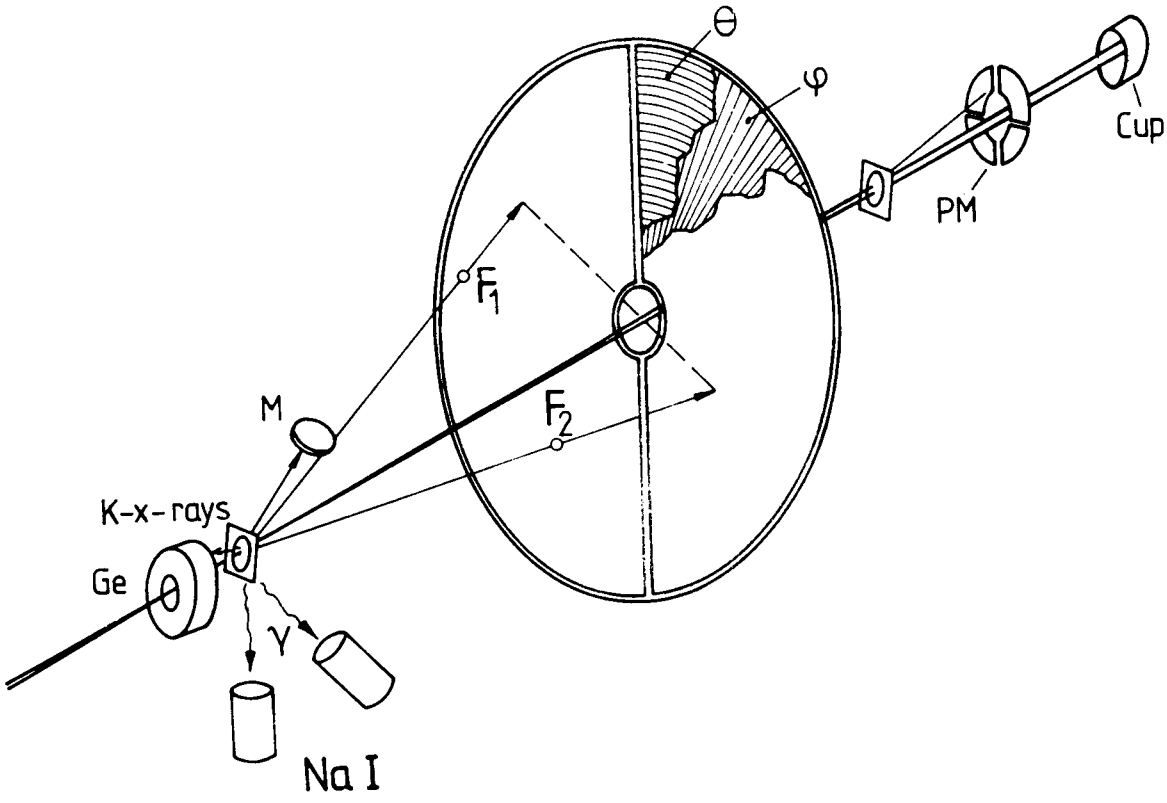

Figure 5:

Experimental arrangement. The target is viewed by a position sensitive parallel-plate detector, built in a ring shaped geometry. In this way it is adapted to the kinematics of the symmetric fragmentation processes to be studied. Actually, there are two detectors one for measuring Θ_{lab} and another behind it for measuring φ_{lab}. Particles penetrated both detectors. The bunched beam of the UNILAC hits the target, and fission-like products are detected by the ring detectors. Three NaI counters, mounted perpendicular to the beam axis measure the associated gamma-ray multiplicity. A Si counter positioned at 60° relative to the beam axis, is used as a monitor counter for the elastic scattering. A set of four parallel plate counters mounted in front of the Faraday cup is used to controll the beam position.

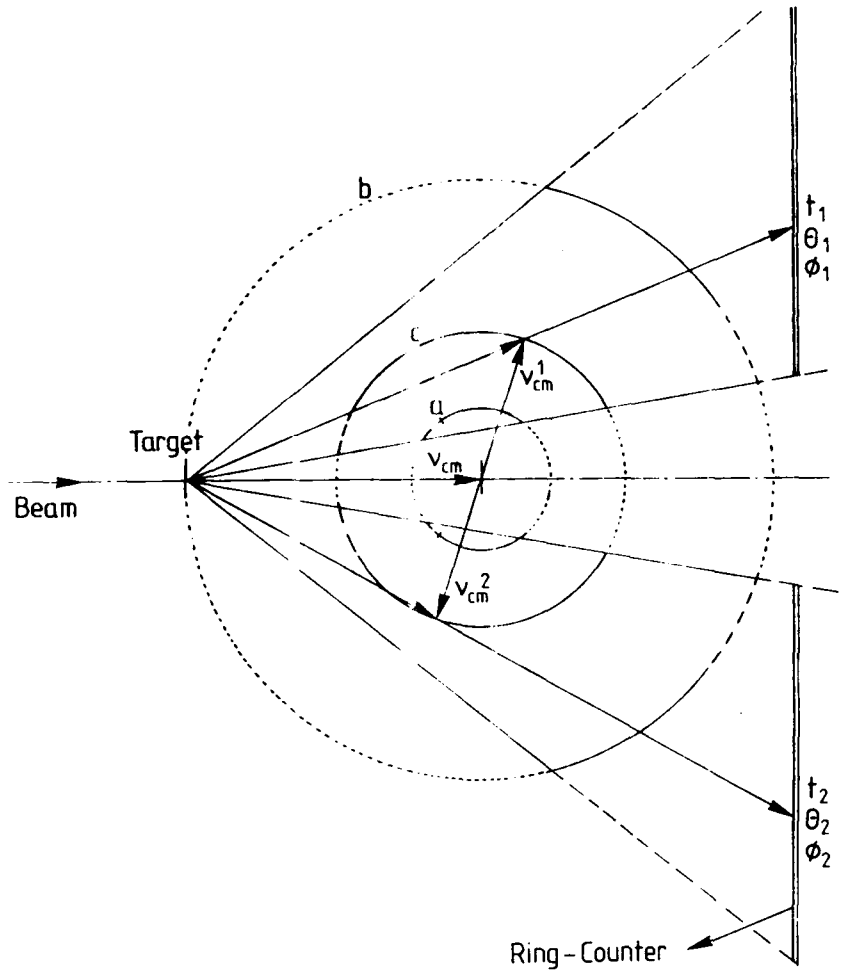

Figure 6:

Velocity diagram for the elastic scattering (a=projectile, b=target) and for the symmetric fragmentation process (c), with the reaction ^{208}Pb + ^{50}Ti at 5.5 MeV/u as example. The center of mass velocity circles are drawn with a solid line in the angular range where both fragments are detected in coincidence by the ring counter, and with a dashed line where only one reaction partner is observed. A dotted line indicates where none of the reaction products are detected. The figure illustrates the differences in acceptance between elastic, quasi elastic and deep inelastic processes on one side and the symmetric fragmentations on the other. The diagram also illustrates that at higher energies, where the grazing angle Θ_{cm} is larger than 90°, the target- and projectile-like scattering products are not likely to be detected at all.

As an example of the type of experimental data one obtains, figure 7 shows the frequency of coincident events plotted in the form of a contour diagram as a function of mass and center of mass angle, Θ_{cm}. The quasi elastic and part of the deep inelastic components are clearly

peaked close to the position of the grazing angle, which happens to lie inside the detection range in this particular example. For masses corresponding to symmetric fragmentation the measured angular distribution $d\sigma/d\Theta$ is almost constant. The weak increase at $\Theta_{cm} = 90°$ indicates a slight deviation from a $1/\sin\Theta$ distribution in $d\sigma/d\Theta$, in a direction of a more isotropic distribution, $d\sigma/d\Omega$ = const. The contour line indicated with small circles delineates the acceptance region of the counter for events with Q-values corresponding to fully relaxed events. For symmetric fragmentation only the extreme forward angles, Θ_{cm} <20°, and backward angles, Θ_{cm} > 160°, are missing.

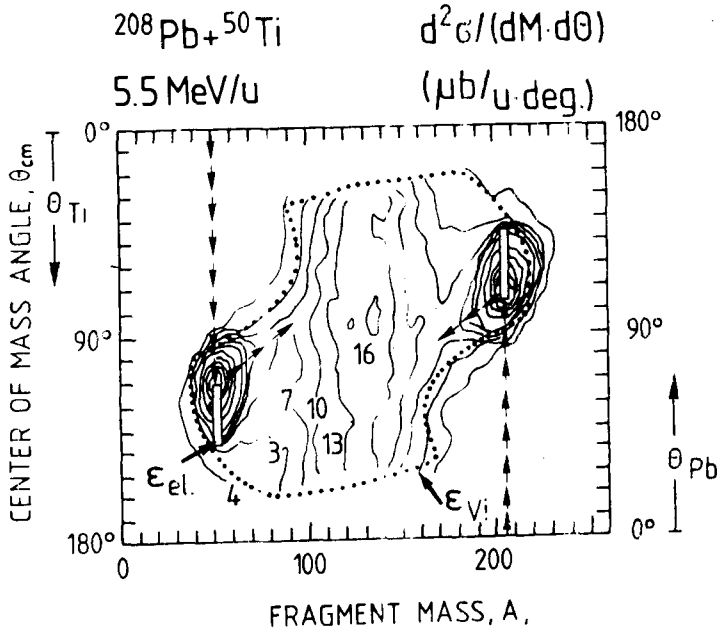

Figure 7

Double differential cross section ($d\sigma/dAd\Theta_{cm}$) is shown as a function of mass and center of mass scattering angle for the reaction Pb + Ti a 5.5 MeV/u. The symmetric masses have a rather flat angular distribution $d\sigma/d\Theta$. The dotted contour line indicates the region within which fully relaxed events are accepted by the ring counter.

Figure 8 summarizes all the results in terms of probability contours as a function of mass and total kinetic energy. The data for a given target are ordered in columns. The laboratory bombarding energy measured in MeV/u is given on the right hand side of the figure. Below each contour plot the center of mass energy E_{cm} in units of the Coulomb barrier V_c is indicated. (The cross section was integrated in angle over the acceptance region of the detection system and extrapolated to the missing angles by assuming a $1/\sin\Theta$ distribution). A number of trends stand out quite clearly. For the lighter targets ^{26}Mg (^{27}Al), and ^{48}Ca the symmetric fragmentation dominates the picture and is completely separated from possible tails of the projectile target-like distributions. For heavier targets the deep inelastic component too becomes visible. At the same time the separation of this component from the symmetric fragments becomes increasingly incomplete, so that for Fe and specially for Ni it becomes difficult to make an unambiguous distinction. In addition, for the heavier targets the symmetric component is relatively weak, and it appears as a separate peak only at incident energies well above the barrier. For the heavy targets and high bombarding energies, the products with intermediate masses clearly increase in relative intensity. These features suggest that the clear distinction between capture and "fusion" on one side, and the scattering processes on the other, eventually breaks down. Nevertheless, the larger fraction of the observed mass yields can be interpreted as the result of either a scattering or a capture process, the latter giving rise to the fission-like products.

Figure 8:

Double differential cross section ($d\sigma/dA,dTKE$) for the binary products as a function of TKE and product mass induced by ^{208}Pb projectiles on ^{26}Mg, ^{48}Ca, ^{50}Ti, ^{52}Cr, ^{58}Fe and ^{64}Ni targets (columns) at incident energies of 5.2, 5.5, 5.9 and 6.5 MeV/u (the energies are indicated for each row on the right hand side of the figure). The cross sections were obtained from an integration over the angular range of observation and from an extrapolation to the unobservable region by assuming a $1/\sin\Theta_{cm}$ distribution. The value of E_{cm}/V_c is indicated below each contour plot.

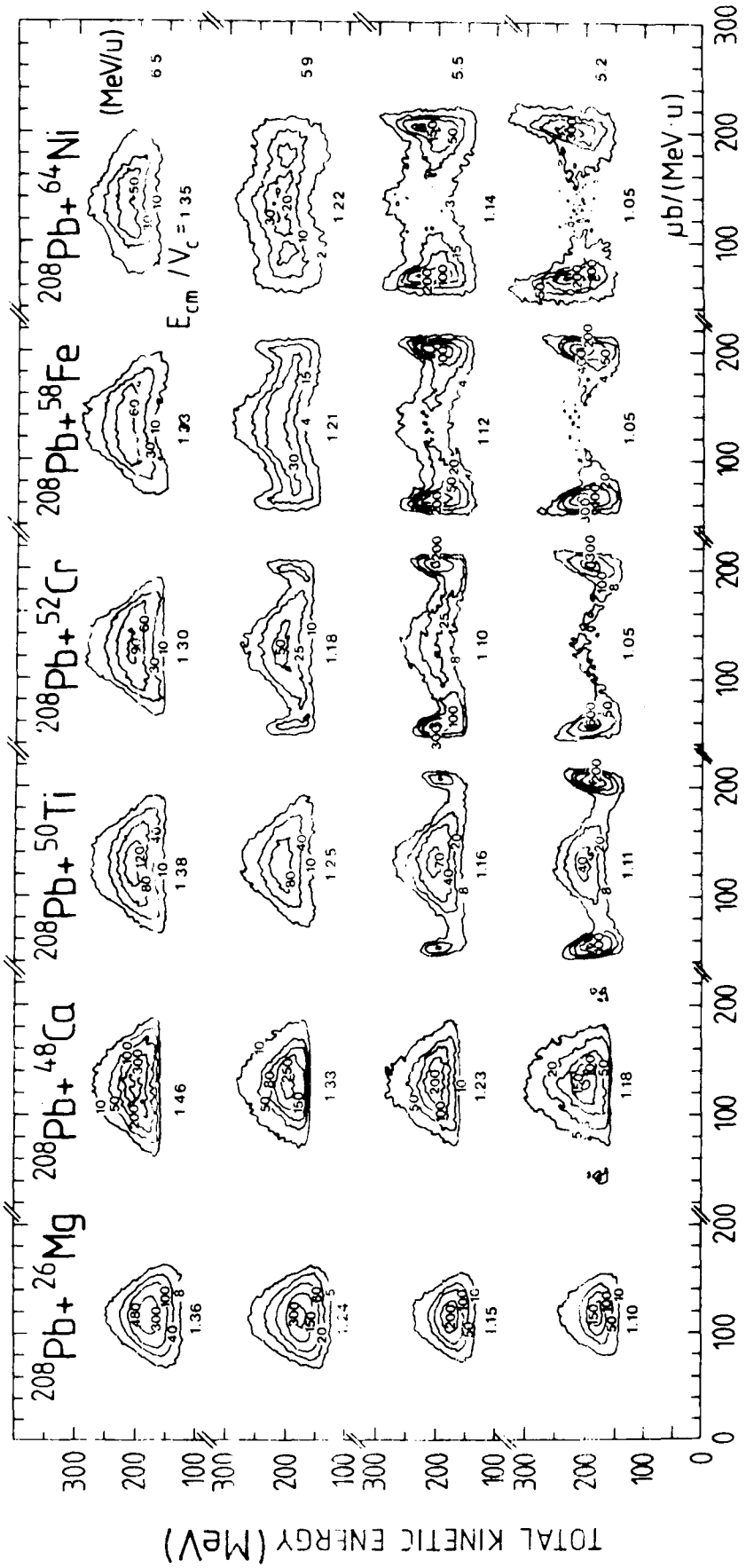
^{208}Pb+ ^{26}Mg
^{208}Pb+ ^{48}Ca
^{208}Pb+ ^{50}Ti
^{208}Pb+ ^{52}Cr
^{208}Pb+ ^{58}Fe
^{208}Pb+ ^{64}Ni
(MeV/u)
E_{cm} /V_c = 1.35
μb/(MeV·u)
TOTAL KINETIC ENERGY (MeV)
FRAGMENT MASS, A

Figure 8

Figure 9 is a projection of the contour plots in figure 8 onto the mass axis (and changing to a semilogarithmic scale). The capture cross sections σ_c are obtained by integrating the events under the symmetric peaks. In those cases where the separation from target-projectile like events is ambiguous, one can at least obtain an upper limit for σ_c by fitting a Gaussian to the yield at symmetry. The width of the Gaussian can be estimated by looking at the widths of the more conspicuous symmetric distributions.

Fig.9 illustrates the transition from the fusion dominated light heavy ion reactions to the scattering dominated reactions associated with the more heavy systems. There is a broad range, where the two types of reactions coexists as well separated reaction channels. The separation into two diatinct final channels must correspond to a separation taking place at some characteristic moment during the reaction and leading further into the two different channels. It seems off-hand most reasonable to think of the moment of contact, before any major mass exchange has taken place, as the decisive one. That is also the moment standard fusion theory assumes to be decisive (see subsections A and B). In this sense there is no difference at all between trying to understand fusion with formation of compound residues, on one hand, and the symmetric fragmentation reaction, on the other. We will therefore first analyse the results in terms of the standard fusion model outlined in subsection B.

Figure 9:

Mass spectra on a logarithmic scale for the same binary products as in figure 8 but integrated over TKE.

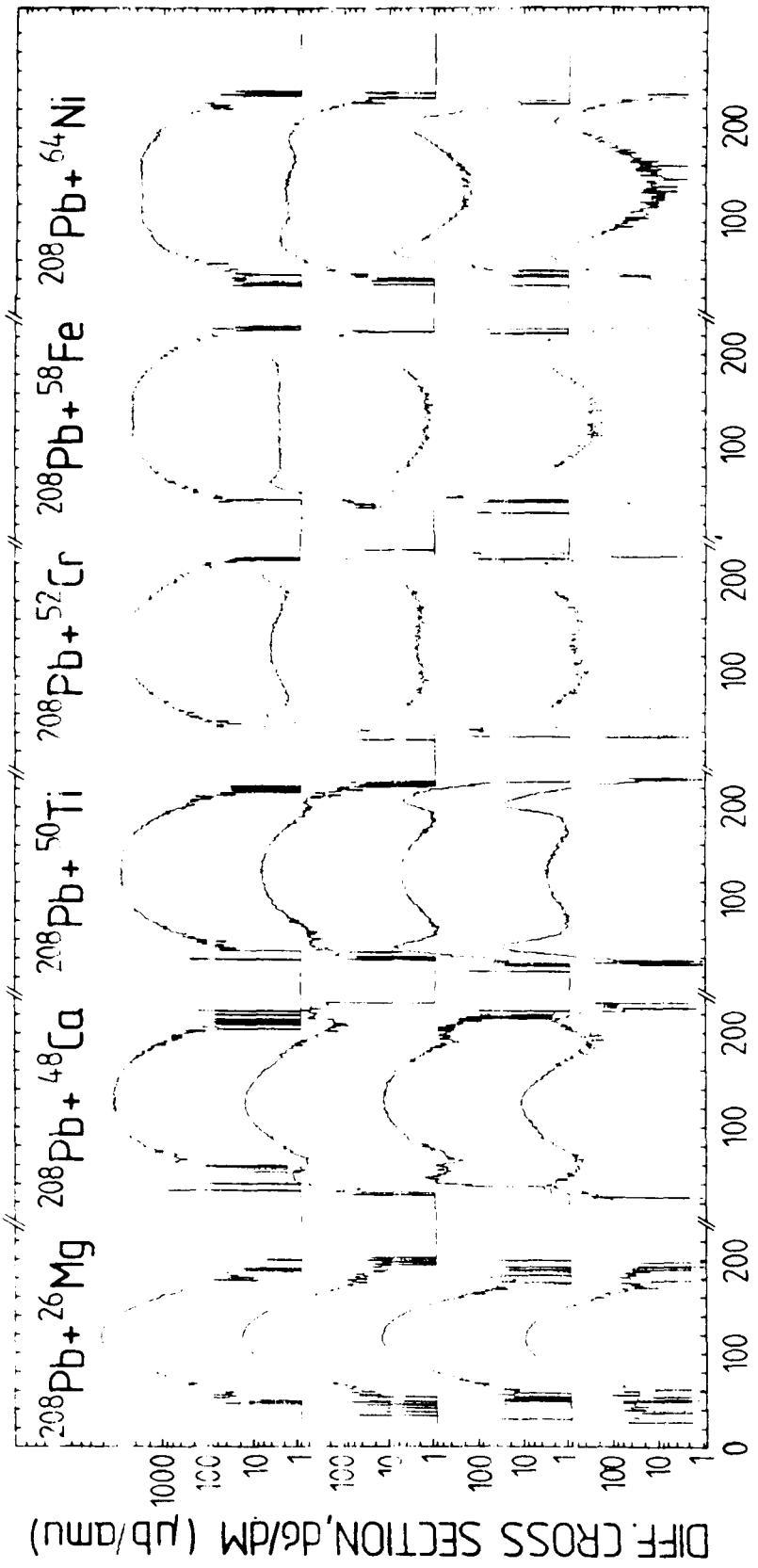
$^{208}Pb+^{26}Mg$
$^{208}Pb+^{48}Ca$
$^{208}Pb+^{50}Ti$
$^{208}Pb+^{52}Cr$
$^{208}Pb+^{58}Fe$
$^{208}Pb+^{64}Ni$
DIFF. CROSS SECTION, dσ/dM (μb/amu)
FRAGMENT MASS, A

Figure 9

E. Comparison of experimental capture cross sections with the predictions of one-dimensional fusion models.

Figure 10 compares theory and experiment in two cases. The excitation functions predicted by the proximity model in its schematic form are shown by thin lines. They can be compared to the experimental cross section for symmetric fragmentation, show as heavy points.

In order to achieve a good fit for the reaction of ^{208}Pb with ^{26}Mg the sum of the radii $C_1 + C_2$ was increased by 0.23 fm in the argument of the function Φ_{prox} in eq.(1), and this change was used for all reactions. There is still a tendency for the experimental capture cross sections to exceed predictions near the Coulomb barrier. This reflects tunneling and shape fluctuations[13,14] neither of which are taken into account by the model. On the whole, this excitation function typifyes a large body of fusion reaction data, recently reviewed by Birkelund et. al.[5]. The raising slope of the excitation functions is a measure of the square of the effective radial separation where capture takes place, cf. fig.2 and eq.(8).

The reaction between ^{208}Pb and ^{50}Ti, shows large deviations from the model prediction. First of all, the threshold is pushed up, and secondly there is a dramatic reduction in the rate at which the experimental excitation functions raise. These effects clearly exceed whatever uncertainty there may be in estimating precisely the yields of symmetric fragmentation; cf. figs. 8 and 9. The rate of raise measure the effective interaction radius according to standar theory. A σ vs. 1/E plot is most suitable for such an analysis, cf. fig.2 .

The results of all measurements with the Pb-beam are plotted in this way in figure 11 and the radius parameters r_F are extracted. According to this figure, the adjustment in effective capture radius, required to fit the data, approaches almost a factor of two (for $^{64}Ni+^{208}Pb$). Such

the barrier to obtain a capture reaction, in contrast to the standard model assumption that always assumes this minimum energy to be zero. Such an "extra push" must apparently be applied when the target Z-value exceeds 20, and it must be increased as more charge is added or when the cross sections, and hence the contributing ℓ-values, increase. It is thus a critical phenomenon, coming into play only when a certain threshold is exceeded.

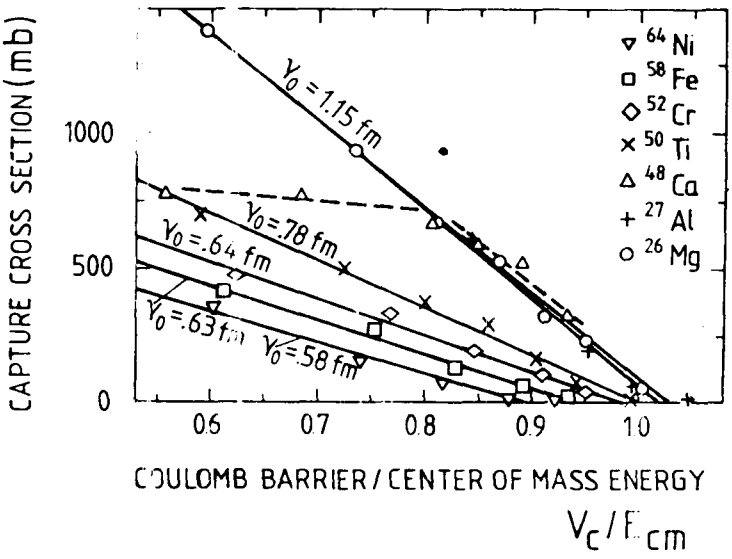

Figure 11

Plot in a V_c/E_{cm}-representation of the symmetric fragmentation component σ_c (capture cross section) extracted from the data presented in figs. 8 and 9. From the slope of the lines through the points, formally, a reduced fusion radius $r_0 (= r_F)$ is derived.

F. More dimensions. Dynamical deformations in the entrance channel.

The brakedown of the one-dimensional fusion model ought not be a surprise. Clearly, nuclei do not behave as frozen spheres. They deform, an rapidly so. The two-center potential, used so much, is hardly more

then a symbolic concept. It tells us whether the net force, during the early stages of approach when the two nuclei have not yet have time to deform, is attractive. This is expressed in terms of the barrier and the pocket in the potential; but the idea of trapping into that pocket has no real physical meaning. Figure 12 illustrates this point.

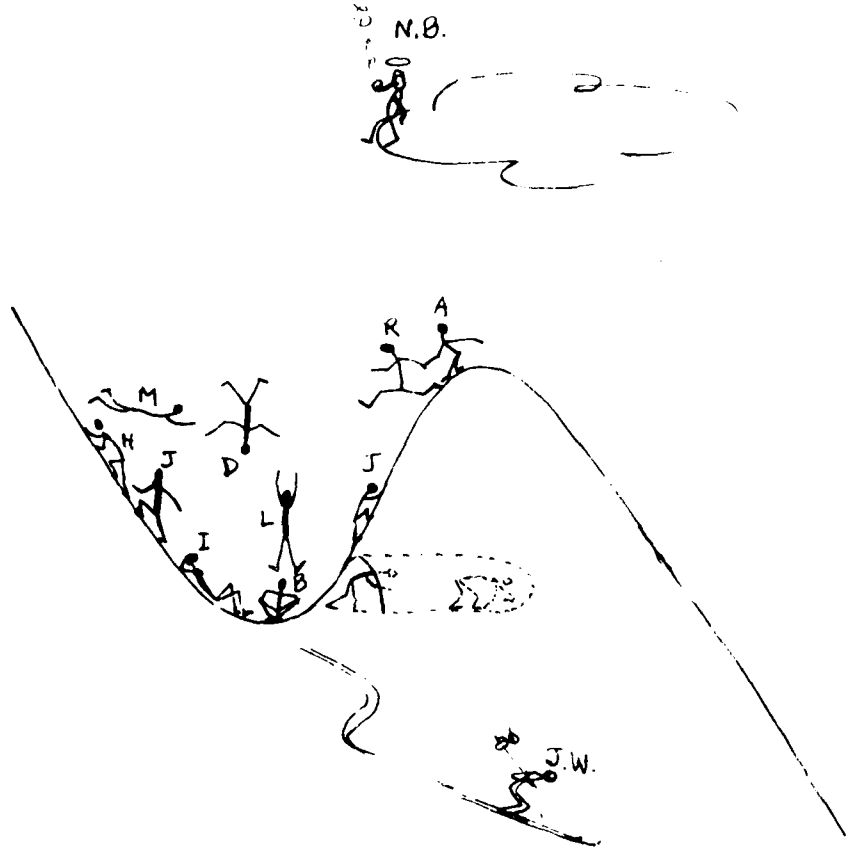

Figure 12

An artist conception of the prevailing preoccupation among the majority of nuclear reaction experts with the one-dimensional picture of the effective interaction potential. The symbols N.B. and J.W. refer to Niels Bohr and John Wheeler, who already in their 1939-paper pointed to the shortcomings of such a picture. (W.J.Swiatecki, private communication, 1981).

Recently, Swiatecki[11] has proposed a more realistic reaction model. The new model breaks with the idea that the capture process can be understood in terms of the static interaction of two spheres. It emphasizes the role of rapid dynamical deformations away from the configuration of two spheres in contact, (and a slower motion in the mass asymmetry coordinate). The formation of a neck is chosen as the most important aspect describing rapid deformations. For a given initial mass asymmetry, the model then examines the shape of the conditional saddle, see fig. 13. Qualitatively, a threshold is reached for systems where the conditional saddle shape becomes almost as compact as two spheres in contact. In this case an excess of inward radial kinetic energy at the point of contact is required in order to reach inside the saddle and get trapped. The model defines the threshold in terms of the ratio of Coulomb and nuclear forces at contact.

When the balance of forces, as expressed by the parameter $(Z^2/A)_{eff}$, reaches a certain threshold value, $(Z^2/A)^{thr}_{eff}$, caputre no more occurs spontaneosly upon contact. Systems beyond the threshold require an extra inward push to become captured. This is what fig. 13 is meant to illustrate in a qualitative way. When expressed in terms of a radial velocity the the extra push is a linear function of $((Z^2/A)_{eff} - (Z^2/A)^{thr}_{eff})$, according to W.J.Swiatecki[11].

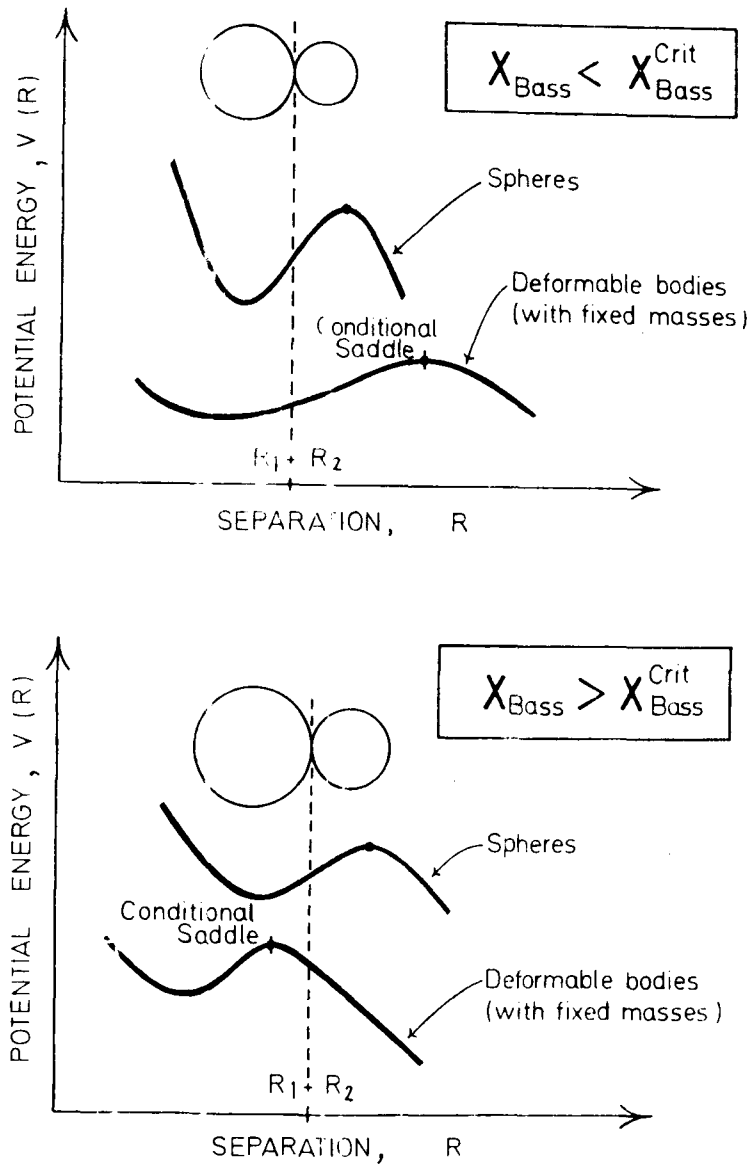

Figure 13

One-dimensional two-center potentials, V(R), showing a reaction barrier and a pocket behind it. These quantities are simple to define in the one-dimensional space of two spheres separated by a variable distance R. Also shown are potential curves appropriate to two deformable bodies with fixed masses. Such curves are much less well defined, because they represent cuts in a many-dimensional deformation space. But there will in general be a well defined saddle point, named the conditional saddle to emphasize the condition of fixed mass asymmetry. The figure illustrates one case (top) where the shape at the conditional saddle is much more elongated than two spheres in contact. In the other case (below) the shape at the conditional saddle point is more compact than two spheres in contact. One may easily visualize that in this case the existence of a pocket in the one-dimensional potential is not sufficient to get trapped and to obtain a long lived reaction complex. An extra inward push that brings the system inside the conditional saddle is required, ref.[11]).

III. W.J.SWIATECKI'S THREE-DIMENSIONAL DYNAMICAL MODEL OF NUCLEAR COALESCENCE AND RESEPARATION IN THEORY AND PRACTICE

A. Central Collisions

There is no better way of familiarizing oneself with the physical ideas contained in the three-dimensional model, and with its implications, than reading the authors own original paper, ref.[11]. It will therefore be reprinted in extenso as an essential part of the subject matter covered here. No doubt you will enjoy the presentation and the lucid style of its author.

1. Introduction

I would like to present a qualitative macroscopic study of what happens when two idealized nuclei touch, the neck between them grows, the mass asymmetry begins to change and, eventually, either a compound nucleus is formed or the system reseparates. The stress will be on the greatest possible simplicity: I will focus on what I believe are a few of the essential physical ingredients of the process and I will then codify them into algebraic equations whose exploitation involves -in the main- only elementary functions and the solution of quadratic or, at most, cubic equations.

2. The dynamical ingredients

A dynamical theory often involves three types of forces: conservative, dissipative, and inertial. In this study, I will focus on the macroscopic aspects of the problem and will consequently use a macroscopic Potential Energy [1], and a macroscopic One-Body Dissipation Function [2,3]. As regards the inertial terms, I will make the following approximation: for necked-in shapes, when the communication between the two pieces is impeded by a relatively thin neck (the "dinuclear regime"), I will use the inertia appropriate to tow non-comunicating pieces (the "binary regime"). Thus I will use just a reduced mass for the relative motion of the mass centers. For shapes without a pronounced neck (the "mononuclear regime"), I will disregard the inertial forces entirely, for there is reason to believe that, in this regime, they are usually small compared to one-body dissipative forces. So this is the physics that will go into my machinery:

1. Macroscopic potential energy,
2. Macroscopic dissipation function,
3. Binary inertia in the dinuclear regime and zero in the mononuclear regime.

I will make a schematic division between the mononuclear regime and the dinuclear regime at the point where the window through which the two pieces communicate is half open. The precise meaning of this will become clear after I have described the shape parametrization that I will use.

3. Shape parametrization

In striving for an algebraic theory of a complex process, the choice of appropriate and elegant degrees of freedom is half the battle. Figure 1 shows the best I could do to date: two spheres with radii R_1, R_2 and center separation r, connected by a portion of a cone with semiopening angle θ. There are three degrees of freedom (the absolute minimum required to describe the type of processes we are after). They are

1. Asymmetry variable $\Delta = \dfrac{R_1 - R_2}{R_1 + R_2}$ (1)

2. Distance variable $\rho = \dfrac{r}{R_1 + R_2}$ (2)

3. Window-opening variable $\alpha = \left(\dfrac{\sin\theta}{\sin\theta_{max}}\right)^2$. (3)

Here $\sin\theta_{max}$, equal to $(R_1 - R_2)/r$, refers to a fully open window, so that α, which ranges from 0 to 1, is a measure of the degree of communication between the two pieces. I shall take $\alpha = \frac{1}{2}$ to be the boundary between the dinuclear and mononuclear regimes.

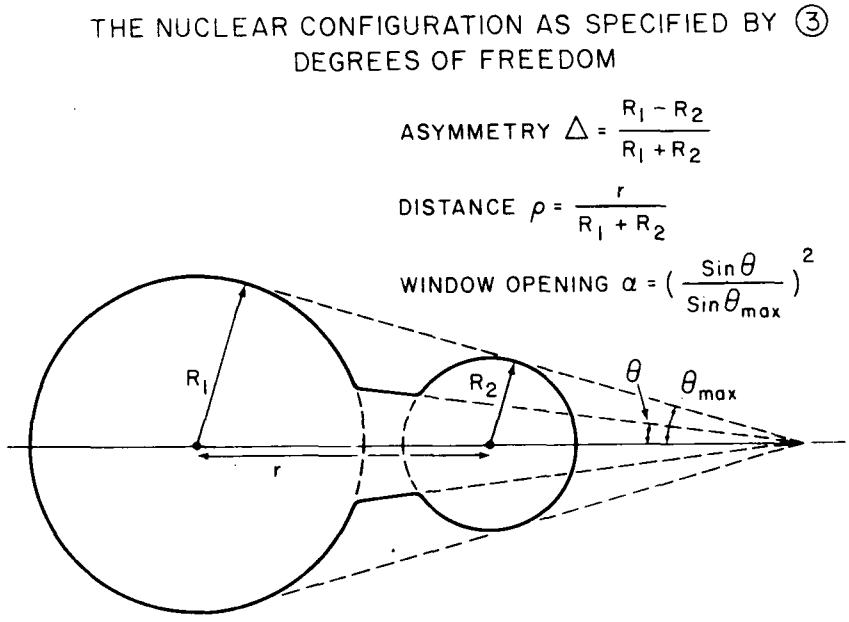

Figure 1:

The nuclear configuration is parametrized by two spheres connected by a conical neck. The asymmetry is specified by Δ, the center-separation by ρ, and the degree of window opening by α. The distance between the tips of the spheres may be positive or negative.

4. The configuration space

The variable Δ ranges from -1 to +1, α ranges from 0 to 1, and ρ from 0 to ∞, so the configuration space is a semi-infinite box, shown in perspective in Fig. 2 and in plan and side view in Fig. 3. The box is bounded by the horizontal planes $\alpha = 0, 1$, by the vertical planes $\Delta = -1, +1$ (only the positive half of the box is shown in Fig. 2), and by a curved surface on the left, corresponding to the minimum window that has to be there when the two spheres intersect. (The volume is always considered renormalized, so there is no implied density doubling anywhere.) The configuration box is a little like a semi-infinite aircraft carrier steaming to the left. The shapes corresponding to various parts of the box are indicated by descriptive labels. The single sphere is anywhere along and to the left of the diagonal lines $\rho = \pm\Delta$ on the overhanging part of the flight deck, where the larger of the two spheres has swallowed up entirely the smaller one. Proceeding along the deck to the right results in more and more elongated conical frustums, capped with spheres. The shapes are reflection symmetric along the ship's midplane. As one descends toward the waterline, the shapes become necked-in. Separating spheres are at the waterline to the right. The aircraft carrier's curved stem corresponds to intersecting spheres.

This then is the layout of the configuration box that will act as the stage for the various dynamical trajectories corresponding to two nuclei coming together, interacting, and either ending as a single sphere on the left or reseparating as two pieces on the right.

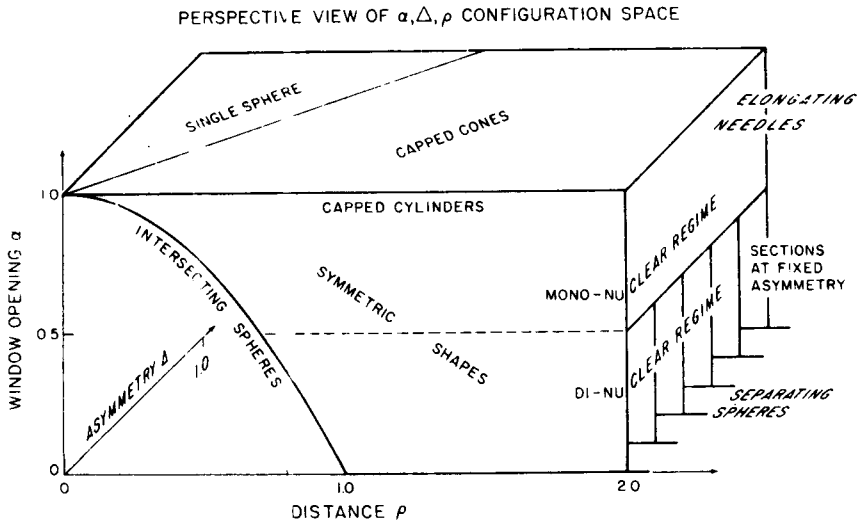

Figure 2

Perspective view of half the "configuration box" (corresponding to $\Delta > 0$). The part shown is bounded by the planes $\alpha = 0,1$ and $\Delta = 0,1$. A curved surface bounds the box on the left. On the right, the box extends to infinity. Various types of shapes correspond to the different parts of the box, as indicated by descriptive labels. In the dinuclear regime, the approximation is made that the configuration space is a stack of noncommunicating sections at fixed asymmetry.

5. The potential energy

The macroscopic potential energy is the usual sum of surface and Coulomb energies. I have found a simple and useful parametrization of the potential-energy surface by starting with an expansion to third order in the neck size, written in terms of a set of special "elegant variables" ν and σ. These variables are defined in terms of α and ρ by

$$\nu \equiv \sqrt{\alpha} \qquad \text{(range 0 to 1)}, \tag{4}$$

$$\sigma \equiv \frac{\rho^2 - 1}{1 - \Delta^2} \qquad \text{(range } -1 \text{ to } \infty). \tag{5}$$

For a small neck, ν reduces to the neck radius in units of twice the "reduced radius" $\bar{R}$ of the system ($\bar{R} = R_1R_2/(R_1 + R_2)$):

$$\nu \to \frac{\text{neck radius}}{2\bar{R}} \quad . \tag{6}$$

Similarly, σ tends to the tip separation of the spheres in units of $2\bar{R}$:

$$\sigma \to \frac{\text{tip separation}}{2\bar{R}} \quad . \tag{7}$$

As the configuration tends to a sphere (i.e., $\rho \to \pm\Delta$), σ tends to -1.

In terms of these variables, the potential energy, taken with respect to the energy of tangent spheres and written in units of the quantity $8\pi\bar{R}^2\gamma$, may be approximated by the following cubic:

$$\eta \equiv \frac{PE - PE_{tg}}{8\pi\bar{R}^2\gamma} = \nu\sigma - \nu^2 + \nu^3 - X\sigma \quad . \tag{8}$$

This cubic arises from an expansion of the energy to third order in a small quantity ε, with ν regarded as of order ε and σ as of order ε^2. The quantity X is an "effective fissility parameter" (identical with Bass' parameter x [4]) given by

$$X = \frac{Z_1 Z_2 e^2/(R_1+R_2)^2}{4\pi\gamma\bar{R}} \tag{9}$$

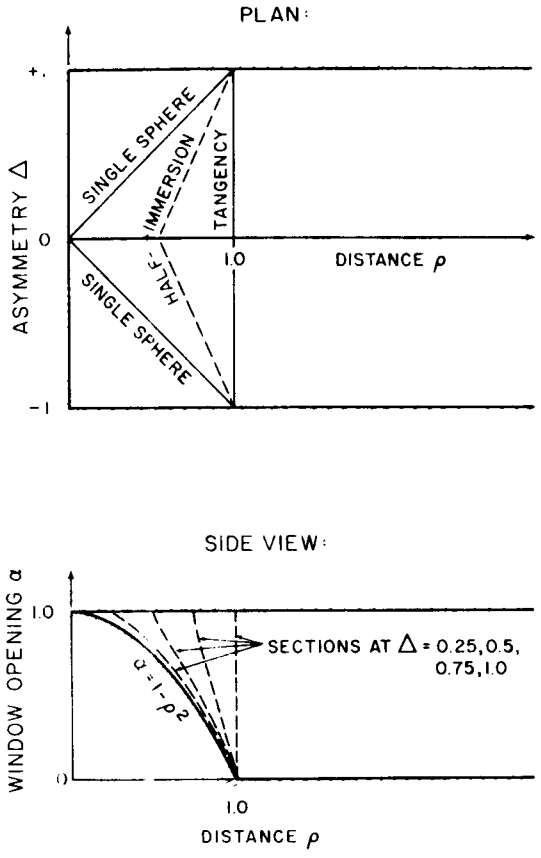

Figure 3

Plan and side view of the configuration box from Fig.2 . The side view suggests a similarity of the box with the shape of an aircraft carrier. The flight deck is carried forward on a curved bow and overhangs the hull in the triangular regions labeled "single sphere". The two spheres describing the shape are tangent at ρ=1. "Half-immersion" corresponds to shapes where the center of the smaller sphere has just entered the larger sphere. Full immersion takes place for $\Delta<\rho$ and leads to a single sphere for the resulting shape.

where Z_1e, Z_2e are the electric charges on the two pieces and γ is the surface-energy coefficient. This "effective fissility parameter" X is analogous to the usual fissility parameter and is a measure, for dinuclear systems, of the importance of the repulsive electric force $Z_1Z_2e^2/(R_1+R_2)^2$ compared to the attractive nuclear surface-tension or "proximity" force $4\pi\bar{R}\gamma$. For a system with a given mass number, the dependence of X on asymmetry is readily verified to be

$$X = X_o \frac{(1-D)^2}{1+3D} \quad , \tag{10}$$

where

$$X_o = \frac{Z^2e^2}{16\pi\gamma R^3} \quad , \tag{11}$$

$$D = \Delta^2 \quad , \tag{12}$$

and Ze,R refer to the charge and radius of the combined system. The fissility parameter X_o is identical, apart from a factor, with the usual fissility parameter x defined by $3Z^2e^2/40\pi\gamma R^3$.

6. Conditional and unconditional saddle points

The configurations where the potential energy η is stationary with respect to all small variations of Δ, ρ, α are true (unconditional) saddles, of which the symmetric Bohr-Wheeler and asymmetric Businaro-Gallone saddles are the most important.

Configurations where η is stationary with respect to ρ,α *when the asymmetry* Δ *is frozen* are also important in the dinuclear regime where the asymmetry degree of freedom is inhibited to a greater or lesser extent. These are "conditional" saddles, the equilibrium being conditional on the inhibition of the asymmetry. For the location $\bar{\nu}$, $\bar{\sigma}$ of a conditional saddle one finds, by differentiation of Eq. (8),

$$\bar{\nu} = X \quad , \tag{13}$$

$$\bar{\sigma} = 2\bar{\nu} - 3\bar{\nu}^2 = 2X - 3X^2 \quad . \tag{14}$$

The saddle-point energy follows as

$$\eta(\bar{\nu},\bar{\sigma}) = -X^2 + X^3 \quad . \tag{15}$$

One recognizes here a useful static scaling rule of our model:

"The dimensionless conditional saddle-point properties (such as the relative degree of window opening and the energy deviation from tangent spheres expressed in unts of $8\pi\bar{R}^2\gamma$*) are functions of the effective fissility parameter* X *alone, and independent of asymmetry."*

For symmetric systems, the conditional saddles become the unconditional Bohr-Wheeler saddles, since the frozen-asymmetry condition is then redundant.

Because our energy expression for η is relatively simple, the properties of all the saddle points, including the Businaro-Gallone asymmetric shapes, can be written down in closed form. For example, the fission-barrier energy (the energy of the Bohr-Wheeler saddles), in units of the surface energy of the spherical shape, follows as

$$\xi = \frac{\text{PE-PE}_{\text{sphere}}}{4\pi R_\gamma^2} = a - bX_o - cX_o^2 + cX_o^3 \qquad (16)$$

where

$$a = 2^{1/3} - 1 = 0.259921 \quad ,$$

$$b = \frac{12}{5} - \frac{17}{10} 2^{1/3} = 0.258134 \quad ,$$

$$c = 2^{-5/3} = 0.314980 \quad .$$

Equation (16) is compared with an accurate computer calculation [1] in Fig. 4. In the present approximation, the Bohr-Wheeler family of symmetric saddle-point shapes starts as tangent spheres at $X_o = 0$, elongates until $X_o = 1/3$, then contracts to become, at $X_o = 2/3$, a pair of tangent spheres connected by a neck that is four-ninths open, and finally becomes a single sphere at $X_o = 1$. The degree of opening of the neck (window) is ½ when $X_o = 1/\sqrt{2} \approx 0.7$. All this is roughly in agreement with exact calculations, especially if the fissility parameter X_o is taken to be defined not in terms of fundamental constants through Eq. (11), but as the "relative fissility," i.e., the value of the charge on the system divided by that critical value which makes the Bohr-Wheeler saddle-point (in the model in question) coincide with the sphere (and causes the fission barrier to vanish or nearly vanish). We may then make the following identifications:

$$X_o \leftrightarrow x = \frac{3Z^2e^2}{40\pi\gamma R^3} \quad , \qquad (17)$$

$$X \leftrightarrow x_{\text{eff}} = \frac{3Z_1Z_2e^2/(R_1+R_2)^2}{10\pi\gamma\bar{R}} = x\,\frac{(1-D)^2}{1+3D} \quad . \qquad (18)$$

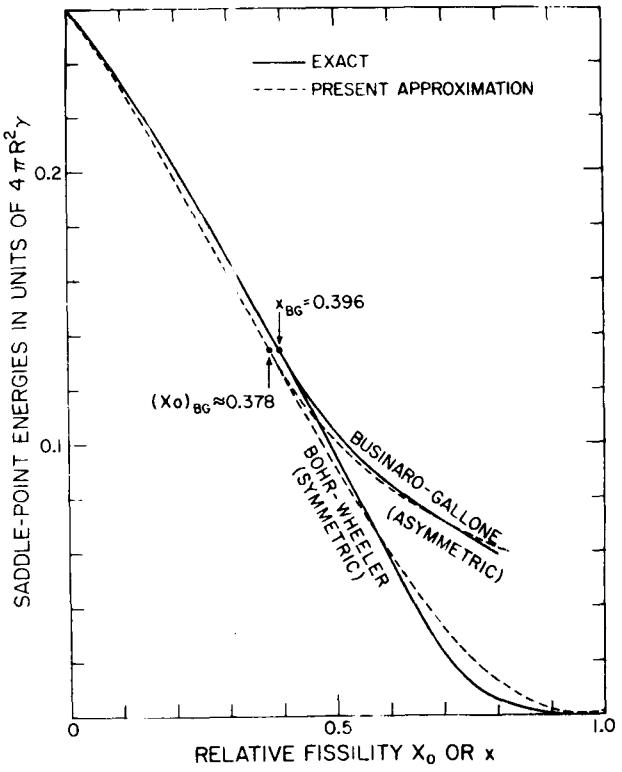

Figure 4

Comparison of the energies of the Bohr-Wheeler and Businaro-Gallone saddles as calculated in our approximation (using a cubic potential energy) with accurate values calculated with the aid of electronic computers. The relative fissility X_o or x may be regarded as the charge on the system, divided by the value that makes the Bohr-Wheeler saddle spherical. The critical bifurcation point, where the Businaro-Gallone saddles branch off, is indicated by an arrow.

These equations differ by a factor 6/5 from Eqs. (9) and (11). The above implicit definition of X_o and the identication of X_o with x underlies the plot in Fig. 4. Figure 4 also shows the asymmetric Businaro-Gallone saddles peeling off at the point $(X_o)_{BG}$, given by

$$(X_o)_{BG} = \frac{14}{57} + \frac{4\sqrt{163}}{57} \cos\left(60° + \frac{1}{3}\cos^{-1}\frac{3587}{652\sqrt{163}}\right)$$

$$= 0.378174 \quad , \tag{19}$$

to be compared with the correct value $x_{BG} = 0.39_6$. The energy of the Businaro-Gallone shapes is also compared with the results of computer calculations in Fig. 4.

All in all it would seem that the energy expression for η, Eq. (8), inspired by a third-order expansion in the neck size, when expressed in terms of the "elegant variables" ν, σ, continues to provide a rough parameterization of the potential-energy surface all the way up to the spherical shape.

7. The dissipation function

This is a crucial physical ingredient in our study and it governs the overall character of the dynamics. I started from the Wall Formula for the rate of energy dissipation $\dot{Q}$ in the mononuclear regime and the Wall-and-Window formula in the dinuclear regime. The Wall formula reads as follows [2]:

$$\dot{Q} = \rho\bar{v}\oint (\dot{n} - D)^2 \, d\sigma \quad . \tag{20}$$

The Wall-and-Window formula is given by [3]:

$$\dot{Q} = \tfrac{1}{4}\,\bar{\rho v}\cdot\Delta\sigma\cdot(u_t^2 + 2u_r^2) + \bar{\rho v}\oint_{\text{fragment 1}}(\dot{n} - D_1)^2 d\sigma + \bar{\rho v}\oint_{\text{fragment 2}}(\dot{n} - D_2)^2 d\sigma \ . \tag{21}$$

Here ρ is the nuclear mass density, $\bar{v}$ is the mean nucleonic speed, $\dot{n}$ is the normal velocity of a surface element $d\sigma$, $\Delta\sigma$ is the area of the window, and u_t, u_r are the tangential and radial components of the relative motion of the two pieces. The quantity D (not to be confused with Δ^2 in Eq. (10)) is a "normal drift velocity component" of the particles about to strike a surface element. It ensures the conservation of linear (and angular) momentum. (Without D, a uniformly translating nucleus would be losing energy.) Under a certain assumption, discussed in [2], D becomes a known function of the configuration and its state of motion, so that the integrals in Eqs. (20) and (21) can be evaluated.

As in the case of the potential energy, I used expansions of Eqs. (20,21) to cubic order in the neck size, expressed them in terms of the elegant variables ν, σ, and used the resulting equations for *all* neck sizes. For small necks, the resulting formulae may thus be expected to be semi-quantitative (within the other idealizations of the theory), but for large necks they are only qualitative.

8. The kinetic energy

For head-on collisions, I took the kinetic energy as

$$KE = \begin{cases} \tfrac{1}{2} M_r \dot{r}^2 & \text{for } \alpha < \tfrac{1}{2} \\ 0 & \text{for } \alpha > \tfrac{1}{2} \end{cases} . \tag{22}$$

Here M_r is the reduced mass of the separated fragments.

I shall comment on possible extensions to noncentral collisions later.

9. Equations of motion

In the dinuclear regime, the resulting equations of motion for ν,σ end up looking like this:

$$\mu \frac{d^2\sigma}{d\tau^2} + \nu^2 \frac{d\sigma}{d\tau} + \nu - X = 0 \quad , \tag{23}$$

$$\frac{d\nu}{d\tau} = \frac{2\nu - 3\nu^2 - \sigma}{\nu(\sigma+\nu^2)} \quad , \tag{24}$$

where

$$\tau = \frac{\text{time}}{t_u} \quad , \tag{25}$$

$$t_u = \text{natural time unit} = \frac{\rho\bar{v}\bar{R}^2}{\gamma} \quad , \tag{26}$$

and

$$\mu = \text{dimensionless reduced mass}$$

$$= \frac{M_r}{2\pi(\rho\bar{v})^2\bar{R}^4/\gamma} \quad , \tag{27}$$

where $M_r = m\,A_1A_2/A$, with $m = 931\ \text{MeV}/c^2$. (A_1,A_2 are the mass numbers of the separated fragments and A is their sum.)

The structure of the equations of motion leads to the following dynamical scaling rule: *"For two dinuclear systems with the same values of the dimensionless reduced mass* μ *and of the effective fissility* X, *the dynamical evolutions resulting from head-on collisions should be similar, provided lengths are measured in units of (twice) the reduced radius* $\bar{R}$ *and times in units of* $\rho\bar{v}\bar{R}^2/\gamma$."

In practice, it will turn out that the dependence of dynamical calculations on μ is relatively slight for many systems of interest, so that the time evolutions of dinuclear systems should, in fact, be approximately similar provided only the effective fissilities X are the same.

In the mononuclear regime, the equations of motion are somewhat more complicated. The natural unit of length is then R and a natural unit of time is

$$t_o = \frac{\bar{\rho v} R^2}{4\gamma} \tag{28}$$

The single dimensionless parameter in the equations is the relative fissility X_o, since inertia is neglected.

Let us now look at some results.

10. Normal modes

The equations of motion are sufficiently simple so that approximate solutions in closed form may be found in several cases of interest. In particular, the normal modes of motion near the saddle points can be analyzed and explicit formulae for the characteristic times can be written down.

In the mononuclear regime there are three fully overdamped normal modes near the Bohr-Wheeler saddle. One is an exponentially growing fission mode with characteristic e-folding growth time T_f; the second is an exponentially decaying "transverse" mode with characteristic time T_t; and the third is the asymmetric mode with characteristic time T_Δ. In the dinuclear regime there are two modes: an exponentially

growing fission mode, as before, and an oscillating transverse mode with a characteristic time T_{osc} (i.e., with a period $2\pi T_{osc}$) and a characteristic damping time T_t.

The three characteristic times T_f, T_t, T_Δ, or T_f, T_{osc}, T_t are shown as functions of X_o in Fig. 5. The scale on the left is in units of 10^{-22} sec. On the right is a scale in MeV for the quantities $\hbar/T$.

Note the following qualitative features: The characteristic time for the fission mode changes by more than an order of magnitude from values $\sim 10^{-22}$ sec for light nuclei to a few times 10^{-21} sec for heavy nuclei. The asymmetry mode has a similarly sluggish time scale for heavy nuclei. For lighter nuclei, the (stable) asymmetry mode is inhibited by the neck constriction and, moreover, its restoring force tends to zero at the Businaro-Gallone point $(X_o)_{BG}$. Its characteristic decay time tends, therefore, to ∞ as X_o tends to ~ 0.4. All this suggests that the characteristic time for the asymmetry mode (when $X_o > 0.4$) may always remain fairly long (e.g., in excess of about one or a few times 10^{-21} sec).

The characteristic time of the overdamped transverse mode is much shorter than that of the fission mode for heavy nuclei. For lighter nuclei, the transverse mode has a damped oscillatory character which, for very light systems, should, in fact, have only moderate or even small damping. The transverse mode in those cases consists of a stable to and fro oscillation of the two pieces, with an associated swelling and contraction of the neck, which might also be described as a giant quadrupole resonance of the saddle shape, or as a quasimolecular mode. The energy of this resonance for light nuclei might be several MeV or even in excess of 10 MeV for the lightest systems (see Fig. 5).

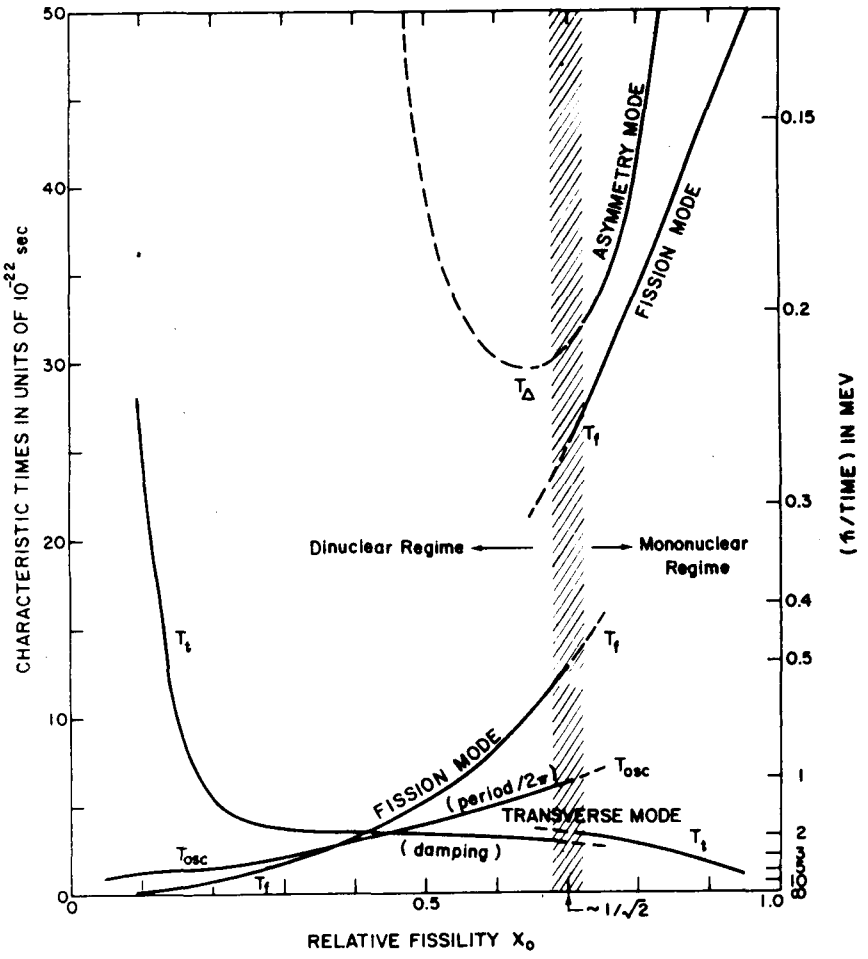

Figure 5

The characteristic times of the normal modes of motion in the vicinity of the Bohr-Wheeler saddle. To the right of the shaded band, in the mononuclear regime, all the modes are overdamped, with exponential growth or decay times as shown. In the dinuclear regime, the fission mode is a growing exponential, and the transverse mode is an oscillation with angular frequency T_{osc}^{-1} and damping time T_t .

11. Dinucleus (deep-inelastic), mononucleus (quasifission) and capture (compound-nucleus) reactions

Figure 6 shows three dynamical trajectories for a collision between two mass-104 nuclei at three energies: 0, 3.6 and 10 MeV above the interaction barrier. The total system has $A \approx 208$ and $Z \approx 82$, which corresponds to a fissility $X_0 = 0.7$. [In all the examples I will show, the total system is chosen to be on the valley of beta-stability, with $N-Z = 0.4A^2/(A+200)$]. The reaction is symmetric, so everything happens in the midplane of the configuration box, at $\Delta = 0$. Figure 6 shows some of the equipotential lines which delineate the saddle point whose energy is 0.033 in units of the surface energy $4\pi R^2\gamma$. This corresponds to a fission barrier of some 19 MeV. The approach of the two nuclei corresponds to a trajectory along the ρ-axis, moving from right to left. At the point $\rho = 1.0$, the two spheres touch, and the first curve shows the subsequent dynamical evolution in the case where there is zero energy in excess of the barrier.

The dots on the trajectory mark equal intervals of time corresponding to 1/10 of the natural time unit $\rho\bar{v}R^2/4\gamma$. In the present case this unit is 12×10^{-22} sec, so the time between dots is 1.2×10^{-22} sec.

Note the very rapid initial growth of the neck, the leveling out, and the subsequent approximately linear decrease in the *neck area* (the variable α is proportional to the area). This means that the neck radius, proportional to $\sqrt{\alpha}$, snaps with a vertical tangent. The whole reaction lasts about 16×10^{-22} sec from contact to snapping, and it takes place entirely outside the saddle point. Even so, some energy has been dissipated during the neck growth and collapse, and the two

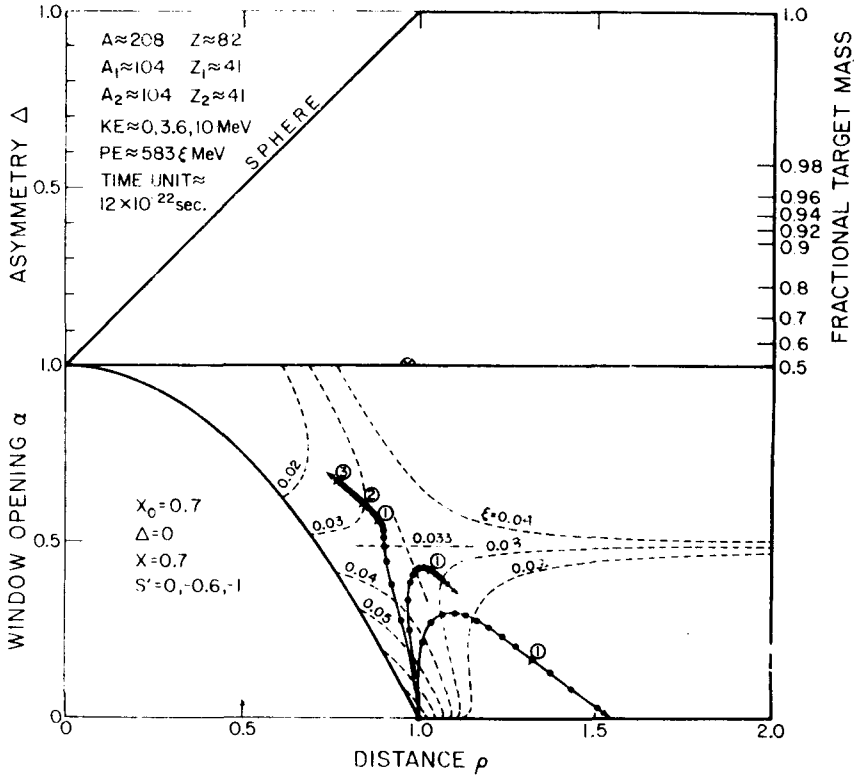

Figure 6

Example of a dynamical study of symmetric collisions between two medium-weight nuclei ($A_1 = A_2 \approx 104$, $Z_1 = Z_2 \approx 41$). The total system is characterized by a fissility $X_o = 0.7$. The lower part of the figure gives a projection on the α-ρ plane and the upper part a projection on the Δ-ρ plane of the configuration space. The first and second trajectories, with energies 0 and 3.6 MeV above the interaction barrier, fail to fuse and reseparate after dissipating some energy. With 10 MeV above the barrier, fusion takes place (third trajectory). Dots are spaced at 1/10 of the natural time unit, i.e., at 1.2×10^{-22} sec. Circled dots indicate the lapse of a full time unit. The dashed lines are equipotentials, with energy expressed in units of the surface energy of a single sphere (about 583 MeV) and with reference to the energy of the spherical configurations. The location of the saddle point is indicated by the crossing equipotentials in the α-ρ plane and by a semicircle with a cross in the Δ-ρ plane (upper part of the figure). The asymmetry is specified by Δ on the left and by the fractional target mass on the right. The quantities S' are dimensionless injection velocities for the three trajectories.

fragments would have less energy at infinity than that corresponding to the interaction barrier, which is what they started with.

The second trajectory in Fig. 6, with 3.6 MeV above the barrier at injection, also fails to be captured inside the saddle, although it hovers just outside it for a somewhat longer time. The third trajectory, with 10 MeV, gets captured easily, enters the mononuclear regime, and then creeps toward the spherical shape.

We thus see two distinct classes of reactions or trajectories: trapping and nontrapping ones, leading to a compound nucleus and a dinucleus respectively. The latter process would probably be recognized as a deep-inelastic reaction. In addition, there would, of course, be elastic reactions that never established proper nuclear contact, and quasielastic reactions, which the present model is too crude to bring out as a separate type.

The above situation changes drastically if one goes to lighter (symmetric) systems with lower values of the fissility X_o (see Fig. 7 for an example of a system with $X_o = 0.4$). The saddle point for a light system has $\rho > 1$, i.e., the saddle shape is more elongated than tangent spheres. Hence, after contact and neck growth, the system finds itself comfortably inside the saddle and heads without hesitation toward the spherical compound nucleus. There will still be elastic and quasielastic reactions, but the deep inelastic reactions will have disappeared(in head-on collisions)

The opposite happens if one goes to heavier systems, with higher values of X_o. Figure 8 shows a case with $X_o = 1$, corresponding to a super-heavy system with $A \approx 320$, $Z \approx 120$. In trying to make such a super-

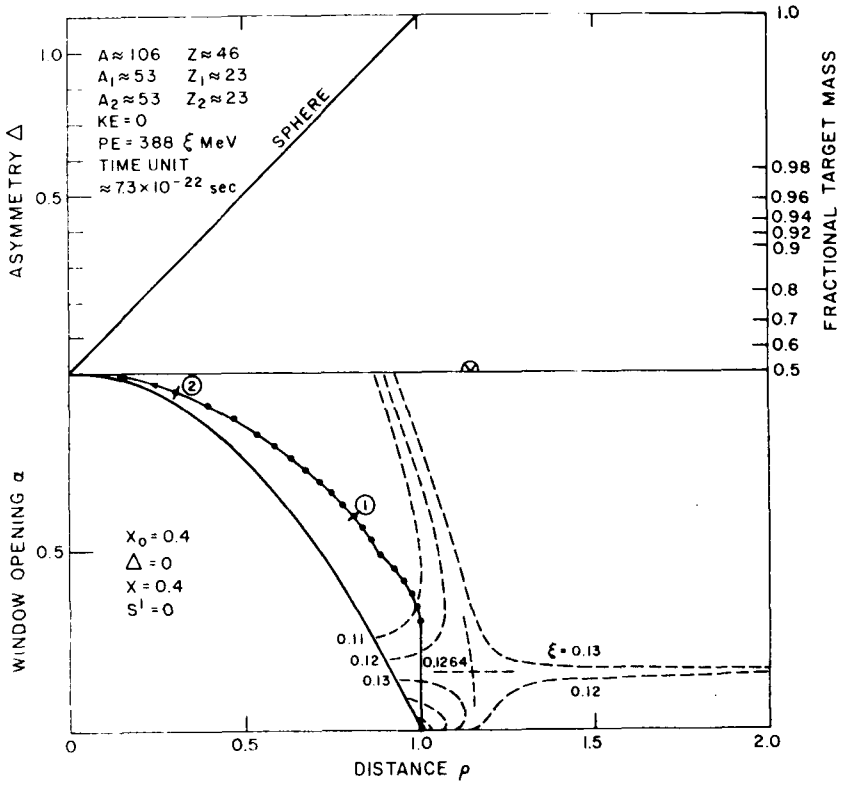

Figure 7

This is like Fig.6 but refers to a lighter system with X_o = 0.4 (A≈106, Z≈46). The saddle-point shape is now more elongated than the tanget configuration and automatic capture into a compound nucleus takes place even with zero injection velocity. Note the discontinuity in the slope of the trajectory at α = 1/2, which reflects the discontinuous transition from the dinuclear to the mononuclear regime.

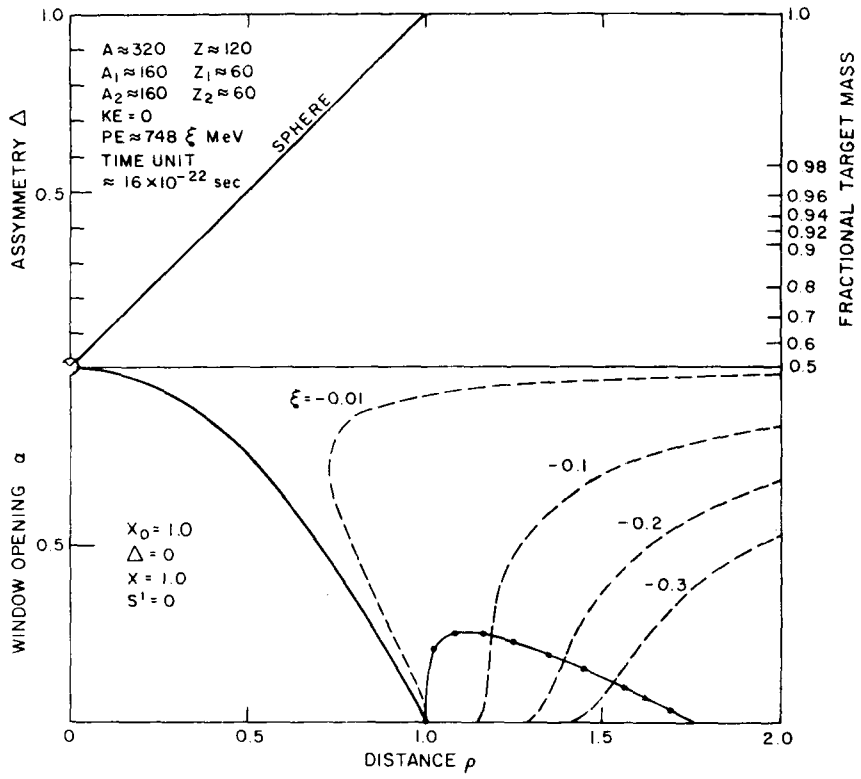

Figure 8

This is like Fig.6 but for a super-heavy system with fissility X_o = 1 (A≈320, Z≈120). The saddle point (crossed circle) is now the sphere at ρ=0, α=1. The trajectory with zero energy above the barrier never comes close the spherical configuration.

heavy nucleus by colliding two equal pieces with $A_1 = A_2 = 160$, $Z_1 = Z_2 = 60$, one is faced with a potential-energy landscape that slopes monotonically away from the spherical configuration on the left. The trajectory shown corresponds to starting with zero kinetic energy at the barrier and, clearly, one never even gets close to the spherical configuration (where a compound-nucleus pocket might exist because of shell effects).

In the present model, the critical fissility X_c above which, for the first time, a compound nucleus refuses to form automatically (and deep-inelastic reactions would be expected to make their appearance in head-on collisions), turns out to be about 0.57. Recall that the saddle is more or less as compact as the tangent configuration at $X_o = 2/3 \approx 0.67$. The difference between 0.67 and 0.57 is a reflection of the fact that during neck growth the fragments begin to separate and, consequently, in order to achieve capture, the contact configuration must be somewhat more compact than the saddle, i.e., X_o must be somewhat less than 2/3.

Two things can be done if one has a system with $X_o > X_c$ and one nevertheless wants a compound nucleus. The first is to increase the bombarding energy, as already illustrated in Fig. 6. This works if X_o is not too much above X_c. The other possibility is to go to an *asymmetric* target-projectile combination. A dramatic illustration of this is provided by Fig. 9. Here we have the same super-heavy system (with $X_o = 1$, $A \approx 320$) as before, but the asymmetry is very large, with $A_1 \approx 296$, $Z_1 \approx 111$, and $A_2 \approx 24$, $Z_2 \approx 9$. (This corresponds to $\Delta = 0.4$.) The *effective* fissility is now only $X = 0.4768$. This means that in

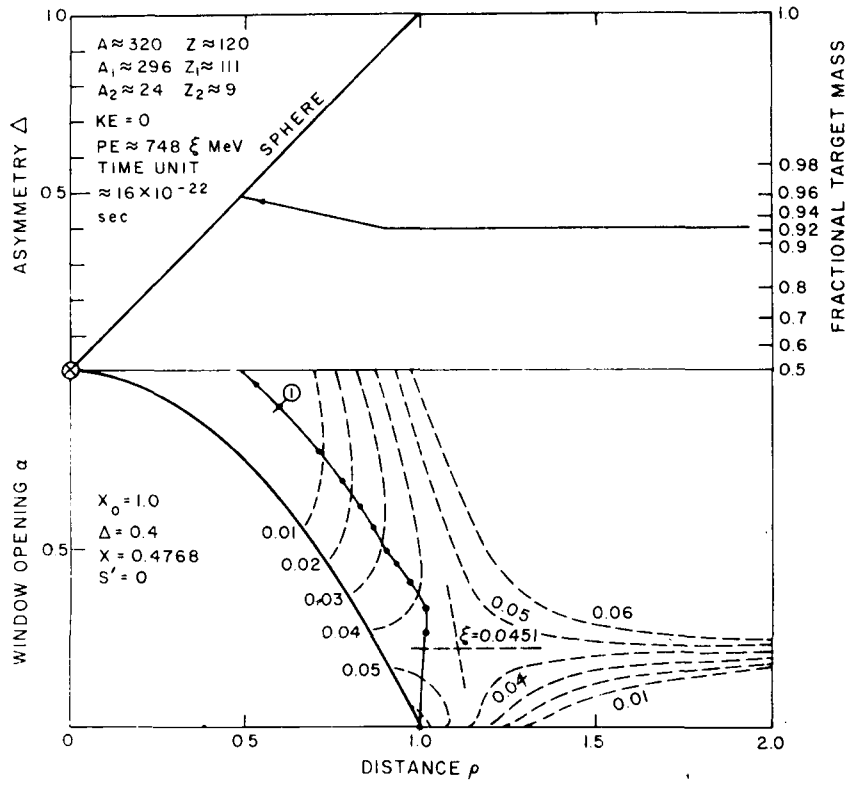

Figure 9

The total system is the same as in Fig.7 , but the asymmetry corresponds to $\Delta = 0.4$($A_1 \approx 296$, $Z_1 \approx 111$ and $A_2 \approx 24$, $Z_2 \approx 9$). The equipotentials refer now to a section at $\Delta = 0.4$ (and not to the midplane $\Delta = 0$, as in Figs. 6 and 7). The conditional saddle is more elongated than the tanget configuration and automatic capture inside this saddle takes place. The system then proceeds to fuse and reaches the spherical sahpe without hesitation.

the dinuclear regime, the system behaves like a much lighter and less fissile nucleus. The equipotential lines in Fig. 9, displayed for a section at $\Delta = 0.4$, show the location of the *conditional* saddle point, which is now less compact than the tangent configuration (contrast this with the true saddle, all the way to the left). As a result, the trajectory starting with zero kinetic energy at the top of the barrier has now no difficulty in being captured and proceeds toward the left. After it has entered the mononuclear regime, the asymmetry gets unfrozen and begins to increase somewhat, as shown in the upper part of Fig. 9. This makes little difference and the spherical configuration is attained without difficulty in about one time unit.

If, with X_o fixed at 1, the asymmetry is made less extreme, the automatic capture eventually comes to an end. It turns out that this coincides with the point when capture inside the *conditional* saddle fails to take place, for X less than about 0.57. The asymmetry Δ of that point is given by solving $0.57 \approx (1-D)^2/(1+3D)$, which leads to $\Delta \approx 0.346$ and $A_1 \approx 287$, $Z_1 \approx 108$ and $A_2 \approx 33$, $Z_2 \approx 12$ (see Fig. 10).

By carrying out a variety of such trajectory calculations for systems with different fissilities and asymmetries, one learns an interesting fact: the condition for automatic capture inside the conditional saddle is, to a fair approximation, simply that the *effective* fissility X should be less than X_c, with X_c estimated as roughly 0.57. (This is in accordance with our approximate dynamic scaling rule resulting from neglecting the relatively slight dependence on μ). Moreover, this scaling rule also suggests that when X is somewhat above X_c the extra push, or extra velocity above the barrier needed

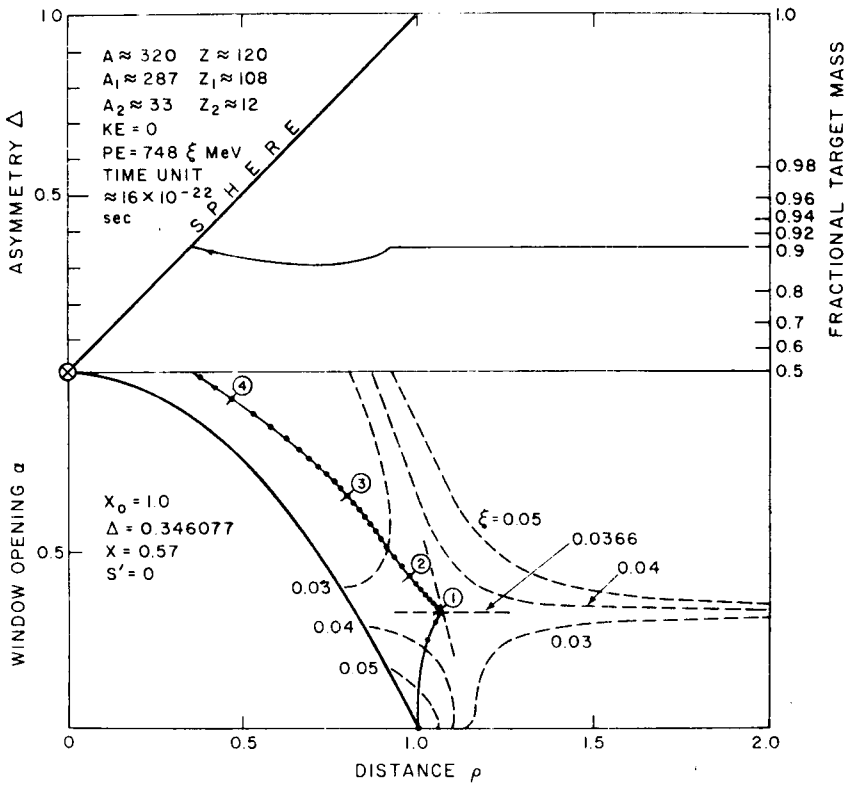

Figure 10

This is similar to Fig.8, but the asymmetry is Δ=0.346077 ($A_1 \simeq 287$, $Z_1 \simeq 108$; $A_2 \simeq 33$, $Z_2 \simeq 12$), which is close to the critical value below which automatic capture does not take place. The effective fissility is X=0.57, and the trajectory only barely manages to be captured inside the conditional saddle. It hovers for about one time unit very close to the saddle.

for capture inside the conditional saddle, should be a function of $X - X_c$ only and, in fact, should have the following appearance:

$$\left(\frac{d\sigma}{d\tau}\right)_{crit} = -a(X - X_c) + \text{higher powers of } (X - X_c) \quad . \qquad (29)$$

Figure 11 illustrates the usefulness of this equation: the dots represent the results of a number of calculations of the critical injection velocity for a variety of systems with different fissilities X_o and different asymmetries. A straight line, with $a \approx 5$, $X_c \approx 0.57$, represents the results fairly well when X is close to X_c. (The scatter of the points reflects the slight dependence on μ.) When the dimensionless variables σ, τ and the effective fissility X (or x_{eff}) are written out in terms of the charge and mass numbers of the nuclei in question, the innocent looking Eq. (29) is equivalent to the following nontrivial statement: "The square root of the extra energy over the barrier needed to ensure capture inside the conditional saddle, when multiplied by the weird combination $A^{1/2}A_1^{-1/6}A_2^{-1/6}(A_1^{1/3} + A_2^{1/3})^{-1}$, should be approximately linear when plotted against the weird combination $Z_1Z_2A_1^{-1/3}A_2^{-1/3}(A_1^{1/3} + A_2^{1/3})^{-1}$."

In other words,

$$\sqrt{KE/MeV} \cdot \frac{\sqrt{A}}{A_1^{1/6}A_2^{1/6}(A_1^{1/3} + A_2^{1/3})} = C_1\left[\left(\frac{Z^2}{A}\right)_{eff} - C_2\right], \qquad (30)$$

where we have introduced the definition

$$\left(\frac{Z^2}{A}\right)_{eff} \equiv \frac{4Z_1Z_2}{A_1^{1/3}A_2^{1/3}(A_1^{1/3} + A_2^{1/3})} \quad , \qquad (31)$$

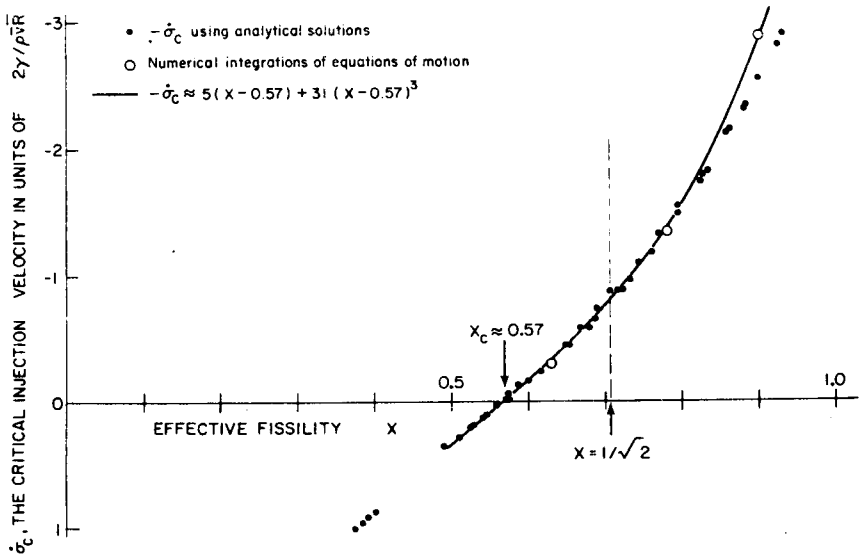

Figure 11

The critical injection velocity (in the natural unit $2\gamma/\rho\bar{v}\bar{R}$) needed for capture inside the conditional saddle is plotted against the effective fissility X. Some 40 different reactions covering a wide range of target-projectile combinations, are represented by the dots. The fair degree of clustering of the dots in a plot vs. X attests to the relatively slight dependence of the trajectories in the dinuclear regime on the inertia parameter μ . For $X > 1/\sqrt{2}$, the conditional saddles enter the mononuclear regime and the continued use of equations of motion appropriate to the dinuclear regime can only provide a lower limit on the critical injection velocity. The dots followed from approximate analytic solutions of the equations of motion. The circles, obtained by numerical integrations, provide spot checks on the accuracy of those solutions.

and C_1, C_2 are essentially constants given by

$$C_1 = \frac{4\sqrt{2}}{45}\left(\frac{3}{\pi}\right)^{1/3}\frac{e^2}{\hbar c}\sqrt{\frac{mc^2}{MeV}}\,a \qquad (32)$$

$$\approx \frac{1}{7}\,, \text{ if } a \approx 5 \text{ is taken as suggested by the present schematic calculations and}$$

$$C_2 = \frac{40\pi r_o^3 \gamma}{3e^2} X_c = \left(\frac{Z^2}{A}\right)_{\text{eff crit}} \qquad (33)$$

$$\approx 26\text{-}27, \text{ if } 0.57 \text{ is taken as the estimate for } X_c.$$

The functional form of Eq. (30) follows on dimensional grounds from the structure of the equations of motion; the actual values of the slope C_1 and intercept C_1C_2 carry quantitative information on the magnitude of the dissipation in the dinuclear regime and could eventually provide a test of the window formula.

Figure 12 shows loci of equal values of the effective fissility X in a plot of the asymmetry Δ against the fissility X_o. For $X \lesssim 0.57$, automatic capture into a compound nucleus takes place. For $X \gtrsim 0.57$, an extra push, described by Eq. (29) or (30), is required for capture inside the conditional saddle. (The conditional saddle moves into the mononuclear regime at $X = 1/\sqrt{2}$, and Eq. (29) becomes a lower limit only.) Figure 13 is a translation of Fig. 12 from the space of fissility and asymmetry to the essentially equivalent space of A_1 and A_2. The contour lines indicate the extra push in MeV needed to make a pair of nuclei with mass numbers A_1, A_2 fuse beyond the conditional saddle.

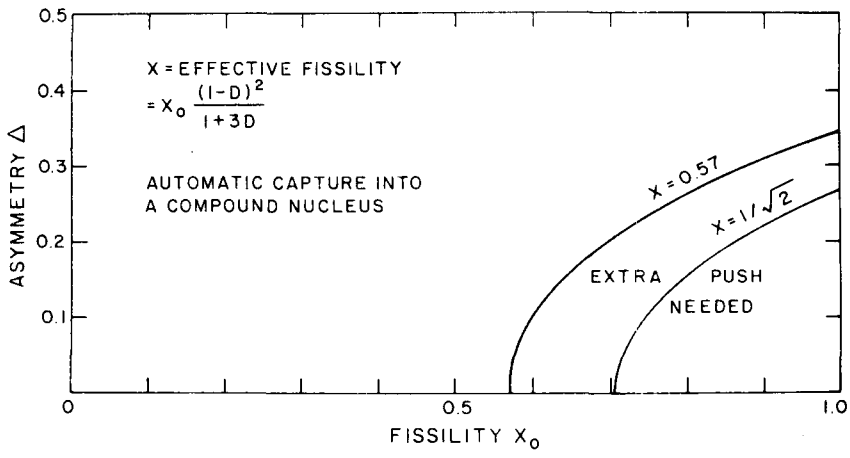

Figure 12

If nuclear reactions are classified according to the asymmetry Δ and the fissility X_o, the Δ-X_o plane becomes divided into two regions, with the effective fissility X less than or greater than X_c (equal to about 0.57 in the present model). For $X \gtrsim 0.57$, deep-inelastic reactions are expected to make their appearance in head-on collisions. For $X \gtrsim 1/\sqrt{2}$ the conditional saddles enter the mononuclear regime and tend to lose their physical significance because of the unfreezing of the asymmetry degree of freedom.

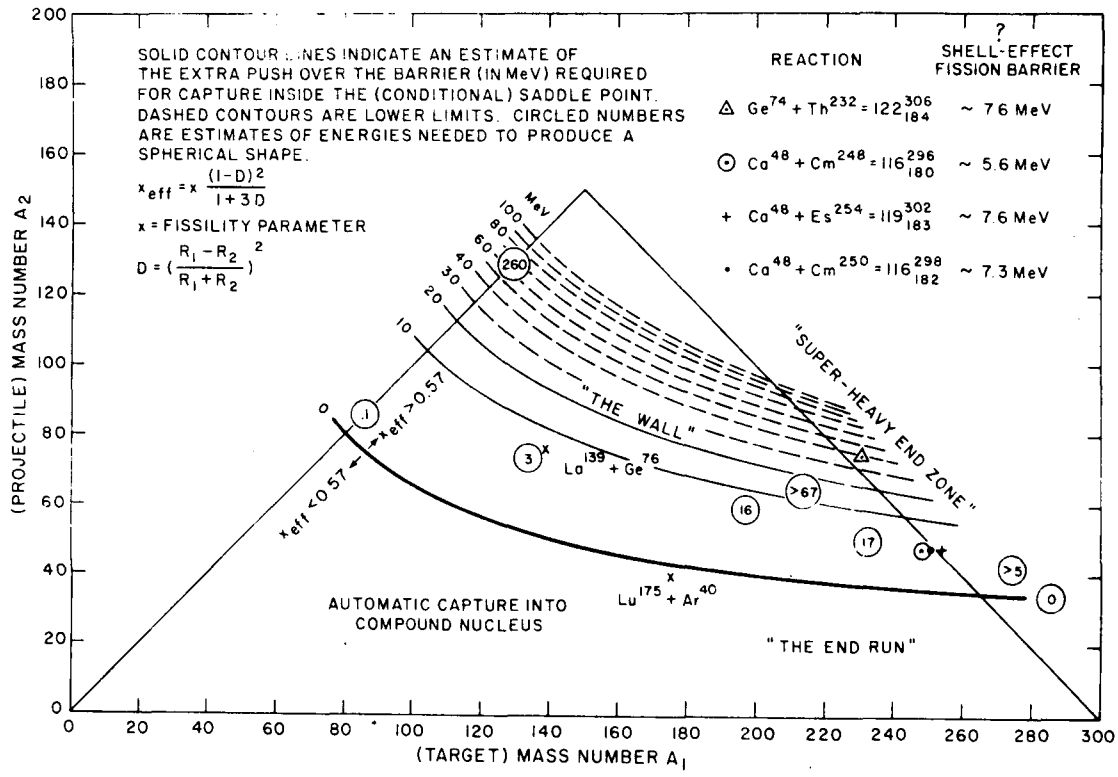

Figure 13

This is a translation of the Δ vs. X_o diagram of Fig.12 into a classification of reactions according to target and projectile mass numbers. The contour lines indicate estimates of the extra energy above the interaction barrier (in MeV) required for capture inside the conditional saddle. Below the zero-MeV contour, automatic capture takes place. Above a contour with 15-20 MeV, the conditional saddle is in the mononuclear regime and the dashed contours are then only lower limits. The circled numbers indicate the energy above the barrier (in MeV) required for compound-nucleus formation (or, in the case of the heaviest systems, for the attainment of the spherical shape). The triangle, circle, dot, and cross indicate approximately the locations of four superheavy-type reactions, listed on the right (together with estimated fission barriers due to hypothetical shell effects). Two other reactions (leading to the same compound nucleus with A=215) are also indicated. The figure suggests that a direct dynamical fusion of two comparable nuclei into a superheavy system is opposed by a huge "wall" requiring tens of even hundreds of MeV in excess of the interaction barrier. The height of the wall drops off precipitously as the asymmetry of the reaction is increased and might be tolerable by the time projectiles with a mass of $A_2 \approx 50$ are used. With projectiles below some mass in the range 30-40, automatic attainment of the spherical shape might be expected (the "end run" into the "superheavy end zone").

Note the critical zero-push contour, below which automatic capture into a compound nucleus takes place. With a mass-40 projectile, there should be no serious problem in making a compound nucleus in a head-on collision with any target in the Periodic Table, except possibly the heaviest. With equal-mass reactions, increasing difficulties would be expected with projectiles heavier than about Kr.

Beyond the 15-20 MeV contour, the conditional saddle enters the mononuclear regime. Now when a trajectory enters this regime, the asymmetry gets unfrozen and a qualitatively new type of reaction may take place, as illustrated by Fig. 14. Here again we have $X_o = 1$ and the asymmetry is 0.3, so automatic capture does not take place (first trajectory). But with a push of 5 MeV, capture inside the conditional saddle takes place and one might have thought that a compound nucleus would result. But look what happens: after beginning to head for home, the trajectory enters the mononuclear regime, and the asymmetry begins to decrease. This results in an increasing Coulomb repulsion (Z_1Z_2 increases), and the trajectory turns around and heads out again. But because such a reversal has to wait for a change in asymmetry, which is a relatively slow process, the time for reseparation is about 3 times longer than in the case of the first trajectory (about 50×10^{-22} sec in absolute value). So even after capture inside the conditional saddle, there was no capture inside the true saddle and no compound-nucleus formation. By ramming with a higher energy (third trajectory, 45 MeV) a compound nucleus can be formed, but there will be a range of energies where capture inside the conditional but not inside the true saddle takes place. Such reactions

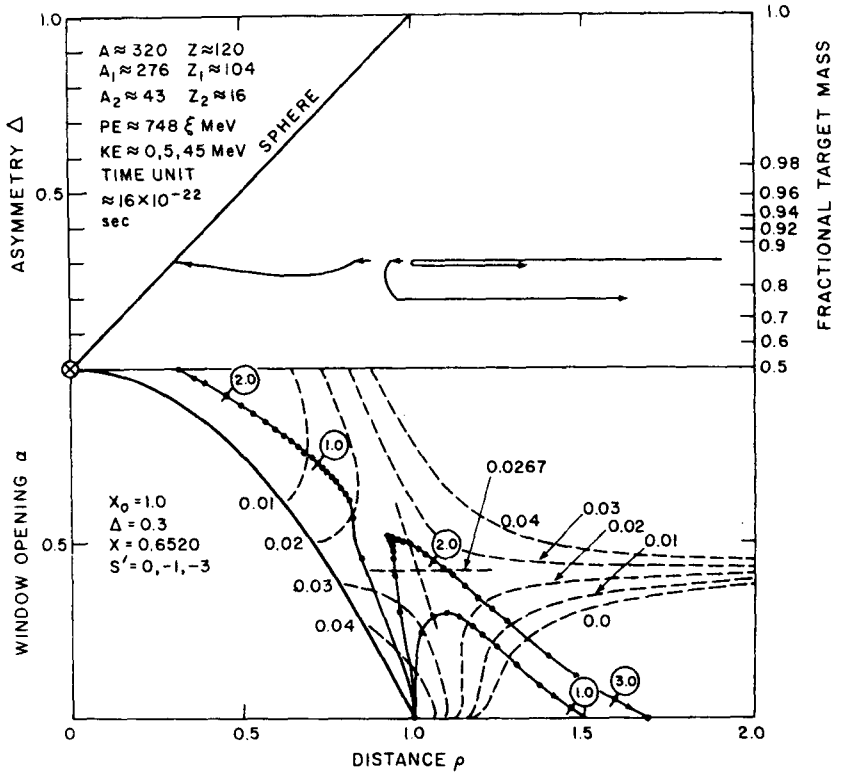

Figure 14

This is like Figs. 6-10 but illustrates the emergence of mononucleus (quasifission) reactions as a species separate from dinuleus (deep-inelastic) reactions. The middle trajectory, with 5 MeV injection energy, is captured inside the conditional saddle but leads to reseparation after a decrease of the asymmetry.

could be called mononucleus reactions. An example of an even longer-lived mononucleus reaction is shown in Fig. 15. Here $X_o = 0.9$, $\Delta = 0.2$, and the injection takes place with 67 MeV above the barrier, which easily ensures capture inside the conditional saddle. At first the trajectory heads for home, but after entrance into the mononuclear regime, it is a competition between the growing compactness of the configuration and the increasing Z_1Z_2 repulsion. The latter wins, but the total time for the reaction is now more than 8 units (more than 120×10^{-22} sec). By that time the asymmetry has drifted practically to zero and the reseparation is into two almost equal pieces. It would probably be very difficult to distinguish such a reaction from the fission of the compound nucleus and "quasifission" might be an appropriate term in this case.

Figure 16 provides another example of dinucleus (deep-inelastic), mononucleus (quasifission) and compound-nucleus reactions. In addition it shows a critical trajectory, with an injection energy close to 16.4 MeV, which would end up at rest at the saddle point, in a state of unstable equilibrium.

The above studies suggest the usefulness of distinguishing between the following regions of configuration space:

1. Compound-nucleus region. The region of the potential energy hollow around the ground state, bounded by the hypersurface in configuration space on which the potential energy is equal to the energy of the fission barrier.

2. Composite-nucleus or mononucleus region. The region outside the compound nucleus region but inside the region where there is a serious neck constriction (e.g., inside a somewhat fuzzy hypersurface

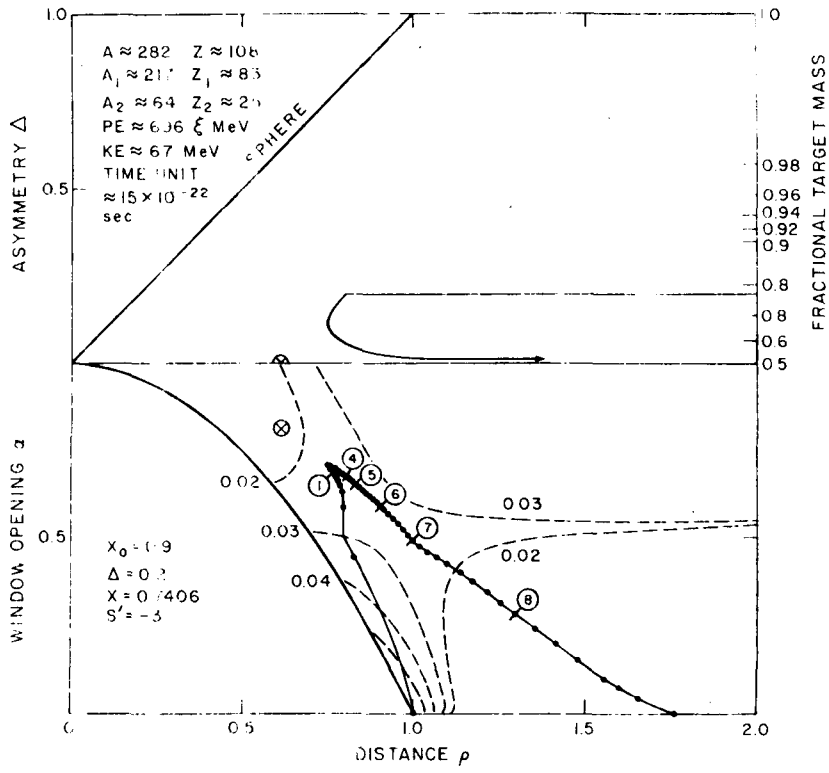

Figure 15

This is another example of a mononucleus reaction, where capture inside the conditional saddle took place but the unconditional saddle was not surmounted. This "quasi-fission" reaction took more than 120×10^{-22} sec and the final division is almost symmetric.

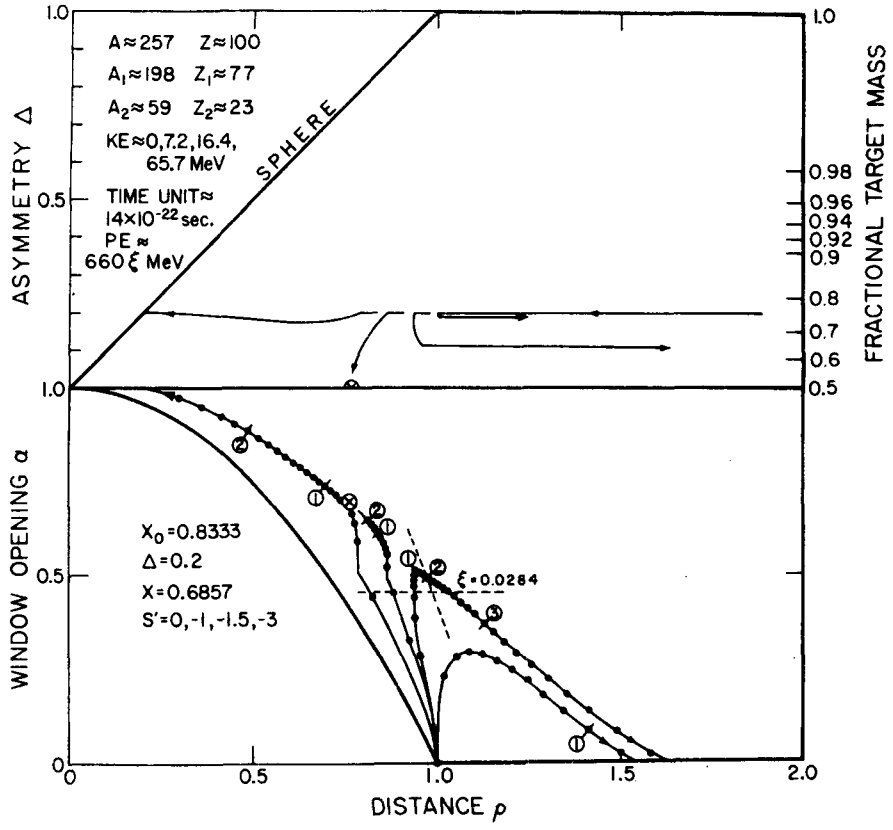

Figure 16

This figure illustrates three types of reactions: (a) deep inelastic (lowest trajectory) following injection with zero energy above the barrier, (b) quasifission, following injection with 7.2 MeV (the other reseparating trajectory), and (c) a compound-nucleus reaction (trajectory on the left, with 65.7 MeV injection energy). The fourth curve corresponds to a critical injection energy close to 16.4 MeV, chosen so that the system would come to rest (in unstable equilibrium) at the unconditional saddle point (indicated by a crossed semicircle).

where the window is about half-open.)

3. Dinucleus region. The region where there is a serious neck constriction (e.g., where the window is less than about half open), but inside the scission hypersurface (this could be defined as the hypersurface where the half-density contour is about to become separated into two, or more, closed surfaces).

4. The binary region. The region outside the scission hypersurface.

In many cases one will probably find a fair correspondence between these four regions and the four types of reactions designated as

1. Compound
2. Quasi-fission
3. Deep-inelastic
4. Quasi-elastic and elastic.

One should remember, however, that only if a system is sufficiently heavy can one expect to see deep-inelastic reactions, and that only if the asymmetry is large enough can one expect the emergence of quasifission reactions as a somewhat distinct category from deep-inelastic reactions. This is because for symmetric systems there is only one saddle to overcome — the unconditional one — and trajectories that are not captured inside it will show a gradual shading of deep-inelastic into quasifission reactions. On the other hand, for sufficiently asymmetric systems, where the conditional saddle is in the dinuclear regime, one may expect a rough distinction between quasifission and deep-inelastic reactions related to the division of the trajectories into those that were or were not captured inside the conditional saddle.

12. Noncentral collisions

If only a small amount of angular momentum is present, the description given above for the time-development of the reaction in the degrees of freedom ρ, Δ, α would continue to be approximately valid provided the proper injection velocity in the distance degree of freedom (ρ) was used as the initial condition. This approximation corresponds to treating the centrifugal and Coriolis forces, as regards their effects on the dynamical development of the shape, as negligible compared to the electric and nuclear forces.

When the amount of angular momentum is large, some limited progress might be made in a simplified scheme where the centrifugal force was retained, but the Coriolis forces still disregarded. One could then try to mock up the centrifugal force by an increase in the electric repulsion, i.e., by the replacement of the effective fissility X by an effective disruption parameter χ defined by

$$\frac{\chi}{X} = 1 + \frac{\text{Centrifugal Force (near contact)}}{\text{Electric Force (near contact)}}$$

$$= 1 + \frac{L^2 M_r (R_1 + R_2)^3}{\mathcal{I}_o^2 Z_1 Z_2 e^2} \quad ,$$

where L is the angular momentum and $\mathcal{I}_o$ is an estimate of the moment of inertia near contact (compare [4]). This suggests the following generalized approximate scaling rule:

"For two dinuclear systems, with possibly different sizes, asymmetries and angular momenta, the dynamical time evolutions in a limited regime can be approximately scaled into each other (by the use of the

natural units of time and length) provided the effective disruption parameters χ are the same."

I intend to study further the usefulness of this approach (see also [3]).

13. Summary

I have sketched an attempt to develop an algebraic theory of the gross macroscopic dynamical shape evolutions in fission and nucleus-nucleus collisions. A crucial physical ingredient was the one-body dissipation function. Even though the price paid for an algebraic theory was the introduction of various more or less drastic technical approximations (that could, in principle, be avoided), the scheme may be useful in suggesting scaling rules and making more precise our intuitive ideas about various types of reactions (deep-inelastic, quasifission, compound-nucleus). There is a wealth of specific information in these studies on normal modes, on reaction times, on energy loss, etc., which I have not been able to present, and the treatment of angular momentum has not progressed very far. Also, I have not been able to give a comparison with experimental evidence, but I look forward to a broad confrontation of theory and experiment in the future. I hope the scheme I have described may prove to be a useful background and a complement to more detailed and realistic microscopic computer studies of the kind that Sven-Gösta Nilsson and his Lund Group were masters of.

Acknowledgment

This report was prepared by the Nuclear Science Division of the Lawrence Berkeley Laboratory under the University of California contract W-7405-ENG-48 with the U.S. Department of Energy.

References:

1. Cohen,S. and Swiatecki,W.J., Ann. Phys. 22, 406 (1963); Blocki,J., Randrup,J., Swiatecki,W.J. and Tsang,C.F., Ann. Phys. 105, 427 (1977) and references therein.
2. Randrup,J. and Swiatecki,W.J., Ann. Phys. 124, 193 (1980) and references therein; Blocki,J., Boneh,Y., Nix,J.R., Randrup,J., Robel,M., Sierk,A.J. and Swiatecki,W.J., Ann. Phys. 113, 338 (1978). See also [3].
3. Swiatecki,W.J., Three lectures on macroscopic aspects of nuclear dynamics, presented at International School of Nuclear Physics, "Ettore Majorana" Center for Scientific Culture, Erice-Trapani, Sicily, March-April 1979, Prog. Particles & Nuclear Physics 4, 383 (1980); Lawrence Berkeley Laboratory preprint LBL-8950, March 1979.
4. Bass,R., Nucl. Phys. A231, 45 (1974).

B. Non-central Collisions

We will first make use of the model in an attempt to understand the new measured excitation functions for symmetric fragmentation of the $^{208}Pb + (^{26}Mg-^{64}Ni)$ systems, see figs. 10 and 11. In doing so, a very important simplifying assumption will be made, namely that the separation between the scattering channel and the fusion (i.e. symmetric fragmentation) channel takes place before the mass asymmetry degree of freedom comes into play. If the initial system becomes caught behind the conditional saddle we shall assume that the system evolves automatically all the way to mass equilibration. Conversely, the scattering cross section (centered around the target-projectile masses) represents those trajectories that did not manage to make their way behind the conditional saddle.

This then restricts the use of the model to two degrees of freedom: separation and neck formation. It also limits the study to the initial steps of the trajectory in the ρ vs α plane. We can then lean heavyly on the scaling law, based on the parameter $(Z^2/A)_{eff}$ eq.(18), and on the approximate linear relationship between the extra push velocity and excess $(Z^2/A)_{eff}$-value, see subsection III A, fig.11 . But even so the application of the model to reaction data necessitates a generalization to non-zero ℓ-values. We need to formulate some kind of equivalence between Coulomb and centrifugal forces, which is valid at least to first order. The precise form of this equivalence must be found.

Following Bass[12] we generalize eq.(16) to non-zero ℓ-values by expressing the ratio of the Coulomb plus centrifugal force to the nuclear force at maximum nuclear attraction, i.e.

$$X_{Bass}(\ell) = \frac{F_{Coulomb} + F_{centrifugal}}{(F_{nuclear})_{max}} \qquad (20)$$

Within the liquid drop model the generalized "effective fissility" is

$$X_{Bass}(\ell) = \frac{e^2}{4\pi\gamma r_0^3} (Z^2/A)_{eff}(\ell) \tag{21}$$

where

$$(Z^2/A)_{eff}(\ell) = (Z^2/A)_{eff}(\ell=0) + g(f\ell)^2 \cdot \frac{A_1 + A_2}{A_1^{4/3} A_2^{4/3} (A_1^{1/3} + A_2^{1/3})^2} \tag{22}$$

Here $(Z^2/A)_{eff}(\ell=0)$ is the quantity defined in eq.(18), $g=4\hbar^2/(m_0 r_0 e^2) = 95.86$ and f takes the values 1, 5/7 or $\mathcal{I}_{12}/(\mathcal{I}_{12} + \mathcal{I}_1+\mathcal{I}_2)$, respectively, depending on the assumption of sliding, rolling or sticking motion. The quantity $\mathcal{I}_{12}$ is the relative moment of inertia, whereas $\mathcal{I}_1$ and $\mathcal{I}_2$ are the intrinsic moments of inertia of each of the two spheres, respectively.

We can now generalize the model to non-zero ℓ-values by assuming the "extra push" $\Delta E_{push}(\ell)$ (i.e. the extra kinetic energy at the barrier needed to achieve capture behind the conditional saddle) to be given by

$$\Delta E_{push}(\ell) = \begin{cases} 0, \text{ for } (Z^2/A)_{eff}(\ell) < (Z^2/A)_{eff}^{thr} \\ a^2 \eta_0 \left[(Z^2/A)_{eff}(\ell) - (Z^2/A)_{eff}^{thr}\right]^2, \text{ for } (Z^2/A)_{eff}(\ell) > (Z^2/A)_{eff}^{thr} \end{cases} \tag{23}$$

Here, a is a general slope factor and η_0 is a dimensional constant depending on the composition of the colliding nuclei

$$\eta_0 = \text{const.}\ A_1^{1/3} \cdot A_2^{1/3} (A_1^{1/3} + A_2^{1/3})^2 (A_1 + A_2)^{-1} \tag{24}$$

$$\text{const.} = (32/45^2)\ (3/\pi)^{2/3}(e^2/\hbar c)^2\ .\ m_0c^2 = 7.60\ .\ 10^{-4} \qquad (25)$$

see ref.[11].

In the next section we shall examine whether the generalized Bass parameter, eq.(20), should be defined in terms of the sliding, rolling, or sticking condition, and we shall treat $(Z^2/A)^{thr}_{eff}$ and the general slope factor, a, as free parameters in order to obtain best fits to experimental data and thus determine empirical values of $(Z^2/A)^{thr}_{eff}$ and a.

One can easily incorporate the effect of the extra push $E_{push}(\ell)$ into the schematic model described in subsection II.B by redefining the interaction barrier in eq.(11) as follows.

$$V_{int}(\ell) = V_{eff}(\ell, R_{int}(\ell)) + \Delta E_{push}(\ell) \qquad (26)$$

Using this definiton one can calculate the capture cross sections from eqs.(11), (12) and (6), with $\Delta E_{push}(\ell)$ given by eq.(23).

C. Comparison with experiment. Best values of $(Z^2/A)^{thr}_{eff}$, slope a, and value of f.

With the formalism of section III.B one can now generate excitation functions for capture behind the conditional saddle. As mentioned, the threshold value of the effective fissility $(Z^2/A)^{thr}_{eff}$ has to be regarded as a free parameter; and similarly for the slope coefficient a in eq.(23). One should also be openminded with respect to the angular momentum dissipation factor f, (eq.(22)).

Figure 14 compares the data with various model runs.

The trends in the measured capture cross sections are well described by the two-dimensional dynamical model, when

$$a = 10 \pm 1,\ (Z^2/A)^{thr}_{eff} = 32.5 \pm 1 \text{ and } f = 5/7 \text{ (rolling)} \qquad (27)$$

The data very clearly show rolling to be the best assumption among the three possible ones. This seems very reasonable, since this is also what the one-dimensional proximity friction model finds. Proximity friction (one-body dissipation) very strongly opposes sliding motion, whereas the forces that damp the rolling motion and eventually leads to rigid rotation (or sticking) are appreciably weaker . Presumably, they are too weak to play any significant role during the initial phase, when the systems evolve towards the conditional saddle.

Figure 14:

Comparison of experimental symmetric fragmentation cross sections with model calculations of capture probabilities. Thin lines are static calculations, like figs. 3 and 10, with the rolling assumption. The heavy dashed line is a best fit based on Swiatecki's dynamical model, again with the assumption of rolling, i.e. parameter value for f equal to 5/7. The dotted lines are attempts to fit the data with the assumption of no angular momentum dissipation (sliding, f=1). The short dashed line corresponds to another attempt with the assumption of full angular momentum dissipation i.e. sticking ($f = (\mathcal{I}_{12})/(\mathcal{I}_{12}+\mathcal{I}_1+\mathcal{I}_2)$).

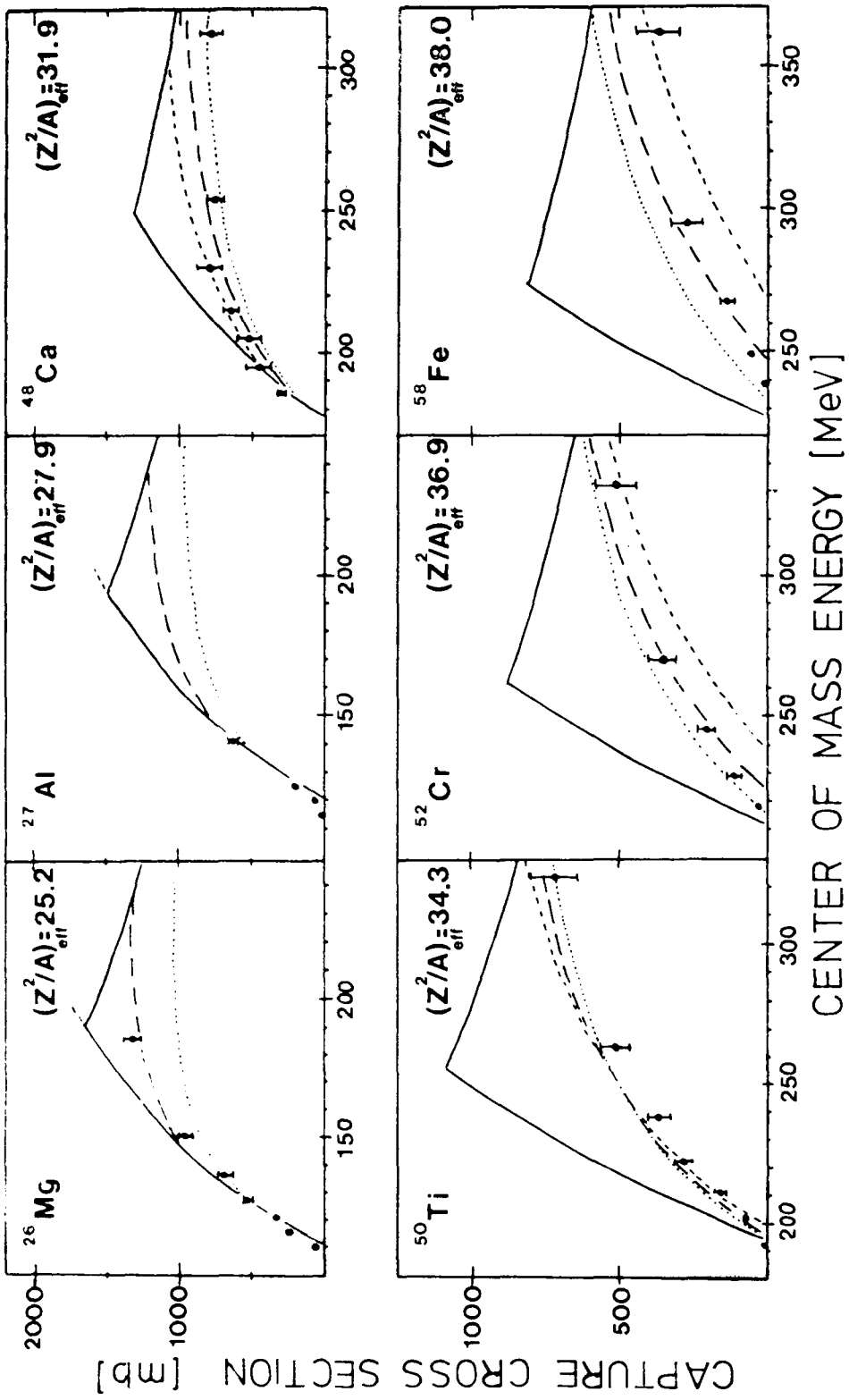
CAPTURE CROSS SECTION [mb]
CENTER OF MASS ENERGY [MeV]
^{26}Mg
$(Z^2/A)_{eff}$=25.2
^{27}Al
$(Z^2/A)_{eff}$=27.9
^{48}Ca
$(Z^2/A)_{eff}$=31.9
^{50}Ti
$(Z^2/A)_{eff}$=34.3
^{52}Cr
$(Z^2/A)_{eff}$=36.9
^{58}Fe
$(Z^2/A)_{eff}$=38.0

Figure 14

But what about the two other parameter?

	Model value Sec.II.A, ref.[11]	Experimental value (fig.14, refs.[9,10]	
$(Z^2/A)^{thr}_{eff}$:	27	32.5±1	(27.a)
a :	5	10±1	

There appear to be quite serious disagreement. Or is it serious? Should one really expect quantitative agreement? After all, the model with its spheres connected by a conical neck cannot be assumed to reflect real nuclear shapes accurately. If only the model renders the trends in the dynamical behaviour, one should be gratified.

Still, it is possible to ask whether the deviations, eq.(27.a), can be understood by examining the differences between realistic nuclear (saddle) shapes and the model imitations of these shapes. This is what Swiatecki has set out to do in a recent draft, ref.[18]. The analysis shows very clearly that the realistic saddle shapes are more elongated than the model shapes. As a consequence, the point where an extra push is needed moves to a higher value of $(Z^2/A)_{eff}$. There is even a quantitative argument for moving it from 27 to 33, bringing it in perfect agreement with the experimental value.

Similarly, the rate of increase in the extra push, expressed in eq.(23) through the parameter a, should be higher than 5 in a more realistic model calculation. This is because the change in realistic saddle shape per unit change of $(Z^2/A)_{eff}$ is more rapid than with the primitive model-shapes. Whether the resulting change in a is just the factor of two found from experiment remains to be seen, after more accurate calculations have been performed.

All in all, the comparison between theory and the capture experiments described in Section II is most satisfactory. We have, so to say, been able to look through the opening in the black box in fig.1 and follow the dynamical evolution beyond the initial contact phase until the system again disappears behind the conditional saddle.

D. Scaling law for fusion cross sections.

It is implied by Swiatecki's model that systems with the same $(Z^2/A)_{eff}(\ell)$-value are dynamically equivalent. The energy has to be measured in units of η_0 , eqs.(24), (25). With the generalization to include centrifugal effects, this means that the many-dimensional space of masses, charges and angular momenta is reduced to a single dimension, expressed through $(Z^2/A)_{eff}(\ell)$, as far as the probability for capture is concerned. It is of great interest to learn to which extend such a scaling is universally valid. This would mean that many different experiments, when fitted in terms of values of the parameters $(Z^2/A)^{thr}_{eff}$ and a, would result in the same parameter values, or at least values lying within a very narrow range, (cf. ref.[19] for an example).

In this section we have seen how important it is to go beyond a one-dimensional description, and we have introduced a three-dimensional model. So far, however, we have only exploited the model in two dimensions, leaving the mass asymmetry degree of freedom in the black box. In the following sections we shall discuss measurements that involves this degree of freedom too, and attempt a qualitative comparison with the full three-dimensional model.

IV. FROM ENTRANCE TO EXIT CHANNEL: GAMMA-RAY MULTIPLICITIES AND SADDLE SHAPES

A. Origin of gamma rays and spin.

With a satisfactory understanding of the cross sections σ_c, maintaining the sharp cut-off assumption and introducing the extra push concept, we may now turn to the measurements of gamma ray multiplicities. Remember, that for each binary reaction event the probability of triggering the NaI-counters in fig.5 is recorded simultaneously. Knowing the solid angles of the gamma counters we may convert this to an average number of gamma rays $\langle M_\gamma \rangle$ emitted (isotropically) in connection with each class of events of a particular mass asymmetry, TKE and center of mass angle. In general M_γ does not vary with energy loss and angle, so only the dependence of M_γ on A_1/A_2 is of interest.

Gamma ray emission is a relatively slow process occuring some 10^{-14} to 10^{-13} sec after the collision. So the gamma rays are emitted long after the binary reaction products have separated. Their shapes are those appropriate to isolated nuclei most of the excitation energy has been disposed of by evaporation of neutrons, but whatever angular momentum was transferred to the products during the reaction is largely preserved.

Even if the fragments posess no angular momentum the excited products will emit gamma rays. This is analogous to neutron capture gamma rays; and about three gamma rays for each product appear to be a realistic number. In addition to this, each product nucleus will emit about $1/2|j_1|$ gamma rays, if $|j_1|$ is its total angular momentum. This is because one gamma ray is assumed to remove two units of spin and the gamma cascades are thought to be streched. Extensive studies of gamma ray emission from

the exchange of particles and energy between them, refs.[21,22]. The statistical components that are parallel to the ℓ_z-components will just smear out the ℓ_z-distribution without changing the average ℓ_z-value much, but the components perpendicular to ℓ_z will systematically increase the total spin value, j . Typical values of the statistical components for deeply inelastic scattering systems of total mass A≈300 are $\langle M^2_{x,y} \rangle^{1/2} \approx 10\text{-}15\hbar$, refs.[21,23]. These will then combine quadratically with the ℓ_z-components.

B. Experimental gamma ray multiplicities.

Figure 15 is a summary of the experimentally measured gamma ray multiplicities as a function of mass asymmetry. The highest multiplicities are found for symmetric mass division with a more or less pronounced drop towards asymmetry. For target-projectile like masses the multiplicity appears systematically low. Remembering that the deep-inelastic products are thought to be associated with high ℓ-values and the symmetric fragments with the lowest ℓ-values compatible with the capture cross section, σ_c (sharp cut-off) this result is surprising. Some of the explanation for this may result from the interpretation of the multiplicities for symmetric masses, which is to follow. And some may be related to inadequacies in the recording of highly asymmmetric events by the ring counter as previously discussed (see section II.D). Still, the systematic decrease with mass asymmetry could contain a message that is not fully understood at present.

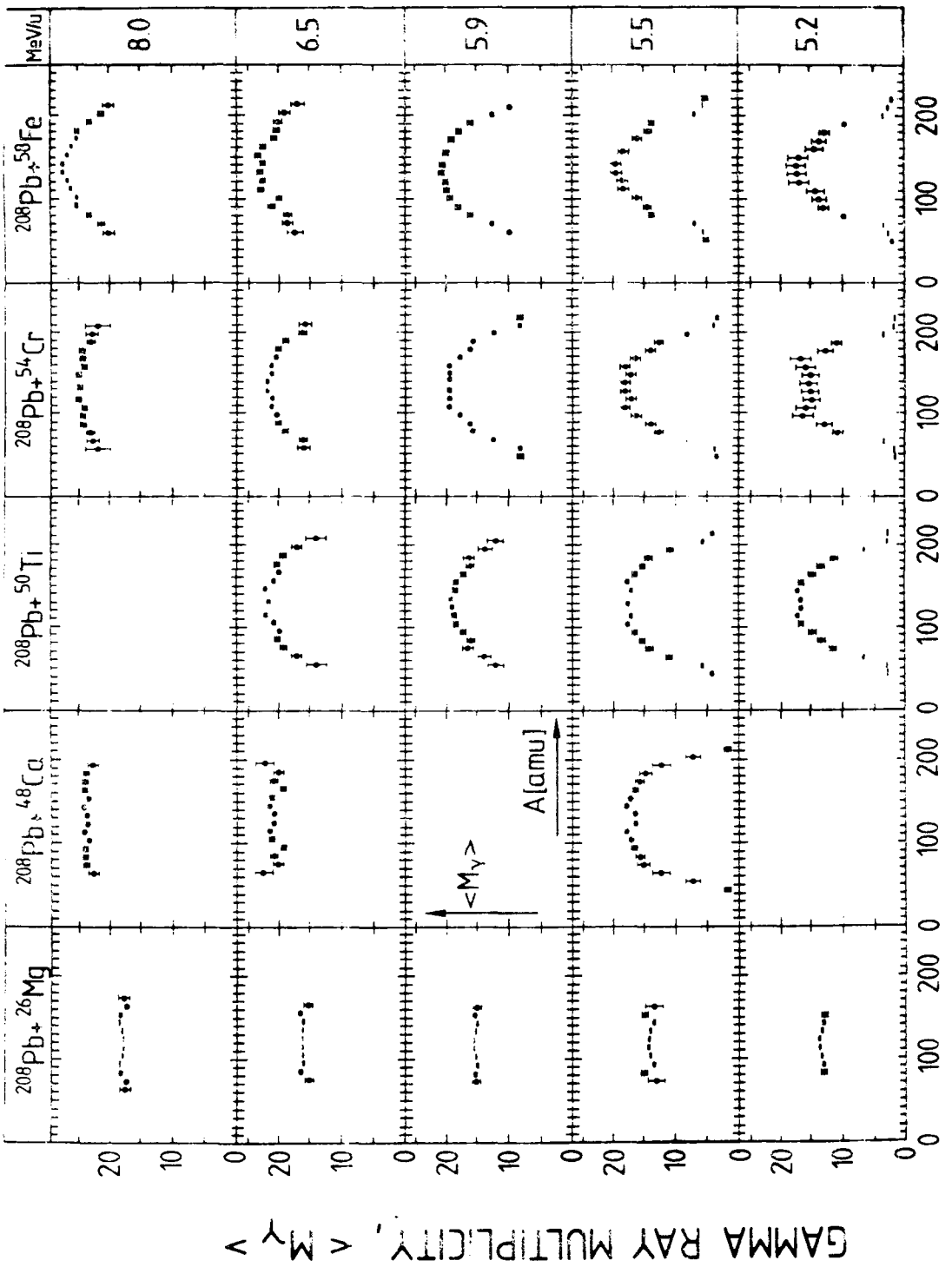

Figure 15:

Average gamma-ray-multiplicity as a function of product mass for the different systems and bombarding energies. The figure gives mean values over the total kinetic energies actually recorded by the particle counter.

However that may be, it is the multiplicity associated with symmetric fragmentation that is of concern to us in the present context, and it is unambiguously defined experimentally. Accordingly, the following analysis will focus exclusively on the symmetric products of the various reactions. One sees from fig.15 that their multiplicity is essentially constant within a broad range of masses around symmetry. They can therefore be associated with the capture reaction in terms of one specific value of the mean multiplicity. (The ratio $\sigma_j/\langle M_j \rangle$ varies between 0.35 and 0.40, which is compatible with a triangular distribution of contributing spin values).

It is natural to expect the gamma ray multplicities to be correlated with the ℓ-values, which contribute to the specific reaction that generates the fragments ultimately emitting the gamma rays. As mentioned above, about 1/7th of the reaction ℓ-value is expected to remain with each fragment as an aligned spin component, ℓ_z . In this spirit the multiplicities are plotted in fig.16 against the cut-off values of ℓ_c derived from the capture cross sections. As clearly seen, the multiplicities correlate very poorly with ℓ_c . There is a systematic tendency for an increased multiplicity as the systems become heavier.

As an alternative, the multiplicities are plotted in figure 17 against the grazing angular momentum, representing the cut-off ℓ-value of the <u>total</u> reaction cross section, c.f. figure 3. The correlation appears much better. It is in fact possible to fit the trend in this figure by assuming a universal tendency for all ℓ-values up to about 70 $\hbar$ to contribute in the usual triangular fashion to the fragment spins and the higher ones to miss. More specifically, a gaussian weight function centered at zero and falling to one half at ℓ = 70 $\hbar$ produces the fit shown with the dashed curve on figure 17. But an interpretation along these lines is incompatible with the interpretation of the capture cross

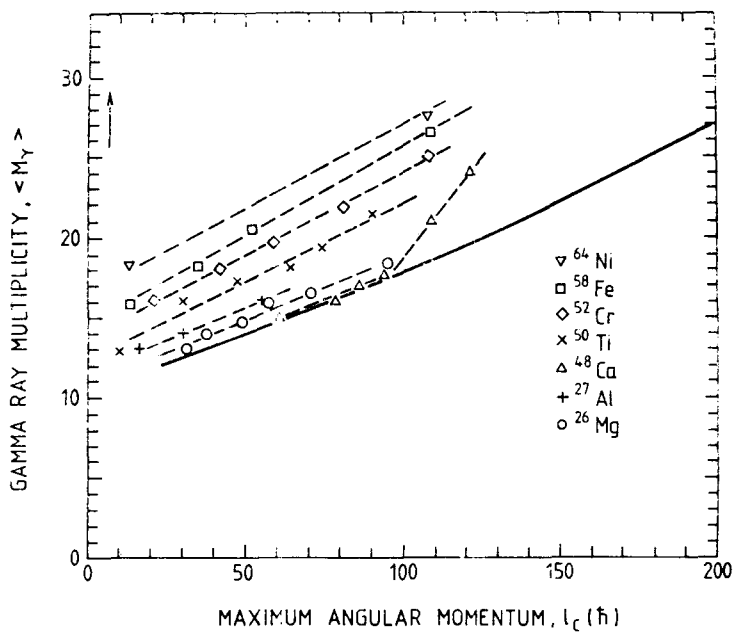

Figure 16:

Average gamma-multiplicity of the symmetric fragmentation products as a function of the angular momentum ℓ_c deduced from σ_c in the sharp cutoff approximation. The dashed lines serve to guide the eye. The solid line is the result of a statistical model calculation for a triangular distribution in ℓ and statistical spin contributions appropriate to the scission configuration, ref.[21]). In addition it is assumed that each fragment emits 3 statistical gamma rays, which do not remove any angular momentum. (The possible effect of neutron emission has been neglected).

sections in section III, where the sharp cut-off assumption, at least in an approximation form is essential. One should therefore seek other explanations for the lack of a simple correlation between the multiplicities and ℓ_c , which stands out so strongly in fig. 16 .

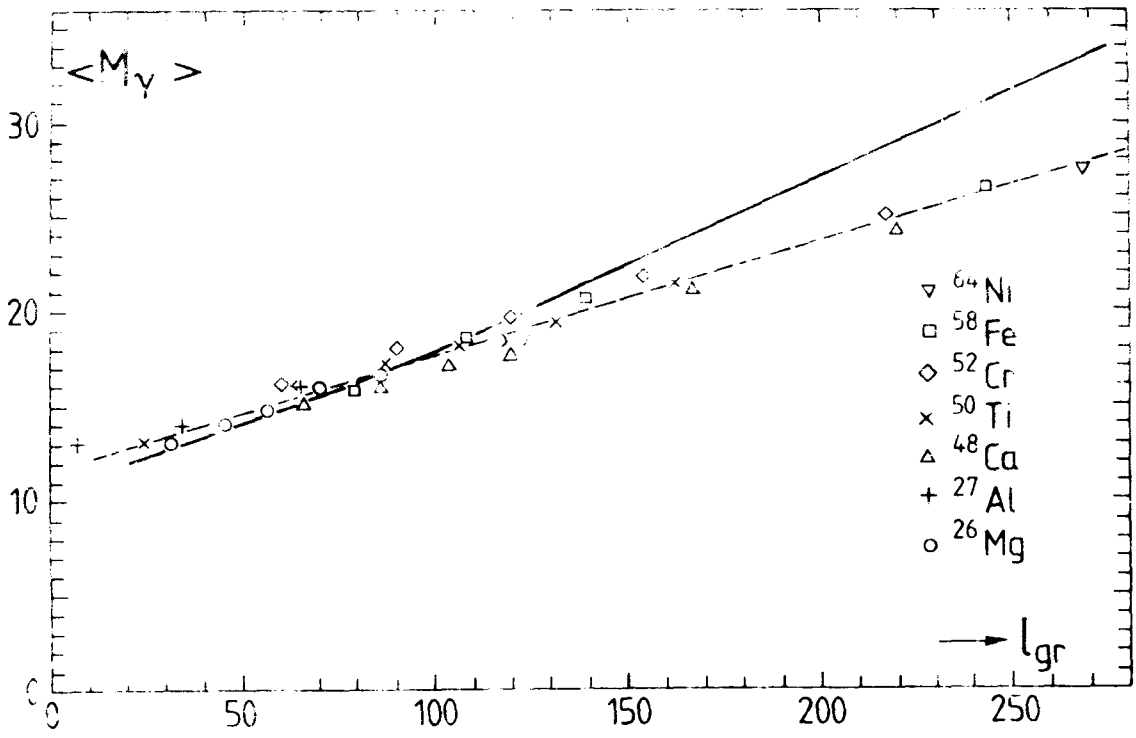

Figure 17:

Average gamma-multiplicity for the symmetric fragmentation as in fig.16, but plotted as a function of the grazing angular momentum. The dashed line is the result of a new statistical model calculation (see text). The solid line is identical to the one on fig.16 .

First of all, according to this figure, the multiplicities are higher than expected on the basis of the aligned angular momenta, even when including statistical spin components $\langle M^2_{x,y} \rangle^{1/2} \approx 10\text{-}15\ \hbar$, see caption to figs. 16 and 17. Presumably, this extra multiplicity originates from some new kind of statistical spin components. The experiment shows that these components become increasingly important as the charge of the composite system increases.

C. Statistical spin components in fission.

This situation is reminiscent of the K-distributions governing angular distributions of fission products in nuclear reactions[24,25]. Compound nucleus fission angular distributions deviate from the $1/\sin\Theta$ law, reflecting a certain statistical smearing of the orientation of the fission axis with respect to directions strictly perpendicular to the angular momentum vector. This is equivalent to non-zero projections, K, of the total ℓ-vector along the fission axis, see figure 18. The magnitude of this smearing can be rather easily understood from a simple thermodynamical argument.

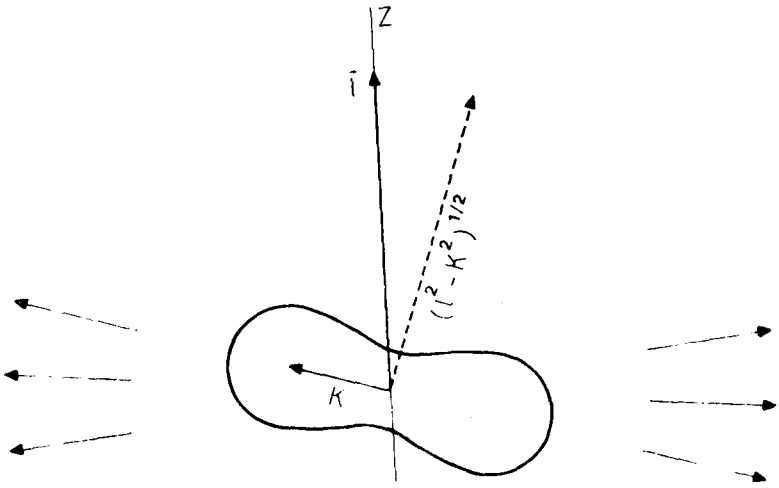

Figure 18:

A given total angular momentum vector $\vec{\ell}$ induced for example in a charged particle fusion reaction and pointing in a direction perpendicular to the beam direction can have a non-zero projection K on the nuclear symmetry axis. The angle between $\vec{\ell}$ and the symmetry axis is generally preserved during the later stages of the fission process, so the angle where the fission products are observed (the angular distribution) is directly related to the value of K.

completely fused systems lie behind this relatively simple picture, see for example ref.[20].

In the case of binary reactions there are two mechanisms that can induce spin into the fragments, one being systematic in nature, the other of statistical origin. The total ℓ-value of the reaction channel invariably will be reflected in the product spins. As discussed in section II, angular momentum is lost from the relative center of mass motion. It reappears as intrinsic angular momentum of the fragments by the amount $(1-f)\ \ell_{tot}$, where f is the factor defined in connection with eq.(22), section II.B . These angular momentum components are parallel to the total ℓ-vector (Z-axis) and perpendicular to the reaction plane. Thus

$$\ell_z = \ell_{1z} + \ell_{2z} = (1-f)\,\ell_{tot} \qquad (28)$$

i.e. the aligned spin components are proportioned to total ℓ. For symmetric fragments separating as spheres, (1-f) is 2/7. Elongating the system before separation will lower this number somewhat. On the other hand, it will be larger for asymmetric systems rotating rigidly (sticking).

For $\ell=0$, ℓ_z is zero, but the two fragments may still be sprinning (in opposite directions) due to statistical spin components. There is evidence for this type of component already in the spontaneous fission of spin-zero (even-even) nuclei, where the fragments actually emit more than the 6 statistical gamma rays expected for spinless fragments. We picture these spin components as the result of a bending motion of the elongating system just prior to scission. When rupture occurs the two halves are turning with spins perpendicular to the separation axis. This is the oldest known example, and more recent studies of the deep inelastic reactions have called attention to quite a number of additional mechanism that can generate statistical spin components in binary systems through

For sufficiently large ℓ-values the K-values will be distributed as a Gaussian around zero with a width $K_0 = \langle K^2 \rangle^{1/2}$, thus

$$K_0^2 = T \cdot \mathcal{J}_{eff} \tag{34}$$

The quantity $1/\mathcal{J}_{eff}$, i.e. the reciprocal difference of the moments of inertia for rotations along the separation direction and perpendicular to it, is a measure of the shape of the rotating nucleus at the point where the statistical equilibrium establishes itself. Using the moment of inertia $\mathcal{J}_0$ of a sphere of the same total mass as a unit, a spherical shape will have the value of $\mathcal{J}_0/\mathcal{J}_{eff} = 0$. Two spheres in contact have the value 1.13 and the more drawn-out scission configuration has a value of about 2, cf. refs.[24,25]. In fission, the point of thermal equilibrium is believed to be the saddle; because there the motion is particularly slow and because axial symmetry is believed to preserve the K-distribution during the more rapid motion from saddle to scission. This is because K, the spin projection on the axis of cylindrical symmetry ought to be a constant of the motion in such a situation. There is ample experimental evidence, based on the measurements of fission fragment angular distributions to show that this picture is correct, see ref.[25]. The fragment angular distributions from charged particle induced compound nucleus fission indeed reflect a smearing in angle between the fission direction and the angular momentum vector. One finds that the effective moments of inertia derived from the experimental K_0-values according to eq.(34) fit very nicely with saddle shapes calculated from liquid drop theory[25].

Of interest in the present context is the fact, that the axial angular momentum components remain with the fragments after separation, and they therefore contribute to the gamma ray multiplicity. This is illustrated in figure 19. In the following subsection we will analyse

the multiplicities on the basis of the hypothesis, that the K-components are the dominating contributors to statistical angular momentum components in the (symmetric) fragments.

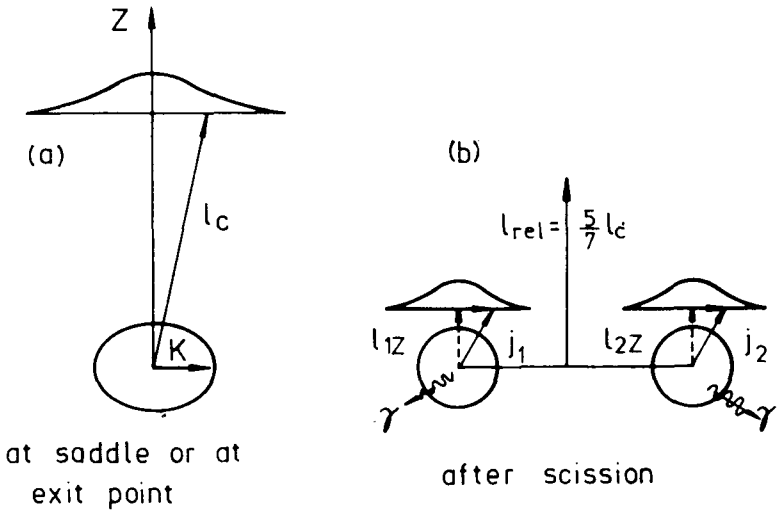

Figure 19:

The total angular momentum of the reaction can contribute to fragment spin, j, in two ways: (i) the rigid rotation around an axis perpendicular to the separation axis leaves about 1/7th of the total ℓ-value with each fragment as aligned spin, ℓ_z. (ii) There will also be a statististically distributed component, K, from the projection of the total ℓ-vector on the separation axis, because this axis is not always strictly perpendicular to the total angular momentum vector. The K-components are carried over with their full values into the fragments.

D. Analysis of gamma ray multiplicities in terms of K_0 and $\mathcal{I}_{eff}$.

The sum j of the lengths of the two spin vectors j_1 and j_2 on fig.19 is measured by the gamma multiplicity after subtraction of the contribution from statistical gamma rays and assuming streched quadrupole ($\Delta j = 2$) radiation:

$$<|j|> = 2(<\ell_z> - \delta) \qquad (35)$$

The average aligned component, $<\ell_z> = <\ell_{1z}> + <\ell_{2z}>$, is obtained from

$$<\ell_z> \approx \frac{2}{3} \cdot \frac{2}{7} \ell_c \qquad (36)$$

where ℓ_c is derived from eq.(6) using the measured capture cross section, σ_c .

Referring again to fig.19 one may to a good approximation write

$$<|j|>^2 = <\ell_z>^2 + <K^2> \qquad (37)$$

When $\ell_c >> K_0$, or typically larger than 60$\hbar$, corresponding to capture cross sections in excess of 200 mb, it is permissible to replace $<K^2>$ with K_0^2 . Eq.(37) then leads to

$$K_0^2 = <|j|>^2 - <\ell_z>^2 \qquad (38)$$

where $<|j|>$ is measured by the multiplicity and $<\ell_c>$ is derived from the capture cross section. From K_0, the effective moment of inertia can then be calculated according to eq.(34). Table 2 presents typical results and compares the experimental values of $\mathcal{I}_0/\mathcal{I}_{eff}$ to the theoretical values expected for rotating, as well as for non-rotating, saddle shapes[8]. Perhaps surprisingly, one sees that the experimental values are rather constant for a given system, and more in agreement with the shape of the non-rotating saddle than with the actually expected rotating saddle shape.

TABLE 2

Values of K_0 and the effective moment of inertia

^{208}Pb+ Target (Z^2/A)	l_c (h)	<j> (h)	$<l_z>$ (h)	K_0 (h)	J_0/J_{eff} Exp. Value	Theory ref. 8) rotating saddle shape	Theory ref. 8) non-rotating saddle shape
^{50}Ti (41.9)	47	22	9	21	0.50	0.36	0.52
	64	24	12	21	0.55	0.26	
	74	27	14	23	0.53	0.18	
	89	31	17	26	0.48	no saddle	
^{52}Cr (43.2)	45	24	9	23	0.44	0.27	0.39
	63	27	12	25	0.42	0.14	
	87	32	17	27	0.42	no saddle	
	116	38	22	31	0.42	no saddle	

The values of l_c , <j> , $<l_z>$, K_0 and $\mathcal{J}_{eff}$ are based on experimental values of σ_c and $<M_j>$, and on eqs. (6), (34), (35), (36), and (38). The temperature is calculated from $T(MeV) = (10\ E^*/A_1 A_2)^{1/2}$ and the moment of inertia of the sphere J_0 is $0.4\ r_0^2(A_1+A_2)^{5/3} = 0.0155(A_1+A_2)^{5/3}(MeV)^{-1}$. The excitation energy E^* ranges from 30 to 150 MeV; although it is calculated for the fused ground state shape it is here taken to be equal to the excitation energy at the shape where the K-distribution is frozen in, i.e. at the saddle or the exit point of figure 19.

Two explanations seem possible. But first it should be observed that eq.(34) is valid for the shape, where the statistical K-distribution is actually frozen in, it does not have to be the saddle shape under all circumstances. The first explanation now assumes that a true compound nucleus is formed and that the system proceeds over the saddle with the correct K-distribution. In rotating system, however, the Coriolis forces are breaking the axial symmetry and the system may therefore continue to adjust its K-distribution during the motion beyond the saddle. The speed of the motion and the strength of the Coriolis interaction will determine when the readjustment ceases to take place. As suggested in fig.19 we may denote this the exit point. The experimental results can be interpreted to mean that the exit point happens to coincide with the saddle shape of the non-rotating system.

The other explanation does not assume true compound nucleus formation. Rather, it pictures the symmetric fragmentation reaction as an amalgamation of the two nuclei during an inward radial motion, which at some point turns around and leads to the symmetric fragmentation. This picture imposes itself in those cases, where the calculated fission barrier has vanished so that there is no saddle, see table 1. In this picture, the turning point suggests itself for the role played by the saddle in the first alternative. But again, the freezing in of the K-distribution may occur at some later stage for strongly rotating systems.

In both cases, the measured value of $\mathcal{I}_0/\mathcal{I}_{eff}$ defines a shape of a certain compactness. If the analysis is correct it allows one to conclude that during the reaction the system was at least as compact as indicated by the $\mathcal{I}_0/\mathcal{I}_{eff}$-values. As the numbers in table 2 and 3 show, shapes much nearer to a single sphere ($\mathcal{I}_0/\mathcal{I}_{eff} = 0$) than to that of two spheres in contact ($\mathcal{I}_0/\mathcal{I}_{eff} = 1.13$) are indicated, especially for the heaviest systems.

E. Comparison with angular distribution measurements.

A crucial point is whether it is permissible to interpret the gamma ray multiplicity measurement the way it has been done above. Many approximating assumptions enter, and several competing effects have to be assumed to be negligible before it becomes possible to extract K_0-values from the measured values of σ_c and $\langle M_\gamma \rangle$.

If the dominating statistical components are indeed those stemming from projections of the total angular momentum on the separation axis as assumed, then there has to be a unique connection between the excess gamma ray multiplicities and the angular distributions. The two types of measurements should lead to the same value of K_0 and of $\mathcal{J}_0/\mathcal{J}_{eff}$.

The accuracy of the measured double-differential cross sections, $d^2\sigma/dAd\Theta_{cm}$, described here and the limitation in angular acceptance, which leaves out the smaller angles -crucial in this context- makes it unrealistic to perform a consistency test on the basis of the angular distribution measurements made with the ring counter. Very recently, however, high precision angular distribution measurements, of systems very similar to those dealt with here, have been reported[26]. Those systems are slightly more asymmetric in the entrance channel, being based on a ^{32}S-beam, but they lead to the same range of composite nuclei. Table 3 is a comparison of the two, very different, determinations of $\mathcal{J}_0/\mathcal{J}_{eff}$. The agreement found here gives strong support to our interpretation of the excess gamma ray multiplicities. (A more stringent theoretical analysis than the one based on eqs. (35) and (38) would nevertheless be desirable).

It is worth noticing, that the determination of K_0 values and of $\mathcal{J}_0/\mathcal{J}_{eff}$ with the aid of angular distribution measurements requires that the fusion-fission reaction is slow enough to allow the system to rotate

many times as it decays. A similar limitation does not apply to the gamma ray multiplicity method. Here, the limiting time is the one required to reach a statistical K-distribution, and that time may be quite short, since an equilibration of this type has been invoked in connection with the fast, strongly damped scattering reactions[21,22].

TABLE 3

Comparison of values of the effective moment of inertia

System	(Z^2/A)	Reciprocal effective moment of inertia $\mathcal{J}_0/\mathcal{J}_{eff}$		
		Experiment		Theory for a non-rotating saddle ref.[8]
		from $\langle M_\gamma \rangle$, this work	from W(0) ref.[26]	
$^{208}Pb + ^{26}Mg$	37.8	0.92		0.98
$^{208}Pb + ^{27}Al$	38.4	0.83		0.92
$^{32}S + ^{197}Au$	39.4		0.89	0.87
$^{208}Pb + ^{48}Ca$	40.6	0.79		0.63
$^{208}Pb + ^{50}Ti$	41.9	0.52		0.52
$^{32}S + ^{232}Th$	42.6		0.38	0.41
$^{208}Pb + ^{52}Cr$	43.2	0.42		0.39
$^{32}S + ^{238}U$	43.2		0.27	0.34
$^{208}Pb + ^{58}Fe$	43.8	0.35		0.30
$^{208}Pb + ^{64}Ni$	44.5	$\approx$ 0.3		0.23
$^{32}S + ^{248}Cm$	44.8		0.36	0.17

The values of (Z^2/A) are those appropriate to the fused systems, listed in the first column. The theoretical values of $\mathcal{J}_0/\mathcal{J}_{eff}$ have been calculated for the corresponding fissility parameters $X = (Z^2/A)\left[50.883(I-1.7826\ I^2)\right]^{-1}$ with $I = (N-Z)/A$.

F. Summary. The evolution in shape from conditional saddle to true saddle.

In this section we have seen that the systematic measurements of gamma ray multiplicities, supported by angular distribution measurements, allow us to get a good look into the black box, fig.1 . The emission of an unexpected excess of gamma rays that increases with the fissility of the total system, brings us a message from the most compact stages of the dynamical evolution from entrance to final separation. Once the two nuclei have made their way behind the conditional saddle of entrance channel they merge very intimately together. They may or may not form a single sphere. We don't know. What we do know is that they become at least as compact as the liquid drop saddle shapes of non-rotating nuclei. For the heavier systems these shapes are much more compact than two touching spheres. They are also more compact than the conditional saddle configuration, being quite close to the shape of a single sphere.

V. FROM ENTRANCE TO EXIT CHANNEL: THE PRE-SCISSION STAGE

The binary coincidence measurements also say something about the final stage of the symmetric fragmentation reaction, i.e. the motion from saddle to scission. In ordinary fission, the total kinetic energy (TKE) of the fragments is to a large extent, if not entirely, due to the Coulomb repulsion acting between the two fragments after they have separated. One finds[16] that this energy is about 30% smaller than the Coulomb energy of two charged spheres in contact, so one concludes that the two pieces are drawn out quite a bit before they part company. If they have a non-zero velocity at scission, they have to be drawn out even more, since now only part of the TKE can be ascribed to the unescapable Coulomb repulsion after scission. There is also a characteristic spread in kinetic energy around the must probable value, which presumably reflects a spread in the degree to which the two fragments are drawn out as the neck between them snaps.

This is the picture we have of the motion from saddle to scission in ordinary compound nucleus fission. Also the deep inelastic reactions show tendencies for the total kinetic energies to become smaller than the Coulomb energy for spheres in contact. So presumably it is the very last stages before scission that matter, not the motion just beyond the saddle.

In figure 20 the total kinetic energies measured with the ring counter are compared to: a) the Coulomb energies of two spheres in contact; and b) the Coulomb energies of two touching fragments with deformations as found in the fission processes[16]. The ridge of the measured distribution around symmetry clearly agrees with case (b), as

we would expect. Thus for the symmetric fragmentation, full equilibration in energy seems to be reached.

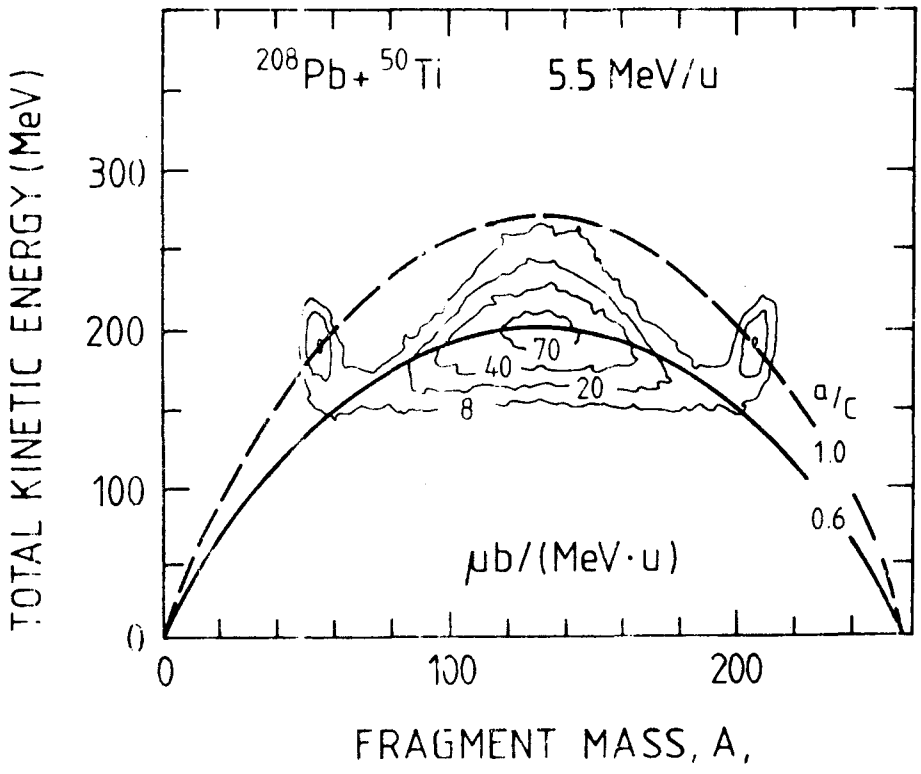

Figure 20:

Measured double differential cross section dσ/dAdTKE shown as a function of mass and TKE. The full line indicates the fragmentation energies derived from fission systematics[16]; the dashed line indicates Coulomb energies of two touching spheres.

Not only does the mean value but also the FWHM of the TKE distribution, Γ_{TKE}, agrees with standard fission measurements. This is demonstrated in figure 21 where the measured Γ_{TKE}-values for each reaction are plotted as a function of the excitation energy in the

corresponding compound nucleus. The data show a monotonic increase of Γ_{TKE} with excitation energy and with target mass: an extrapolation to zero excitation energy gives Γ_{TKE} values, which agree with the standard fission data[25] as indicated on the left hand side of the figure.

All in all these results are no great surprise, but they do offer one more look into the black box , fig.1; revealing something about the dynamics during an important part of the reaction process.

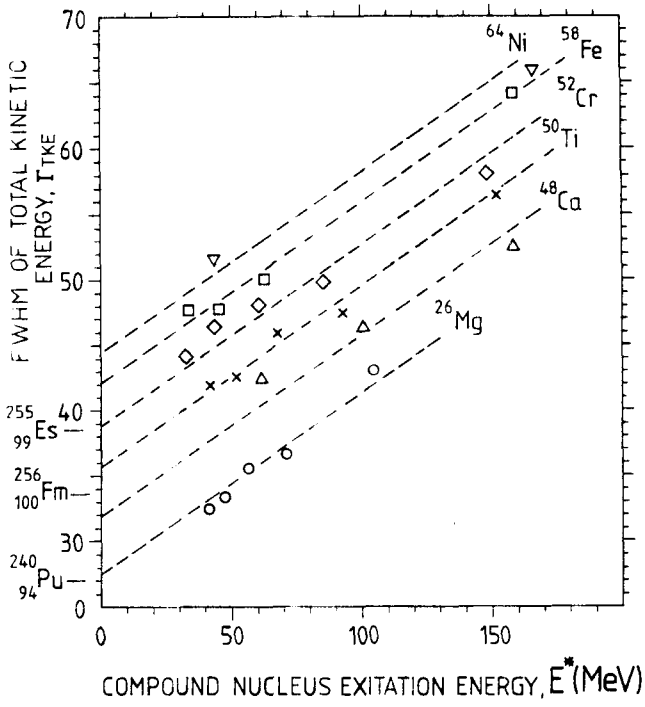

Figure 21:

Full width half maximum of the total kinetic energy distributions for the symmetric fragmentation component, fig.20, (A/2±20 amu) shown as a function of the excitation energy E* in the corresponding compound nucleus. The width increases monotonically with the mass of the composite system. The dashed lines are drawn through the data points by assuming that the slope is the same for all systems investigated. The values extrapolated to zero excitation energy are compared to the one known from ordinary fission[27].

VI. FROM ENTRANCE TO EXIT CHANNEL: ANGULAR DISTRIBUTIONS AND TOTAL REACTION TIMES

If the total kinetic energy measurements are no great surprise, the angular distribution measurements certainly are. They are shown in figure 22.

As mentioned in the introduction, a basic difference between scattering reactions and capture (or fusion) reactions is the different time scales involved. This is well illustrated by fig.22 , where the symmetric and nearly symmetric mass yields seem generally to be evenly distributed in angle, corresponding to decay after many revolutions. By contrast, the target and projectile-like fragments are focussed near the grazing angle and have been in contact only during a fraction of a revolution. The difference is pronounced for the lighter targets but it becomes less pronounced for system like ^{52}Cr and ^{58}Fe plus ^{208}Pb. Apparently, the symmetric fragmentation reaction, with its dramatic redistribution of mass between the reaction partners, can sometimes take place in less time than required for a revolution by 180°.

Figure 22:

Double differential cross section $d^2\sigma/(dA.d\Theta)$ of the same binary products as in fig.8, as a function of the center of mass scattering angle and of the fragment mass.

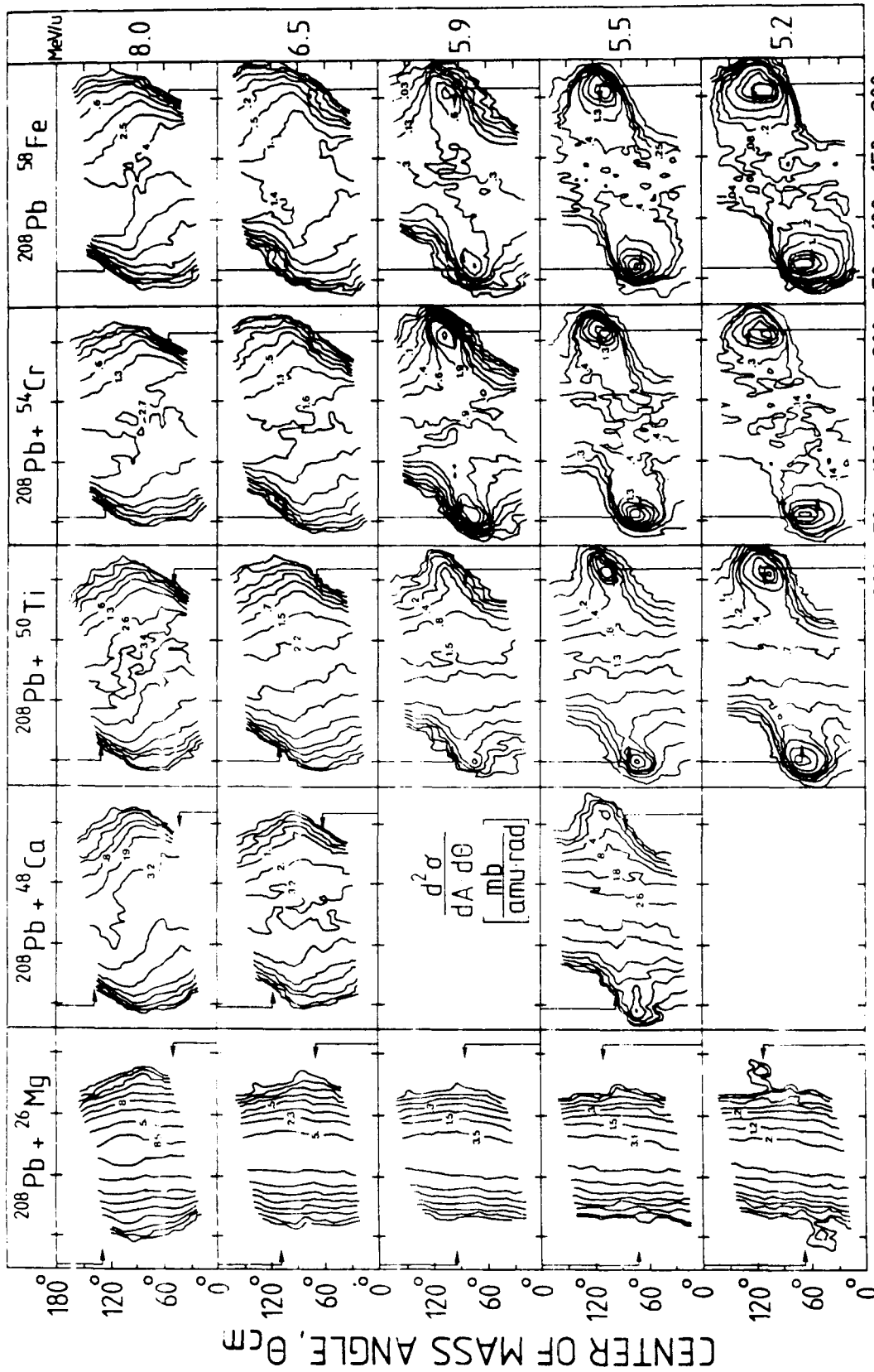
$^{208}Pb + ^{26}Mg$
$^{208}Pb + ^{48}Ca$
$^{208}Pb + ^{50}Ti$
$^{208}Pb + ^{54}Cr$
^{208}Pb ^{58}Fe
MeV/u
8.0
6.5
5.9
5.5
5.2
$\frac{d^2\sigma}{dA\,d\theta}$ $\left[\frac{mb}{amu \cdot rad}\right]$
CENTER OF MASS ANGLE, θ_{cm}
FRAGMENT MASS, A,

Figure 23 focuses the attention on such an example. The cross section under the angle -and energy- integrated symmetric peak corresponds to a cut-off ℓ_c-value of 52 $\hbar$, or an average value $\langle \ell_c \rangle$ = 34 $\hbar$. The system appears to decay before reaching the forward angles. An average deflection of about 120° away from the angle, where a Rutherford trajectory would have placed it, seems a good estimate. With reference to figure 24, the reaction time τ can be estimated according to

$$\langle \tau \rangle = \frac{\langle \Theta \rangle}{\langle \ell_c \rangle} \cdot \langle J \rangle = 12.5 \cdot \frac{\langle \Theta \rangle}{\langle \ell_c \rangle} \cdot \frac{\langle J \rangle}{J_0} \cdot 10^{-21} \text{ sec} \qquad (39)$$

with the numerical constant being the one appropriate for the $^{58}Fe+^{208}Pb$ system. There remains the estimate of $(\langle \mathcal{J} \rangle / \mathcal{J}_0)$, the average relative moment of inertia during the process. Most of the reaction time is presumably spent near the exit point (fig.19), where according to table 3, $J_0/\mathcal{J}_{eff} = J \ (1/\mathcal{J}_1 - 1/\mathcal{J})$ is 0.36 . This corresponds to a value $\mathcal{J}_1 = 1.15\ \mathcal{J}_0$, according to ref.[8]. The remaining time is likely to be spent at larger separations, where $\mathcal{J}$ may approach and even briefly exceed the value $2.2 \cdot \mathcal{J}_0$, appropriate to two spheres in contact. A reasonable weighted average is probably near $\mathcal{J}/\mathcal{J}_0 = 1.3$. According to eq.(39) the resulting average reaction time is then

$$\langle \tau \rangle = 9 \times 10^{-21} \text{ sec} \qquad (40)$$

This is the total time for both coalescence and reseparation. The colaescence time itself that is characteristic for fusion processes in general has to be even shorter. The large differences in time scales for the various reactions appearing in fig.22 may well be due to differences in decay, or resepartion, of the systems; some possessing a fission barrier, others not. It is quite likely that the limit on the coalescence

time, or fusion time, established above has rather general validity.

It is also interesting to note that the total reaction times calculated by Swiatecki, seccion III and ref.[11] , for mass equilibration reactions requiring an extra push between 7 and 70 MeV, ranges from 3×10^{-21}s to 12×10^{-21}s for system similar to those studied here. In the theoretical calculation, the time seems to depend on the magnitude of the extra push. A value near to the one given in eq.(40) seem a quite plausible result to expect from the model, when the extra push is 35 MeV as in the experiment.

The time measurements clearly need to be improved with respect to precision and correct assignment of deflection angle, mass value, and angular momentum. But potentially they do seem to offer good opportunities for gaining insight into the type of dissipation that governs large scale nuclear dynamics. It is already considerable step forward that we can say at least something about the time our systems spends in the black box, fig.1 .

Figure 23:

The $^{208}Pb + ^{58}Fe$ reaction at 5.9 MeV/u, presented in detail. Upper part shows the double differential cross section $d^2\sigma/dAd\Theta_{cm}$ as in fig.22, The open dots indicate the limits of the detection system for fully relaxed events. Center part shows the directly projected mass spectrum after integration over TKE and Θ_{cm}. The bell shaped symmetric fragmentation yield results from the integration over the accesible angles of the double differential cross section of the upper part. Lower part gives the dependence of the average gamma-multiplicity on the product mass. The open dots refer to fully relaxed events only, while the filled dots correspond to all binary events registered by the ring counter.

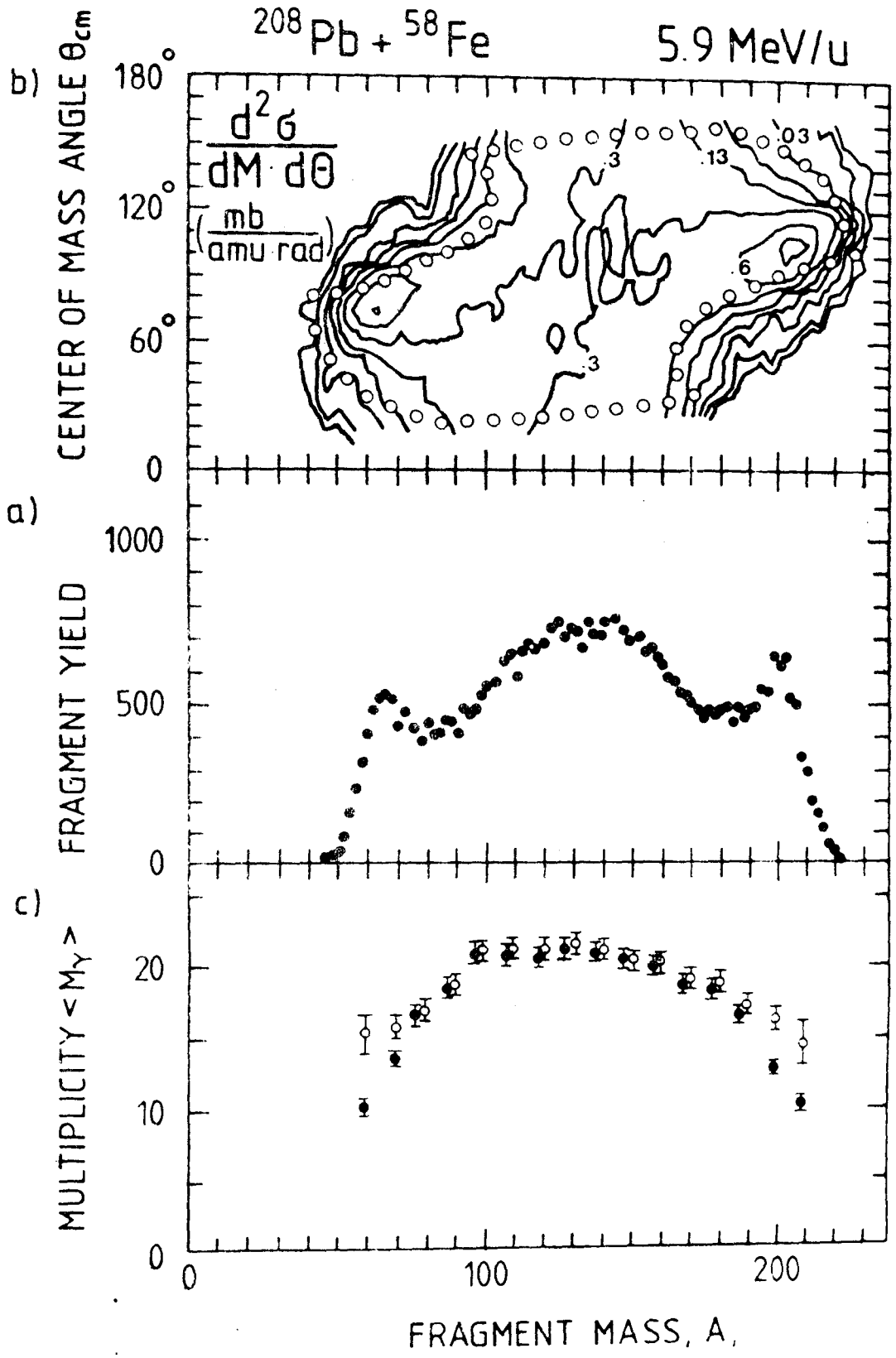
b)
$^{208}Pb + ^{58}Fe$
5.9 MeV/u
$\frac{d^2\sigma}{dM\,d\theta}$
$\left(\frac{mb}{amu\,rad}\right)$
.03
.13
.3
.3
.6
180°
120°
60°
0
CENTER OF MASS ANGLE θ_{cm}
a)
1000
500
0
FRAGMENT YIELD
c)
20
10
0
MULTIPLICITY $< M_\gamma >$
0
100
200
FRAGMENT MASS, A,

VII. SUMMARY AND CONCLUSION

The experiments and the theoretical models discussed here essentially serve to bring fusion reaction studies into focus as means of exploring the dynamical aspects of large scale motion in nuclear matter. Before, fusion seemed only to yield essential information about the static interaction between two nuclei with frozen shapes, whereas the dynamics was explored with the aid of the deep inelastic scattering process (and fission). But fusion involves a more far reaching rearrangement of the two nucleonic systems in contact, so there are good reason to expect that dynamical fusion reaction studies will match if not surpass deep inelastic scattering studies as a source of information about large amplitude nuclear dynamics.

The model we have used assumes friction in the specific form of one-body dissipation to play a decisive role. Two very interesting questions to be explored are how well this model can account in a quantitative way for the measurements, and to what precision it will be possible to develop this type of measurement. Other dynamical models (time dependent Hartree Fock, semiclassical models stressing the shape degrees of freedom, macroscopic friction models, transport theories, etc.) may give different answers. How different no one knows, and there is a danger that they may all fit the experiment with its present lack of high precision. So better experiments are sure to be essential.

For those who attempt to synthesize superheavy elements, advances in understanding more precisely the neccessary conditions for obtaining complete fusion of target and projectile are also of great interest.

REFERENCES:

1) R.Bock (ed.) Heavy Ion Collisions, Vols. I and II, North Holland Publ. Co., Amsterdam, New York, Oxford, 1979.

2) J.Blocki, J.Randrup, W.J.Swiatecki, and C.F.Tsang, Ann. Phys. (N.Y.) 105(1977)427.

3) J.Randrup, Ann. Phys. (N.Y.) 112(1979)356.

4) R.Bass, Phys. Rev. Lett. 39(1977)265.

5) J.R.Birkelund, L.E.Tubbs, J.R.Huizenga, J.N.De and D.Sperber, Phys. Rep. 56(1979)107.

6) B.Heusch, C.Volant, H.Freiesleben, R.P.Chestnut, K.D.Hildenbrand, F.Pühlhofer, W.F.W.Schneider, B.Kohlenmeyer, and W.Pfeffer, Z.Phys. A288(1978)391.

7) C.Lebrun, F.Hanappe, J.F.Lecolley, F.Lefebvres, C.Ngo, J.Péter, and B.Tamain, Nucl. Phys. A312(1979)207.

8) S.Cohen, F.Plasil, and W.J.Swiatecki, Ann. Phys. (N.Y.) 82(1974)557.

9) R.Bock, Y.T.Chu, A.Gobbi, A.Olmi, H.Sann, U.Lynen, W.Müller, S.Bjørnholm, and H.Esbensen, submitted to Phys. Rev. Lett., 1981.

10) R.Bock, Y.T.Chu, M.Dakowski, A.Gobbi, E.Grosse, A.Olmi, H.Sann, D.Schwalm, U.Lynen, W.Müller, S.Bjørnholm, H.Esbensen, W.Wölfli, and E.Morenzoni, sumbitted to Nucl. Phys., 1981.

11) W.J.Swiatecki, Proceedings of Nobel Symposium on Nuclei at Very High Spin, Phys. Scripta, 1981, and Lawrence Berkeley Laboratory, Preprint LBL-10911, 1980.

12) R.Bass, Nucl. Phys. A231(1974)45.

13) R.G.Stokstad, W.Reisdorf, K.D.Hildenbrand, J.V.Kratz, G.Wirth, R.Lucas, and J.Poitou, Z. Physik, A295(1980)269.

14) H.Esbensen, Nucl. Phys. A352(1981)147.

15) J.V.Kratz, A.E.Norris and G.T.Seaborg, Phys. Rev. Lett. 33 (1974)502.

16) V.E.Viola, Nucl. Data Sect. A1(1966)391.

17) N.Bohr and J.A.Wheeler, Phys. Rev. 56(1939)429.

18) W.J.Swiatecki, Lawrence Berkeley Laboratory Report, Preprint LBL-12642, Berkeley, 1981.

19) C.C.Sahm, D.Vermeulen, H.G.Clerc, J.Keller, H.Schulte, K.H.Schmidt, P.Armbruster, F.Hessberger, G.Münzenberg, and W.Reisdorf; Proceedings of IXth Workshop on Gross Properties of Nuclei and Nuclear Excitations, Hirschegg, Austria, 1981.

20) D.L.Hillis, J.D.Garrett, O.Christensen, B.Fernández, G.B.Hagmann, B.Herskind, B.B.Back and F.Folkmann, Nucl. Phys. A325(1979)216.

21) G.Wolschin, and W.Nörenberg, Phys. Rev. Lett. 41(1978)691.

22) B.B.Back and S.Bjørnholm, Nucl. Phys. A302(1978)343.

23) D.v.Harrach, P.Glässel, Y.Civelekoglu, R.Männer, and H.J.Specht, Phys. Rev. Lett. 42(1979)1728.

24) I.Halpern and V.M.Strutinsky, Int. Conf. peaceful uses of atomic energy, Geneva, Vol. 15 (UN, NY, 1958, p.408).

25) R.Vandenbosch, and J.R.Huizenga, Nuclear Fission (1973), Academic Press, New York.

26) B.B.Back, H.G.Clerc, R.R.Betts, B.G.Glagola, and B.D.Wilkins, Phys. Rev. Lett. , to appear 1981.

27) J.P.Unik, J.E.Gindler, L.E.Glendenning, K.F.Flynn, A.Gorski, and R.K.Sjoblom, Proceedings of the Third IAEA Symposium on the Phys. and Chem. of Fission, Rochester, IAEA, Vienna, 1974, Vol. 1, p. 174.

NUCLEI AT VERY HIGH ANGULAR MOMENTUM

S.BJORNHOLM

NIELS BOHR INSTITUTE, UNIVERSITY OF COPENHAGEN
DK-2100 DENMARK.

I. INTRODUCTION. NUCLEAR STRUCTURE UNDER ROTATION.

A. Shape changes

No experimental attempt of making a nucleus rotate with more than 80 units of angular momentum has ever been succesful. This is understood on the basis of the liquid drop model. The nucleus is simply drawn into two pieces by the centrifugal force when the angular momentum approaches 80 $\hbar$ (or even less for very light or very heavy nuclei[1]).

At lower angular momenta the nucleus can be stable, except against gamma-decay, which is a relatively slow process. Experiments with rotating nuclei in fact open a new dimension in the study of nuclear structure[2], and it is certain that dramatic structural changes will take place; because in the end the rotation leads to fission. Figure 1 shows the characteristic shape changes expected on the basis of the liquid drop model for a medium mass nucleus[1].

For non-rotating nuclei we know that shell effects profoundly modify the liquid drop average picture, leading sometimes to prolate equilibrium shapes. The new challenge to nuclear structure experiments is essentially to explore this interplay of average and specific structural properties further, pushing into the region of nuclei under extreme rotation[2].

The theoretical calculation shown in figure 2 illustrates this. The ground state of ^{160}Yb is prolate because of shell effects. But for spin values 50-70 $\hbar$, the shape becomes oblate, as prescribed for a pure liquid drop without shell structure[3].

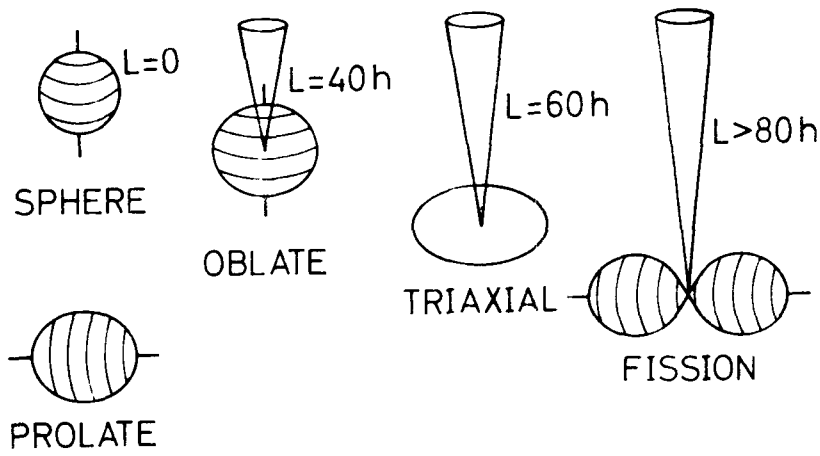

Figure 1:

Schematic illustration of the shape changes in a rigidly rotating nucleus. The axially symmetric, prolate shapes known to exist at low values of angular momentum are not predicted by the liquid drop calculations. They are the result of shell structure.

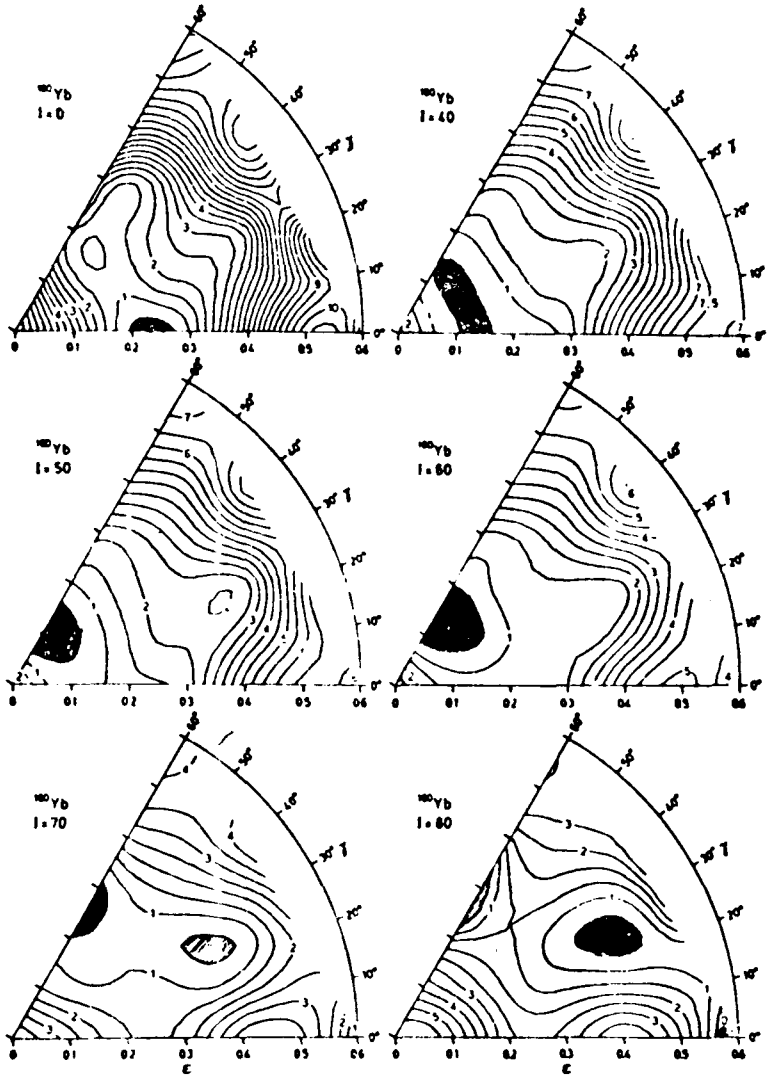

Figure 2:

Potential energy surfaces for six values of angular momentum as a function of a selected two-dimensional class of shapes. The sphere corresponds to $\varepsilon = 0$, and the horizontal axis represents axially symmetric prolate shapes of increasing elongation, rotating around an axis perpendicular to the symmetry axis. The $\gamma = 60^{\circ}$ line represents oblate shapes rotating around the oblate symmetry axis, whereas the area between the two lines corresponds to triaxial nuclei rotating with the largest possible moment-of-inertia. Energy minima are cross-hatched, from ref. 3).

B. Rotation and symmetry

Understanding in detail how the nuclear fermion system will most economically accomodate high angular momenta is by no means trivial. It is already knwon that this depends crucially on symmetry type[4], see figure 3. Prolate nuclei will rotate around an axis perpendicular to the symmetry axis. Angular momentum is carried by the nucleus as a whole, and its rotation frequency is observable as (one half) the frequency of the strongly enhanced E2 radiation. Conversely, in spherical nuclei the angular momentum is carried by one or a few of the valence nucleons through alignment of their individual angular momenta. The energy required for this is a sum of single-particle excitation energies. The radiation emitted is governed by erratically varying and generally small single-particle matrix elements. The essentiall difference from the prolate case is that the angular momentum is parallel to an axis of rotational symmetry. This is also most likely to be the situation with oblate shapes.

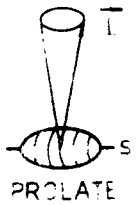

PROLATE

$\bar{I} = \omega \bar{J}$ COLLECTIVE

$E(I) = \frac{I(I+1)\hbar^2}{2J}$ E2-RADIATION

SPHERE

$\bar{I} = \sum \bar{j}_i$ SINGLE-PARTICLE

$E(I) = E_0$ RADIATION

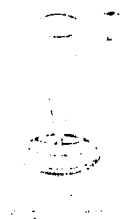

AB SPHERE

Figure 3:

The quantum mechanical description of "rotating" systems will be fundamentally different, depending on whether the rotation axis is parallel to an axis of rotational symmetry or not, see text.

These distinctions are clearly reflected in the observations. Figure 4 compares the nice regular rotational E2-spectrum of the prolate ^{160}Gd-nucleus to the totally irregular spectrum of single-particle transitions along the yrast line of the spherical nucleus ^{154}Er. Similarly, figure 5 illustrates how utterly different the life-times for transitions along the yrast line are in the two cases.

The remainder of this paper should give an impression of the experimental advances towards an understanding of how they change shape as they rotate more and more vigorously.

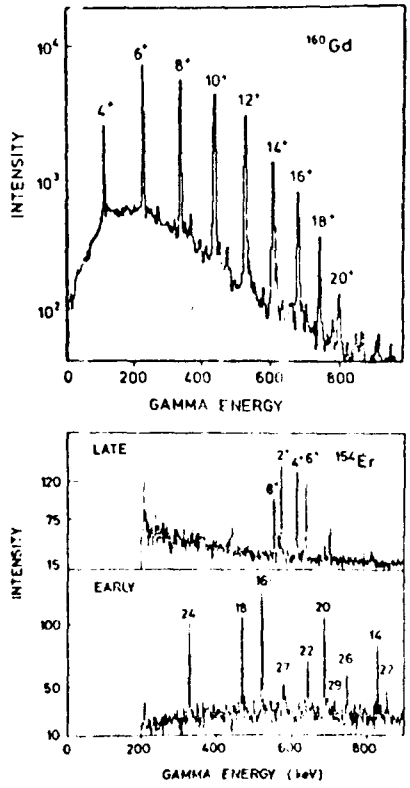

Figure 4:

Gamma spectra from stepwise de-excitation along the yrast line (cf. fig.11) measured with a Ge(Li)-detector. The number at each peak indicates the spin and parity of the gamma emitting stae. Top: Yrast spectrum of the prolate rotor nucleus ^{160}Gd, ref.5). Below: Yrast spectrum of the shell-model nucleus ^{154}Er, ref.6). This spectrum consists of two sequences of gamma-rays, separated by a time delay of 10 ns, which is the half life of the I=10 state (cf. fig.5).

II. SHELL MODEL NUCLEI

A. Yrast traps

Figure 5 illustrates how high-spin states produced by alignment of the spins of a few valence nucleons may have much longer half lives than the 0.1-1.0 ps that is typical of a good rotor nucleus. Extensive searches for high-spin isomers produced in heavy-ion reactions with life-times in excess of 1000 ps reveal that such "yrast traps" are confined to regions just above a spherical shell closure[9], see figure 6.

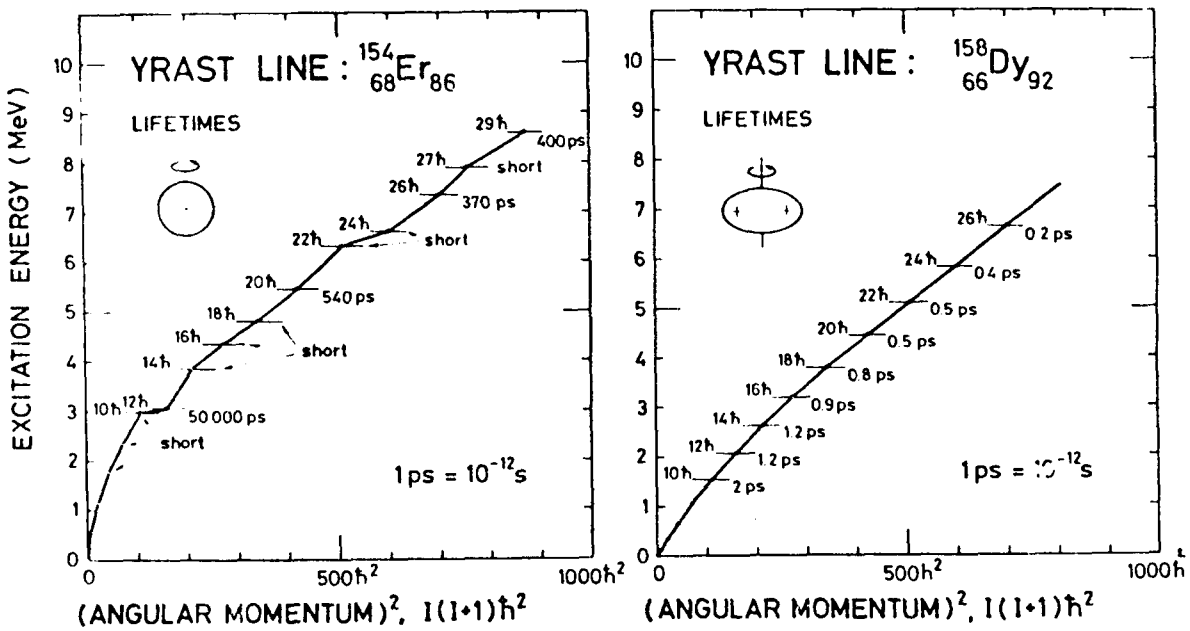

Figure 5:

Lifetimes of yrast states. Left: the shell-model nucleus ^{154}Er, ref.7). Right: the rotor nucleus ^{158}Dy, ref.8).

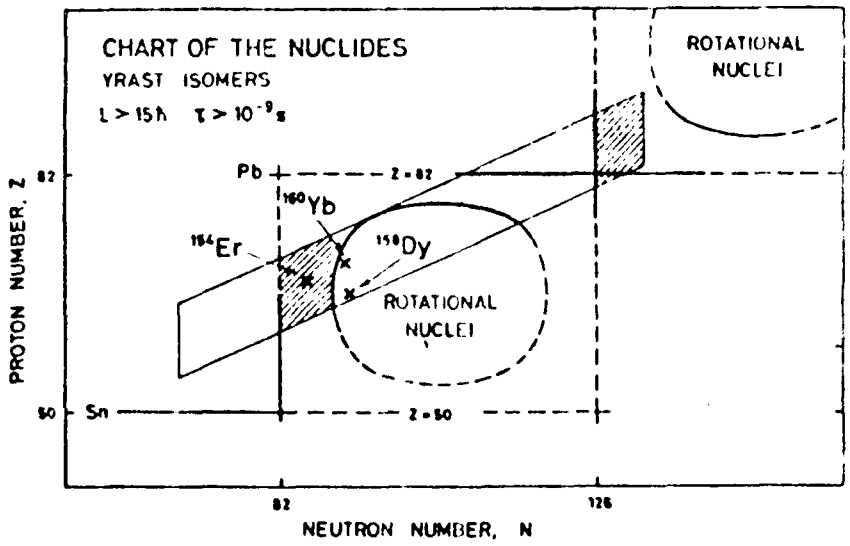

Figure 6:

Nuclei situated in the oblique window indicated on the chart have been produced in heavy-ion reactions and systematically scanned for the occurrence of high spin isomers among thedecay products[9,10]. Only the hatched areas showed positive results. The high spin isomers above ^{208}Pb have been identified and studied especially by groups in Stockholm and Chalk River.

The prolate tc oblate transition predicted according to figure 2 could not be confirmed experimetally through the appearance of a strongly populated high-spin isomer in the otherwise forbidden region of prolate rotor nuclei[9,10]. This result does not exclude such a shape transition; it just says that the oblate yrast states -if they exist- are decaying fast compared to the 1000 ps limit set by the experiment. But there could still be an isomer in the sense that the decay could be slow compared to 0.1-1 ps, which is typical for prolate nuclei (cf. fig.5).

The island just above N=82 is under intensive investigation. The Jülich group[11] has shown in data how a number of yrast staes of spin up to ~25 ħ can be described in terms of one to five totally aligned valence nucleons in a spherical shell-model potential.

In general, the situation is not so clear. At present, high-spin isomers with $t_{\frac{1}{2}} \gtrsim 2$ ns have been identified in virtually all nuclei within a sharply defined island above N=82. Isomers occur whenever Z≤68 and N≤86, ref.[12].

By letting these isomers recoil into the center of a large, hollow NaI-crystal and recording the total gamma-ray energy deposited in the crystal as the isomers decay, it has been possible to measure the isomer excitation energies in a crude way. The highest excitation energy was found with ^{152}Er, where two isomers, one on top of the other, have been shown to lie at 8.5 MeV and 12.5 MeV, with half lives 30 ns and 5 ns, respectively[10,12].

The higher the energy, the higher the spin of such isomers. It has been found that a plot of the energy of known yrast states of nuclei in this vicinity versus $I(I+1)A^{-5/3}$ converges as the spin value increases beyond fifteen, provided the energies are plotted relative to the average droplet energy[12]. With the aid of such a plot, the unknown spin value can be estimated from the excitation energy. For ^{152}Er a value of I~34 ħ is derived for the isomer at ~12.5 MeV.

In a subsequent experiment it has been possible to measure the spectrum of gamma-rays that feed intyo this high-spin state from above, cf. figure 7. Pressumably this spectrum will consist of a number of so called statistical gamma-rays, reflecting heat radiation from states high above the yrast line, followed by a series of interwoven yrast cascades of dipole and quadrupole transitions along and slightly above the yrast line. The quadrupole transitions, being able to jump two units

of spin, will tend to have twice as high energy as the (I=1) dipole transitions.

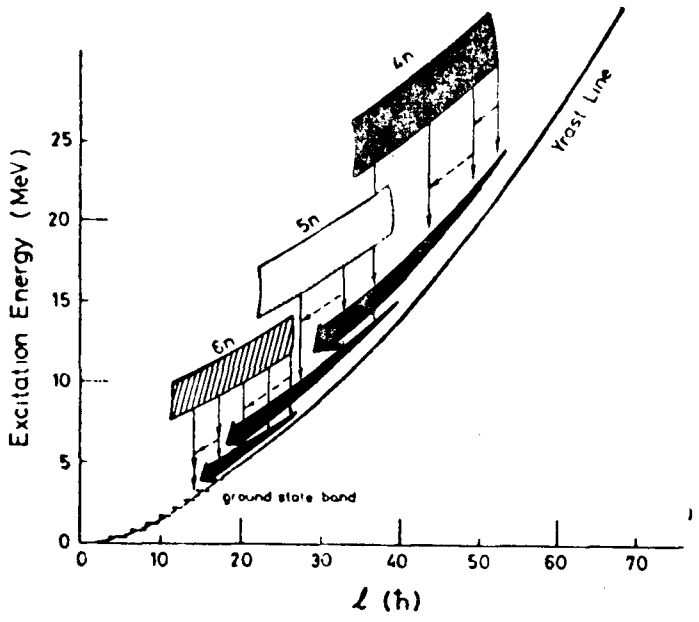

Figure 7

Gamma-ray de-excitation routes following a heavy-ion reaction[13]. At spins higher than 15-25 ħ the gamma cascades along the yrast line appear to follow so many parallel cascades that it becomes virtually impossible to distinguish individual lines in the spectra. This is the case in deformed nuclei at least, where the radiation is made up to E2-transitions. For spherical and oblate nuclei, the yrast cascades could be a mixture of dipole and quadrupole transitions, relatively few in number.

The spectrum, measured with a big NaI-crystal at a large distance from the target is shown on figure 8. It has been corrected for Compton effects and in this way simulates the spectrum of an idealized detector with 100% photo efficiency. As expected, there is a Planck-like radiation spectrum extending exponentially to the highest energies. At lower energies there is additional intensity. An interpretation of this in form of the dipole and quadrupole yrast transitions (fig.7) seems quite plausible. It should be noted that if the ^{152}Er nulceus had developed a prolate deformation as spins just above 34 ħ, then the lower energy, i.e. dipole part of the spectrum of feeding transitions would be

absent; because a prolate nucleus invariably decays by quadrupole and not by dipole radiation once it has reached energies near the yrast line.

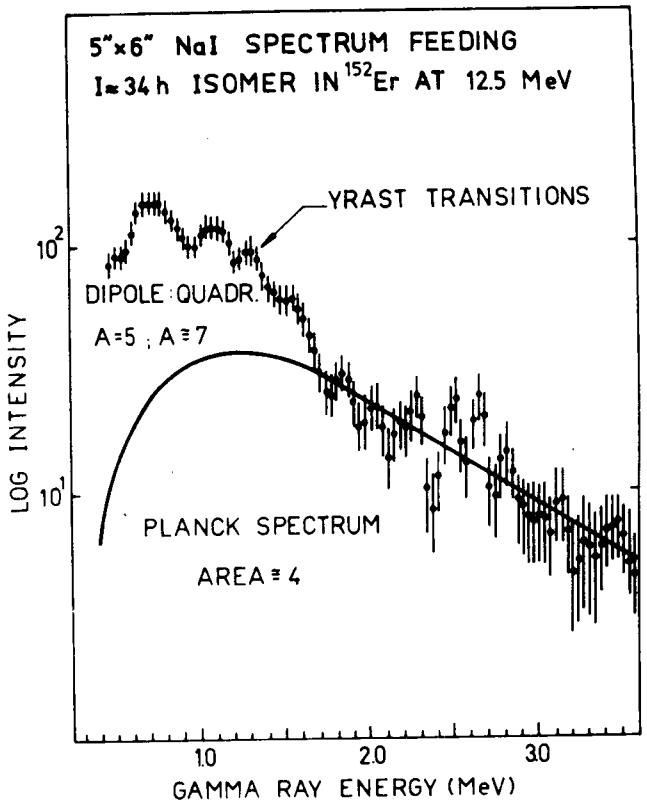

Figure 8:

Low-resolution (NaI) gamma spectrum of transitions feeding the I 34 h isomer of ^{152}Er in the ^{108}Pb(^{48}Ti,4n) reaction at 230 MeV ^{48}Ti-energy[10]. The events contributing to this spectrum have been singled out from all other events by requiring each accepted event to be in prompt coincidence with the beam burst, and at the same time in delayed coincidence with at least two out of eight other counters surrounding the target. Furthermore, the two delayed counts should occur with a relative delay of about 30 ns between them.

There are many unsolved problems in connection with yrast traps and the radiation associated with these. It remains an open and active field. See also section IV.A. .

B. Yrast energies

It is possible to construct the yrast line from a number of well-studied decay shcemes of shell-model nuclei, produced in heavy ion reactions. The best known examples are ^{152}Dy and ^{154}Er, refs.[14] and [6,7,15], respectively.

Figure 9 compares the yrast line of ^{154}Er to the good prolate rotor ^{158}Dy. For rotor nuclei a linear relationship between the yrast energy and the square of the angular momentum is expected according to figure 3 and eq.(6). The slope of the line is inversely proportional to the moment of inertia. As can be seen from fig.9 , the yrast line of the rotor nucleus at first rises steeply, reflecting the reduced moment of inertia of the superfluid ground state. At higher spins the yrast line follows the slope given by the moment of inertia for a rigid rotor, as one should expect for the collective rotation of a non-superfluid prolate configuration.

This model example of a rigid rotor is compared to ^{154}Er, where the "rotation" is described in terms of alignment of the j-values of just a few valence nucleons. The resulting yrast line is more irregular, but its average slope again coincides with that of a rigid rotor -at least within $\pm$(10-20)%. Although the angular momentum is generated by a negligible fraction of the nucleons, the energy required is just the same as if all the nucleons participated in the motion.

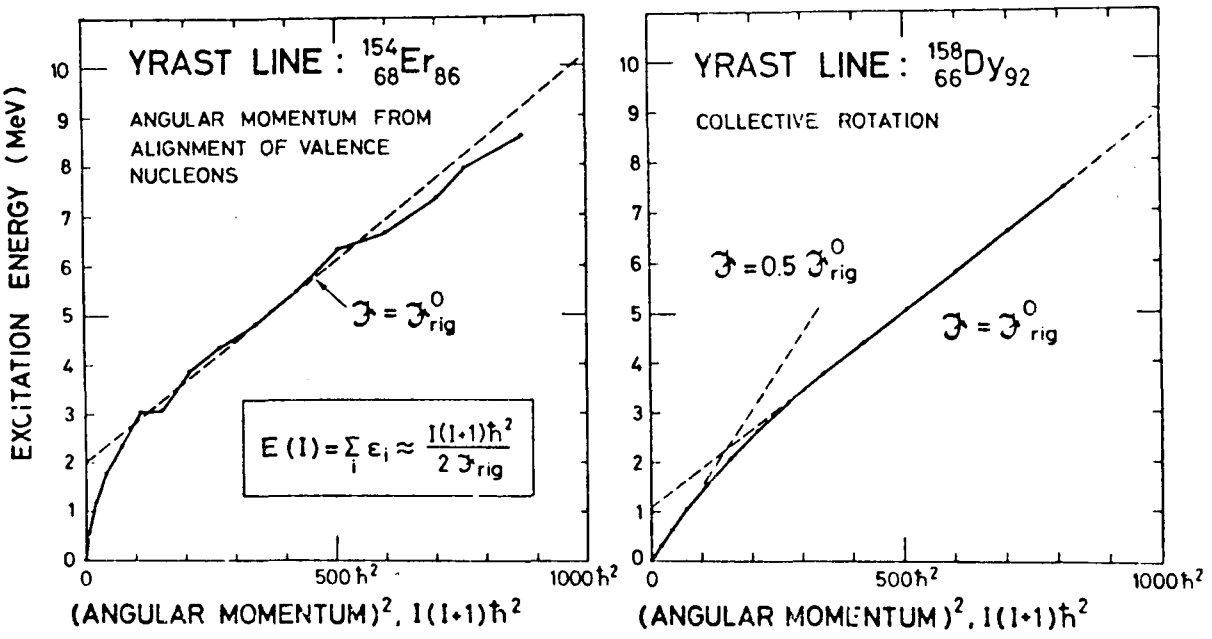

Figure 9:

Comparison of the yrast lines of a shell-model nucleus, ^{154}Er, and a deformed nucleus, ^{158}Dy (ref.[8]).

C. Translation of a fermion system

It is a general feature of fermion systems that the valency particles so to say are able to do all the work required of the system as a whole, in order to produce the result expected classically. Perhaps the following simplified example will help appreciate this.

Suppose a one-dimensional square well with doubly degenerate levels, figure 10. The energy $1/2\ mv^2 \sim N^2$, where N is the quantum

number 1, 2... . The velocity v is then proportional to N, or $v=Nv_0$, where v_0 is the unit of velocity, equal to the velocity in the lowest state with N=1.

One may take the freedom of imagining one particle in each level to be moving left with velocity Nv_0, and the other moving right with velocity Nv_0, (to produce a stationary bound state). The system is now given a translation with velocity v_0. Seen from the moving frame, all the particles keep their velocities relative to the center of mass, which in turn moves with velocity v_0 and C.M. energy:

$$E_{CM} = 2N(1/2\ mv_0^2) \tag{1}$$

since the total mass equals 2 Nm.

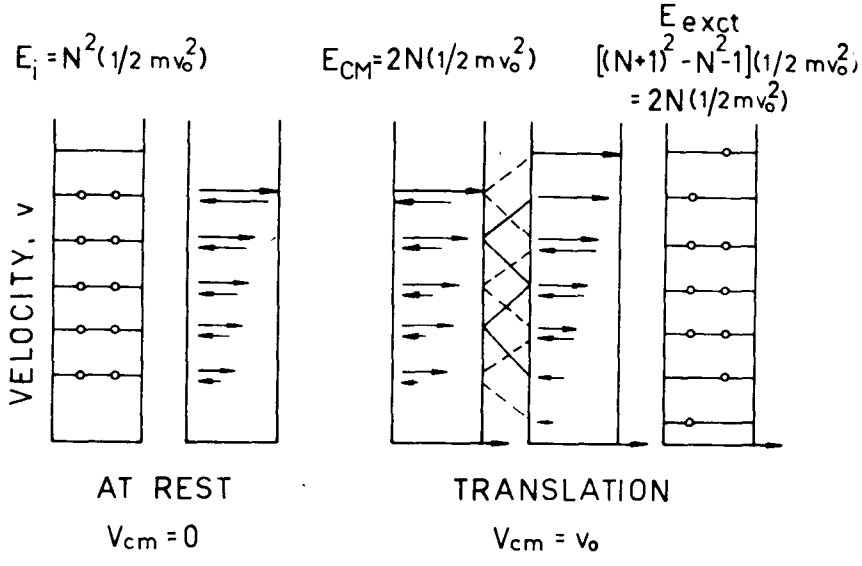

Figure 10:

Translation of a one-dimensional square well, filled with Fermi particles. The translation velocity has been chosen to be equal to the particle velocity in the lowest state.

This is what one expects classically. But one may also look at the velocity distribution of the articles measured in the rest frame. One sees that a reshuffling of particles takes place, but the net result is just a promotion of one particle from the top level N to the (N+1)-level and another from N=1 to N=0. The energy required for this excitation is:

$$E = (N+1)^2(1/2\ mv_0^2)^2 - N^2(1/2\ mv_0^2) - 1(1/2\ mv_0^2)$$

$$= 2N(1/2\ mv_0^2) \qquad (2)$$

In other words, the same result as the picture of a uniform translation, but described in terms of excitation of just two particles.

III. DEFORMED NUCLEI

A. Band structures

In prolate nuclei, rotations used to be described exclusively in terms of collective motion, and one does indeed observe beautiful, regular band structures and spectra. An especially fine example[16] is shown in figure 11. The superfluid ground state is seen to have a higher yrast slope and hence a smaller-than-rigid moment of inertia, as opposed to most of the internally excited band structures. This leads to band crossings.

Figure 11:

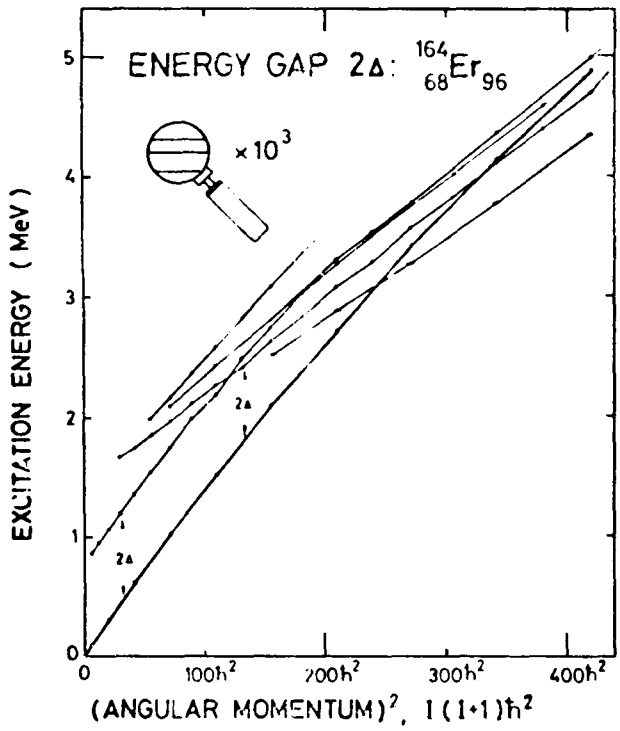

Rotational bands in a typical rotor nucleus, ^{164}Er, ref.[16]. The superfluid ground state band is drawn with a slightly heavier line. The slope of the higher excited bands corresponds approximately to rigid rotation. This mucleus offers an example of gapless superfluidity: for spins above 15 ħ (I(I+1)>225) the energy gap 2Δ between the superfluid ground band and the rigidly rotating, excited bands has disappeared. This figure also illustrates the nature of the yrast line, as the divide between low energy, where no states can exist; and an upper region, where the level density increases steadily.

B. Rotational alignment, backbending

A closer analysis shows these crossings to be a more general phenomenon related to the alignment of single-particle orbitals with the rotation axis[17,18]. This is illustrated in figure 12. It means that also in deformed nuclei are some of the valence nucleons able to

contribute to the build-up of high angular momentum at minimum cost. Here the collective and single-particle motion are sharing the task as opposed shell-model nuclei where a few valence particles are doing the job alone.

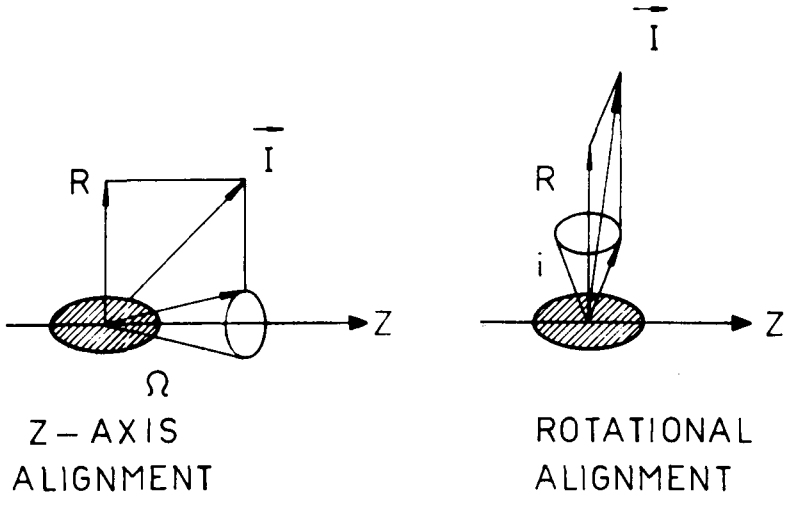

Figure 12:

Schematic illustration showing the difference between alignment of single-particle orbitals along the symmetry axis of the deformed potential (Z-axis), and along the rotation axis (x-axis).

Alignment takes place at a critical angular frequency of the collectively rotating core, and the system jumps into a new configuration with higher total angular momentum, but lower rotation frequency of the core. This new configuration will in turn give rise to a collective rotational band as the rotation frequency of the core increases again. The core frequency is directly observable as one half the frequency of the emitted E2-radiation (except for the inter-band transitions near the crossing between two bands). This is how back-bending comes about.

The tendency for different valence-protones and -neutrons to respond to the rotation of the core by aligning their angular momentum along the rotation axis varies considerably, being most pronounced for orbitals originating from high-j shell-model states.

As described for example, by Frauendorf[19], shell structure enters as an important element into the description of the rotation of deformed nuclei through this mechanism.

C. Aligned-particle spin, i.

Alignment leads to a picture[19,20] of the yrast line consisting of a number of segments, each characterized by increasing collective rotation with a more or less constant contribution, i, from the aligned particles, figure 13. The curvature of each segment is by necessity stronger than the curvature of the envelope of the segments that make up the yrsat line. We are thus dealing with two curvatures, and since the curvature is a measure of the moment of inertia, we are dealing with two moments of intertia $\mathcal{J}_{coll}$ and $\mathcal{J}_{eff}$, respectively.

The band curvature measures $\mathcal{J}_{coll}$:

$$E_{rot} = R^2 \frac{\hbar^2}{2\mathcal{J}_{coll}} = (I-i)^2 \frac{\hbar^2}{2\mathcal{J}_{coll}} \tag{3}$$

$$E_\gamma = 4R \frac{\hbar^2}{2\mathcal{J}_{coll}} = 4(I-i) \frac{\hbar^2}{2\mathcal{J}_{coll}} \tag{4}$$

$$\Delta E_\gamma = 8 \frac{\hbar}{2\mathcal{J}_{coll}} \tag{5}$$

The curvature of the yrast envelope measures $\mathcal{J}_{eff}$:

$$E_{yrast} \approx I^2 \frac{\hbar^2}{2\mathcal{J}_{eff}} \tag{6}$$

$$\langle E_\gamma \rangle \approx 4I \frac{\hbar^2}{2\mathcal{J}_{eff}} \tag{7}$$

$$\Delta\langle E_\gamma \rangle \approx 8 \frac{\hbar^2}{2\mathcal{J}_{eff}} \tag{8}$$

For the lower lying, discrete band structures the quantity $\Delta\langle E_\gamma\rangle$ (eq.8) has little meaning and J_{eff} is derived from eq.(7). Conversely, ΔE_γ in eq.(5), and therefore J_{coll} is oftern well defined. Then eq.(4) can be used to derive R and hence i, assuming that I is known from the experiment.

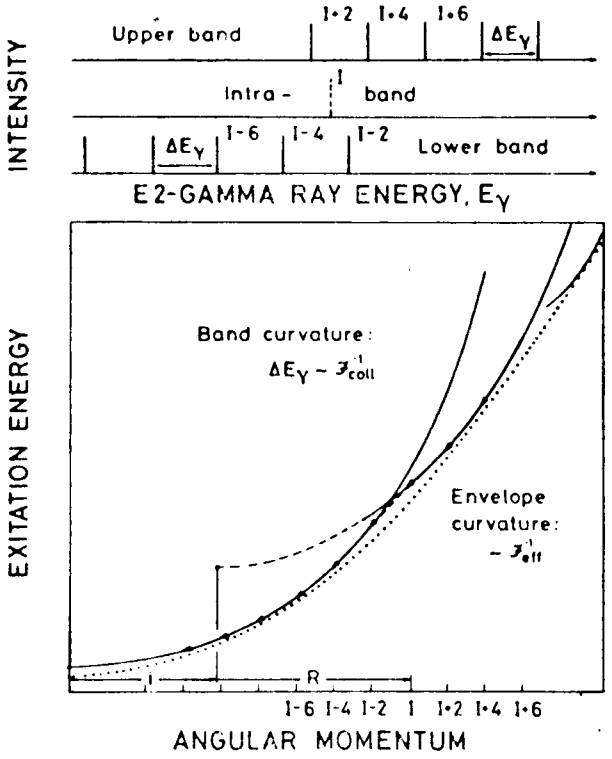

Figure 13:

Schematic illustration of a band crossing (below) leading to the backbending phenomena in the observed spectra (above). Note that the abscissa is I, not I(I+1) as in the previous figures. Heavy arrows indicate gamma transtions in a cascade. The inter-band transition is dashed.

D. Bands in the continuum region

The above description is of particular interest, when one wants to push the experiment towards higher values of angular momentum.

It has been known for a long time that above I~25 it becomes virtually impossible to study the discrete band structures. Above this spin value, the gamma-rays follow so many parallel paths that nothing but continuum spectra without any fine structure information can be observed, fig.7. In spite of this, new, ingenuous experimental techniques have been developed, allowing the two curvatures to be determined separately. A coincidence technique can measure ΔE_γ of eq.(5), i.e. the change in gamma-ray energy along the cascades actually selected in the E2 de-excitation process. This is averaged over all the cascades allowing an average value J_{coll} to be determined from eq.(5). Measurements of singles spectra, on the other hand, can identify how the average E2 gamma-energy $\langle E_\gamma \rangle$ of unrelated cascades increases with increasing total spin, measuring in this way $\Delta \langle E_\gamma \rangle$ of eq.(8) and hence $\langle J_{eff} \rangle$.

Figure 14 illustrates this difference between a coincidence and a sigle measurement.

The two types of measurements could eventually lead to the same experimental result. In a way one should expect that. The gamma-ray cascades sample the "band" structure over a considerable energy interval above the yrast line, where the level density for a given spin value becomes large. This is the only way of understanding the disappearance of discrete lines in the spectra. The persistence of scallop-shaped band structures is equivalente to negligible interactions between close-lying bands of varying internal excitation. It means that the angular momentum, i, contributed by the (aligned) particles will remain constant within the excited band segment. One may question whether such a

separation of the motion is realistic in a region of close-lying levels, compare figure 15.

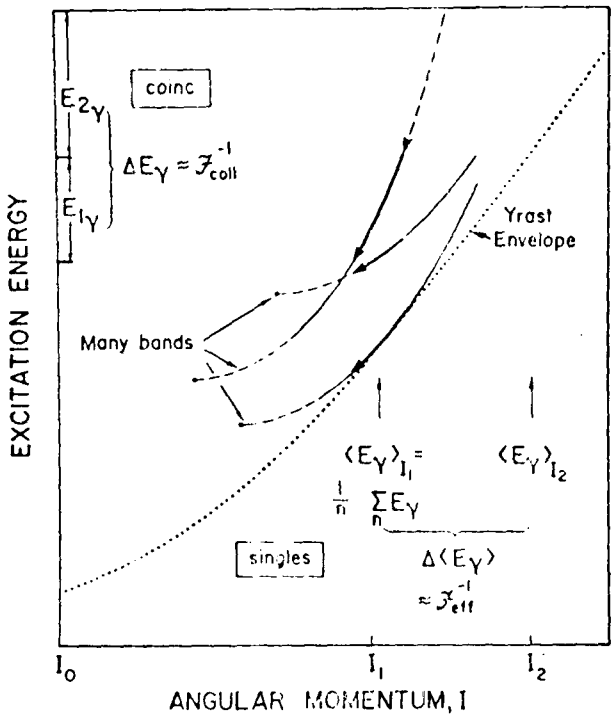

Figure 14:

Schematic illustration of multiband structures in the continuum region. Gamma cascades proceed stepwise along the strongly curved segments. This is the operational definition of a segment, or band. A gamma-gamma coincidence measurement will be sensitive to the increments in gamma-ray energy along the segments. If they all have (nearly) the same curvatures, the increments will everywhere be (nearly) the same, compare fig.18 . A measurement of non-concident gamma-rays connecting states of spin I with states of spin I-2 will give a broad spectrum of transition energies, but the average energy will correspond closely to the slope of the envelope representing the yrast line. This slope can be change in slope measures the curvature of the yrast line, cf. fig.17.

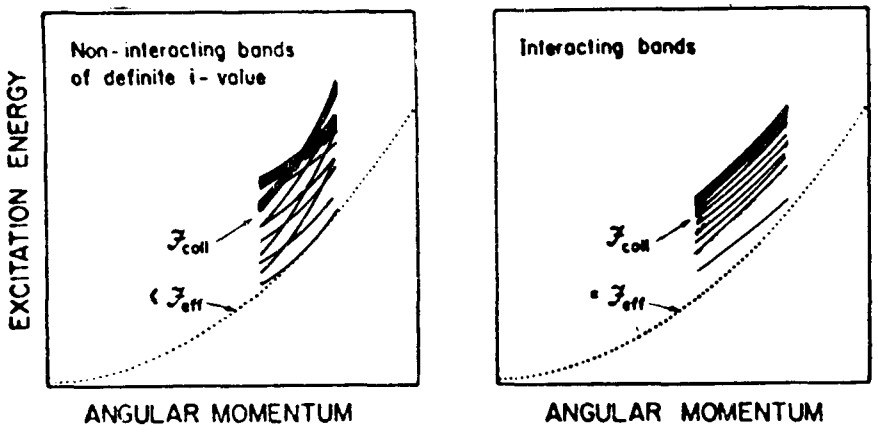

Figure 15:

Two different hipotheses for band structures in the energy region above the yrast line. This energy region is defined as the region actually sampled in the gamma de-excitation process, fig.7. The absence of discrete lines in the spectra indicates that this region must at least comprise twenty bands, possibly thousands.

1. Singles measurementes

The total energy of the complete gamma cascades can be measured by placing the target in the center of a large NaI crystal, leaving a small hole to record the probability of hitting another NaI-detector, placed some distance away, simultaneously. This probability increases the larger the number of gamma-rays in the cascade is, and thus measures the gamma-ray multiplicity, M_γ. Not surprisingly, one finds[21] that the higher the total energy release of the cascade, the larger the multiplicity, figure 16.

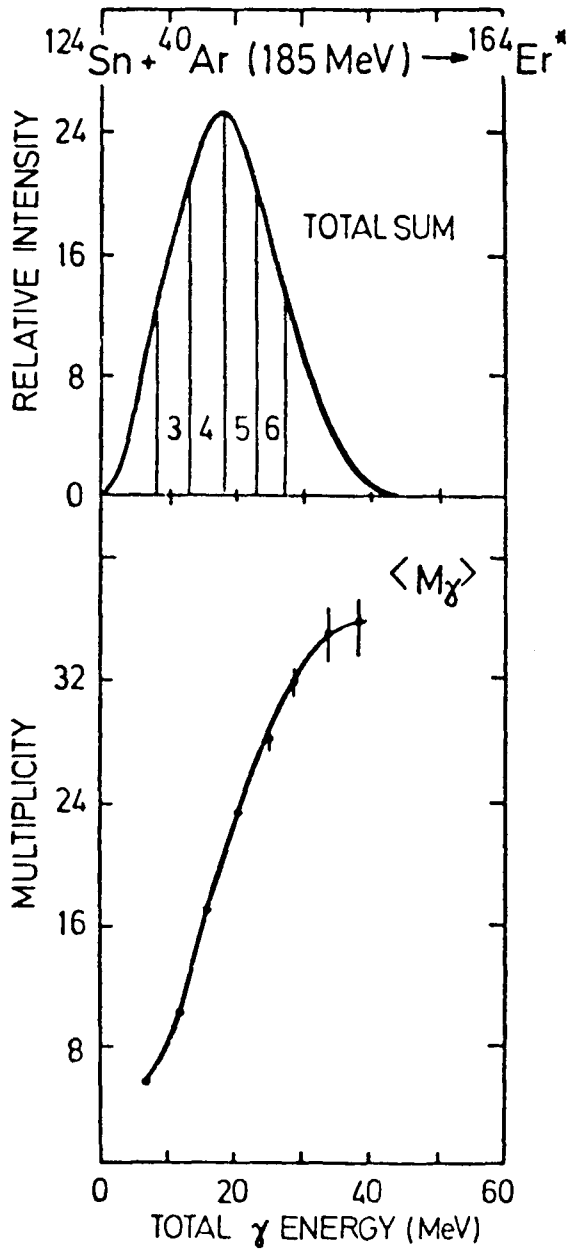

Figure 16:

Top: total sum spectrum of gamma-rays emitted after the $^{124}Sn+^{40}Ar$ reaction. Below: multiplicity of the gamma cascades measured as a function of the total sum energy above, ref.21).

Figure 17 shows the shapes of the spectra for four values of the energy and hence multiplicity. The three differences, (fig.17 below), show the gamma-rays of a rather well defined energy $\langle E_\gamma \rangle$ are added to the spectrum when the multiplicity is increased. And this energy grows with increasing angular momentum of the system as measured by M_γ . The added gamma-rays have all the characteristics of stretched

E2-transitions and hence $\Delta\langle E_\gamma\rangle$ of eq.(8) is just $(\langle E_\gamma\rangle_2 - \langle E_\gamma\rangle_1)/(M_{\gamma_2} - M_{\gamma_1})$. The resulting value of $2\mathcal{J}_{eff}/\hbar^2$ for ^{160}Er is 150 MeV^{-1}, which is very close to the rigid moment of inertia.

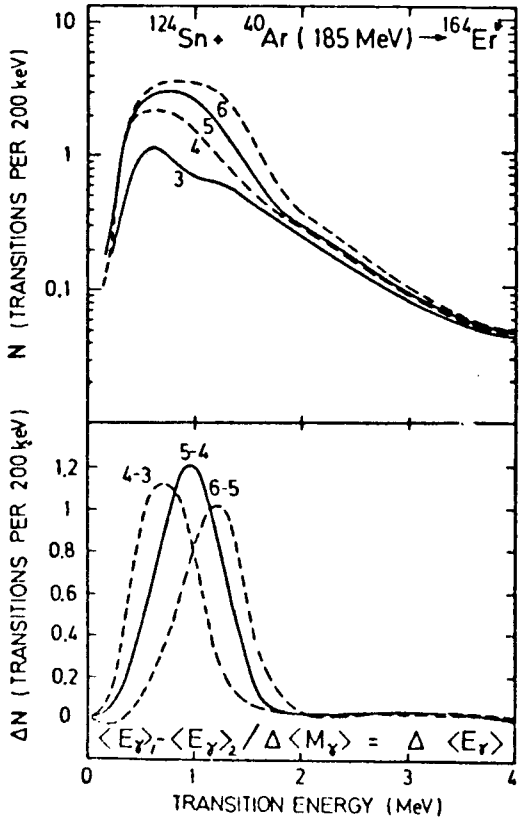

Figure 17:

Top: number of gamma transitions per 200 keV per event for consecutive 4 MeV wide slices of the total sum spectrum shown on top of fig.16. Bottom: the difference E between consecutive gamma-ray spectra above, ref.21).

2. Coincidence Measurements

Two Ge(Li) detectors recording gamma-emission from a heavy-ion reaction will detect gamma-rays, belonging to individual cascades. If these are rotational, one will, for a selected energy in one detector,

find coincident lines in the other detector at higher and lower energy, but not at the same energy, figure 18. The coincident lines will lie at characteristic distances, $n(\Delta E_\gamma)$, from the selected energy, with $n=1,2,\ldots$. If ΔE_γ and hence the collective moments of inertia are not too different for various bands, the two-dimensional gamma-gamma coincidences of all possible cascades along bands will exhibit a characteristic intensity pattern. This is shown on figure 19.

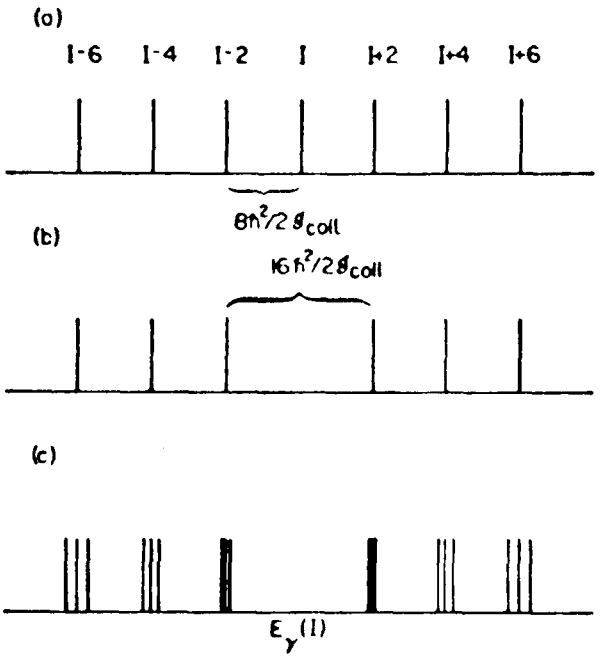

Figure 18:

(a) The evenly spaced lines in a singles spectrum of transition along an idealized rotational band. (b) The spectrum observed in coincidence in counter 2 with a gate on the line I in counter 1. (c) Same as (b) but for the case of three rotational bands with slightfully differing moments of inertia, from ref.[22].

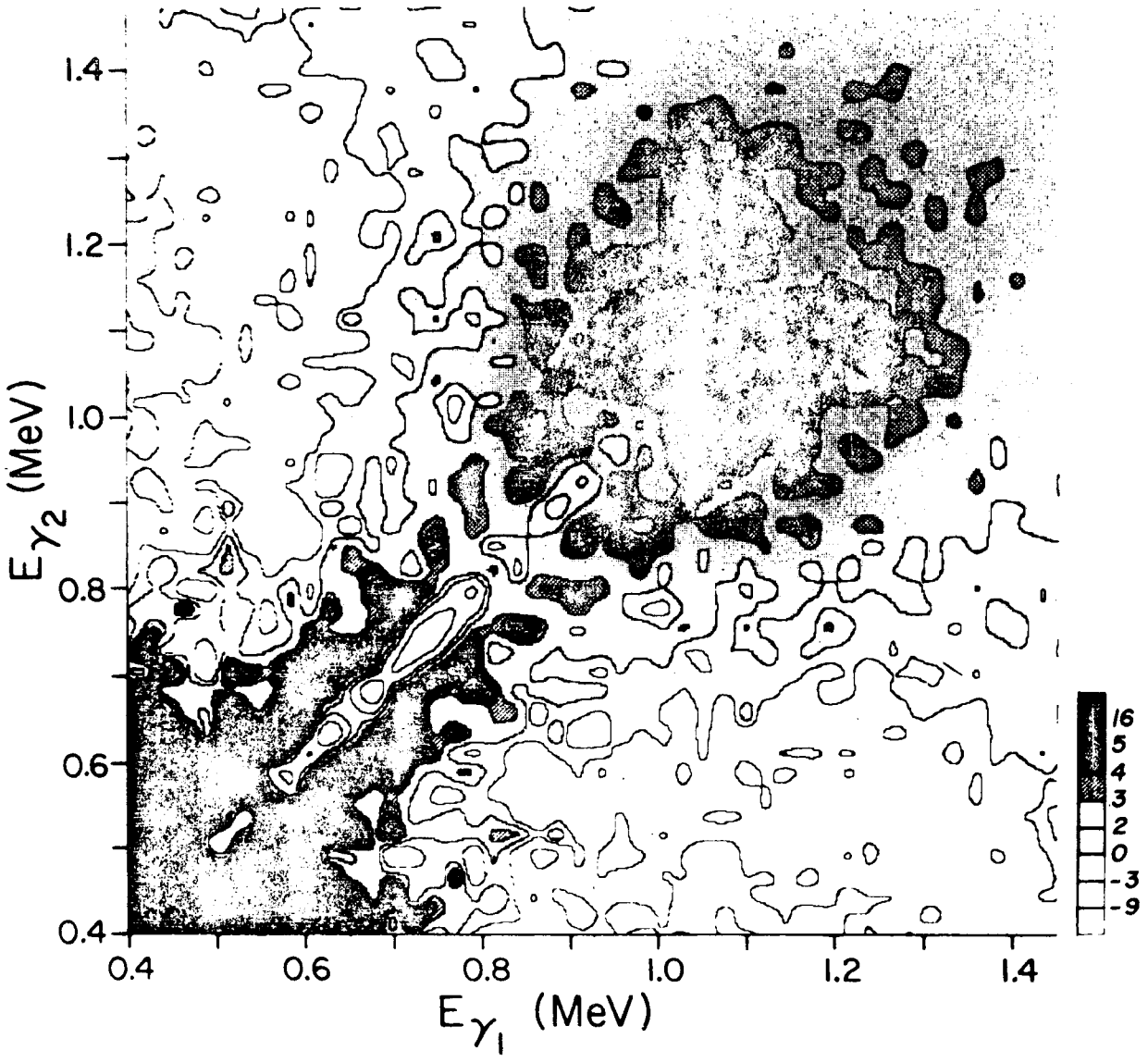

Figure 19:

Experimentally determined two-dimensional correlation spectrum of gamma-gamma coincidences from the reaction $^{124}Sn(^{40}Ar,xn)$ at 185 MeV, recorded with Ge(Li) detectors[23].

Along the diagonal there will be a valley, and parallel to this one each side there will be one or several ridges. The widths of the valley is a measure of $2\langle\Delta E_\gamma\rangle$. It can be traced as a function of E_γ being equal to $2\hbar\omega$. Projecting the coincidence frequencies along three

different lines perpendicular to the valley gives the result shown on figure 20. The valley and a repetititve system of ridges are clearly seen up to gamma-energies of 1200 keV. And the values for the collective moment of inertia that can be read from fig. 20 are clearly seen up to gamma-energies of 1200 keV. And the values for the collective moment of inertia that can be read from fig.20 are clearly smaller than the effective moment of inertia, 150 MeV^{-1} found from the singles measurements described above (subsect. 1).

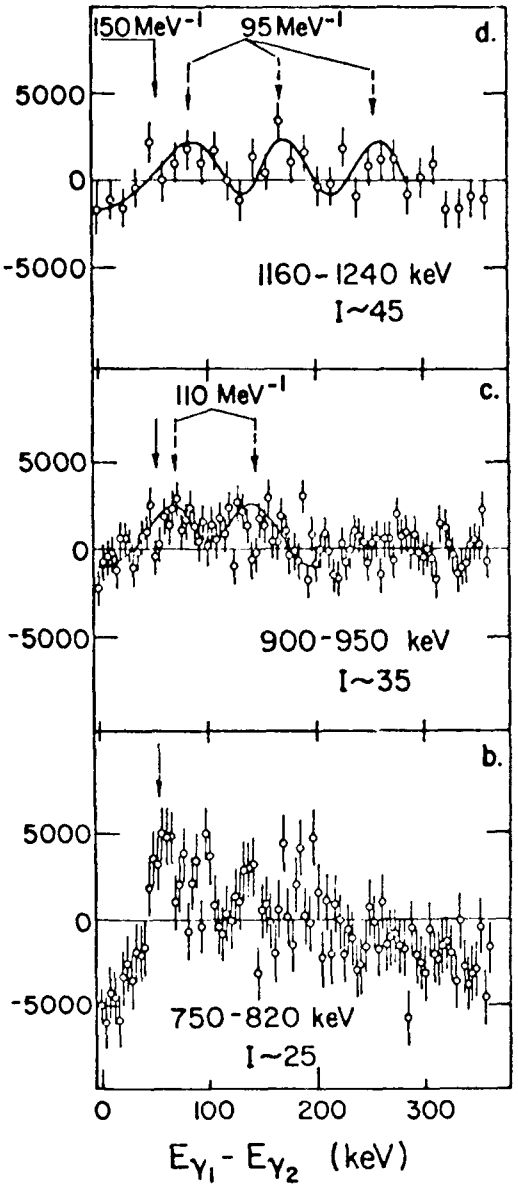

Figure 20:

Projections perpendicular to the diagonal valley on fig.19 for three slices of gamma-ray energies as indicated on the figure. The average gamma-ray energy of each slice has been converted to an average value of the angular momentum, using eq.(7) and a value of 150 MeV^{-1} for $2\,\mathcal{J}_{eff}/h^2$, ref.[23].

3. Two moments of inertia

From fig.14 it should be clear that the average slope of the individual bands is approximately identical to the slope of the yrast envelope, when measured at a given value of the total angular momentum I. It is the curvatures that differ. The slope is measured by the transition energy, E_γ, and the approximate equality of slope allows one to identify E_γ of eq.(4) with $\langle E_\gamma \rangle$ of eq.(7). This leads to

$$\frac{I-i}{I} = \frac{\mathcal{J}_{coll}}{\mathcal{J}_{eff}} \qquad (9)$$

From this and the widths of the valley, fig.20 table 1 can be constructed. The experimental results summarized in the table clearly demonstrate that even in the continuum region the gamma cascades follow bands that are more curved than the yrast line itself[23]. Thus the situation described on the left hand side of fig.15 appears to prevail. Whatever the reason, the close lying bands above the yrast line do not mix strongly. So even in a moderately hot, rapidly rotating nucleus there remains a separation of the motion into a collective component and a component due to the aligned particle motion plus in addition a component describing other internal excitations. For each band, the intrinsically excited configuration including the aligned part reamins constant, while the rotating core slows down under emission of collective E2 quanta. The moment of inertia ($\mathcal{J}_{coll}$) of this core rotation is smaller than the rigid moment of inertia ($\mathcal{J}_{eff}$) and tends to decrease as more particles align. This presumably reflects that the aligned particles cannot contribute to the inertia of the rotating core, see also ref.[23].

A. Shell model nuclei, ^{147}Gd

There is a very recent result, obtained by the Chalk River group[24], that demonstrates the predicted transition from a spherical to an oblate shape quite unabiguously. This group has succeeded in measuring the quadrupole moment of a 9 MeV, 600 ns isomer in $^{147}_{64}Gd_{83}$ with an assumed spin value equal to 49/2. The result, 3 barns, indicates an oblate deformation with $\varepsilon = -0.2$.

Figure 21 shows how the analysis is made. Alignment of five valence particles in a strictly spherical potential leads to a quadrupole moment of at most 1.5 barns unless the core itself is assumed to be polarized into an oblate shape by the aligned particles.

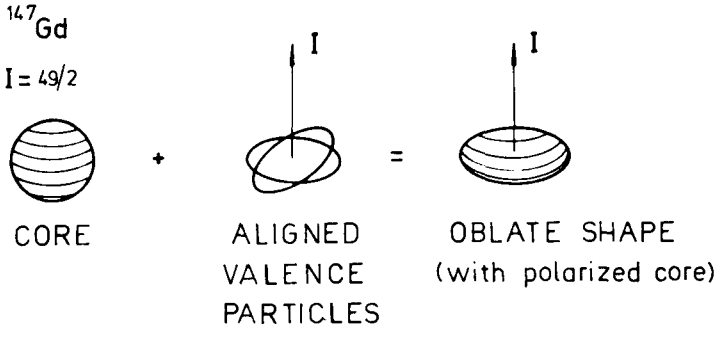

Def. ϵ	Quadrupole Moment barns				
0	0	+	1.5	=	1.5
0.2	1.5	+	1.5	=	3.0
Exp.					3.0

Figure 21:

Summary of the measurement of the quadrupole moment of an isomeric state in ^{147}Ge, and interpretation.

Table 1:

$^{124}Sn + {}^{40}Ar \rightarrow {}^{164}Er(x,n)$; $E({}^{40}Ar) = 185$ MeV

h MeV	I	$\mathcal{J}_{coll}$ MeV^{-1}	$\mathcal{J}_{eff}$ MeV^{-1}	i
.400	25 ħ	(130)	150	(4) ħ
.470	35 ħ	110	"	10 ħ
.600	45 ħ	95	"	17 ħ

IV. SHAPE CHANGES

Recent experiments have added much to the understanding of how a quantified fermion system actually absorbs angular momentum most economically, and how it radiates. Invariably, the structure aspects associated with particle states near the Fermi surface are playing a prominent role.

According to fig.1 one should also expect major shape changes to occur; and as fig.2 indicates, an interplay of average trends and shell effects is anticipated.

B. Deformed nuclei

On figure 22 the measured effective moments of inertia for Er nuclei are compared with the prediction of a rigidly rotating liquid drop. The slight increase with rotation frequency conforms qualitatively with the expected trend. It has not so far been possible to push the experiments into the region where very dramatic shape changes are expected (super-backbending).

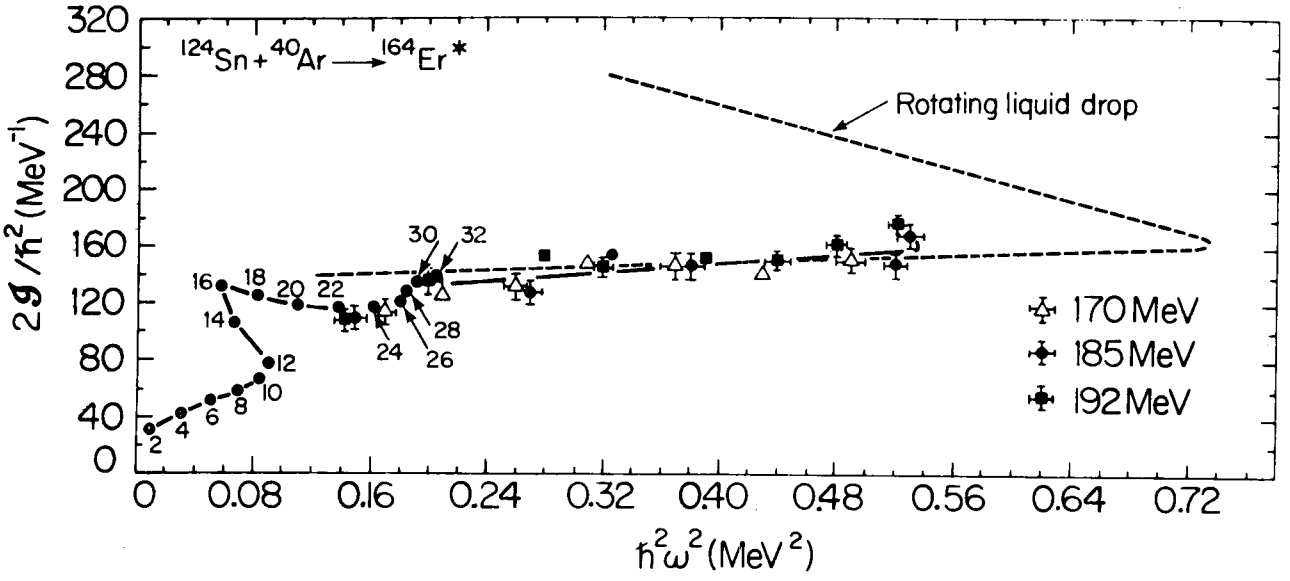

Figure 22:

Plot of effective moments of inertia as a function of the square of the (average) core rotation frequency, ref.[23]. Dashed line indicates the rotating liquid drop predictions according to ref.[1], cf. also fig.1 .

According to theory, some prolate nuclei should have a tendency to become **oblate** -going through triaxial shapes as shown in fig. 2. Rotational alignment is potentially a mechanism for this shape change, see figure 23.

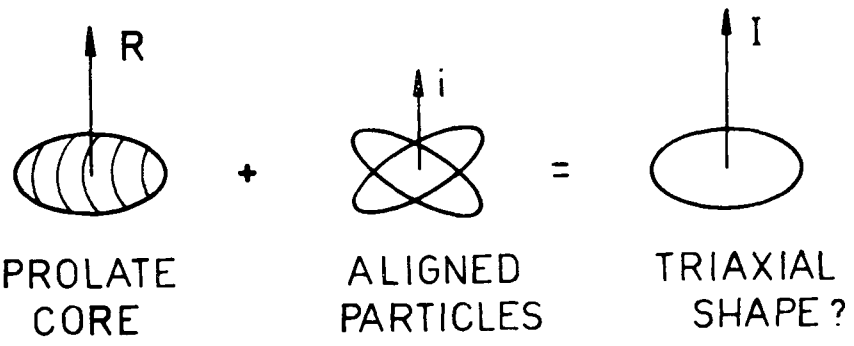

Figure 23:

Rotational alignment may produce triaxial shapes.

The aligned particles are approximate eigenstates of j and therefore axially symmetric with repect to the rotation axis, x. The core, on the other hand, is axially symmetric with respect to the z-axis. Superposition of these two components leads to a triaxial system. Whether or not the aligned particles are able to polarize the core sufficiently to produce a physically signifcant effect, is one of the many exciting questions that still remain open.

C. Shapes and shells

The study of the effect of shell structure on the shape changes induced by rotation is another question that future experiments will

have to answer. Considering the wealth of ingenious, new techniques that continues to appear, there seems to be very good prospects for decisive advances towards this goal in the near future.

Acknowledgements.

The author wishes to thank O.Andersen, C.K.V.Baba, M.A.Deleplanque, T.Døssing, S.Frauendorf, J.D.Garrett, B.Herskind, T.L.Khoo, G.Leander, B.R.Mottelson, J.Pedersen, G.Sletten, and F.S.Stephens, for access to unpublished material and for many simulating discussions.

REFERENCES:

1) S.Cohen, F.Plasil, and W.J.Swiatecki, Ann. of Phys. 82(1974)557.

2) A.Bohr and B.R.Mottelson, Physica Scripta 10A(1974)13.

3) C.G.Anderson, S.E.Larsson, G.Leander, P.Möller, S.G.Nilsson, I.Ragnarsson, S.Aberg, R.Bengtsson, J.Dudek, B.Nerlo-Pomorska, K.Pomorski, and Z.Szymański, Nucl. Phys. A268(1976)205.

4) A.Bohr and B.R.Mottelson, Nuclear Structure, Benjamin, N.Y. 1975, Vol. 2.

5) P.Fuchs, H.Emling, E.Grosse, D.Sxhwalm, H.I.Wollersheim, and R.Schulze, Gesellschaft für Schwerionenforschung, Darmstadt, FRG, Annual Report, 1977, p.195.

6) P.Aguer, G.Bastin, J.P.Thibaud, D.Barneoud, J.Boutet, and C.Foin, Z.Phys. A285(1978)59.

7) P.Aguer, G.Bastin, A.Charmant, Y. El Mastri, P.Hubert, G.Janssens, C.Michel, J.P.Thibaud, and J.Vervier, Phys. Lett. 82B(1979)55.

8) H.Emling, P.Fuchs, E.Grosse, D.Schwalm, R.S.Simon, H.J.Wollersheim, and D.Pelte, Gesellschaft für Schwerionenforschung, Darmstadt, FRG, Annual Report, 1977, p.66.

9) J.Pedersen, B.B.Back, F.M.Bernthal, S.Bjørnholm, J.Borggreen, O.Christensen, F.Folkman, B.Herskind, T.L.Khoo, M.Neiman, F.Pülhofer, and G.Sletten, Phys. Rev. Lett. 39(1977)990.

10) C.K.V.Baba, S.Bjørnholm, J.Borggreen, O.Christensen, F.Folkman, B.Herskind, R.Lieder, J.Pedersen, R.S.Simon, and G.Sletten, unpublished results, 1980.

11) P.Kleinheinz, Lecture given at the Argonne Symposium on High Spin Phenomena in Nuclei, ASHPIN Conf. Rep., Argonne, USA, 1979.

12) J.Borggreen, S.Bjørnholm, O.Christensen, A.Del Zoppo, B.Herskind, J.Pedersen, G.Sletten, F.Folkman, and R.S.Simon, Z. Phys. (1980) to appear.

13) R.S.Simon, M.V.Banaschik, R.M.Diamond, J.O.Newton, and F.S.Stephens, Nucl. Phys. A290(1977)253.

14) T.L.Khoo, R.K.Smither, B.Haas, O.Häusser, H.R.Andrews, D.Horn, and D.Ward, Phys. Rev. Lett. 41(1978)1027.

15) C.Baktash, E.der Mateosian, O.C.Kistner, and A.W.Sunyar, Phys. Rev. Lett. 42(1979)637.

16) O.C.Kistner, A.W.Sunyar, and E. der Mateosian, Phys. Rev. C17(1978)1417.

17) F.S.Stephens and R.S.Simon, Nucl. Phys. A183(1972)157.

18) F.S.Stephens, Rev. Mod. Phys. 47(1975)43.

19) S.Frauendorf, Contribution to the Proceedings of the International Symposium on Extreme States, Dresden (DDR), Febr., 1980.

20) A.Bohr and B.R.Mottelson, Proc. Conf. on Nuclear Structure, Tokyo 1977, p.157.

21) H.J.Körner, D.L.Hillis, C.P.Roulet, P.Aguer, C.Ellegaard, D.B.Fossan, D.Habs, M.Neiman, F.S.Stephens, and R.M.Diamond, Phys. Rev. Lett. 43(1979)490.

22) R.M.Diamond, Proceedings of the Summer School at Serre-Chevalier, Physique des ions lourds de 30 MeV par nucléon, Sept. 1979, p.39 .

23) M.A.Deleplanque, F.S.Stephens, O.Andersen, J.D.Garrett, B.Herskind, R.M.Diamond, C.Ellegaard, D.B.Fossan, D.L.Hillis, H.Kluge, M.Neiman, C.P.Roulet, S.Shif, and R.S.Simon, preprint, 1979.

24) O.Häusser, H.-E. Mahnke, J.F.Sharpey-Shafer, M.L.Swanson, P.Taras, D.Ward, H.R.Andrews, and T.K.Alexander, Phys. Rev. Lett. 44(1980)136.

INVITED TALKS

ON THE QUANTUM MECHANICS OF DIC

A TROPICAL RHAPSODY ON NORTHERN THEMES(*)

A.F.R. de Toledo Piza

Instituto de Física, Universidad de Sao Paulo
C.P. 20516, 01000 Sao Paulo, S.P., Brasil

During the last decade an important and, to a large extent unanticipated new facet became incorporated to the explored aspects of the dynamics of nuclear systems. This came about through experimental investigation, and later through theoretical studies of the so called Deep Inelastic Collisions (DIC) between heavy ions[R1]. The capturing point was the identification of aspects of such collisions that are strongly suggestive of diffusion or relaxation-like processes (correlations between Q-value and preferred scattering angle, interpretations in terms of a "collisions time" related to the preferred scattering angle and behavior of distributions of final state dynamical variables as functions of such a "collision time", for instance). This led to a branch of theoretical investigations centered on the use of transport-like (irreversible) dynamical equations and on methods akin to those of non-equilibrium statistical mechanism. These equations typically describe the diffusion-like time evolution of probability distributions associated with relevant

---

(*) Rhapsody: 1- A short epic poem, or a portion of a longer epic, recited by a rhapsodist at one time.

2- A confused or disconnected series of sentences or statements, composed under excitement, and without dependence or natural connection; a confused or rambling composition.

3- In music, a composition of irregular form and in the style of an improvisation.
(Webester's New Twentieth Century Dictionary)

observable quantities, a circunstance that readily poses the problem of their connection with an ultimate, underlying quantum mechanical evolution with different general properties. The introduction of coarse-grained descriptions can, eventually, bridge the gap[N1], but it should be borne in mind that this will only lead generally to properly irreversible behavior provided the underlying, reversible dynamics has adequate mixing properties[N2,R2]. This point appears not to have been sufficiently emphasized, may be due to the circunstance that reasonable, albeit mixing-nonspecific randomness assumption have readily given rise to acceptable transport-type equations through coarse - graining procedures.

Besides this "statistical" branch, however, a different line of approach to the DIC developed from more standard approaches to the physics of nuclear structure, in which the "irreversibility" aspects of these phenomena are considerably de-emphasized. It contains both the Time-Dependent Hartree-Fock (TDHF) description of the collision of heavy ions[R3] and the so called Coherent Surface Excitation Model (CSM) of heavy ion reactions[R4]. The TDHF uses a single determinant to describe the state of the colliding systems at all times. As this constraint is incompatible with the characteristic linear structure of quantum mechanical phasespaces ("super-position principle"),but still allows for enough structure for a classical phase-space (symplectic structure on the complex Grassman manifold), one gets a hybrid theory with a strong classical flavor and plagued with interpretation problems some of which may yet turn out to be quite revealing when properly understood (e.g. interfragment correlations in final states). The CSM, on the other hand, makes deliberate use of classical dynamical equations both for the relative motion of the colliding fragments and for the considered "intrinsic" degrees of freedom, which are taken to be nuclear fields (possibly damped) known, from nuclear structure studies, to be endowed with strong

coherence properties. The model has been also provided with a statistical annex to describe mass (and the associated momentum) transfer through the use of proximity ideas. A crucial point deserving special emphasis, however, is that correlated quantum fluctuations of intrinsic and scattering degrees of freedom in the final state have been found to be an essential ingredient for the proper interpretation of the (classical) dynamical results[N3].

* * *

Let us pause here for a slightly more technical recollection of this point. If one treats the intrinsic collective fields quantum-mechanically, still keeping the classical treatment of the relative motion, one finds that, provided the coupling of relative motion to the harmonic fields is linear in the latter, and provided they are initially in their ground state, they are driven by the time-dependent interaction due to the relative motion (any relative motion) into coherent states of the form

$$|I\rangle = e^{-\frac{|I|^2}{2} + I a^\dagger} |0\rangle$$

where the c-number complex amplitude I(t) is given in terms of a time integral of the time-dependent interaction f(t) :

$$i\dot{I}^*(t) = \frac{1}{\sqrt{w}} \int^t dt' f(t') e^{-iwt'}$$

w being the oscilator frequency of the field, The same result has been obtained in a different context via the more abstruse technique of looking for saddles[R5] of path integral representation of the inclusive effective propagator for relative motion, when the latter is duly stuffed with the appropriate fully quantal influence functionals for the linearly coupled harmonic fields and it contains an inconsistency which appears

to be typical of such mixtures of classical and quantum mechanics in a single game: the mean square fluctuation of the total energy is not conserved in such partly-classical dynamical schemes, so that energy conservation (appart from damping effects!) holds only "on the average"[N4]. This actually comes about in a very natural way, which can be described as follows. Being described in classical terms, relative motion takes place along a trajectory and with a prescribed time dependence; relative kinetic energy is therefore a well defined quantity at any time (forget mass transfer, for simplicity!). This classical motion, however, generates a time-dependent "external" force acting on the intrinsic (quantum!) system that is thereby unitarily driven away from its initial state, say one of its "free" eigenstates. This external driving will then, in general, change the (quantum) dispersion of intrinsic energy which can become quite large and eventually freezes once the collision process is completed.

One may also, perhaps instructively, consider the classical relative motion as a "classical limit" of some wave-packet motion. In doing so, however, one realizes that the partly-classical treatment corresponds to a factorized ansatz for the complete amplitude in a relative motion factor and an intrinsic factor. From this point of view one may consider this type of treatment as envolving a "mean field approximation"[R6] of sorts, namely one which will specifically rule out correlations between intrinsic and collective degrees of freedom[N5].

Now, it is through correlations of precisely this sort that such a general requirement as detailed energy conservation can be properly installed in the theory[N6]. The CSM copes with this problem within the bounds of a fully classical treatment, by introducing a dispersion in the initial conditions of the (classical) intrinsic modes to stand for the quantum fluctuations inherent to their ultimately quantum constitu-

tion, an approach which is strongly reminiscent of semi-classical treatments of inelastic collision processes which are popular among chemist[N7,R7].

* * *

We may, however, take a different turn at this point and consider what are the devices through which a fully quantum treatment of the collision copes with these matters. A reasonable enough description of the initial state (for a time-dependent description) can be written as

$$\langle \vec{r} \mid t=0 \rangle = |I_o\rangle \langle \vec{r} \mid U[\vec{k}_o, \vec{r}_o] \rangle$$

This is a factorized pure state displaying a definite intrinsic factor $|I_o\rangle$ and a pre-collision couple of wave-packets centered a distance $\vec{r}_o$ appart and with relative mean momentum $\vec{k}_o$. An explicit representation for the intrinsic factor will not be needed here. While the description of the pre-collision set-up by a pure state is strictly speaking unrealistic due to incoherent inhomogeneities of the beam, statistical fluctuations of the initial state take place within energy intervals which are negligible in view of the order of magnitude of collision times. This is therefore a negligible ingredient from the point of view of the final product distributions.

Now let this state evolve unitarily through the hamiltonian $H = H_I + H_r + V_{rI}$. The action of the interaction term V_{rI} will "desseparate" the state of the system, i.e., will destroy the factorized form through the establishement of correlations involving r and intrinsic variables. A convenient way of writing the state is then (Schrodinger decomposition)[R8]

$$\langle \vec{r} \mid t \rangle = \langle \vec{r} \mid e^{-iHt} \mid t=0 \rangle = \sum_n A_n(t) \mid I_n(t) \rangle \langle \vec{r} \mid U_n(t) \rangle$$

where $\langle I_n(t) | I_{n'}(t)\rangle = \delta_{nn'}$, $\langle U_n(t) | U_{n'}(t)\rangle = \delta_{nn'}$ and phases can be arranged so that the $A_n(t)$ are always real. In this representation, the interaction of r and intrinsic variables appears as a dependence of the $A_n(t)$ on time, as shown by the evolution law

$$\dot{A}_m(t) = Im \sum_n \langle I_m(t) C_m(t) | H | I_n(t) C_n(t)\rangle A_n(t)$$

which gives $A_m=0$ when $V_{rI}=0$ (R9). While being rather peculiar from many points of view, this representation has the nice features of explicitely displaying both the minimal <u>form</u> of correlations between intrinsic and relative degrees of freedom <u>and</u> the maximal coherence of each subsystem when considered separately. This information is contained in the decomposition into doubly orthogonal terms n and in each of the normalized states $|I_n(t)\rangle$, $|U_n(t)\rangle$ respectively. Having in mind specifically a scattering situation in which, for simplicity, only inelastic channels are taken into account (i.e., all channels are defined by the vanishing of the interaction term V_{rI} of H) (N8), it is easy to verify that, for large enough times, the intrinsic energy fluctuation in each of the $|I_n(t\to\infty)\rangle$ can eventually be made to vanish, i.e., each term of $\langle r|t\to\infty\rangle$ can eventually become associated with a definite channel. This comes about through the vanishing of the overlaps between relative motion wave-packets in the standard channel decomposition of $\langle r|t\rangle$ through the spatial separation of packets having different inelasticities. This, in fact, makes the channel decomposition identical with the Schrodinger decomposition. The complete overall quantum coherence of $|t\rangle$ is of course guaranteed, together with detailed energy conservation requirements, which result obviously in the intrinsic-relative motion correlations.

If one now wishes to concentrate on observables pertaining to relative motion alone (such as $d^2\sigma/dE\, d\Omega$, for instance), the relevant information is contained in

$$tr_I\left[\langle\vec{r}|t\rangle\langle t|\vec{r}'\rangle\right] = \sum_n A_n^2(t)\,\langle\vec{r}|U_n(t)\rangle\langle U_n(t)|r'\rangle$$

which represents a statistical mixture of orthonormal states with probabilities A_n^2 . Similarly, the state of the intrinsic subsystem is given by the mixture

$$tr_{\vec{r}}\left[\langle\vec{r}|t\rangle\langle t|\vec{r}'\rangle\right] = \sum_n A_n^2(t)\,|I_n(t)\rangle\langle I_n(t)|$$

where the same weights A_n^2 appear. The time-dependence of the weights is caused by the interaction term $V_{\vec{r}I}$ of the hamiltonian H, the asymptotic decoupling of H_I and $H_{\vec{r}}$ in a scattering situation leading eventually for their stabilization, as well as of the states $|U_n\rangle$ and $|I_n\rangle$.

* * *

We may now use these diverse elements in order to set up a conceptual scheme form which to approach the physics underlying the DIC, and the apparent irreversibility taking place in these processes in particular, As a first point, we see that as far as observations done on a given subsystem are concerned (such as $d^2\sigma/dEd\Omega$), the system behaves as a statistical mixture governed by weights (such as $A_n^2(t)$) but can still show coherence properties governed by the factor states (such as $\langle r\,|U_n(t)\rangle$). Thus the properties of this statistical mixture depend not only on the dynamical properties as given by the hamiltonian H but also on the particular subsystem which is brought into focus in the observation. This means that we can produce, in principle, a large, potential multiformity of mixtures out of a given completely coherent state, corresponding to different subsystem decompositions of the system as a whole, The ideal "a priori" symmetry of different decompositions is distorted, however, when one finds oneself restricted to observations that are not

just ideal but actually carried out in practice. That this is not just a very prosaic and incidental type of constraint is illustrated by the fact that similar restrictions are also involved as a basic ingredient in dynamical analyses of quantum measurements[R10], where they ultimately dispose with certain correlations given by the unitary dynamical law of quantum mechanics. A certain parallelism, therefore, suggest itself between the observed entropy generation in DIC and that which accompanies quantum measurements in general.

In the case of DIC one should expect any observability constraints to be related a) to the nature of the degrees of freedom in terms of which the asymptotic decoupling that results for the unbound character of the system undergoing the collision is naturally expressed (i.e., giving asymptotically stationary probabilities A_n^2 in the associated Schrodinger decomposition of the state vector) and b) to the occurrence of semiclassical regimes in association with the degrees of freedom distinguished in a given Schrodinger decomposition. To the extent that one considers just asymptotic measurements (cross sections), the Schrödinger decomposition will eventually coincide with the channel decomposition of the state vector, and statement a) expresses the difficulty of implementing observables detecting correlation terms (interference effects) involving different physical channels. Excluding such observables, the relevant information will be given essentially by the asymptotic values of the A_n^2 (t) and by the relative motion states $\langle r|U_n\rangle$, and contained in the reduced density matrix tr_I $\{\langle r|t\rangle\langle t|r'\rangle\}$ having these objects as ingredients. To the extent that a transport theory (such as that of Weidenmuller[R1]) gives a good description of this quantity, it implies that the final reduced density matrix can be linked to initial conditions by means of an "effective" irreversible dynamical law. The validity of the results given by such a dynamical law at <u>intermediate</u> times, of course, remains untested. Such validity would be associated with a

transport type (master) equation for the time evolution of $tr_I \{\langle r|t\rangle\langle t|r'\rangle\}$ at all times. From the point of view of observations done on the corresponding subsystem, then, the process could be described as an "approach to equilibrium", and therefore endowed with mixing properties, as mentioned earlier. These mixing properties, however, must be again associated not only to the dynamical law for the entire system (i. e., to the hamiltonian H) but also to the particular decomposition of the system that one considers.

To the extent that the Schrodinger decomposition approaches the channel decomposition, the residual coherence present, say, in the relative states $\langle r|U_n\rangle$ is trivial, in the sense that it is given just by the form of the initial wave-packet (assumed to be as narrow as needed in momentum space to eliminate distortion effects coming from the energy dependence of scattering amplitudes) and by energy conservation (apart from the scattering amplitude itself). At finite times, however, correlations would be nontrivial and related in particular to collective effects enegaged by the interaction V_{rI}. One can also conceive of other Schrodinger type decompositions (i.e., one that singles out some degree of freedom other than r, such as the orientation of the principal axes of the quadrupole tensor of the system) which could be relevant at finite times and fall under an observability criterion such as b) above, Phenomenological regularities scketched at the beginning appear to indicate that the corresponding "effective" dynamics of such varied decompositions must be intimately interlocked. These coherent effects, conspicuous at finite times, are alien to the statistical transport theories. Their works, however, preside, albeit in ghostly form, the collision dynamics in approaches like TDHF or CSM.

References and Notes:

R1 - Proceedings of the Caen Conference Jour.Phys. (Supl.) C5, 1976
D.K.Scott, in "Theoretical Methods in Medium Energy and Heavy Ion Physics, K.W.McVoy and W.A.Friedman, Eds., Plenum Press 1978.

R2 - P.Claverie and S.Diner, Israel Jour. of Chem. 19 (1980)54.
M.C.Nemes, A New Approach to Irreversibility in Deep Inelastic Collisions, preprint, 1981.

R3 - S.E.Koonin, in Progress in Particle and Nuclear Physics 4 (1980)283.

R4 - R.A.Broglia, C.H.Dasso and A.Winther, NORDITA preprint 80/16;
H.Esvensen, NORDITA preprint 79/45.

R5 - K.Möhring and U.Smilanski, Nucl.Phys. A338 (1980)227.

R6 - K.Möhring and U.Smilanski, Preprint HMI-P 80/7 Th.
C.R.Willis and R.H.Picard, Phys.Rev. A9 (1974) 1343.

R7 - P.Pechukas, Phys.Rev. 181 (1969)166, ibid. 174.
R.A.Marcus, Jour.Chem.Phys. 54 (1971)3965. ibid. 56(1972)311; ibid. 59(1973)5135.
W.H.Miller, Adv.Chem.Phys. 25(1974)69.

R8 - E.Schrödinger, Proc. Cambridge Phil.Soc. 31(1935)555. ibid. 32(1936) 446.

R9 - O.Kübler and H.D.Zeh, Ann.Phys. (N.Y.) 76(1973)405.

R10- K.Hepp. Helv.Phys. Acta 45(1972)237.
J.S.Bell, Helv.Phys. Acta 48(1975)93.
M.Cini. M. de Maria, G.Mattioli and F.Nicolo, Found. of Phys. 9(1979)479.

N1 - This is a comprehensive reference to coarse-grained descriptions, intended to cover not only the approach developed by Nöremberg (see R1 and references cited therein) but also that based on the use of ensembles of random hamiltonians, as developed by Weidenmüller and collaborators. Such ensembles are used in statistical theories of spectra to describe average properties of stationary states of a complex system. In transport theories of nuclear collisions they are likewise related to average properties of the intrinsic states. Their use in transport theories implies thus some sort of "idealized" coarse graining, the idealization consisting in the replacement of an actual "coarse sampling" by a judiciously defined "dynamical fuzzying". (see also N2).

N2 - This refers to coarse-grained observation of a system that is allowed to time-evolve according to its full microscopic dynamical law. The "increasing mixing character" of coarse-grained probability distributions for DIC under time evolution has been discussed in R2 (MCN). This is related there to the bistochastic character of the matrix that represents the change in the distributions. It should be noted, however, that bistochasticity does not imply dynamical approach to coarse-grained equilibrium without other assumptions. If $\rho(t)$ is the coarse-grained distributions, then $\rho(t_1) = B(t_1-t_0)\rho(t_0)$ and $\rho(t_2) = B(t_2 t_0)\ (t_0)$, both $B(t_1-t_0)$ and $B(t_2 t_0)$ being bistochastic matrices defined by the microscopic, reversible dynamical law. For $t_2>t_1>t_0$, however, the relation between $\rho(t_2)$ and $\rho(t_1)$ is more complicated, and in particular (t_2) can be less mixed than $\rho(t_1)$. (while it is guaranteed that both are more mixed than $\rho(t_0)$. This possibility is explicitely ruled out by restricting the microscopic dynamical law in the appropriate way ("mixing" dynamical law).

N3 - Part of these correlations manifest themselves in TDHF calculations, which make no assumption as to the factorizability of the final state into parts corresponding to each of the final fragments. TDHF calculations are however constrained by the overall determinantal ansatz, and the detailed effects of this constraint on the possible final correlations appears not to have been sufficiently explored.

N4 - Cf. the brief communication made by A.Einstein to the Brazilian Academy of Sciences, on the 7th of May of 1925, on experiments done by Geiger and BOthe on the idea of "statistical energy conservation" of Bohr, Kramers and Slater. A transcription of this communication appears in Suplemento Cultural de "O Estado de Sao Paulo", 81(1978)p.3, in an article by R.V.Caffarelli on Einstein's visit to Rio de Janeiro.

N5 - The mean field of TDHF is based on an entirely different sort of factorization (factorization of the many-body density into one-body density factors) which does not single out collective and intrinsic parts. Correlations between these parts are however allowed, provided they are tailored to fit the determinantal constraint (see also N3).

N6 - The need for detailed energy conservation affects also transport descriptions, whenever they make use of a classical treatment of the degrees of freedom associated with the relative motion of fragments.

N7 - These treatments aim aminly at the calculation of scattering amplitudes to definite channels, unlike in the CSM treatment of DIC, which has an inclusive character. In the single channel problem, the question of energy conservation is taken care of automatically as shwon in detail e.g. in Pechukas, Ref. R7. Inclusive treatments as proposed in R5 and R6 (which follow closely the path marked by Pechukas) involve precisely the mixture of classical and quantum mechanics that leads to problems regarding detailed energy conservation.

N8 - This can be extended to more complicated cases (e.g., involving rearangement) at the expense of enough technical complications (e.g.: to treat the transference of a group of particles one can analyse the wave function in terms of three components associated with the transferred group and with initial and final "cores", respectively).

A NEW TOOL IN NUCLEAR SPECTROSCOPY: PAIR EXCHANGE REACTIONS

D.R.Bes, O.Dragún and E.E.Maqueda

Departamento de Física, Comisión Nacional de Energía Atómica
1429 Buenos Aires, Argentina

In this seminar we explore the possibility of using the reaction between heavy ions that exchange a pair of protons by a pair of neutrons as a tool for spectroscopic studies. The interest has been prompted by the recent observation[1] of the reaction $^{40}Ca(^{14}C,^{14}O)^{40}Ar$ and the possible specificity of this process for the excitation of some ellusive collective modes.

For a first estimate we make the simplifying assumption that the transition operator Q can be written in terms of two particle transfer operator P. Namely, if the pair transfer operator P is given by

$$P_\lambda = \sum_{j_\tau \geq j'_\tau} g(j,j',\tau,\lambda)\,[c^+_{j\tau}\,c^+_{j'\tau}]^\lambda\,(1+\delta_{j\tau,j'\tau})^{-1/2} \qquad (1)$$

where λ is the pair angular momentum and τ labels the type of particle (proton or neutron), the pair exchange operator Q is assumed to be

$$Q_I = \sum_{\substack{j_n \geq j'_n \\ j_p \geq j'_p \\ \lambda_n\,\lambda_p}} g(j_n,j'_n;n,\lambda_n)\,g(j_p,j'_p;p,\lambda_p) \times \frac{[[c^+_{jn}c^+_{j'n}]^{\lambda_n}[c_{jp}c_{jp}]^{\lambda_p}]^I}{\sqrt{(1+\delta_{jnj'n})(1+\delta_{jpj'p})}} \qquad (2)$$

The weighting factors g are characteristic of the two nucleon transfer reaction process.

As a simple example of the effects of that process on a heavy nucleus we consider the case of a target with one proton pair more and one pair neutron

less than the closed shell. The possible transitions for each kind of particles are schematically depicted in figure 1 and correspond to a) [a')] the annihilation of a proton [neutron] pair addition [removal] phonon; b) [b')] the creation of a particle-hole phonon and c) [c')] the creaction of a proton [neutron] pairing removal [addition] phonon.

The final states of the residual nucleus may be any combination of the transitions (a), (b) and (c) with (a'), (b') and (c'). It is therefore possible to populate i) the ground state of the closed shell system ((a)+(a')); ii) proton or neutron pairing two-phonon states ((c)+(a') or (a)+(c')); iii) proton and neutron pairing four-phonon states ((c)+(c')); iv) particle-hole phonon states ((a)+(b') and (b)+(a')), and v) two particle-hole phonon states ((b)+(b')).

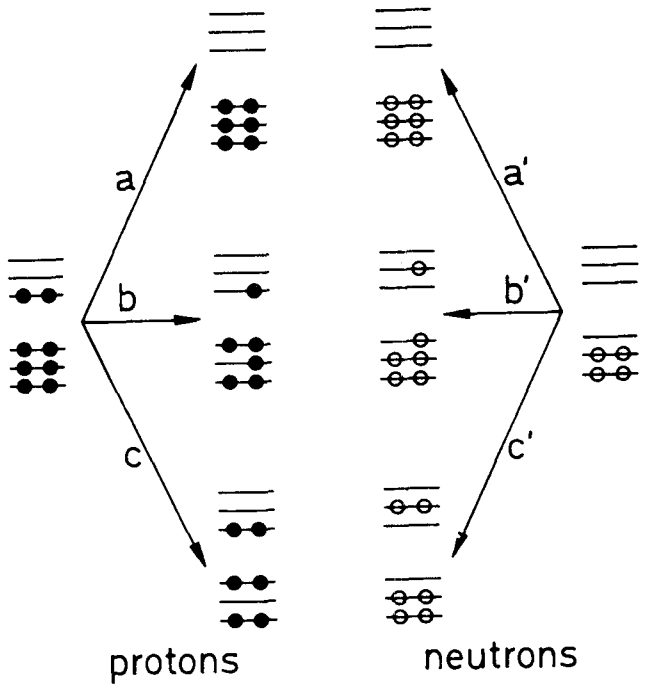

The states around doubly magic nuclei are constructed using as building blocks TDA boson creation operators $\Gamma^{+}(\nu,\alpha,\tau,\lambda)$. The phonon type is labelled by alpha, corresponding a(r) to the addition (removal) pairing phonons and 0

to the particle-hole phonon. By convention $\tau = 0$ for particle-hole phonons. Any extra label that may be needed to specify the phonon (i.e. order of the TDA root) is indicated by ν. The phonon creation operators Γ^+ are expressed in terms of fermion creation and annihilation operators,

$$\Gamma^+(\nu,a,\tau,\lambda) = \sum_{k\geq k'} X(\nu,a,\tau,\lambda;kk') \frac{[c^+_{k\tau} c^+_{k'\tau}]^\lambda}{(1+\delta_{k\tau,k'\tau})^{1/2}} \qquad (3a)$$

$$\Gamma^+(\nu,r,\tau,\lambda) = \sum_{k\geq k'} X(\nu,r,\tau,\lambda;h,h') \frac{[c_{h\tau} c_{h'\tau}]^\lambda}{(1+\delta_{h\tau,h'\tau})^{1/2}} \qquad (3b)$$

$$\Gamma^+(\nu,0,0,\lambda) = \sum_{k,h,\tau}{}' X(\nu,0,\tau,\lambda,kh) [c^+_{k\tau}.c_{h\tau}]^\lambda \qquad (3c)$$

for pair addition, pair removal and particle-hole modes respectively. Single particle states above (below) the Fermi energy are denoted by k(h).

We are interested in the two nucleon transfer amplitudes $T(\nu,\alpha',\alpha,\tau(\tau')\lambda)$ for transitions populating the states $|\nu,\alpha',\tau',\lambda\rangle$ from initial states $|1,\alpha,\tau,0\rangle$. They can be calculated by means of the operators P of eq.(1) which are written in terms of the phonon creaction operators Γ^+. In particular the transition matrix elements corresponding to the two body transfer processes of fig.1 result,

$$(a)\quad T(\nu,a,0,p,\lambda) = \langle \nu,a,p,\lambda \,|\, \sum_{k\geq k'} g(k,k',p,\lambda)\ \frac{[c^{+}_{kp}\, c^{+}_{k'p}]^{\lambda}}{(1+\delta_{kk'})^{1/2}}\ |0\rangle$$

$$= \sum_{k\geq k'} X(\nu,a,p,\lambda;k,k')\, g(k,k';p,\lambda) \qquad (4a)$$

$$(a')\quad T(\nu,r,0,n,\lambda) = \langle \nu,r,n,\lambda \,|\, \sum_{h\geq h'} g(h,h';n,\lambda)\ \frac{[c_{hn}\, c_{h'n}]^{\lambda}}{(1+\delta_{hh'})}\ |0\rangle$$

$$= \sum_{h\geq h'} X(\nu,r,n,\lambda;h,h')\, g(h,h';n,\lambda) \qquad (4b)$$

$$(b)\quad T(\nu,0,a,p,\lambda) = \langle \nu,0,0,\lambda \,|\, \sum_{kh} g(k,h,p,\lambda)\, [c_{kp}\, c_{hp}]^{\lambda}\, |1,a,p,0\rangle$$

$$= \sqrt{2} \sum_{kh} \frac{1}{\sqrt{2k+1}}\, X(1,a,p,0,k,h)\, X(\nu,0,p,\lambda;kh)_{x} \qquad (4c)$$
$$\times\ g(k,h,p,\lambda)$$

$$(b')\quad T(\nu,0,r,n,\lambda) = \langle \nu,0,0,\lambda \,|\, \sum_{kh} g(k,h,n,\lambda)\, [c^{+}_{kn}\, c^{+}_{kn}]^{\lambda}\, |1,r,n,0\rangle$$

$$= \sqrt{2} \sum_{k,h} \frac{1}{\sqrt{2h+1}}\, X(1,r,n,0;kh)\, X(\nu,0,n\lambda;k,h)_{x} \qquad (4d)$$
$$\times\ g(k,h,n,\lambda)$$

Within the present approximation we can similarly calculate the amplitudes for the pair exchange transitions. Aside from Q-effects in the two particle transfer and effects due to angular momentum mismatch in the pair exchange the matrix elements of the operator Q_I can be simply related to the four two-body amplitudes (4). If the target nucleus A is represented by a proton addition and a neutron removal phonon (as in fig.1) we obtain the following expression for the pair exchange amplitudes relative to the ground state.

$$\frac{\langle(\nu,r,p,\lambda),(1,a,p,0)\,|\,Q_\lambda\,|\,A\rangle}{\langle g.s.\,|\,Q_0\,|\,A\rangle} \cong \frac{T(\nu,r,0,p,\lambda)}{T(1,a,0,p,0)}$$

$$\frac{\langle(1,r,n,0),(1,a,n,\lambda)\,|\,Q_\lambda\,|\,A\rangle}{\langle g.s.\,|\,Q_0\,|\,A\rangle} \cong \frac{T(\nu,a,0,n,\lambda)}{T(1,r,0,n,0)}$$

$$\frac{\langle(1,r,n,0)\,[(\nu,a,n,\lambda)(\omega,r,p,\sigma)]^I\,(1,a,p,0)\,|\,Q_I\,|\,A\rangle}{\langle g.s.\,|\,Q_0\,|\,A\rangle} \cong$$

$$\cong \frac{T(\nu,a,0,n,\lambda)}{T(1,r,0,n,0)}\,\frac{T(\omega,r,0,p,\sigma)}{T(1,a,0,p,0)}$$

$$\frac{\langle\nu,0,0,\lambda|\,Q_\lambda\,|\,A\rangle}{\langle g.s.\,|\,Q_0\,|\,A\rangle} \cong \frac{T(\nu,0,a,p,\lambda)}{T(1,a,0,p,0)} + \frac{T(\nu,0,r,n,\lambda)}{T(1,r,0,n,0)} \tag{5}$$

$$\frac{\langle[\omega,0,0,\sigma)(\nu,0,0,\lambda)]^I\,|\,Q_I\,|\,A\rangle}{\langle g.s.\,|\,Q_0\,|\,A\rangle} \cong$$

$$\cong \left(1+\hat{\delta}_{\omega\sigma,\nu\lambda}\right)^{-1/2}\left[\frac{T(\omega,0,r,n,\sigma)}{T(1,r,0,n,0)}\,\frac{T(\nu,0,a,p,\lambda)}{T(1,a,0,p,0)} + \right.$$

$$\left. + (-)^{\sigma+\lambda-I}\,\frac{T(\omega,0,a,p,\sigma)}{T(1,a,0,p,0)}\,\frac{T(\nu,0,r,n,\lambda)}{T(1,r,0,n,0)}\right]$$

where $\langle g.s.|\,Q_0\,|A\rangle = T(1,a,0,p,0)T(1,r,0,n,0)$.

We now apply the above formalism to the case of pair exchange reactions on a target of ^{208}Pb leading to states in ^{208}Pb.

The two particle transfer amplitudes are obtained from the ratios

$$\frac{T(0,\alpha,\alpha',n,\lambda)}{T(1,r,0,n,0)} = \left\{\frac{d\sigma\left(^{206}Pb\,(t,p)^{208}Pb(\nu,\alpha,n,\lambda)\right)}{d\sigma\left(^{206}Pb\,(t,p)^{208}Pb(g.s.)\right)}\right\}^{1/2}$$

$$\text{and}\quad \frac{T(0,\alpha,\alpha',n,\lambda)}{T(1,a,0,n,0)} = \left\{\frac{d\sigma\left(^{210}Pb\,(p,t)^{208}Pb\,(\nu,\alpha,n,\lambda)\right)}{d\sigma\left(^{210}Pb\,(p,t)^{208}Pb\,(g.s.)\right)\,(2\lambda+1)}\right\}^{1/2} \tag{6}$$

We use in (6) the cross sections observed in the region[2,3] and for protons we assume the same ratios as for neutrons. The corresponding values are given in Table 1.

Table 1

$(t,p)^{BHNH,IBF}$		$(p,t)^{IBF}$	
$\nu,\alpha,\alpha',\tau,\lambda$	$\frac{T(\nu,\alpha,\alpha',\tau,\lambda)}{T(1,r,0,n,0)}$	$\nu,\alpha,\alpha',\tau,\lambda$	$\frac{T(\nu,\alpha,\alpha',n,\lambda)}{T(1,a,0,n,0)}$
1,a,0,n,0	0.66	1,r,0,n,0	1.07
1,a,0,n,2	0.47	1,r,0,n,2	0.47
1,0,r,n,3	0.19	1,0,a,n,3	0.11
1,0,r,n,5	0.26	1,0,a,n,5	0.13
1,0,r,n,2	0.04	1,0,a,n,2	0.16

The cross sections for populating states in ^{208}Pb via pair exchange reactions (relative to g.s. cross section) are given in Table 2. They are obtained using eqs.(5) and Table 1.

Table 2

Residual State (rs)	Ers (MeV)	$d\sigma_{rs}/d\sigma_{gs}$
(1,0,0,3)	2.61	0.6
(1,0,0,5)	3.20	1.8
(1,0,0,2)	4.08	0.3
(1,a,n,0)(1,r,n,0)	4.86	0.5
$[(1,0,0,3)^2]^6$	5.20*	.01
(1,a,p,0)(1,r,p,0)	5.30*	1.9
(1,a,n,2)(1,r,n,0)	5.55+5.80	1.1
$[(1,0,0,3)(1,0,0,5)]^8$	5.81*	.08
(1,a,p,2)(1,a,p,0)	6.37*	1.0
$[(1,0,0,5)^2]^{10}$	6.40*	.05
(1,a,n,0)(1,r,n,0)(1,a,p,0)(1,r,p,0)	10.16*	1.0

*The asterisks denote estimated values of the excitation energy.

The present rough estimate confirms the possibility of populating the proton pairing vibrational states (5.30 MeV, 6.37 MeV) as well as the neutron pairing states (4.86 MeV, 5.50 MeV). The situation is not so promising concerning the double octupole states (5.20 MeV), unless the angular momentum mismatch would favour by a large factor the population of a I=6 state relative to lower I states. However, other particle-hole states with $I \geq 5$

which have been observed[3] in the vicinity of 5 MeV can provide a serious background. Similarly, it is doubtful that the four-phonon state (10.16 MeV) (which is similar to the alpha-vibration[4] state) has more chances of being found with the pair exchange reactions than with the Hg^{204} (t,p) reaction[5]. Both processes are equally favoured from the point of view of the parentage.

References:

1) D.M.Drake et al., Phys.Rev. C45(1980)1765.
2) H.H.Bjerregaard et al., Nucl.Phys. 89(1966)337.
3) G.Igo, P.Barnes and E.Flynn, Ann.Phys. New York 66(1971)60.
4) R.A.Broglia and P.F.Bortignon, Phys.Lett. 65B(1976)221.
5) R.M.De Vries et al., Phys.Lett. 67B(1977)19.

DEPENDENCE OF ENERGY LOSS OF HEAVY IONS ON THE NUMBER OF THE STOPPING MEDIUM

M.N.Rao

Instituto de Física, Universidade de Sao Paulo
Sao Paulo, Brasil

The periodic structure observed in the stopping cross sections for alpha-particles as a function of the nuclear charge of the stopping medium has been understood quantitatively by target atomic shell effects, which give rise to a variation of the mean ionization potential. Starting from Hartree-Fock-Slater atomic wave functions, the ionic charge distributions are calculated taking into account the specific shell structure of the target atom. The stopping cross sections are obtained using Lindhard's statistical approach and agree fairly well with data.

The situation becomes much less clear for the stopping of heavier ions. While experimental data are largely limited to projectiles with nuclear charge $Z>40$, theoretical descriptions of the stopping power for heavy ions are exceedingly complicated by the fact that the charge of the ions can continuously change during their passage through the target and the target electronic orbitals are strongly perturbed.

In measurements of nuclear gamma-ray lifetimes by the Doppler Shift Attennuation (DSA) technique, the amount of the shift depends both on the lifetime of the excited state and the rate of slowing down of the recoil. Thus a good knowledge of the stopping mechanism of heavy ions becomes important, as factors, such as the finite size of the target atoms and the appropriate effective charge, which influence the stopping mechanism can significantly affect the measured lifetimes.

We have measured the stopping powers of Ag ions at low velocities ($\beta \sim 1\%$) using a method described by Shane and Seaman[1]. An ^{16}O beam of

30-55 MeV was used to produce Coulomb excited target nuclei in flight. The Doppler shifted energy of the gamma-rays emitted in the decay of the nuclear state is used to measure the ion velocity, after passing through the stopping material and losing a fraction of its initial recoil energy. Beam projectiles scattered in the backward direction and detected in coincidence with the gamma-rays select target ions recoiling in a cone near 0° (figure 1).

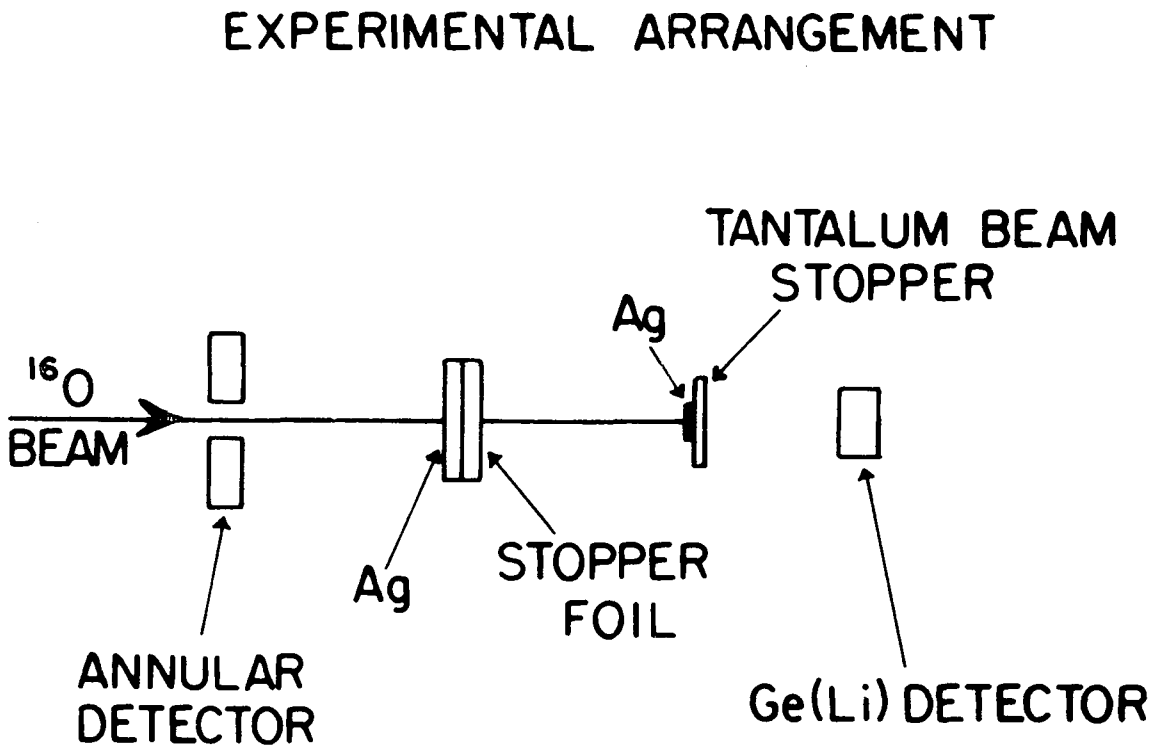

Figure 1

A number of precautions were taken to avoid systematic errors in the measurements. A small amount of Ag deposited by evaporation on a Ta stopper enables the observations of the stopped gamma-ray simultaneously with the shifted one, as also the calibration gamma-ray from the Coulomb excited Ta. We also introduce in the coincidence spectra gamma-

rays with energies in the region of interest using standard radioactive sources.

A computer program DELMAX is used to calculate the maximun shift possible corrected for the geometry and the target thickness. The results of this calculation were verified by actual measurements of the maximun shift by allowing the Ag to recoil into vacuum. This enables the initial velocity of the Ag ions to be found and thus the energy loss ΔE of the ions in passing through the stopper foil is calculated. The thickness of the foil is measured by i) weighing , ii) alpha-gauge measurements , and iii) Rutherford backscattering technique.

Since in the low recoil velocity region dE/dx may be highly non-linear with E, and the energy loss E is a large fraction of the initial recoil energy, we use the following procedure to extract dE(E)/dx from the measured $\Delta E, \Delta x$.

One writes, following the theoretical approach of Lindhard, Scharff and Schiott (LSS)[2)]

$$-\frac{dE}{dx} = \eta S(E) + k' E^{p}$$

where S(E) is the nuclear stopping power. We vary (η,p) close to the LSS values (η=1; p=0,5) and determine k' such that the equation

$$\Delta x = \int_{E_1-\Delta E}^{E_1} (\eta S(E) + k' E^{p})^{-1} \, dE$$

is satisfied. We arrive at a value for the dE(E)/dx at an energy E, by selecting dE(dx) at an energy such that different functions based on k' and (η,p) give a minimum spread (1%) in values for dE/dx.

We have so far measured dE/dx of Ag ions in foils of V, Fe, Ni, Zr and Pd, each at 4 different initial recoil velocities. Typical $\bar{E}$ values are around 100 keV/amu. Figure 2 shows a typical measurement of Ag in Zr.

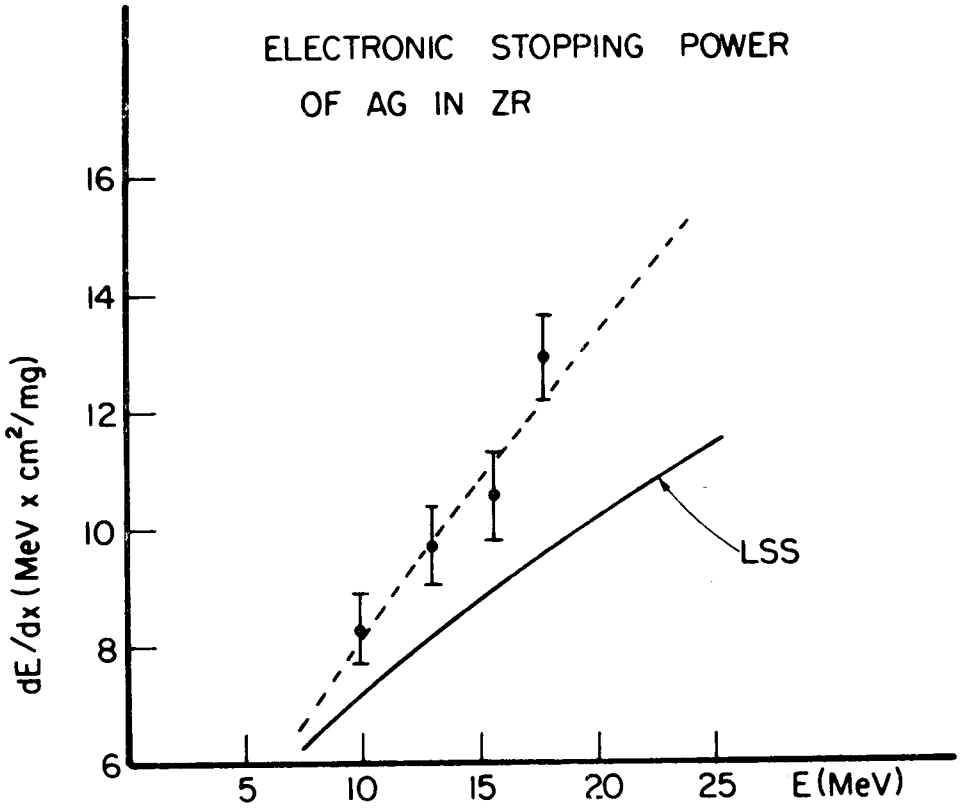

In the absence of a knowledge of the effective charge of the recoiling ions theoretical calculations assume the ion to be fully stripped (the so-called high-energy limit) and the effective charge is defined by the relation

$$[Z_1^*(V,Z)]^2 \equiv \left(\frac{S_{exp}}{S_{theory}}\right) Z_1^2$$

In the theoretical approaches to the problem one defines[3] a simplified stopping function ignoring any dynamic interaction of the target on the ion, as

$$S = P(\rho_{Z_1^*}, V) \times T(\rho_{Z_2}, V)$$

where S is the stopping power and P is a function of the ion properties only ($\rho_{Z_1^*}$ is the dynamic charge distributions of the ion and V its

velocity) and T is a function of the charge distributions ϱ_{Z_2} and the ion velocity. With this definition of the simplified stopping function, the stopping is primarily dependent on individual ion and target charge distributions and not on the dynamic details of the ion-target interaction. If one can approximate the function P, the stopping of any ion can be predicted, if one knows the stopping of any other ion (protons, for example), in the same material, at the same velocity. By such a comparison one has:

$$\frac{S_{HI}}{S_p} = \frac{P(Z^*_{HI}, V)}{P(Z^*_p, V)}$$

Using Ziegler's empirical analytic representation[3] for the ratio on the right han side (obtained from 127 HI- target combinations) we obtain the solid curve in fig. 3 for the stopping of Ag ions as a function of Z_2 The experimental data are also shown in the figure.

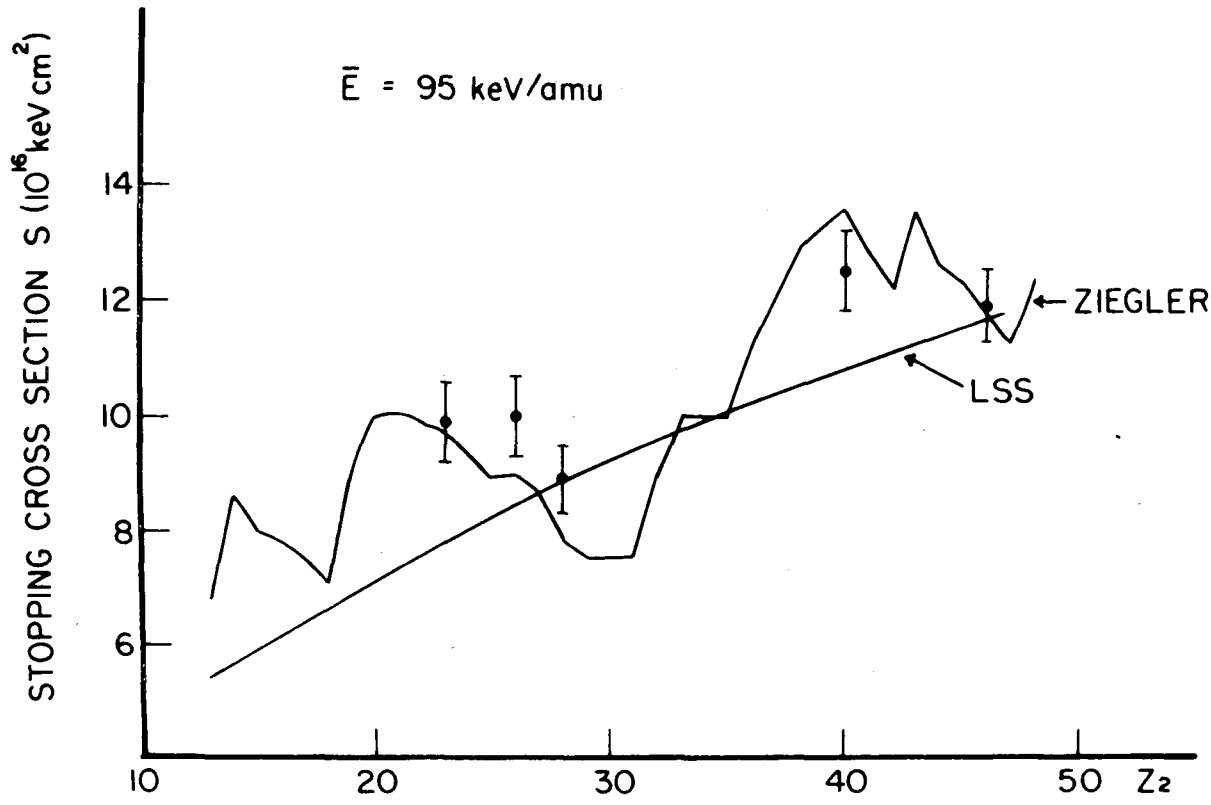

We propose to extend the measurements to other Z_2's between 13 and 50. An experiment is planned using a similar technique to study the energy loss of a heavy ion in a target of the same element as the ion (Ag in Ag, for example). Such measurements may yield valuable information for the interpretation of thick target DSAM data on nuclear lifetimes.

This work was performed in collaboration with Mr. R.V.Ribas and Dr. W.A. Seale, and was partially supported by CNPq.

References:

1) K.C.Shane and G.G.Seaman, Phys. Rev. B8(1973)86.
R.V.Ribas et al, Phys. Rev. A21(1980)1173.

2) J.Lindhard et al, K. Dan Vidensk, Selsk, Mat. Fys. Medd. 33, N°14 (1963).

3) Stopping and Ranges of ions in matter, J.F.Ziegler, vol. 4, Pergamon Press (1977).

SCHRODINGER DAMPING OF COLLECTIVE MOTION

S.Hernández

Departamento de Física, Facultad de Ciencias Exactas y Naturales,
Universidad de Buenos Aires

In this talk I will review same aspects of general theory of time-evolution of open systems, discuss some applications to nuclear physics and report part of our research in collaboration with B.Remaud from University of Nantes in France and C.Dorso from Universidad de Buenos Aires. We observe that the main features of heavy ion collisions in the deep inelastic regime consist of a) a large energy transfer from relative to intrinsic motion, probably via de excitation of some dorway states and b) the appearance of convection and transport processes, as evidenced by a moderate charge and mass exchange between the collision partners. From a many-body system point of view, the source for transport processes and relaxation towards thermal equilibrium is the two-body interaction V_{ij}, whose existence fixes the microscopic length and time scale.

The characteristic scales for an interacting many body system are (v_F being an average velocity, like the Fermi velocity in the nuclear matter case).

	Length	Time
Microscopic	Interaction range r_0	Collision time $\tau_c = r_0/v_F$
Micro-macro	Mean free path $\ell \sim 1/\sigma_n$	Relaxation time $\tau_r = \ell/v_F$
Macroscopic	Length of variation of macroscopic magnitudes $L \sim f/\lvert\vec{\nabla} f\rvert$	Hydrodinamic time $\tau_H = L/v_F$

One generally speaks of Markovian processes whenever $\tau_c \ll \tau_r$, and the evolution is said to take place in a hidrodynamic regime if $\tau_r \ll \tau_H$. Now, some collective modes in nuclear systems associated with charge transfer (giant dipole resonance in spherical nuclei and charge asymmetry relaxation in DIC) possess a typical wavelength of the order of the nuclear radius, the hydrodynamic time (time that a particle travelling with the mean velocity needs to travel through the inhomogeneity) being of the order of τ_r . In addition, the period of such modes is comparable to τ_c. Consequently a hydrodynamic description of the damping of these modes could be inadequate and one is tempted to go back to the microscopic origin of fluid equations, to search foa a better approach. We then consider the evolution of the density operator of a nucleus, as given by the Schrödinger - von Neumann equation,

$$i\hbar \frac{\partial \rho}{\partial t} = L\rho \tag{1}$$

with solution

$$\rho(t) = e^{-iLt}\rho(0) \tag{2}$$

with

$$L = [H, \ ] \tag{3}$$

Assume now that one can decompose ρ as

$$\rho = \rho_0 + \rho_c \tag{4}$$

where ρ_0 depends upon the coordinates of interest (the collective ones) and ρ_c depends upon the irrelevant (intrinsic variables) and contains the coupling between the distinct degrees of freedom. The separation of irrelevant variables through projection techniques[1-7] gives rise to a <u>master equation</u> or propagation equation for the vacuum ρ_0,

$$i\hbar \frac{\partial \rho_0}{\partial t} = L_0 \rho_0 + \quad \text{flow term (free propagation)}$$

$$+ i \int_0^t d\tau\, \psi(\tau)\, \rho_0(t-\tau) \quad \text{Collision term (exhibits the memory effects)}$$

$$+ U_{0c}\, \rho_c(0) \quad \text{Propagation of the initial correlations}$$

In the markovian case ($\tau_c << \tau_r$), i.e; when a good separation of time scales is available, one could find an asymptotic regime for , valid for $\tau_c < t < \tau_r$, described by a kinetic equation,

$$i\hbar \frac{\partial \tilde{\rho}_0}{\partial t} - L_0 \tilde{\rho}_0(t) + i \int_0^\infty d\tau\, \psi(\tau) e^{i\theta\tau} \tilde{\rho}_0(t) = \Theta\, \tilde{\rho}_0(t) \qquad (5)$$

where the effective generator of evolution or kinetic operator θ is nonhermitian and satisfies the nonlinear integral equation,

$$\Theta = L_0 + i \int_0^\infty d\tau\, \psi(\tau) e^{i\theta\tau} \qquad (6)$$

As an application of this general theory, a nuclear collective mode described by ρ_0 would evolve in time as indicated by the master or the kinetic equation, keeping its coherence, while the correlation density ρ_c describes the fluctuations upon the coherent motion associated with single particle (s.p.) diffusion. This picture could be valid for low frequency modes, like relative motion or mass transfer in DIC, but charge oscillation modes deserve a detailed treatment, since a kinetic model is of dubious application in view of the overlapping characteristic time scales. One could choose the following alternative :
a) do not look for a kinetic equation; solve instead the master equation and, b) look for a Schrodinger - type of evolution, i.e; consider $\rho_0 \sim |\psi><\psi|$ namely a pure state. This ought to be considered as a simplifying assumption valid for rather low temperature as compared with the eigenfrequency of the mode under consideration for example, consider

that typical temperatures reached in DIC do not exceed 2 to 3 MeV, while a typical quantum of dipole excitation is about 15 MeV for medium to heavy nuclei.

Under hypothesis a) and b) we face the problem of propagation of pure states in a dissipative field, an ancient subject in Quantum Mechanics that so far has been approached from several viewpoints[8]. We rule out those attempts of quantizing classical damped motion[9] as well as heuristic considerations for the invention of frictional Hamiltonians[10] and summarize the state of the problem as follows, paying special consideration to the damped harmonic oscillator case, with unperturbed Hamiltonian

$$H_o = \frac{k}{2}\hat{x}^2 + \frac{1}{2m}\hat{p}^2 \qquad (7)$$

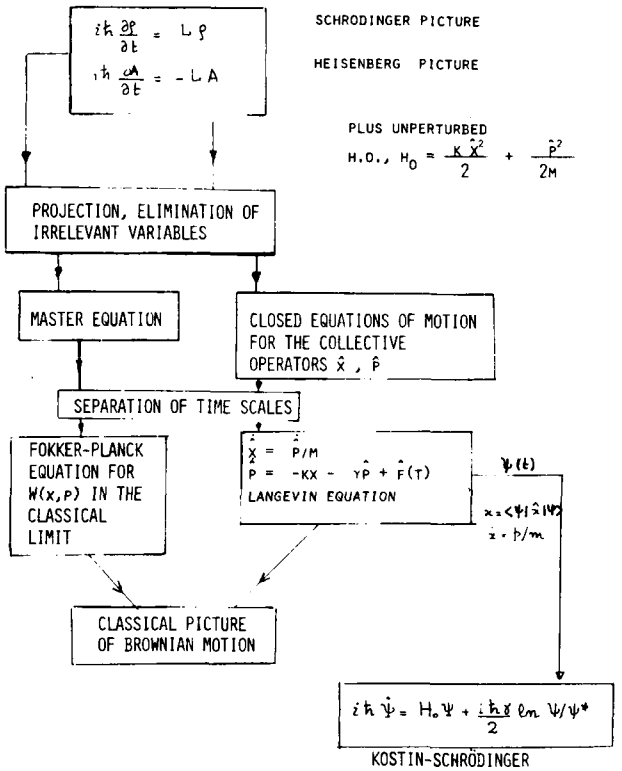

The Kostin-Schrödinger equation possess some of the features to be desired from a dissipative equation, except for a serious drawback: it does not damp almost any initial condition. Rather, it posseses at least two basis of stationary-like solutions, namely the gaussons[11] (similar to the oscillator eigenfunctions) and the breathing coherent states[12] (similar to the Glauber coherent states). Our present approach consists of utilizing the projection technique for the derivation of the master equation for an open system, actually an oscillator coupled to a dissipative environment, that represents a nuclear collective mode coupled to the intrinsic degrees of freedom. Considering a total Hamiltonian,

$$H = H_S + H_R + H_{RS} \tag{8}$$

where S stands for system and R for reservoir, and a decomposition

$$\rho(t) = \rho_S(t)\, \rho_R + \rho_c(t) \tag{9}$$

where ρ_R is a reference state for the heat reservoir, one realizes that the vacuum $\rho_0(t) = \rho_S(t)\, \rho_R$ can be extracted out of $\rho(t)$ with the projection operator

$$P = \rho_R\, T_R \tag{10}$$

Letting $Q = 1 - P$ and with the notation $L_{00} = PLP$, $L_{0C} = PLQ$, etc., one can write for the Schrödinger - von Neumann equation the two components,

$$i\hbar \dot{\rho}_0 = L_{00}\rho_0 + L_{0c}\rho_c \tag{11a}$$

$$i\hbar \dot{\rho}_c = L_{c0}\rho_0 + L_{cc}\rho_c \tag{11b}$$

Integration of (11b) and subtitution into (11a) gives

$$i\hbar\dot{\rho}_0 = L_{00}\rho_0 - i\int_0^t L_{0c}\, e^{-iL_{cc}\tau/\hbar} L_{c0}\rho_0(t-\tau) + L_{0c}\, e^{-iL_{cc}t/\hbar}\rho_c(0) \quad (12)$$

with $T_R\,\rho_0(t) = \rho_s(t)$, we find a <u>reduced master equation</u>,

$$i\hbar\dot{\rho}_s = (L_s + \overline{L}_{Rs})\rho_s + i\int_0^t \overline{\Psi}(\tau)\rho_s(t-\tau)\,d\tau \quad (13)$$

with the collision operator,

$$\overline{\Psi(\tau)} = T_R\left[H_{Rs}, e^{-iQH\tau/\hbar}\left[H_{Rs}, \quad\right] e^{iH\tau}\right] \quad (14)$$

We now look for solutions $\rho_S = |S\rangle\langle S|$ or $\rho_S^2 = \rho_S$ (pure states) following the lines:

a) multiply by ρ_S on the left and on the right using the rule

$\rho_S\, A\, \rho_S = \langle A\rangle\rho_S$; b) Add up and get

$$i\hbar\frac{\partial}{\partial t}\rho_s^2 = (L_S + \overline{L}_{Rs})\rho_s^2 + \{\Psi\rho_s, \rho_s\} \quad (15)$$

c) use $\rho_S = \rho_S^2$;

$$i\hbar\frac{\partial\rho_s}{\partial t} = (L_S + \overline{L}_{Rs})\rho_s + \{\Psi\rho_s, \rho_s\} \quad (16)$$

d) inquire whether

$$\{\Psi\rho_s, \rho_s\} = [W(\rho_s), \rho_s] \quad (17)$$

If this happens, the evolution equation is

$$i\hbar\dot{\rho}_s = [\mathcal{H}, \rho_s] \quad (18)$$

or equivalently

$$i\hbar \frac{\partial}{\partial t} |s\rangle = \mathcal{H} |s\rangle \tag{19}$$

with

$$\mathcal{H} = H_s + H_{RS} + W \tag{20}$$

a non hermitian operator.

The existence condition for W can be seen to be

$$Q\, H\tau \simeq H\tau \tag{21}$$

or $P\, H\tau \simeq 0$, indicating that the integration times (of the order of the mean life of the collision kernel, τ_c) ought to be short compared to the characteristic time of P H. In this case, $\mathcal{H}$ is the solution of a non-linear integral equation,

$$\begin{aligned}\mathcal{H} = H_s + H_{RS} - \\ -i\int_0^\infty d\tau\, T_R\{ H_{RS} e^{-iH\tau} H_{RS} \langle e^{-i\mathcal{H}^+\tau} e^{iH\tau}\rangle \\ - H_{RS} e^{-iH\tau} \langle e^{-i\mathcal{H}^+\tau} H_{RS} e^{iH\tau}\rangle - e^{-iH\tau} H_{RS} \times \\ \times \langle e^{-i\mathcal{H}^+\tau} e^{iH\tau} H_{RS}\rangle + e^{-iH\tau} \langle e^{-i\mathcal{H}^+\tau} H_{RS} e^{iH\tau} H_{RS}\rangle \} \rho_R e^{i\mathcal{H}\tau}\end{aligned} \tag{22}$$

In particular, the weak ($H \simeq H_S + H_R$) - plus-linear ($H_{RS} \simeq \lambda \Gamma_R(x_R) x$) coupling approximation gives a frictional potential

$$W \propto \lambda^2 D\, \hat{x}^2 = \lambda^2 D\, (\hat{x} - \langle \hat{x} \rangle)^2 \tag{23}$$

where

$$D = \int_0^\infty d\tau\, \overline{\Gamma\, \Gamma(\tau)} \tag{24}$$

CHARGE-EXCHANGE COLLECTIVE STATES

F.Krmpotić

Departamento de Física, Facultad de Ciencias Exactas,
Universidad Nacional de La Plata,
1900, Buenos Aires, Argentina.

1. Introduction

Change-exchange reactions, such as (p,n), (^{3}He,t), (π^+,π°), etc., and the corresponding charge conjugate processes, are very interesting for various reasons:

i) They provide an excellent tool to probe the nucleus with respect to the isospin dependent terms of the nuclear residual interaction. In particular, it has served as a tool to study the role of π- and ρ-exchanges in generating spin-isospin dependent forces and on the importance of the isobar Δ in low-energy nuclear processes.

ii) From the theoretical point of view, they have many features is common with the beta-decay processes and the charge-exchange gamma-decays.

iii) There is a great variety of charge-exchange vibrational fields which can be experimentaly investigated in many nuclei.

iv) The nuclear photoresonances and the giant magnetic resonances can be seen in a wider perspective when they are recognized as a single component of an isovector mode, whose additional components represent the charge-exchange modes.

2. Classification of the vibrational fields

The quantum numbers it has always that are associated to the nuclear modes of excitation are determined by the symmetries of the fields that give rise to them. The collective vibrations are by non means and exception. These may be classified according to the properties of the spatial, spin and isospin parts of the specific operator

$$\mathcal{M}(\kappa,\sigma,\lambda,\mu;\tau\mu_\tau) = \sum_{i=1}^{A} r_i^\kappa \left\{ Y_\kappa(i) \otimes \sigma^\sigma(i) \right\}_{\lambda\mu} \tau^\tau_{\mu_\tau} \qquad (1)$$

where the spin and isospin dependence are contained, respectively, in

$$\sigma^\sigma_{\mu_\sigma}(i) = \begin{cases} 1 & \sigma=0 \quad \text{(non-spin-flip)} \\ \sigma_{\mu_\sigma}(i) & \sigma=1 \quad \text{(spin-flip)} \end{cases}$$

$$\tau^\tau_{\mu_\tau} = \begin{cases} 1 & \tau=0 \quad \text{(isoscalar)} \\ \tau_{\mu_\tau} & \tau=1 \quad \text{(isovector)} \end{cases}$$

The quantum numbers $\kappa, \sigma, \lambda, \tau$ and μ_τ stand; respectively, for the orbital angular momnetum, the spin, the total angular momentum ($\vec{\lambda}=\vec{\kappa}+\vec{\sigma}$), the isospin and the third component of the isospin carried by the excitation. For example, $\tau=0$ corresponds to isoscalar excitations; $\tau=1$ corresponds to isovector excitations; when $\sigma=1$ there are spin-flip processes, etc. The parity of the vibrational quanta is determined by the orbital multipole order

$$\pi = (-)^\kappa$$

The charge conserving excitations ($\mu_\tau=0$) are usually classifed in the same way as the corresponding inverse gamma transitions, i.e. as <u>electric</u> or non-spin-flip modes ($\sigma=0$) and <u>magnetic</u> or spin-flip modes ($\sigma\neq\emptyset$).

Accordingly, the charge-exchange fields ($\mu_\tau = \pm 1$) can be labeled in the same way as the corresponding inverse $\beta^{\pm}$-decays, i.e., as allowed ($\kappa=0$), first forbidden ($\kappa=1$), second-forbidden ($\kappa=2$), etc.. Furthermore the allowed excitations may be of Fermi-type ($\sigma=\lambda=0$) and of Gamow-Teller type ($\sigma=\lambda=1$). There are four first-forbidden collective fields; one being of vector or non-spin-flip type ($\sigma=0,\lambda=1$) and three of axial-vector or spin-flip type ($\sigma=1,\lambda=0,1,2$).

2.1 Vibrations in nuclei with N=Z

In a nucleus with N=Z, the ground state isospin is $T_0=0$ and the intrinsic motion is rotationally invariant in isospace, if we ignore the effects of the Coulomb field.

The charge conserving excitations can be written schematically as

$$|\tau=0\rangle = \frac{1}{\sqrt{2}}\left(|pp^{-1}\rangle + |nn^{-1}\rangle\right)$$

$$|\tau=1\rangle = \frac{1}{\sqrt{2}}\left(|pp^{-1}\rangle - |nn^{-1}\rangle\right)$$

where p refers to a proton-particle state and p^{-1} to a proton-hole state. The isoscalar modes are charge symmetric and involve neutrons and protons moving in phase; the isovector modes with $\mu_\tau = 0$ are charge antisymmetric and involve oscillations of neutrons and protons against each other (neutron-proton polarization).The charge-exchange excitations produce states in isobaric nuclei and are of the type $|np^{-1}\rangle$ and $|pn^{-1}\rangle$ for $\mu_\tau = 1$ and $\mu_\tau = -1$, respectively.

The number of particle-hole excitations, leading to nuclear states with isospin $T=\tau=1$ and the Z component $M_T=\mu_\tau=+1,0$, and -1, is controlled only by the mode-selection-rules but do not depend on μ_τ. The situation for a dipole mode ($\kappa=0$) in ^{40}Ca nucleus is illustrated in Figure 1; it is

supposed that the selection rule $\Delta N=1$, being N the principal oscillator quantum number, is strictly valid.

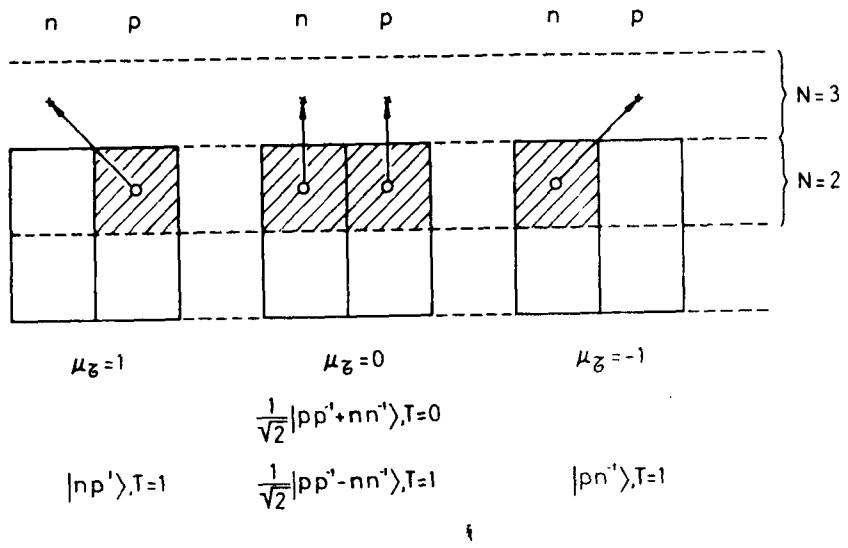

Figure 1.

Particle-hole excitations associated with dipole modes in the ^{40}Ca nucleus ($N=Z;T_o=0$). The hatched domains represent the particle orbits below the Fermi level and with the principal oscillator quantum number N=2. A dipole field promoves the particles from the orbitals with N=2 into the orbitals with N=3. The Coulomb field which makes the proton potential to have fewer bound state than the neutron potential, is ignored.

Excitation modes with $\tau=0$ and 1 are shown in Figure 2. For a given mode with $\tau=1$, the collective states with different components belong to an isobaric triplet (analog states) and their energies are given by the simple reaction

$$E(\tau=1,\mu_\tau=\pm1) = E(\tau=1,\mu_\tau=0) - \mu_\tau \Delta E_{coul} \qquad (2)$$

where ΔE_{Coul} is the Coulomb energy desplacement. Furthermore the transition strengths

$$S(\lambda,\tau=1,\mu_\tau=0) = B(\lambda,T=1) = \frac{|\langle I_f=\lambda, T_f=1 \| \mathcal{M}(\lambda,\tau=1) \| I_i=0, T_i=0\rangle|^2}{3(2\lambda+1)} \qquad (3)$$

for a field with the structure characteristic of the operator $\mathcal{M}(\lambda,\tau=1,\mu_\tau)$, are independent of μ_τ. Here, the matrix element is reduced both in spin and in isospin.

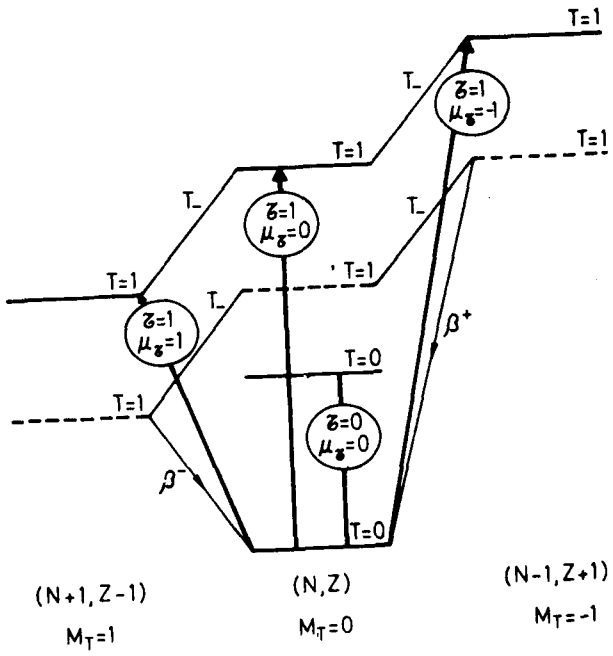

Figure 2:

Excitation of $\tau=0$ and $\tau=1$ vibrational modes in a nucleues with $T_o=0$. The symbol T_- stands for the isospin lowering operator which connects the isobaric analog states. The ground states of the adjacent nuclei and their analog state in the target are indicated by dashed lines. No quantitative significance is to be atached to the relative position of the levels.

Clearly, in nuclei with N=Z, the study of charge-exchange excitations do not yield any additional information, with respect to that obtained from the analysis of charge conserving modes, unless we are interested in

inquiring on the violation of isobaric symmetry through the Coulomb forces, magnetic forces, neutron-proton mass difference, small charge-dependent components in the strong interactions, etc.. All these effects are completely ignored in the present discussion.

2.2 Vibration in nuclei with N Z

In nuclei which have non-zero isospin in the ground state the number of particle-hole excitations depends, both on the mode-selection-rules and on the neutron excess; the Pauli principle leads to a reduction in the number of proton orbitals that can be excited into the neutron orbitals and a corresonding increase, in the number of neutrons that can be promoved into the proton orbitals[1]. The patern of the dipole particle-hole excitations in a doubly-open shell nucleus is schematically illustrated in Figure 3.

An isovector particle-hole operator with $\mu_\tau=1$ acting on the ground state of a nucleus with $T_0\neq 0$ lead uniquely to states with isospin T_0+1 and third component T_0+1. This follows from the nature of the excitation operator and the fact that the isospin of a state cannot be smaller than its third component. In the case however where $\mu_\tau=0$, both states with isospin T_0 and T_0+1 can be excited while finally the $\mu_\tau=-1$ processes lead to all possible isospin values viz. T_0+1, T_0 and T_0-1. The corresponding intensitites for a multipole operator $\mathcal{M}(\lambda,\tau=1,\mu_\tau)$ are now given by[2-4]

$$\mathcal{S}(\lambda,T,\mu_\tau) = \langle T_0 T_0\ 1\ \mu_\tau \mid T_0, T_0+\mu_\tau\rangle^2\, \mathcal{B}(\lambda,T) \qquad (4)$$

where

$$\mathcal{B}(\lambda,T) = \frac{|\langle I_f=\lambda, T_f=T \,|||\, \mathcal{M}(\lambda,\tau=1) \,|||\, I_i=0, T_i=T_0\rangle|^2}{(2\lambda+1)(2T+1)} \qquad (5)$$

are the transition probabilities reduced both in angular momentum and isospin. The total transition strength for a given orientation in isospace are defined as

$$S(\lambda,\mu_\tau) = \sum_T \mathcal{B}(\lambda,T,\mu_\tau) \qquad (6)$$

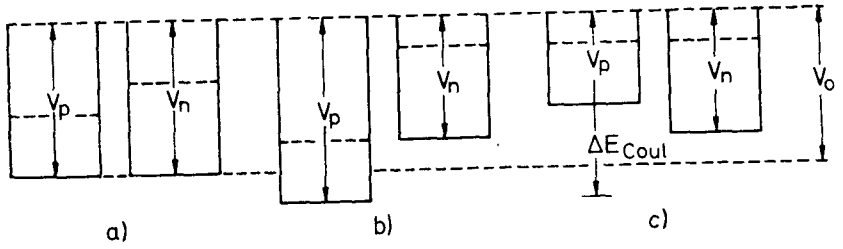

Figure 3:

Interplay between the symmetry potential V_1 Coulomb energy desplacement ΔE_{Coul} in a nucleus with N>Z : i) when V_1 is neglected, the average nuclear potentials in which the protons and neutrons move (V_p and V_n, respectively) are equal to V_1 (fig.3a); ii) when V_1 is included the proton potential becomes deeper; whereas the opposite is true for the neutrons (fig.3b); iii) when, finally, the Coulomb forces are included, the bottom of the proton potential is moved upwards; as a result there are fewer bound states for protons than for neutrons (fig.3c).

A simple way to estimate the unperturbed strengths $S^{(0)}(\lambda,\mu_\tau)$ is based on the use of the recipe of Macfarlane[5] and French[6] (monopole sum rule). After dividing convenientely the shell-model orbitals into the filled (f), the valence (v) and empty (e) orbitals, and in such a way that no transition of the type v→v or f→e is possible, one has

$$S^{(0)}(\lambda,\mu_\tau) = \frac{1+|\mu_\tau|}{6(2\lambda+1)} \sum_v \left\{ \frac{\langle N_v^p(\mu_\tau)\rangle}{2j_v+1} \sum_e \langle j_v \| M(\lambda,\tau=1) \| j_e \rangle^2 \right. \\ \left. + \frac{\langle N_v^h(\mu_\tau)\rangle}{2j_v+1} \sum_f \langle j_f \| M(\lambda,\tau=1) \| j_v \rangle^2 \right\} \tag{7}$$

Here, the single-particle matrix elements are reduced with respect to both spin and isobaric spin, $\langle N_v^p(\mu_\tau)\rangle$ is the expectation value in the target state, of the number of active particles for the excitation $(\tau=1,\mu_\tau)$, and $\langle N_v^h(\mu_\tau)\rangle$ denotes the corresponding mean numbers of holes.

Knowing the total strengths $S(\mu_\tau)$, the B(T) values and the partial stengths $\mathcal{S}(T,\mu_\tau)$ are obtained from expression (4) and (6). Explicitly,

$$\mathcal{S}(T=T_0+1,\mu_\tau=1) = B(T=T_0+1) = S(\mu_\tau=1) \tag{8a}$$

$$\mathcal{S}(T=T_0+1,\mu_\tau=0) = \frac{B(T=T_0+1)}{T_0+1} = \frac{S(\mu_\tau=1)}{T_0+1} \tag{8b}$$

$$\mathcal{S}(T=T_0,\mu_\tau=0) = \frac{T_0}{T_0+1} B(T=T_0) = S(\mu_\tau=0) - \frac{S(\mu_\tau=1)}{T_0+1} \tag{8c}$$

$$\mathcal{S}(T=T_0+1, \mu_c=-1) = \frac{B(T=T_0+1)}{(2T_0+1)(T_0+1)}$$

$$= \frac{1}{(2T_0+1)(T_0+1)} \; S(\mu_c=1) \tag{8d}$$

$$\mathcal{S}(T=T_0, \mu_c=-1) = \frac{1}{T_0+1} \; B(T=T_0)$$

$$= \frac{1}{T_0} \; S(\mu_c=0) - \frac{1}{T_0(T_0+1)} \; S(\mu_c=1) \tag{8e}$$

$$\mathcal{S}(T=T_0-1, \mu_c=-1) = \frac{2T_0-1}{2T_0+1} \; B(T=T_0-1)$$

$$= S(\mu_c=-1) - \frac{1}{T_0} S(\mu_c=0) + \frac{S(\mu_c=1)}{T_0(2T_0+1)} \tag{8f}$$

One should notice that due to the Pauli principle

$$S(\mu_c=-1) \geq S(\mu_c=0) \geq S(\mu_c=-1) \tag{9}$$

and consequently,

$$B(T=T_0-1) \geq B(T=T_0) \geq B(T=T_0-1) \tag{10}$$

This means that the strength $\mathcal{S}(T=T_0+1, \mu_c=0)$ is reduced with respect to the strength $\mathcal{S}(T=T_0, \mu_c=0)$ not only by the geometrical suppression factor $1/T_0$, but also by the dynamical suppression factor $B(T=T_0+1)/B(T=T_0)$. A similar comment is pertinent for the three $\mu_c=-1$ partial strengths. In the weak coupling model of Fallieros et al [ ], the quantities $S(\mu_c)$ are independent of μ_c. As a consequence, the B(T) are independent of T and the relative excitation strengths for different final states are given simply by the geometrical factors (Clebsch-Gordon coefficients) displayed in relation

(4). Such an approximation is, however, only valid when neither neutron orbitals nor proton orbitals from the neutron excess region do not particpate in the excitation process (there is no coupling between T_0 and the vibrational motion); the corresponding phonon is considered to be a definite entity and rotates freely in isospin space.

The total uperturbed strengths are related as

$$2\,S^{(0)}(\mu_c=0) = S^{(0)}(\mu_c=1) + S^{(0)}(\mu_c=-1) \tag{11}$$

On the other hand, the following relations hold

$$S(\mu_c=-1) - S(\mu_c=1) = N-Z \tag{12}$$

and

$$S(\mu_c=-1) - S(\mu_c=1) = \frac{T_0}{\pi} \langle r^2 \rangle_{n\,exc} \tag{13}$$

for the Gamow-Teller and first-forbidden excitations, respectively; $\langle r^2 \rangle_{nexc}$ is the mean square radius in the neutron excess region[1,7].

The neutron excess implies, in addition, that the neutron and protons are subject to somewhat different average nuclear potentials, namely

$$V = V_0 + \frac{1}{2} t_z \frac{N-Z}{A} V_1 \quad \begin{cases} t_z = 1/2 & \text{neutrons} \\ t_z = -1/2 & \text{protons} \end{cases} \tag{14}$$

Comparing the last term with a similar term in the Weizsäcker mass formula (symmetry energy) we obtain the estimate $V_1 \approx 100$ MeV. The interplay of the Coulomb potential with the symmetry term on the proton and neutron single-particle potentials is shown in Figure 3.

The static isovector potential acts on the isospin carried by the vibrational motion in such a manner as to favour states with low total isospin. The coupling energy can be estimated from eq.(14),

$$H' = \frac{V_1}{A}(\vec{\tau}.\vec{T}_0) = \frac{V_1}{2A}X \qquad (15)$$

where $X=T(T+1)-T_0(T_0+1)-2$. The particle-hole interaction also favour states with low total isospin, as it will be seen from the discussion which follows. The pattern of the isovector dipole non-spin-flip excitations ($\lambda=1,\pi=1,\sigma=0,\tau=1$) in ^{90}Zr nucleus is shown in Figure 4.

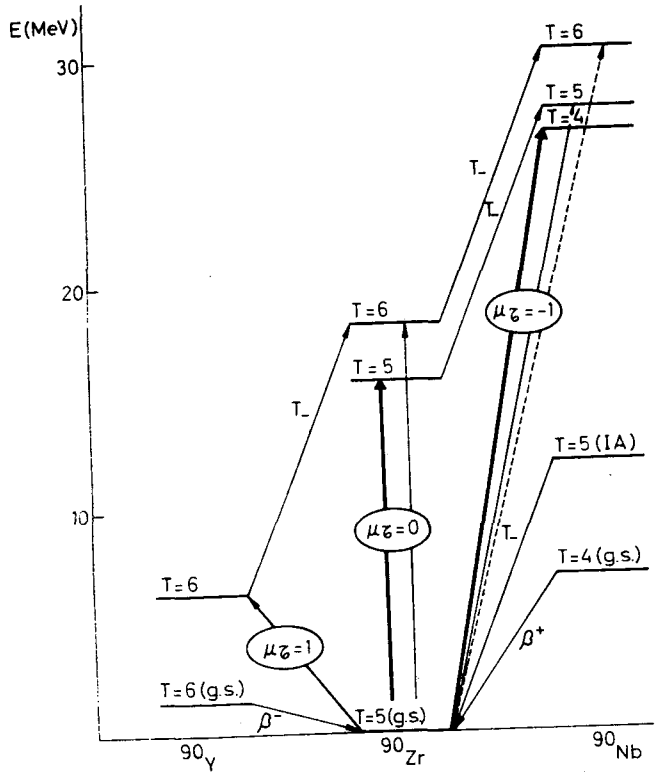

Figure 4:

Estimated excitation energies for the non-spin-flip dipole resonances in ^{90}Zr, within schematic model. The thickness of the lines that begin in the ground state of ^{90}Zr represent the transition stregnths. The symbol T_- stands for the isospin lowering operator which connects the isobaric analog states.

3. Qualitative features of the first-forbidden resonances.

3.1 Excitation energies and the transition strengths

ALthough we will limit our attention to the first-forbidden excitations, most of the results, which will be presented below, are also

valid with some minor changes, for other charge-exchange collective states (Gamow-Teller, second forbidden, etc.).

We assume a degenerate model for the single-particle energies and the radial wave funcitons are approximated by those of an harmonic oscillator. Furthermore, we introduce a very schematic force of the form

$$H(\sigma) = \frac{1}{2} \chi_\sigma \sum_{\mu,\mu_\tau} \mathcal{M}^+(\sigma,\lambda\mu;\mu_\tau)\, \mathcal{M}(\sigma,\lambda\mu,\mu_\tau) \tag{16}$$

where $\chi_0 \equiv \chi_V$ and $\chi_1 \equiv \chi_A$ are, respectively, the vector and axial-vector coupling constants and $\mathcal{M}(\sigma,\lambda,\mu;\mu_\tau) \equiv \mathcal{M}(\kappa=1,\sigma,\lambda\mu;\tau=1,\mu_\tau)$ is the multipole operator defined in eq.(1). The corresponding unperturbed energies are

$$\ell^{(0)}(T,\mu_\tau) = \varepsilon + \frac{V_1}{2A} X - \mu_\tau \Delta' E_{Coul} \tag{17}$$

with

$$\varepsilon = \hbar\omega_0 = 41\, A^{-1/3} \text{ MeV} \tag{18}$$

In the Tamm-Dancoff approximation (TDA) the transition strengths are not affected by the residual interaction ($\mathcal{J}(T,\mu_\tau) \equiv \mathcal{J}^{(0)}(T,\mu_\tau)$) while the perturbed excitation energies are given by[4,8]

$$\begin{aligned} e(\sigma,\lambda;T\mu_\tau) &= e^\circ(T,\mu_\tau) + \chi_\sigma B^{(0)}(\sigma,\lambda;T) \\ &= \varepsilon + \chi_\sigma S^{(0)}(\sigma,\lambda,\mu_\tau=0) + \frac{X U_\sigma}{2T_0} - \mu_\tau \Delta E_{Coul} \end{aligned} \tag{19}$$

where

$$U_\sigma = U_0 - \chi_\sigma \Delta_S \;;\quad U_0 = \frac{V_1 T_0}{A} \;;\quad \Delta_S = \frac{T_0 \langle r^2\rangle_{n\,exc.}}{2\sigma} \tag{20}$$

The unperturbed strengths $S^{(0)}(\sigma,\lambda;\mu_t=0)$ are given by the relations

$$S^{(0)}(\sigma=0,\lambda=1,\mu_t=0) = \frac{3}{8\pi} A^{4/3} \hbar m^2 \tag{21}$$

and

$$S^{(0)}(\sigma=1,\lambda,\mu_t=0) = S^{(0)}(\sigma=0,\lambda=1,\mu_t=0)\,(1+\delta_\lambda) \tag{22}$$

where

$$\delta_1 = \frac{2}{3A}\langle 0|\sum_{i=1}^{A}\vec{\ell}(i)\,\vec{\sigma}(i)\,|0\rangle = 2\hat{o}_1 = -2\hat{o}_2 \tag{23}$$

with $|0\rangle$ denoting the target state[7,9]. Moreover, the $B^{(0)}(\sigma,\lambda;T)$-values are obtained from relations (8) with

$$S^{(0)}(\sigma,\lambda;\mu_t=\pm 1) = S^{(0)}(\sigma,\lambda,\mu_t=0) \mp \Delta_S \tag{24}$$

which follows from eqs.(11) and (13). It should be noted that the neutron excess in units of the number of particles in a major shell of the harmonic oscillator reads

$$\gamma = \Delta_S\left[S^{(0)}(\sigma=0,\lambda=1,\mu_t=0)\right]^{-1} \simeq 0.76\, A^{-2/3}(N-Z) \tag{25}$$

$$D_+ = e\,(T=T_0+1,\mu_t=0) - e\,(T=T_0,\mu_t=0)$$

$$= e\,(T=T_0+1,\mu_t=-1) - e\,(T=T_0,\mu_t=-1), \tag{26a}$$

$$D_- = e(T=T_0, \mu_c=-1) - e(T=T_0', \mu_c=-1) \tag{26b}$$

take a very simple term, in TDA, namely

$$D_+ = \frac{T_0+1}{T_0} U \tag{27a}$$

$$D_- = U \tag{27b}$$

In the random phase approximation (RPA) the unperturbed excitation energies for a given orientation in isospace μ_c are written as

$$E^{(\omega)}(\mu_c) = \sum_{T}' \langle T_0 T_0 1 \mu_c | T, T+\mu_c \rangle^2 e^{(\omega)}(T, \mu_c) \tag{28}$$

or

$$E^{(\omega)}(\mu_c) = \varepsilon + \mu_c (U_0 - \Delta E_{coul}) \tag{29}$$

After introducing the residual interaction the corresponding energies and transition stregths read[1,4].

$$E(\sigma,\lambda;\mu_c=0) = K_0(\sigma,\lambda) = \left\{ \varepsilon (\varepsilon + 2\chi_\sigma S^{(\omega)}(\sigma,\lambda,\mu_c=\sigma)) \right\}^{1/2} \tag{30a}$$

$$S(\sigma,\lambda;\mu_c=0) = \varepsilon S^{(\omega)}(\sigma,\lambda;\mu_c=0) \left\{ K_0(\sigma,\lambda) \right\}^{-1} \tag{30b}$$

$$E(\sigma,\lambda;\mu_c=\pm 1) = K(\sigma,\lambda) + \mu_c (U_\sigma - \Delta E_{coul}) \tag{30c}$$

$$S(\sigma,\lambda;\mu_c=\pm 1) = \left\{ \varepsilon S^{(\omega)}(\sigma,\lambda;\mu_c=0) + \chi_\sigma \Delta_S^2 \right\} \left\{ K_0(\sigma,\lambda) - \mu_c \Delta_S \right\}^{-1} \tag{30d}$$

where

$$K(\sigma,\lambda) = \left\{ \left[K_0(\sigma,\lambda) \right]^2 + \left[\chi_\sigma \Delta_S \right]^2 \right\}^{1/2} \tag{30e}$$

Usually in RPA, the energies of the dominant transitions, leading to the fully aligned states $M_T=T'$, are approximated by the energies $E(\mu_c)$, i.e.

$$e(T=T_0+\mu_c, \mu_c) \cong E(\mu_c) \tag{31}$$

in which case the energy splittings $D_\pm$ read

$$D_+ = U + K - K_0, \tag{32a}$$

$$D_- = U - K + K_0. \tag{32b}$$

If on the other hand it is assumed that a relation similar to (28) also holds for the perturbed energies, namely that

$$E(\mu_c) = \sum_T \langle T_0 T_0 1 \mu_c | T, T_0+\mu_c \rangle^2 e(T, \mu_c) \tag{28'}$$

one has

$$e(T=T_0+1, \mu_c=1) = K + U + \Delta E_{coul} \tag{33a}$$

$$e(T=T_0, \mu_c=0) = \frac{T_0+1}{T_0} K_0 - \frac{K-U}{T_0} \tag{33b}$$

$$e(T=T_0-1, \mu_c=-1) = \frac{2T_0+1}{2T_0-1}(K-U) - \Delta E_{coul} - \frac{1}{T_0(2T_0-1)}\{(2T_0+1)K_0 - K - U\} \tag{33c}$$

and[4,10]

$$D_+ = \frac{T_0+1}{T_0}(U + K - K_0) \tag{34a}$$

$$D_- = U - \frac{2T_0+3}{2T_0-1}(K-K_0) \qquad (34b)$$

The partial transition strengths $\mathcal{B}(T,\mu_z)$ are obtained from the total transition streghts by making use of relations (8). The results for the isovector dipole non-spin-flip excitations ($\tau=1,\pi=1,\sigma=0,\lambda=1$) in ^{90}Zr nucleus, within RPA and with V_1=100 MeV and χ_0=0.20 MeV.fm^{-2}, are shown in Figure 4.

The change in the energy associated with the spin-orbit interaction in the single-particle field mainly implies a greater spread for the spin-flip modes of rank one and two than for the remaining two excitations. In order to illustrate this fact we resort again to a schematic model. We assume that there are two single-particle orbitals with the orbital quantum numbers ℓ and $\ell'=\ell+1$, each of them being split into two states by the spin-orbit interaction. The former two states are assumed to be filled and the latter two empty and the effect of the neutron excess is not considered. The reduced transition probabilities between the states are evaluated in the asymptotic limit ($\ell \gg 1$) and the results are displayed in Figure 5.

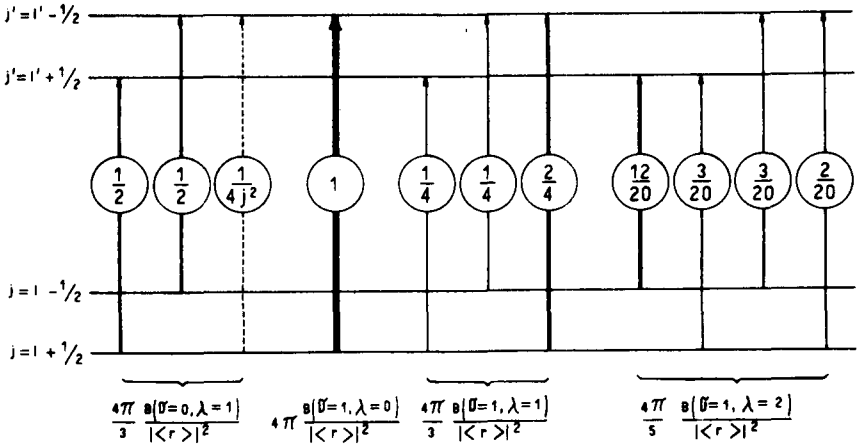

Figure 5:

The B(σ,λ) values in units of $(2\lambda+1)|\langle r\rangle|^2/4\pi$ between two single-particle orbitals with the quantum numbers and $\ell'=\ell+1$, evaluated in the asymptotic limit ($\ell\gg1$). The thickness of the vertical lines represent the transition strengths given in the circles.

3.2 Estimates of the coupling strengths

Assuming that both the static and the vibrational isovector fields are dominantly volume effects, Bohr and Mottelson[1] arrived to the following result for the vector coupling constant

$$\chi_V = \frac{\pi V_1}{A\langle r^2\rangle} \quad ; \quad \langle r^2\rangle = \frac{3}{5}(1.2\,A^{1/3})^2 \text{ fm}^2 \tag{35}$$

where V_1 is the parameter appearing in the symmetry potential (14). The average potential in the nucleus does not provide a similar relation for the axial-vector stregth χ_A as the density deformation with $\sigma=1$ is odd under time reversal.

Recently, Suzuki and Sagawa[11] derived separable interactions equivalent, in the RPA, to zero-range density-dependent interactions of the form

$$V(\vec{r}_1,\vec{r}_2) = \left\{ t_0\left[1+\chi_0\,\frac{1+\vec{\sigma}(1)\cdot\vec{\sigma}(2)}{2}\right] + \frac{1}{2}\,t_3\,\rho_0\left(\frac{\vec{r}_1+\vec{r}_2}{2}\right)\right\}\delta(\vec{r}_1-\vec{r}_2) \tag{35}$$

where $\rho_0(\vec{r})$ is the nuclear density in the ground state. The above expression is obtained by dropping the velocity dependent terms from the highly successful Skyrme-type force[12,13]. They were able to show that if one assumes a transition density for the $\sigma=0$ mode with the following spacial dependence

$$\langle 0|\sum_{i=1}^{A}\delta(\vec{r}_1-\vec{r}_2)\,\tau_{\mu_\tau}(i)\,|\sigma=0,\lambda=1,\mu;\mu_\tau\rangle \propto \rho_0(r)\,r\,Y_{1\mu}(\theta\varphi) \tag{36}$$

which corresponds to volume vibrations, the interaction (35) can be replaced, in RPA calculations, by a separable force like the one appearing in eq.(16) with χ_V given by eq.(35) and

$$V_1 = -\left[(1+2\chi_0) t_0 + \frac{1}{2} t_3 \rho_0(\vec{r}) \right] \rho_0(\vec{r}) \qquad (37)$$

If one introduces into this expression each one of the six different accepted choices for the parameters of the Skyrme force[12,13] and takes $\rho_0(\vec{r})=0.17$ nucleons/fm^3, one obtaines for V_1 values that range from 140 MeV to 200 MeV.

For the $\sigma=1$ modes the immediate generalization of eq.(36) is

$$\langle o | \sum_{i=1}^{A} \delta(\vec{r}-\vec{r}_i) \vec{\sigma}(i) \tau_{\mu_t}(i) | \sigma=1, \lambda\mu, \mu_t \rangle \propto \rho_0(r) r \vec{Y}_{(11)\lambda\mu}(\theta,\varphi) \qquad (38)$$

where, now, a vector spherical harmonic appears. Following the scheme of ref.[11] one finds[7] then

$$\chi_A = \chi_V + \frac{2\pi\chi_0 t_0 \rho_0}{A\langle r^2 \rangle} \qquad (39)$$

Again, for different choices of the parameters one gets for the ratio χ_A/χ_V values ranging from -0.17 to 1.5 . This indicates that the spin dependence of the Skyrme force is not reliable, which can be understood if one remebers that its parameters are fitted to ground state properties of even-even nuclei only[14].

3.3 Polarizability

It is a well known fact that the major modifications in an effective one-particle moment are induced by the frist order collective contributions, which involve the emission or absorption of a virtual phonon with the quantum numbers equal to those of the bare moment. The higher-order contributions i.e., the vertex corrections and the self-energy corrections have a tendency to cancel each other (the cancelation is exact

in the asymptotic limit[15]). Consequently, the first-forbidden charge-exchange vibrations will polarize dominantly the first-forbidden beta-decay moments. The renormalization of the single-particle β^- moment is illustrated by the diagrams in Figure 6.

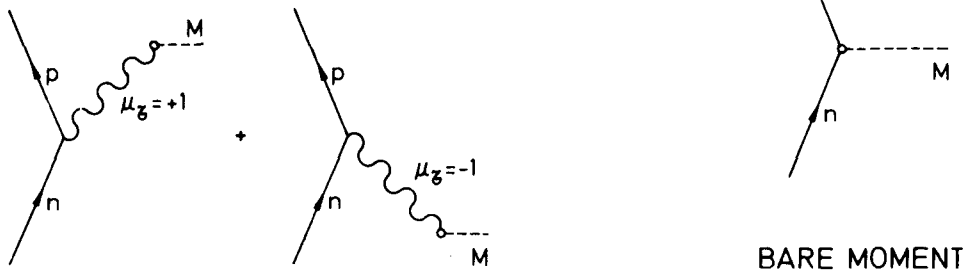

Figure 6:

Renormalization of single-particle β^- moment resulting from the corresponding charge exchange mode; all the quantum numbers of the polarization field are equal to the quantum numbers of the bare vertex.

Moreover, when one takes the advantage of the conservation of the vector current (CVC), which connects the β^- vector current J^V_μ and the electromagnetic current J^{el}_μ through the relationship

$$e\, J^V_\mu = -g_v \left[T_-, J^{el}_\mu \right] \tag{40}$$

it follows that the β^- moment $\langle f \| i\mathcal{M}(\sigma_v, \lambda=1) \| i \rangle$ ($i\mathcal{M}(\sigma_v, \lambda=1) = -g_v \mathcal{M}(\sigma=1, \lambda=1, \tau=1, \mu_z=-1)$) is related to the E1 gamma moment $\langle f \| i\mathcal{M}(E1) \| IA, i \rangle$ by

$$\langle f \| i\mathcal{M}(\sigma_v, \lambda=1) \| i \rangle = g_v \frac{(2T_i)^{1/2}}{e} \langle f \| i\mathcal{M}(E1) \| IA, i \rangle \tag{41}$$

where the state $|\, IA; i\rangle \equiv T_- |\, i\rangle / \sqrt{2Ti}$ is the isobaric analog (IA) of the state $|\, i\rangle$ and e and g_v are, respectively, the electric and weak-vector

coupling constants; the axial coupling constant will be denoted by g_A. The eq.(41) implies that the same polarization effects as for the beta decay moments $\langle f \| i\mathcal{M}(\rho_V, \lambda=1) \| i \rangle$ will take place for the charge-exchange E1 gamma decay from the IA state and the beta decay in ^{141}Ce is shown in Figure 7.

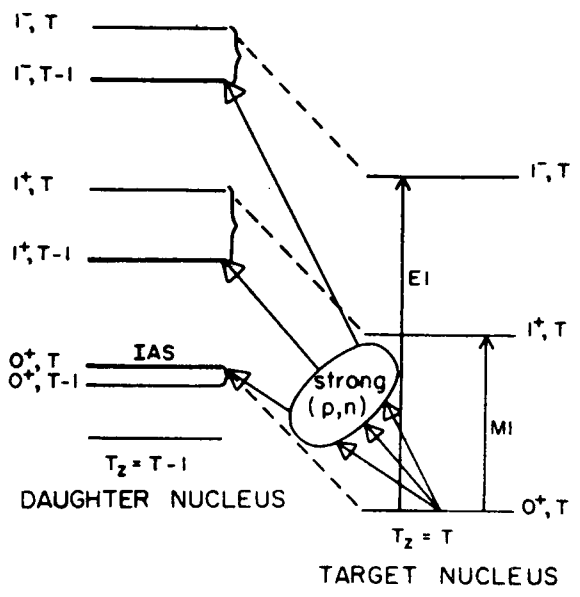

Phys Rev.
Krupotic 7C (1973) 469
(fig 1)

Figure 7:

Schematic diagram of β^- decay and the isobaric analog E1 gamma process.

The polarizability P(ω) induced by a field with the same symmetry as the beta moment in question is defined by

$$\langle \hat{\mathcal{M}}(\lambda) \rangle = \langle \mathcal{M}(\lambda) \rangle (1 + P(\omega)) = \langle \mathcal{M}(\lambda) \rangle (1 - P^{(0)}(\omega))^{-1} \qquad (42)$$

where ω is the frecuency of the beta transition and $P^{(0)}(\omega)$ is the response of the independent-particle system. In the RPA reads[1)]

$$P^{(0)}(\omega) = -\chi \left(\frac{S^{(0)}(\mu_c=-1)}{E^{(0)}(\mu_c=-1) \mp \hbar\omega} + \frac{S^{(0)}(\mu_c=1)}{E^{(0)}(\mu_c=1) \pm \hbar\omega} \right) \qquad (43)$$

where the upper and lower signs correspond to $\mu_c = \pm 1$. For $\hbar\omega \approx 0$, corresponding to transitions between nuclei close the beta-stability line,

the renormalization implied by eq.(43) is the same for the moments with $\mu_c = \mp 1$. Moreover, if we neglect the difference between the vector and axial vector strengths (see eq.(22)) and, following Bohr and Mottelson[1], use the approximation

$$\mp^{(0)}(\mu_c = \mp 1) = \epsilon(1 \pm \nu) \tag{44}$$

the response $P^{(0)}(\omega=0)$ takes the form

$$P^{(0)}(\omega=0) = -2\zeta \tag{45}$$

with

$$\zeta = S^{(0)}(\mu_c=0)\chi/\epsilon = 2.9\times10^{-3} A^{S/3} \chi \ fm^2/MeV \tag{46}$$

Several studies of the polarization phenomena in frist-forbidden beta transition were performed, through the analysis of the experimental data. As an example, we mention the results for the $7/2^-$ $5/2^+$ transition in the ^{141}Ce nucleus[16],

$$\begin{aligned} P_{V,\lambda=1} &= -0.63 \pm 0.08 \\ P_{A,\lambda=1} &= -0.59 \pm 0.11 \\ P_{A,\lambda=2} &= -0.74 \pm 0.10 \end{aligned} \tag{48}$$

where $P \equiv P(\omega=0)$. Consequently,

$$\begin{aligned} \zeta_{V,\lambda=1} &= 0.85^{+.37}_{-.24} \\ \zeta_{A,\lambda=1} &= 0.72^{+.45}_{-.26} \\ \zeta_{A,\lambda=2} &= 1.4^{+1.2}_{-.5} \end{aligned} \tag{49}$$

and

$$\chi_{V,\lambda=1} = \left(.29^{+.13}_{-.08}\right) \cdot 10^3 A^{-5/3} \text{ MeV fm}^{-2} \qquad (50)$$

$$\chi_{A,\lambda=1} = \left(.25^{+.15}_{-.09}\right) 10^3 A^{-5/3} \text{ MeV fm}^{-2}$$

$$\chi_{A,\lambda=2} = \left(.5^{+.4}_{-.2}\right) 10^3 A^{-5/3} \text{ MeV fm}^{-2}$$

On the other hand, from the analysis of the gamma decay of the $I^\pi = 7/2^-$ isobaric analog resonances to the $I^\pi = 5/2^+$ ground state in ^{141}Pr, it was found that[17]

$$P_{V,\lambda=1} = -0.74 \pm 0.06$$

or

$$\zeta_{V,\lambda=1} = 1.42^{+.58}_{-.36}$$

$$\chi_{V,\lambda=1} = \left(.49^{+.20}_{-.12}\right) 10^3 A^{-5/3} \text{ MeV fm}^{-2} \qquad (51)$$

It is worth noting that from eq.(35) one has

$$\chi_{V,\lambda=1} = 3.64\, V_1\, A^{-5/3} \text{ MeV fm}^{-2} \qquad (52)$$

4. Experimental information

The Fermi resonances are known since the discovery of a well-defined isobaric multiplet structure by Anderson and Wong[18]. The first clear evidence of the concentration of the Gamon-Telller (GT) strength was seen by Doering et al.[19] through the ^{90}Zr(p,n)^{90} reaction at incident proton energies of 35 and 45 MeV and $\Theta = 0°$ (see figure 8). This GT resonance was latter confirmed by a subsequent ^{90}Zr(^{3}He,t)^{90}Nb experiment at 130 MeV in Jülich[20] and other at 80 MeV in Grenoble[21].

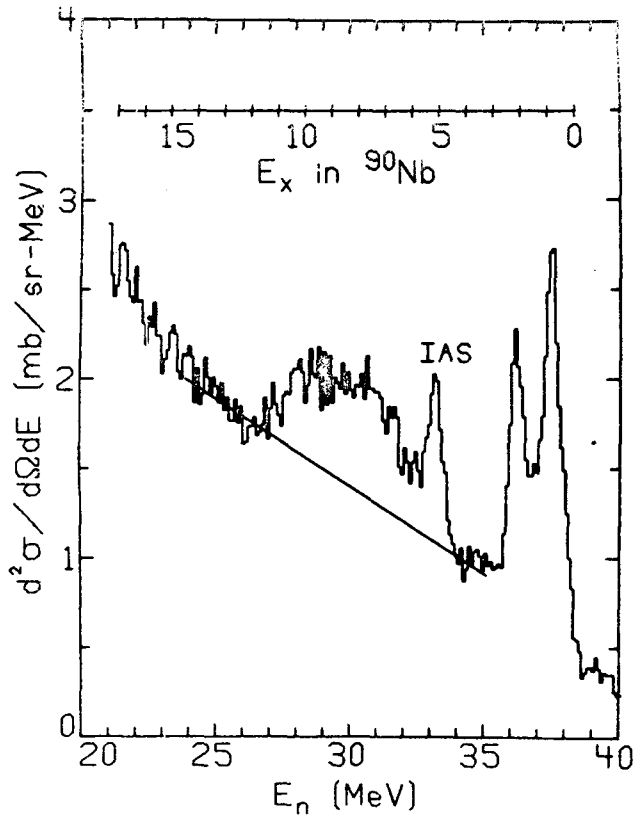

Figure 8

Differential cross section versus neutron energy for $^{90}Zr(p,n)^{90}Nb$ at E_p=45 MeV and θ =0°. The straight line represents the background fit to regions adjacent to the broad peak and IAS (from ref.[19]).

The availability of intermediate energy protons at the Indiana University Cyclotron Facility (IUCF) has served as a stimulus for further investigations of the (p,n) reaction. In a study of the $^{90}Zr(p,n)^{90}Nb$ reaction at E_p=120 MeV, Bainum et al.[22] measured neutron angular distributions and found, in addition to the IAS and a T=4 giant GT resonances, two additional peaks at 13.4 MeV and 17.9 MeV in ^{90}Nb, which were interpreted, respectively, as the T=5 component of the GT resonance and a T=4 first-forbidden oscillation (see figure 9). A similar $\mathcal{K}$ =1 resonance was also observed by Horen et. al.[23] in the $^{208}Pb(p,n)^{208}Bi$ reaction at 120 and 160 MeV. The cross section of this resonance at the first maximum was found to be comparable to that of the giant GT resonance at 0° and behaved similarly as a function of proton energy, since the GT resonance is excited via the spin-isospin component of the residual

interaction, it was argued[23] that the excitation of $\sigma\tau$=1 resonance also involves $\sigma\tau$=1 and, hence, could have $I^{\pi}=0^{-}$, 1^{-} or 2^{-}. They have also observed two weak peaks at 22.9 MeV and 24.6 MeV in ^{209}Bi and suggested to be the isobaric analogs of the M1 states in ^{208}Pb (i.e. the $T=T_0=22$ components of the GT strength).

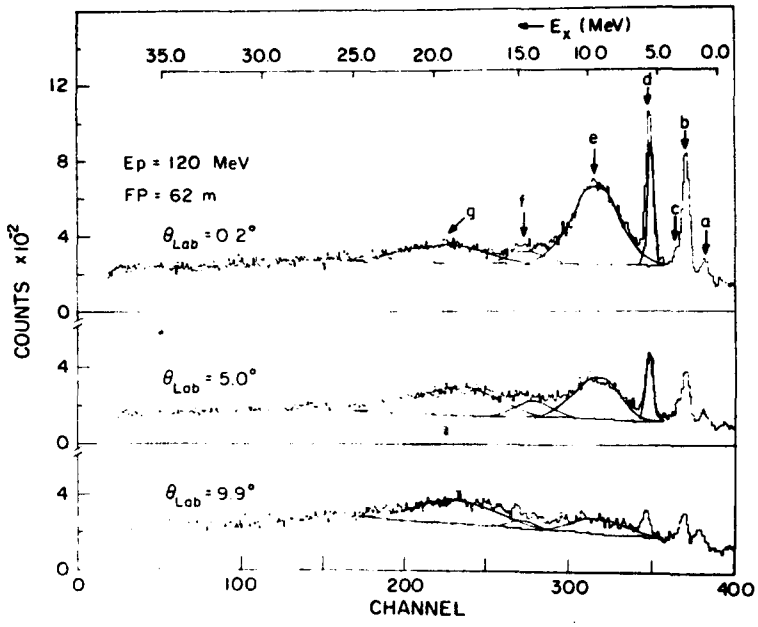

Figure 9

Time-of-flight neutron spectra for ^{90}Zr(p,n)^{90}Nb reaction at Θ =0°, 5° and 10° laboratory angles. The peaks labeled d, e, f and g are assumed to be, respectively, the Fermi resonance, the T=4 and T=5 GT states and a first-forbidden collective state (from ref.[22]).

Quite recently, Sterreburg et al.[24] have measured neutron spectra at small angles resulting from the bombardent with 45 MeV protons on 17-target from ^{90}Zr to ^{208}Pb. Common features to the spectra were:

i) a sharp peak representing the isobaric analog state or the Fermi resonance,

ii) a broad peak (FWHM$\sim$3-4 MeV), interpreted as a GT state with isospin $T=T_0-1$, at a slightly higher but target dependent excitation energy, and,

iii) a similarly broad peak $\sim$ 10 MeV above the first bump which was suggested to be the $T=T_0-1$ component of the giant vector-dipole resonance.

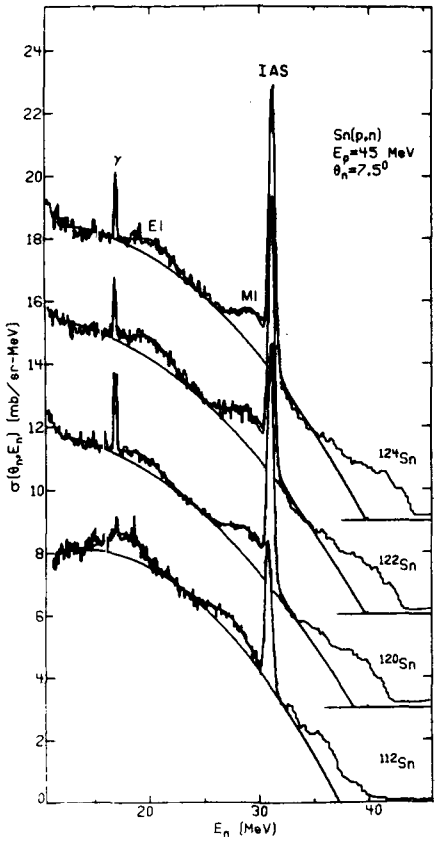

Figure 10

Neutron spectra for ^{112,120,126,124}Sn(p,n) measured at 7.5°. The base lines for ^{120}Sn, ^{122}Sn and ^{124}Sn are shifted for display purposes (from ref.[24]).

Figure 10 shows the neutron time-of-flight spectra for four Sn isotopes. In addition to the IAS at about 31 MeV neutron energy and the sharp gamma-ray peak leaking through the pulse-shape disciminator, two broad peaks are clearly visible in all four spectra. As one can see, both peaks shift towards the IAS as the neutron excess increases. This effect is even more visible in figure 11 where the neutron spectra are shifted in energy so that the IAS peaks all fall on the same vertical line, thereby graphically corrected for the Coulomb displacement energies.

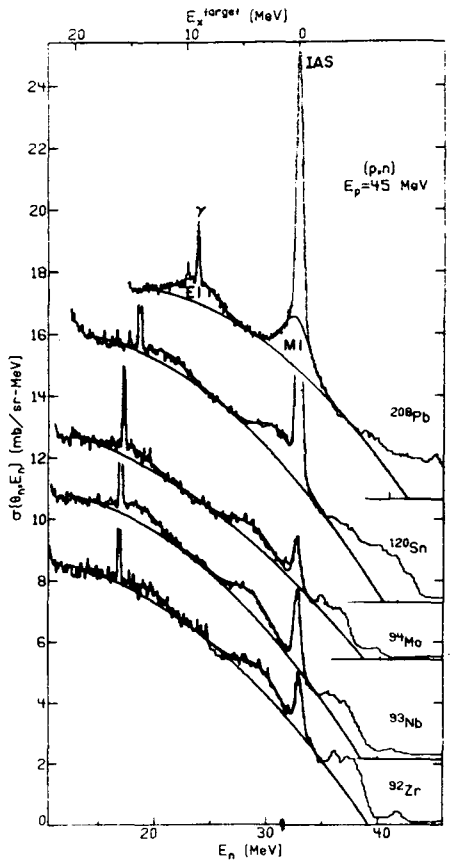

Figure 11:
Neutron spectra for ^{92}Zr, ^{93}Nb, ^{94}Mo, ^{120}Sn and ^{208}Pb corrected for Coulomb displacement energies. The ^{93}Nb spectrum was measured at 11°, the other at 7.5°. The upper four spectra are shifted for display purposes. The bottom scale gives the neutron energies for ^{92}Zr only; the upper scale gives the calibration for the excitation energies in all the target nuclei, (from ref.[24]).

In a recent study[25] at IVFC, with incident proton energies of 120, 160 and 200 MeV and neutron flight path of 60-70 m, were measured the excitation energies of the GT and first-forbidden resonances for a number of targets (^{90,92,94}Zr, ^{112,116,124}Sn, ^{169}Tm and ^{208}Pb). Neutron time-of-flight spectra for θ=45°, i.e., near a maximum[22,23] in a the differential cross section for $\mathcal{K}$=1 and at E_p=200 MeV are shown in figure 12.

Since the calculations have shown[26,27] that the strength of the central spin-isospin component increases by more than a factor of two with

increasing proton energy between E_p=100 and 200 MeV, it was suggested[25] that the χ =1 bump should correspond to a axial-vector resonance (or to a superposition of axial -vector resonances). Moreover, Horen et al.[25] have argued that both bumps, when measured with respect to the IAS, could be represented by linear functions of (N-Z)/A,

$$E_{GT} - E_{IAS} = 6.7 - 30\ (N-Z)/A \quad (MeV) \quad ,$$
$$E_{\chi=1} - E_{IAS} = 13.6 - 33\ (N-Z)/A \quad (MeV) \quad . \qquad (53)$$

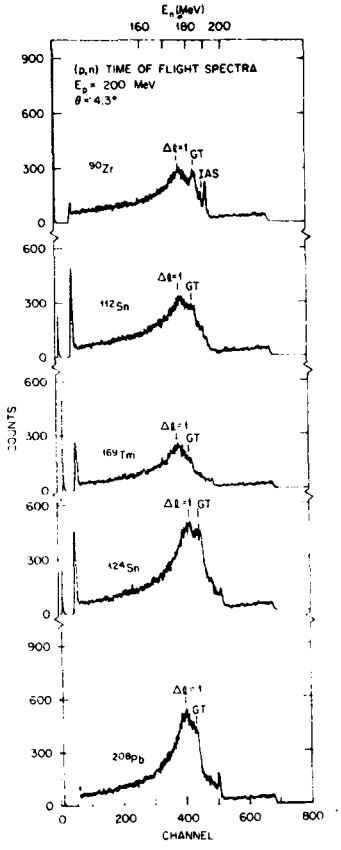

Figure 12:

Time-of-flight spectra at 4.3° for the (p,n) reaction at E_p=200 MeV for target of ^{90}Zr, ^{112}Sn, ^{169}Tm, ^{124}Sn and ^{208}Pb (from ref.[25]).

5. Numerical estimates

In a series of papers[28-32] in the arly 1960's, Fukita, Ikeda and Fujii explored the description of IAS in terms of proton particle-neutron hole pairs and subsequently hypothesized the existence of a collective GT resonance.

Gapanov and Lyvtotostanskii[33] have used the theory of finite Fermi systems and made microscopic calculations of the excitation energies and strengths of the IAS and GT resonances for a number of nuclei from Ar to La. Their predicted energy differences, $E_{GT}-E_{IAS}$ are in good agreement with the experimental results[25] for ^{116}Sn and ^{124}Sn; however, those for $^{90,92,94}Zr$ all on a parallel line about 2 MeV above than the measured values.

Recently, the theory of finite Fermi system has also been employed by Krmpotic et al[34] to calculate the first borbidden oscillations (with and without spin flip) for ^{208}Pb. It turned out that the transition strengths for these excitations were concentrated in the energy region of 19-26 MeV, measured with respect to the ground state of ^{208}Pb. They predicted the $\lambda=1, \sigma=0$ resonance to be located about 2.9 MeV above the IAS, while the second broad peak observed in the (p,n) energy. For the spin flip transitions, they[34] find the main strength of the $\lambda=0$ resonance to be concentrated about 6.6. MeV above the IAS, the $\lambda=1$ about 6.0 MeV, and the $\lambda=2$ resonance to be more fragmentated with the largest component about 0.3 MeV above the IAS. Moreover, the greater concentration of strength associated with the $\lambda=1$ component would imply that the $\chi=1$ structure should dominate. The position of the $\chi=1$ peak, reported by Horen et al.[25] is in qualitative agreement with this picture, but a detailed comparison will have to await final decomposition of the spectra and further analysis of the data.

The excitation energies and the $^{208}Pb(p,n)^{208}Bi$ cross sections of the allowed and first-forbidden resonances, were later calculated by Krewald et al.[35] and by Osterfeld et al.[36], respectively. They used the generalized Landau-Migdal interaction which includes in addition to the zero-range terms also the one-pion and one- -exchange potentials explicitely. In order to explain the excitation energies it was essential to use the Skyrme-III single particle spectrum ($\frac{m^*}{m}$ = 0.76) instead of the experimental one ($\frac{m^*}{m}$ = 1). Moreover, in the work of Osferfeld et al.[36] it was shown that the experimentally observed x=1 resonance in the $^{208}Pb(p,n)^{208}Bi$-reaction is a superposition of all possible first-forbidden modes. The fact that the theoretical spin-flip strengths overestimates the experimental values appreciably, was interpreted by Bohr and Mottelson[37] and by Brown and Rho[38] in terms of admixtures of Δ -particle-nucleon hole components in the RPA wave functions.

The above mentioned microscopic calculations allow for a detailed comparison of the theory with experiment. On the other hand, when the collective states are observed throughout the periodic table, the macroscopic models and the schematic calculations may provide us with the meaning of the systematic which reflects the structure. According to them, we can understand the structure of collective modes in an intuitive and intelligible way, and elucidate the difference between various kinds of nuclear collective motion in terms of few collective parameters. In view of these considerations, we discuss below the experimental results for the charge-exchange resonances in the framework of the schematic model presented in section 3 (see also refs.[4,10,39]).

In Table 1 we list the excitation energies of the first-forbidden modes, relative to the excitation energy of the IAS (namely $E(\sigma,\lambda,\mu_\tau=-1)-\Delta E_{Coul}$). The experimental data were taken from the works of Horen et al.[23] and Sterrenburg et al.[24]. The calculated values were obtained from

eqs.(30) with V_1=115 MeV and χ_1/χ_0 = 3/4. There was no other free parameter in the calculation. The overall agreement between the experimental results and the theoretical estimate for the excitation energies of the vector mode is quite satisfactory. A similar statement is valid for the position of the axial vector peak if one assumes that it is mainly build up from the x=1 resonance.

Finally it might be worthwile to mention that in the context of the theoretical formalism presented here, the energies of the first-forbidden mode can be approximated in the form (in MeV)

$$E(\sigma=0,\lambda=1,\mu_2=-1) - \Delta E_{coul} \simeq 75 A^{-1/3} - 22.6 \left(\frac{N-Z}{A}\right) + 7.2 \left(\frac{N-Z}{A}\right)^2 A^{-1/3}$$

$$E(\sigma=1,\langle\lambda\rangle,\mu_2=-1) - \Delta E_{coul} \simeq 70 A^{-1/3} - 28.8 \left(\frac{N-Z}{A}\right) + 5.4 \left(\frac{N-Z}{A}\right)^2 A^{-1/3} \qquad (54)$$

where the last equation refers to the aritmetic mean over λ and should be compared with the second expression in (53).

The work presented in this talk results mainly from a collaboration with Kanzo Nakayama and Alfredo Pio Graleao from the University of Sao Paulo, Brazil.

TABLE 1

Excitation energies of the first-forbidden resonances relative to the energy of the IAS.

TARGET	EXPERIMENT		THEORY			
	$\sigma=0\ \lambda=1$ a)	$\sigma=1, \lambda=2$ b)	$\sigma=1\ \lambda=0$	$\sigma=1\ \lambda=0$	$\sigma=1\ \lambda=1$	$\sigma=1\ \lambda=2$
^{90}Zr	14.5	12.9	14.9	13.5	12.8	11.4
^{91}Zr	14.6	--	14.7	13.2	12.5	11.1
^{92}Zr	14.5	12.5	14.6	12.9	12.3	10.8
^{94}Zr	14.2	12.0	14.2	12.5	11.7	10.2
^{96}Zr	14.0	--	13.9	12.0	11.3	9.6
^{93}Nb	14.4	--	14.6	13.3	12.5	11.0
^{94}Mo	14.7	--	14.6	13.6	12.8	11.1
^{96}Mo	13.7	--	14.3	13.1	12.3	10.5
^{97}Mo	13.8	--	14.1	12.8	12.0	10.2
^{98}Mo	13.4	--	14.0	12.6	11.7	9.9
^{112}Sn	13.2	10.2	13.5	12.4	11.7	10.1
^{116}Sn	13.1	9.3	12.8	11.0	10.5	9.4
^{120}Sn	11.8	--	12.2	9.9	9.5	8.5
^{122}Sn	11.0	--	12.2	9.7	9.2	8.4
^{124}Sn	10.6	7.3	12.0	9.6	9.0	8.2
^{169}Tm	--	7.6	10.9	7.9	7.7	7.4
^{208}Pb	9.0	6.4	9.9	7.5	6.8	6.3

a) Sterrenburg et al.[24]

b) Horen et al.[25]

References:

1) A.Bohr and B.Mottelson, Nuclear Structure (Benjamin, NY, 1975), Vol.II.

2) D.F.Peterson and C.J.Veje, Phys.Lett. 24B(1967)449.

3) S.Fallieros and B.Goulard, Nucl.Phys. 147(1970)593.

4) F.Krmpotic, Nucl. Phys. A351(1981)365.

5) M.H.Macfarlane, in Isobaric spin in nuclear physics, ed. J.D.Fox and D.Robson (Academic, NY, 1966) p.383.

6) J.B.French, in Many body description of nuclear structure and reactions, Proc. Int. School of Physics Enrico Fermi, Course 36, ed. C.Bloch (Academic, N.Y., 1966) p.278.

7) K.Nakayama, A.Galeao and F.Krmpotic, to be published.

8) R.O.Akyüz and S.Fallieros, Phys.Rev.Lett. 27(1971)1026.

9) T.Suzuki, Phys.Lett. 83B(1979)147.

10) F.Krmpotic, Phys.Rev.Lett. 46(1981)1261.

11) T.Suzuki and H.Sagowa, preprint RIFP-404 (Kyoto University, 1980).

12) D.Vautherin and D.M.Brink, Phys.Rev. C5(1972)626.

13) M.Beiner et al., Nucl.Phys. A238(1975)29.

14) G.Bertsch and S.F.Tsai, Phys.Rep. 18C(1975)125.

15) V.Paar, Phys.Lett. 60B(1976)232.

16) O.Civitarese, F.Krmpotic, M.C.Cambiaggio and L.Szybisz, Phys.Rev. C7(1973)768; L.Szybisz, F.Krmpotic and M.A.Fariolli, Phys.Rev. C1(1974)624.

17) H.Ejiri, Nucl.Phys. A166(1971)594.

18) J.D.Anderson and C.Wong, Phys.Rev.Lett. 7(1961)250.

19) R.R.Doering et al., Phys.Rev.Lett. 35(1975)1691.

20) A.Galonsky et al., Phys.Lett. 74B(1978)176.

21) D.Ovazza et al., Phys.Rev. C18(1978)2438.

22) D.E.Bainum et al., Phys.Rev.Lett. 44(1980)1751.

23) D.J.Horen et al., Phys.Lett. 95B(1980)27.

24) W.A.Sterremburg et al., Phys.Rev.Lett. 45(1980)1839.

25) D.J.Horen et al., Phys.Lett. 99B(1981)383.

26) F.Petrovich, The (p,n) reaction and the nucleon-nucleon force, eds. C.D.Goodman et al., (Plenum Press, N.Y., 1980) p.115.

27) W.G.Lore, The (p,n) reaction and the nucleon-nucleon force, eds. C.D.Goodman et al., (Plenum Press, N.Y., 1980) p.23.

28) K.Ikeda, S.Fujii and J.I.Fujita, Phys.Lett. 2(1962)169.

29) K.Ikeda, S.Fujii and J.I.Fujita, Phys.Lett. 3(1963)271.

30) J.I.Fujita, S.Fujii and K.Ikeda, Phys.Rev. 133(1964)B549.

31) K.Ikeda, Prog. Theor. Phys. 31(1964)434.

32) J.I.Fujita and K.Ikeda, Nucl.Phys. 67(1965)145.

33) Yu.V.Gaponov and Yu.S.Lyutostanskii, Yad. Fis. 16(1972)484 [Sov.J.Nucl.Phys. 16(1973)270]; Yad. Fis. 19(1974)62 [Sov.J.NucL.Phys. 19(1974)33].

34) F.Krmpotic, K.Ebert and W.Wild, Nucl.Phys. A342(1980)407.

35) S.Krewald, F.Osterfeld, J.Speth and G.E.Brown, Phys.Rev.Lett. 46(1981).

36) F.Osterfeld, S.Krewald, H.Dermawan and J.Speth, to be published.

37) A.Bohr and B.R.Mottelson, Phys.Lett. 100B(1981)10.

38) G.E.Brown and M.Rho, to be published.

39) F.Krmpotic and F.Osterfeld, Phys.Lett. 93B(1980)218.

PARTICIPANTS

1. INVITED LECTURES

Sven Bjørnholm	Niels Bohr Institutet University of Copenhagen DK-2100 Denmark
Malcolm Macfarlane	Department of Physics Indiana University Bloomington, Indiana, U.S.A.

2. PARTICIPANTS

Achterberg Erhard	CNEA
Acosta de Mehr María T.	CNEA
Behar Moni	TECHINT/CNEA
Bes Daniel	CNEA/CONICET
Bozzolo,Guillermo	UNLP/CIC
Cambiaggio Cristina	CONICET
Ceballos Alberto E.	CNEA
Civitarese Osvaldo	UNLP/CONICET
Debray Mario E.	CNEA
Do Barros Solange	UFRJ
Dragún Olga	CNEA
Dukelsky Jorge	CNEA
Dussel Guillermo	CNEA
Hendrik Alejandro J.	CNEA
Herrero Armando	CNEA
Milevich Alberto	CNEA
Cattone Aníbal	CNEA
Hernández Susana	CONICET/UNBA
Huck Hugo	CNEA
Krmpotic Francisco	UNLP
Macchiavelli Augusto	CNEA
Maqueda Ernesto	CNEA/CONICET
Marcondes Helene	USP
Mariscotti Mario A.J.	CNEA
Martí Guillermo	CNEA
Massmann Herbert	U.CH
Perazzo Roberto P.J.	CNEA/CONICET
Pereira Malta Corací	USP
Pérez Martha	CNEA
Perez Ferreira Emma	CNEA
Pomar Cayetano	CNEA
Proto Araceli	CNEA
Otero Dino	CNEA
Testoni Jorge	CNEA

Toledo Piza Antonio	USP
Rao Narayana	USP
Reich Silvia	CNEA
Sofía Hugo	CNEA
Ventura Edgardo	CNEA

CNEA: Comisión Nacional de Energía Atómica
CONICET: Consejo Nacional de Investigaciones Científicas y Técnicas
UNLP: Universidad Nacional de La Plata
UNBA: Universidad Nacional de Buenos Aires
UFRJ: Universidad Federal de Río de Janeiro
USP: Universidad de Sao Paulo
U.CH: Universidad de Chile

IMPRESO EN CNEA - JUNIO 1982